THE UNIVERSITY of ADELAIDE

Radiation Effects in Glasses for Intrinsic Optical Fibre Radiation Dosimetry

by

Christopher A. G. Kalnins

A thesis submitted in fulfillment of the degree of Doctor of Philosophy

in the

Faculty of Sciences
School of Chemistry and Physics
University of Adelaide, Australia

August 2015

Abstract

An optical fibre device has been developed for the purpose of detecting ionising radiation using optically stimulated luminescence. Characterisation of glass materials has been performed, after which optical fibres were fabricated for experiments to demonstrate sensing of ionising radiation.

Fluoride phosphate glass was tested for its capability to sense ionising radiation, primarily using the mechanism of optically stimulated luminescence. The characteristics of the material were determined using a combination of spectroscopy, and thermally and optically stimulated luminescence tests. The sensitivity to ionising radiation was improved by introducing dopant ions into the glass; doping of fluoride phosphate glass with Tb^{3+} was found to increase the intensity of the optically stimulated luminescence response by an order of magnitude, from 7.56×10^6 counts/g/Gy to 100.7×10^6 counts/g/Gy.

Optical fibres were fabricated from fluoride phosphate glass using the extrusion method for fibre preform manufacture. The fabrication process was optimised in each of the extrusion, preform processing and fibre drawing stages to achieve optical fibres with loss of between 0.5 - 1 dB/m for undoped fibres, and between 1 - 4 dB/m for Tb^{3+}-doped fibres. Optical fibres were used for ionising radiation sensing experiments, where the optically stimulated luminescence response was measured following both beta and X-ray irradiation. Following a dose of 14.6 ± 0.5 Gy, optically stimulated luminescence signals were observable using optical fibre lengths of up to 2.6 m, with an integrated OSL intensity of 44.1 ± 13.0 counts.

Silica glass was also tested as an alternative material to perform optical fibre measurements using optically stimulated luminescence. The material was characterised and optical fibres were fabricated with a loss of 0.5 dB/m. Following a dose of 15.5 ± 0.5 Gy, optically stimulated luminescence signals were observable using optical fibre lengths of up to 8.6 m, with an integrated OSL intensity of 385.7 ± 43.4 counts.

Declaration

I, Christopher A. G. Kalnins, declare that this thesis titled 'Radiation Effects in Glasses for Intrinsic Optical Fibre Radiation Dosimetry' and the work presented in it are my own.

I certify that this work contains no material which has been accepted for the award of any other degree or diploma in my name, in any university or other tertiary institution and, to the best of my knowledge and belief, contains no material previously published or written by another person, except where due reference has been made in the text. In addition, I certify that no part of this work will, in the future, be used in a submission in my name, for any other degree or diploma in any university or other tertiary institution without the prior approval of the University of Adelaide and where applicable, any partner institution responsible for the joint-award of this degree.

I give consent to this copy of my thesis, when deposited in the University Library, being made available for loan and photocopying, subject to the provisions of the Copyright Act 1968.

I also give permission for the digital version of my thesis to be made available on the web, via the University's digital research repository, the Library Search and also through web search engines, unless permission has been granted by the University to restrict access for a period of time.

Signed

Date

Acknowledgements

Firstly I would like to thank my supervisors: Heike Ebendorff-Heidepriem, Nigel Spooner and Tanya Monro. Your patience and guidance through each stage of this work has been invaluable and without it, this thesis would not exist.

For their technical support, I wish to thank Alastair Dowler, Herbert Foo, Kevin Kuan, Rachel Moore, Kenton Knight, Peter Henry and Donald Creighton. Your assistance with fibre drawing, glass and preform fabrication, and 3D thermoluminescence spectrometry has been invaluable.

The Institute for Photonics and Advanced Sensing and The School of Chemistry and Physics have been instrumental in creating a fantastic working environment, both professionally and socially. In particular I would like to express my pleasure to have worked within the Environmental Luminescence, Chemical and Radiation Sensing, and Fabrication groups.

For their financial support and usage of equipment and facilities, I would like to thank the Defence Science and Technology Organisation. For usage of fabrication facilities, the South Australian node of the Australian National Fabrication Facility is also acknowledged.

On a personal note, I would like to extend my gratitude to my family who have supported and encouraged me not just through this thesis, but through my whole life. Mum, Dad and Nici, you've been an inspiring family to grow up in.

For bringing not only fun and warmth, but also a strong feeling of belief and encouragement, my gratitude goes out to Antonija. Thank you for being by my side.

For their dark and bitter humour, without which I could not have seen the bigger picture of life, I must thank all my friends. I appreciate every single one of you and what you bring into my life. Many of you are also pursuing research degrees, and I have enjoyed the solidarity as we question our life choices.

Lastly and perhaps most importantly, I would like to acknowledge EDM, chocolate and the peace found at 2 am.

Contents

Summary

This thesis contains a study of the feasibility of detecting ionising radiation with an optical fibre, specifically using the mechanism of optically stimulated luminescence. This work addresses the particular case where the radiation sensing occurs within the optical fibre material, and not in a separate material otherwise spliced to a fibre. The optical fibre therefore acts as both the sensing component of the device, and the waveguiding component which carries a signal to the detector. This work fills a void in the already-established range of optical fibre dosimetry technologies, and provides an alternative method for performing optical fibre dosimetry.

To achieve the project goals, glass materials were studied for their optical, luminescence and radiation detecting properties. These glasses were then fabricated into optical fibres, and these fibres tested in a variety of radiation environments. Work was initially performed with fluoride phosphate glasses, where the glass was characterised and then altered by the addition of various dopant ions to improve its radiation detecting sensitivity. Silica glasses were later studied as a comparison to fluoride phosphate glasses. Also presented is the fabrication of these glass materials into optical fibres of suitable quality to perform distributed sensing measurements of ionising radiation. The performance of the optical fibres are studied under both beta and X-ray irradiation conditions, and their usefulness as dosimeter devices is assessed.

Chapter 1 outlines the context and motivation behind the presented work, and provides a short introduction to the theory behind the experimental work. *Chapter 2* explores the various properties of the materials used for optical fibre fabrication, primarily focusing on fluoride phosphate glasses. In *Chapter 3*, the modification of fluoride phosphate glasses with dopant ions in order to improve the sensitivity as a radiation detecting material is presented. *Chapter 4* presents the fabrication of the radiation sensitive material into optical fibres of sufficient mechanical strength and optical quality for radiation sensing experiments. The radiation sensing experiments for which these optical fibres were used are shown in *Chapter 5*. *Chapter 6* presents an alternative material, silica, and shows how in some areas it can be superior to the materials discussed in previous chapters. *Chapter 7* summarises the experimental work and gives an appraisal on

the feasibility of using this novel method of radiation sensing in real-world applications; this is followed by a summary of future directions for this area of research.

List of Figures

List of Tables

Chapter 1

Introduction

This introductory chapter will begin by summarising the main aim of the project and how it fits within the context of already established radiation detection technologies. The background of the field of radiation dosimetry and optical fibre radiation sensors will then be presented in further detail. Following this, a brief overview of the theory relating to radiation detection and luminescence is provided.

1.1 Introduction to Radiation Dosimetry

1.1.1 History of Dosimetry

Radiation dosimetry is the process of detecting and quantifying an absorbed dose of ionising radiation [1–4]. When ionising radiation is incident upon a material, energy may be deposited into the material through a variety of mechanisms. Dosimetry seeks to detect this energy deposition and quantify both the location and magnitude of the deposited energy.

Following the discovery of ionising forms of radiation in the late 1800s, discovery of its dangers and adverse health effects soon followed. In the early 1900s, various methods of detecting ionising radiation were developed - including colorimetric, chemical, photographic, solid state colouration and fluorescence methods [1]. The most successful method, however, was the ion chamber, due to its convenience, sensitivity, stability and reproducibility [1, 2]. In 1925 the International Commission on Radiological Units (ICRU) was established, which thereafter classified the Rontgen as a unit of measuring ionising radiation [1, 2]. Closely following this was the invention of the Geiger-Müller Counter, developed by Hans Geiger and Walther Müller in the late 1920s [5, 6]. Subsequently, the development of nuclear reactors and weapons as well as medical radiation therapy pushed dosimetry into new directions. In more recent decades, the usage of radiation has continued to spread into a wide array of applications.

Different aspects of dosimetry are required, depending on the application. As such, the methods of performing dosimetry have likewise diversified into the many different physical mechanisms and measurement methods we see in modern dosimeter devices. In some situations, such as in the case of an accident, it is simply enough to detect ionising radiation in order to respond quickly. In this case an exact measurement of the dose is of secondary importance to rapid detection and response. In other situations, such as in radiotherapy for cancer treatment, it might be necessary to create a precise map of energy deposition within a material with little importance placed on the time it takes to do so. Each different dosimetry application, therefore, has its own set of requirements.

1.1.2 Examples of Dosimetry

Several examples of dosimetry applications will be described here in order to provide context to the field of dosimetry as a whole.

Personal Dosimeters Personal dosimeters are used extensively in any industry where people may be exposed to ionising radiation [1, 7, 8]. They are frequently small, unobtrusive detection devices worn by the person at all times while within the environment and are frequently personalised for job function and exposure risk. These devices measure the cumulative dose absorbed and hence give a measurement of the amount of radiation the person has been exposed to over a period of time. For this application, dosimeters need to measure precise amounts of absorbed dose, in order to calculate if there are any potential health concerns. Due to this, the materials used for personal dosimetry are carefully studied so their response is well known, reproducible, calibrated and easily measured. Personal dosimeters may be required to produce a real-time readout, or measurements may be performed after a period of time in a laboratory. Thermoluminescent Dosimetry (TLD) badges are commonly used, as are carbon fibre electroscope ion chambers.

Structural and Environmental Monitoring Dosimetry is used to measure radiation levels in a radiation field, be it natural or artificial; obvious examples include nuclear facilities, particle colliders and medical oncology facilities [7, 9, 10]. Environmental dosimetry is also used in a wide range of other situations. Space flight requires dosimetry due to the high cosmic radiation flux incident on space-craft outside the protection of the earths atmosphere [1]. This is also applicable to high-flying aircraft [11–13]. Mining operations require the continuous monitoring of particulates and radon in the air, this is also applicable to many buildings and structures built part-way into the ground. Mining operations working with radioactive minerals such as uranium also require continuous monitoring and radiation surveys and equipment testing also utilise very similar tools.

Environmental dosimetry may also be performed in natural environments to determine the background radiation levels due to cosmic rays and naturally occurring radioisotopes [1, 7]. While not high, these background environmental levels are directly applicable to areas such as optical dating of minerals for archaeological and geological applications [8, 14, 15].

Environmental monitoring techniques may also include those used for emergency response in the event of an accident, leakage or meltdown. In such cases portable, highly accurate devices which are sensitive to the various types of radiation are required.

All the above applications may make use of a variety of sensing methods and phenomena, such as ion chambers, Geiger-Müller tubes, thermoluminescence and optically stimulated luminescence.

Medical Physics Medical physics is an interesting area to consider, as it involves several different dosimetry requirements, using several different dosimeter devices [7,16]. Firstly, the beam quality coming from a linear accelerator is monitored using a very thin ionisation chamber, through which the beam passes. Dose delivery to a patient can be estimated by the known specifications of the beam, the treatment plan and the anatomy of the patient. However each of these estimates contains uncertainties and a method of verifying dose at the treatment site is desirable. This requires a dosimeter to be placed at the entry or exit point of the beam into the patient. Two examples of devices which may be used to measure dose delivery to the patient are thermoluminescent dosimeters and silicon diodes. The theory of thermoluminescence will be discussed in more detail in Section 1.3.2. Within the treatment environment, staff will wear personal dosimeters to monitor long-term cumulative exposure. Finally, dosimeters are used in the treatment environment, both within the treatment room and outside it, to monitor any leakage of ionising radiation.

Further to these fundamental treatment-specific uses of dosimetry in the field of medical oncology, other dosimetry methods are also used. Modelling is used extensively with programs such as GEANT4 to design treatment plans and perform other simulations involving ionising radiation [17]. Gel dosimeters are used as water equivalent phantoms and enable a three dimensional map of dose deposition, they can be used to help characterise new radiation sources and testing of new techniques [18]. Finally and perhaps most relevant to the work presented in this thesis, is the use of in vivo dosimeters, where small dosimeter devices are placed inside the patient at the treatment site, allowing more precise measurement of the absorbed dose. Optical fibre probes are ideal for this application and are discussed further in later sections.

1.2 State-of-the-Art of Optical Fibre-Based Radiation Sensing

The use of optical fibres in the field of radiation dosimetry has been studied since 1969, where radioluminescence (RL) in optical fibres was used to monitor radiation during radiological measurements [19]. Since this time many different methods have been developed, utilising the various different properties of optical fibres and optical fibre materials optimised for specific dosimetry requirements.

Optical fibres can be used in several different ways to perform dosimetry. The fundamental use of an optical fibre is to guide light from one point to another and in this way optical fibres are useful in dosimetry, when ionising radiation is detected by the production of light. In addition, ionising radiation may modify the light-guiding prop-

erties of an optical fibre and hence the fibre itself acts as a dosimeter. Furthermore, ionising radiation may also produce light within the fibre, making the optical fibre both a sensing material and its own signal collection device. These different methods are all dependent on the physical mechanism used to detect the ionising radiation. In the following sections several different detection mechanisms will be presented and their use with optical fibres described.

1.2.1 Radioluminescence

Radioluminescence (RL), also known as scintillation, is a luminescence effect caused when ionising radiation interacts with certain materials. When energy from the ionising radiation is deposited in the material, electrons are excited and electron-hole pairs formed. During subsequent electron-hole recombination, the recombination pathway may pass through a radiative transition, producing luminescence. Recombination of electron-hole pairs is generally fast in most materials, happening within several nano or microseconds, the luminescence is therefore produced only throughout the duration of the radiation exposure. Further information on RL can be found in the literature [20, 21].

RL is a well established luminescence tool and was initially studied at the turn of the 20th Century [22]. Development of photomultiplier tubes in the 1940s then enabled the development of sensitive RL-based radiation detectors [23]. Study of the RL in optical fibres was performed several years later with the introduction of plastic RL filaments, which were used for their waveguiding ability as imaging devices for high energy physics applications [24, 25]. Since these early studies, many new RL optical fibre materials have been developed.

There are two classes of RL fibre dosimeter: intrinsic and extrinsic. An intrinsic system measures the RL occurring inside the material of the optical fibre itself, as many of these early studies demonstrate. Recent research in this area has focused on the development of novel glasses and plastics, thereby tailoring the RL behaviour for certain applications [26–29]. The intrinsic design allows sensing along the length of the optical fibre, any part of the fibre which is exposed will create a signal. This property is useful for 'distributed sensing' applications where a wide area needs to be monitored, such as wrapping around storage drums of radioactive waste products [30].

Extrinsic RL fibres are made by splicing a RL material onto the end of a radiation insensitive optical fibre. As will be explained in Section 1.2.6, this method is useful for medical applications and many groups have developed dosimeters of this type using RL crystals [31–35] and plastics [36–38].

Due to the multitude of efficient RL materials known today, research in this area has focused on improving optical efficiency and suppressing RL and Čerenkov radiation 'stem effects' in the optical fibre. For example, RL can be isolated spectrally [39], or using time-gating methods [40, 41].

1.2.2 Photodarkening

Photodarkening occurs when sufficient optical power at a short wavelength (such as UV wavelengths) is coupled into an optical fibre; this causes the formation of colour centres which decrease the transmission of the fibre. Colour centres in glass also form when exposed to other forms of ionising radiation, such as beta particles and high energy photons. Photodarkening can therefore be used as a dosimetry technique whereby the transmission of an optical fibre is monitored: a decrease in transmission indicating exposure to, or the presence of, ionising radiation.

This technique was first developed in 1974-6, when glass optical fibres were studied for their transmission properties after exposure to radiation [42]. Eventually, fibre dosimeters were deployed on satellite experiments in 1977-1978, measuring real-time absorbed dose [43].

Polymer fibres have also shown to be effective for gamma dosimetry, where dyed poly methyl methacrylate (PMMA) was used for measurements in the 30 Gy – 40 kGy region [44, 45]. Various glass materials have also been demonstrated as effective photodarkening fibre dosimeters [46, 47].

Silica optical fibres also make efficient sensors using the photodarkening method. Generally, the fibres are doped, such as with aluminium, phosphorus or germanium [48] to facilitate the formation of colour centres during irradiation.

1.2.3 Thermoluminescence

While an important tool for many dosimetry applications, thermoluminescence has not been studied extensively as a method to pair with optical fibre technology. This is mostly due to the interrogation requirement, heat, as opposed to the optical interrogation used for all other methods. Nonetheless, several studies were performed where thermoluminescent phosphors were spliced to the ends of optical fibres. The interrogation of the phosphor was performed using an IR beam coupled into the fibre, which heats the detector crystal, allowing thermoluminescence to occur [49].

1.2.4 Bragg Gratings

Fibre Bragg gratings [50] are used for many applications, utilising the change in Bragg wavelength caused by external perturbations such as temperature and strain [51]. Ionising radiation has also been found to shift the Bragg Wavelength, therefore creating the possibility of using a fibre Bragg grating as a dosimetry system [52–54].

1.2.5 Optically Stimulated Luminescence

This method is addressed last, but is the most relevant to this thesis. Optical fibre dosimetry using optically stimulated luminescence (OSL) has been performed previously, but only as an extrinsic method, where a radiation-sensitive material is spliced onto the end of an optical fibre. This method has been used with a variety of dosimeter phosphors, most notably Al_2O_3:C [55], which are in most cases spliced onto commercial silica optical fibres. Many studies show the results of coupling an Al_2O_3:C crystal to a commercial optical fibre under a variety of different configurations [56–63]. Various materials other than Al_2O_3:C have also been used for this purpose such as KBr [64], SrS:Ce:Sm [65], and BeO [35, 66]. OSL optical fibre dosimeters can also be used as RL optical fibre dosimeters, where the RL is used to measure real-time exposure, and the OSL component used to measure the cumulative dose [41].

Among the various OSL materials spliced to optical fibres for the purposes of dosimetry is Cu^+-doped fused quartz, which comes closer to the scope of this project than any other study in the literature. Fused quartz glasses were initially studied for their thermoluminescence properties for the purposes of dosimetry, however experiments were tested on undoped samples [67, 68]. Experiments soon followed which explored the luminescence properties of Cu^+-doped silica and fused quartz glasses, where both optically and thermally stimulated luminescence was studied [69–72]. These studies showed the Cu^+-doped silica is an effective radiation-sensing material, with linear TL and OSL responses over a dose range of 4 orders of magnitude (0.01 – 10 Gy). TL results showed minimal fading of the 325 ℃ TL peak 24 hours after an exposure, indicating the material could be suitable for storage of dose information. A Cu^+-doped silica glass was later fabricated into thin rods for use as an optical fibre dosimeter probe for medical applications [73, 74], short lengths of this glass rod were spliced onto commercially acquired silica fibre for the purposes of carrying the optical signal to the detector. Results showed the devices were useful for sensing measurements, they gave a linear optical response over a wide dosage range, plus a RL component was also available for analysis. This RL signal from the material has been explored in conjunction with time-gating protocols for dosimetry in linac photon beams [75, 76].

The luminescence and dosimetry properties of Cu^+ are therefore well established in the literature, however the optical properties of this material are not so well reported. There is no indication on the transmission quality of any of the Cu^+-doped glasses investigated, and no loss measurements reported for the optical fibres fabricated from these glasses. Given that only millimeter lengths of Cu^+-doped silica optical fibre were used, which were then spliced onto undoped fibres for transmission of the signal, this suggests the glass has poor transmission and cannot be used as long lengths. On the other hand, it is suggested the desired application requires the use of point-sensors, rendering the use of a long length of sensitive fibre irrelevant to the application for which they were developed.

The use of OSL in glass materials has therefore been considered, but not explored in-depth beyond their basic optically and thermally stimulated luminescence properties. Neither has there been a serious effort to make optical fibres from these glasses, beyond using short lengths of 'fibre' as OSL active chips spliced onto commercial optical fibres, which is not unlike the plethora of studies utilising various other types of OSL phosphor crystals. There is therefore a lot of work to be performed in this area, and hence it forms the main body of the research presented in this thesis.

1.2.6 Comparison of Extrinsic and Intrinsic Sensing Methods

In previous sections both intrinsic and extrinsic methods have been mentioned, such as for methods using RL and OSL. In this section the difference between intrinsic and extrinsic sensing methods will be further elaborated upon. Both of these optical fibre dosimeter architectures are demonstrated in Figure 1.1.

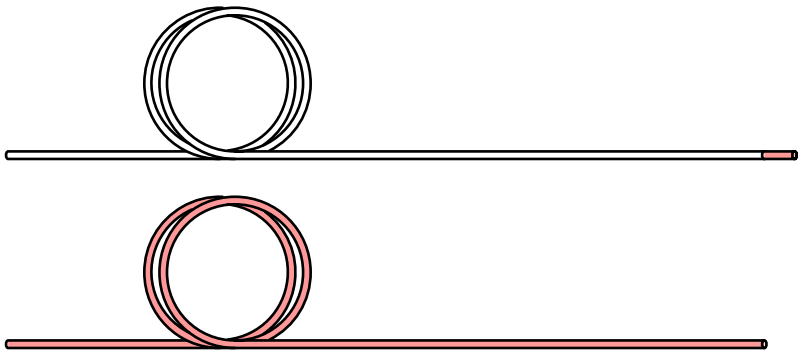

Figure 1.1: Extrinsic (top) and intrinsic (bottom) optical fibre architectures. Red indicates the region over which the radiation sensing phosphor is active.

Extrinsic An extrinsic sensor uses a radiation sensitive crystal phosphor coupled to a passive optical fibre waveguide. The radiation detection occurs in the phosphor, which emits an optical signal. The optical fibre is used to carry this signal to a detec-

tor. In this instance the optical fibre is used only as a waveguide to carry an optical stimulation to the detector chip, and to collect a signal and guide it to a detector. This method provides good spatial resolution, as the dosimeter crystal is a single-point source, making it suitable for medical applications. The long, thin, geometry of an optical fibre-coupled RL chip is ideal for in vivo measurements of radiation dosage at a tumor site. Development of these devices is therefore medically focused, as is shown in many recent studies utilising RL and OSL [41]. As the small dimensions of the phosphor material removes the need to be optically transparent, or capable of being fabricated into an optical fibre, these phosphors are often far more sensitive than the glasses used for intrinsic sensing measurements. While ideal for point-measurements, extrinsic sensors cannot perform distributive sensing.

Intrinsic An intrinsic system is one where the optical fibre is both the radiation-sensing medium, and the waveguide used to carry the optical signal to a detector. This method therefore allows distributive measurements, where an optical fibre is placed in an environment and can sense ionising radiation anywhere along its length. Furthermore, in a spatially extended radiation environment, the signal can be integrated along the entire length of the fibre, allowing improved signal to noise. This method also offers the potential to perform spatially resolved measurements using optical time domain reflectometry and time of flight techniques [77, 78]. For intrinsic methods the glass material out of which the fibre is made has to be carefully selected. In addition to being a sensitive radiation detecting phosphor, it must be optically transparent and capable of fabrication into optical fibres. As was mentioned for extrinsic phosphors, this limits the range of materials available for this purpose, hence intrinsic dosimeter materials are generally less sensitive.

1.2.7 Advantages of Fibre-Based Sensing

In the previous sections several methods of using optical fibres to sense ionising radiation were presented. Each method has its advantages and limitations. In general, optical fibres are desirable because their geometry, long length and small diameter allows sensing in conventionally inaccessible places, such as within a human body - with minimal disturbance to the surrounding environment. For intrinsic optical fibre sensors, this long length is also desirable in terms of interaction length and signal collection capability.

In addition, unlike several other common techniques (such as supercavitation neutron dosimeters, gel dosimeters, Geiger-Müller tubes and ion chambers), detection signals are optical. This allows immediate detection and processing using established, off-the-

shelf optical detection methods and equipment.

The fabrication of optical fibres, once a method is established, is also relatively inexpensive. For light-guiding purposes, many different types of optical fibre are available commercially. When specific glasses need to be fabricated, once made, a small quantity of glass is capable of producing hundreds of meters of optical fibre at a time.

1.3 Luminescence Theory

1.3.1 Optically Stimulated Luminescence

Optically stimulated luminescence (OSL) is a phenomenon occurring in certain materials following an interaction with ionising radiation. It has widespread application as a method of determining the age of sediments in the field of geochronology [14] as an improvement on thermoluminescence dating in all but a few specialised circumstances. OSL was also developed as a potential method for personal and environmental dosimetry applications as a result of having several advantages over thermoluminescence, including rapid read-out, no thermal damage of materials and low power requirements.

Fundamentally, the OSL mechanism involves the excitation of electrons into an excited state, from where they are metastably trapped; subsequent optical stimulation allows the trapped charge to escape and relax back to the ground state via a radiative transition, producing luminescence. A thorough explanation of the OSL mechanism can be found in the literature [4, 15, 79], but will also be summarised here. The explanation considers irradiation of glass with beta particles, as this is the material and radiation type most relevant to this project. A schematic demonstrating each step of the OSL process can be seen in Figure 1.2. This luminescence captured by the guided modes will be carried down both directions to each end, where it is detected.

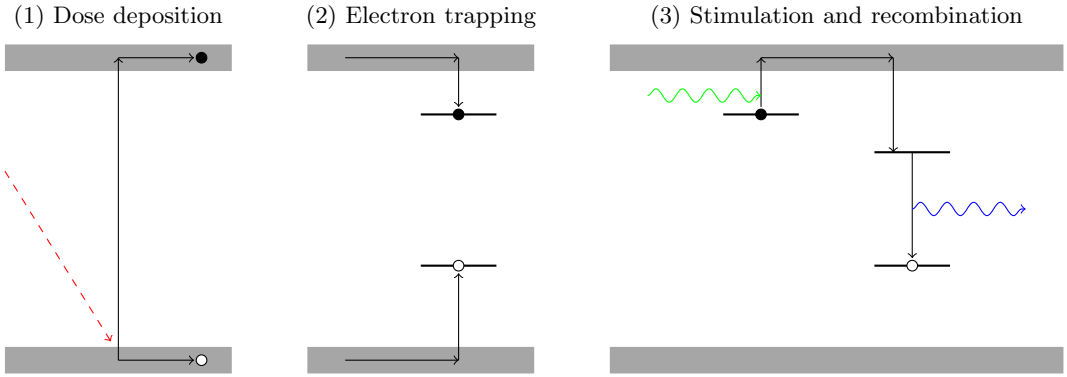

Figure 1.2: Mechanism of optically stimulated luminescence, showing 1) dose deposition 2) electron trapping and 3) stimulation and recombination. Ionising radiation is shown in red, optical stimulation in green and stimulated luminescence emission in blue.

Physical Description

Dose Deposition When a beta particle is incident on the glass material, its energy is lost through a number of pathways, such as through production of secondary electrons or bremsstrahlung [4]. Irradiation of a sample will also involve irradiation of the material around the sample[1], in which further secondary electrons and bremsstrahlung are produced. This combination of secondary electrons and high energy photons will then further deposit their energy within the glass material, creating a large population of electrons in an excited state. These electrons are able to move freely through the conduction band of the material.

Electron Trapping With movement through the conduction band, excited electrons may come across radiative transitions by which an electron-hole pair may recombine. This produces RL, and is useful for many applications, such as is described in Section 1.2.1. In certain materials, however, there exist energy levels situated energetically slightly lower than the conduction band, caused by defects in the material lattice or by impurities or dopants. Electrons moving through the conduction band may become trapped in these levels. Depending on the energy difference between the trap level and the conduction band, the lifetime of the trapped electrons may range from nanoseconds to millions of years. In a material with sufficiently deep traps, a proportion of electrons initially excited by the radiation exposure will now remain in these traps, storing the dosage information. Holes are similarly metastably trapped at suitable defects.

Stimulation and Recombination When interrogation of the glass material is desired, stimulation in the form of an optical signal is applied to the material. This optical stimulation excites electrons out of their trapped state and into the conduction band, from where they may then move freely. As occurred in the previous step during RL, an electron-hole pair may recombine in a radiative transition, producing the luminescence signal. It is the detection of this luminescence signal which provides the dosage information stored by the trapped electrons.

During stimulation, electrons may fall back into traps before they encounter recombination centres. Additionally, tunnelling of charge may occur between adjacent traps. These, and other effects, lead to a rich variety of decay kinetics during optical interrogation.

[1] For experiments presented in this thesis, the surrounding material is predominately aluminium.

Within an Optical Fibre

Following irradiation and optical stimulation, an optical fibre made of an OSL material will produce luminescence from all points within its volume. Photons will be emitted randomly in all directions (4π), shown in blue in Figure 1.3 (2). Of the photons emitted in 4π, only photons emitted within a certain solid angle will be captured by the guided mode(s) of the optical fibres, shown in darker blue in Figure 1.3 (2).

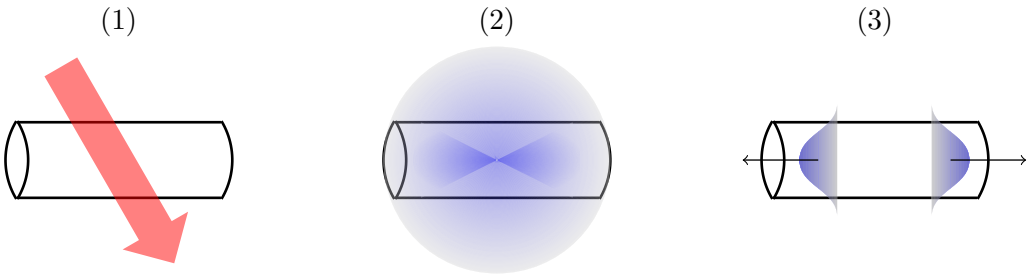

Figure 1.3: (1) Ionising radiation deposits energy. (2) Luminescence is emitted in 4π (blue), only a fraction is captured by the guided modes of the fibre (darker blue). (3) This captured luminescence is guided in each direction down the fibre.

Detection and Analysis

Filtering of OSL signals To detect OSL, any optical detector may theoretically be used. However, the intensity of an OSL signal is frequently low, which in practice limits the detection to apparatus designed specifically for low light applications. Photomultiplier tubes and single photon avalanche diodes are examples of such detectors.

Due to the luminescent signal being a product of optical stimulation, filtration is required to isolate the luminescence wavelength from the stimulation wavelength. It is therefore necessary to use a stimulation wavelength sufficiently removed from the luminescence wavelength (unless working in the time-resolved domain). In addition, the stimulation wavelength is generally chosen to be longer than the wavelength of the luminescence signal to ensure no fluorescence is produced within the material, which would increase the background noise. Filtration is further complicated by a stimulation intensity many orders of magnitude higher than the luminescence intensity, this renders most common interference filters, usually operating at approximately four orders of magnitude of rejection, ineffective. Coloured glass filters are therefore commonly used for isolation of OSL signals, thick filters can reject many orders of magnitude at certain wavelengths. Coloured glass filters are not, however, as versatile as interference filters which can be manufactured to pass or reject specific wavelength regions. In practice, coloured glass filters are often restricted to certain wavelength regions.

The emission wavelength of the OSL material and the wavelength of the optical stim-

ulation therefore need to be chosen carefully to suit the transmission properties of the filter.

Data Analysis After a successful OSL measurement, the detected luminescence will have the appearance of the trace shown in Figure 1.4. The OSL signal is the result of the depletion of a population with time, therefore the OSL intensity will appear as a 'shine down' curve, the intensity decreasing as the population of trapped electrons is depleted. The kinetics of an OSL decay curve can be complex, depending on the properties of the OSL material. The decay measured from many OSL materials only approximately follows the first order exponential kinetics expected from the depletion of an excited population. This is due to many materials containing electron traps at a variety of energy levels and with different lifetimes; the probability of stimulation from these traps therefore varies. Other possible effects also occur, such as tunneling between traps, which further complicates the measurement.

When analysing OSL results, the luminescence is generally integrated over a region beginning from the onset of optical stimulation and ending when the intensity is reduced to the background noise. This is shown by the light grey region in Figure 1.4. Depending on the signal-to-noise desired for a measurement, this integration region may be adjusted.

Within this thesis where OSL intensities are reported, it will be the integrated OSL counts as depicted in Figure 1.4. Where appropriate, integrated OSL values are also normalised for the mass of the OSL material and for the applied dosage of ionising radiation.

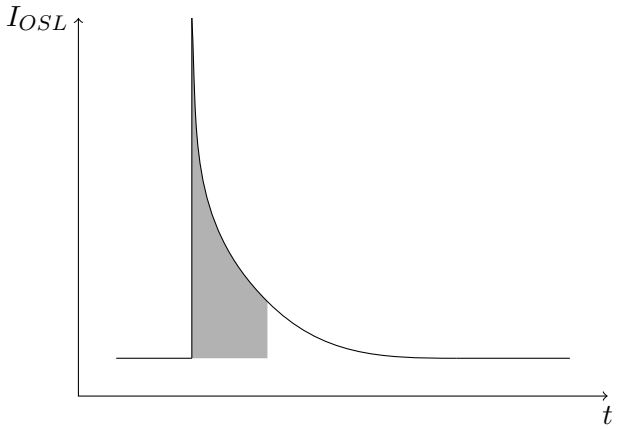

Figure 1.4: Integrated area of OSL signal.

1.3.2 Thermoluminescence

Thermoluminescence (TL) is a phenomenon related to OSL, where a population of trapped electrons and holes is formed due to ionising radiation, and which are then stimulated out at a later time to produce luminescence. The fundamental theory of TL is very similar to OSL, with the exception of the means of stimulation of electrons from traps. Where OSL uses optical stimulation (photons), TL uses thermal stimulation (phonons) to excite trapped electrons into the conduction band, where they are free to move to recombination centres. The TL mechanism is shown in Figure 1.5.

It was developed as a dosimetry technique and is commonly used today for a variety of dosimetry applications, such as in personal monitoring badges [80]. It is a technique formerly used extensively for archaeological dating of fired materials such as pottery [81]. Although it is not the sensing mechanism used within the optical fibres presented in this thesis, it is a valuable tool for analysing the luminescence properties of the materials. Many TL experiments will be presented in later chapters, therefore a brief description of the theory and its usage is provided here.

Physical Description

Dose Deposition and Electron Trapping Similar to OSL, described in Section 1.3.1, when radiation is incident on the glass material it causes the excitation of electrons into the conduction band, from where they may become trapped at suitable defects. Electrons in shallow traps, where the difference in energy between the trap and the conduction band is small, may be thermally stimulated out by the low energy phonons present at room temperature. Electrons in deeper traps, with a larger difference in energy between the trap depth and the conduction band, will not be stimulated out at room temperature and consequently the trapping lifetimes may be very long, up to millions of years.

Thermal Stimulation and Recombination To analyse a material, thermal stimulation is applied to free the trapped electrons into the conduction band. This thermal stimulation is applied carefully in a gradual heating of the sample, where heating rates of between 1-5 K/s are commonly used. This gradual heating allows luminescence data to be obtained as a function of sample temperature, yielding information about the magnitude of the trapped charge population; and also about trap depths and structures.

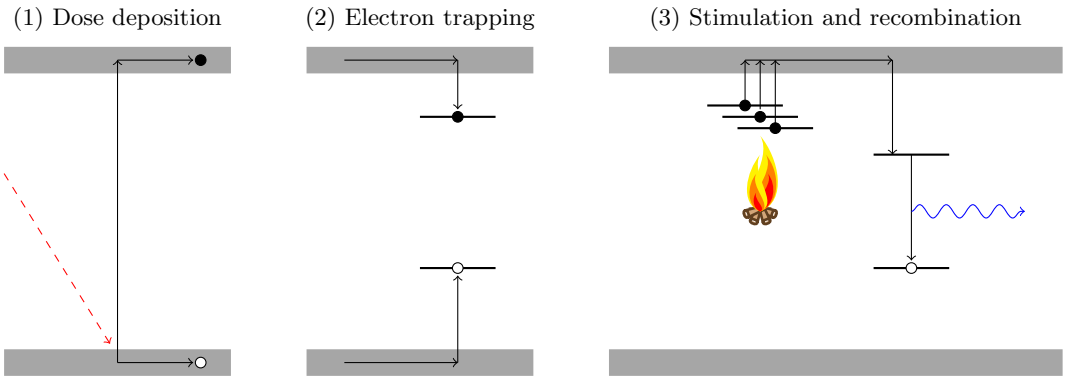

Figure 1.5: Mechanism of thermoluminescence, showing 1) dose deposition 2) electron trapping and 3) thermal stimulation and recombination. Ionising radiation is shown in red, thermal stimulation by a campfire and the stimulated luminescence in blue.

Detection and Analysis

Filtering of TL signals As no optical stimulation is used, TL signals do not have to be filtered before detection. In certain situations it may be desirable to utilise filters in order to isolate and study the TL signal from certain wavelength regions in a material. If the sample is to be heated to a temperature much above 300 °C then near IR and red rejection filters are necessary in order to reject incandescence produced from the heating plate. In other cases where shallower traps are used, it may be beneficial to collect the maximum amount of luminescence from a sample, in which case all filters may be removed.

It should be noted that quartz filters are often used as windows shielding the PMT in situations where the material is mounted onto the sample holding disc with a silicon oil spray; this is to ensure no contamination of the detector is caused by evaporation of silicon oil during the heating phase. Quartz filters are transparent in the relevant waveband and have a negligible effect on the luminescence signal, losing approximately 4% at each air-quartz interface.

Data Analysis Data from TL measurements provides a series of 'glow peaks', a depiction of which is offered in Figure 1.6. Analysis of glow curves can provide information on the trap lifetimes, trap depths and frequency factors. Peak temperatures, integration of peak intensity, and analysis of the initial peak rise all offer useful information.

A variety of TL analysis techniques are available with which to characterise a material, such as initial rise TL, TL emission spectroscopy and TL fading. The method used to perform these more detailed TL measurements will be provided in later chapters.

At temperatures above 300 °C incandescence from the heating plate will begin to interfere with the luminescence signal, the effect of this on the data has also been depicted

in Figure 1.6, where a continuously-increasing rise in counts is seen with respect to temperature. This incandescence can be corrected for by performing a second TL measurement on the now-depleted sample to obtain a background, which is used to subtract both the incandescence signal and detector noise.

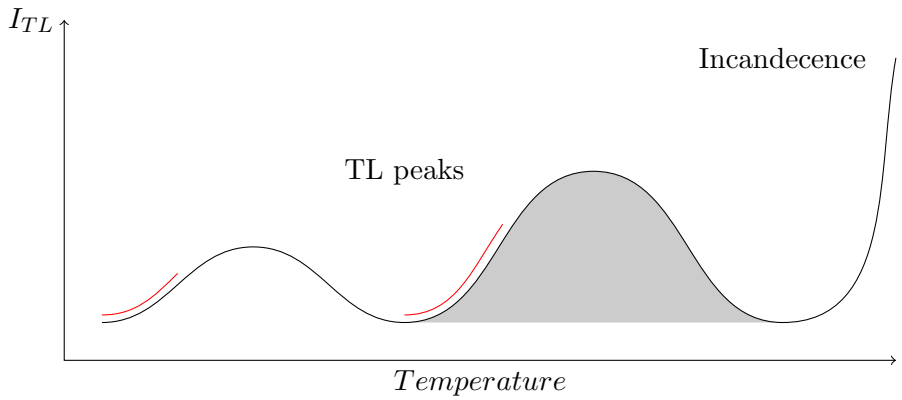

Figure 1.6: Glow peaks of a thermoluminescence 'glow curve', showing where data may be integrated to analyse a given peak. Red lines indicate the region used for 'initial rise' TL measurements. The sharp rising feature at higher temperature is a depiction of the incandescence signal.

1.4 Dose Deposition Within Materials

The way in which dose is deposited by ionising radiation into a material depends on the type of radiation, its energy and the material with which it is interacting [2]. High energy particles will generally move through a thin layer of material and while there may be interactions, little energy may actually be deposited before the particle exits the material. As such, dose is generally deposited by secondary particles with lower energy when their energy is completely absorbed within the material. It is these low-energy particles which create the population of excited electrons involved in the OSL mechanism, where there is sufficient energy to excite an electron to the conduction band, but not sufficient energy to cause ionisation.

As a beta particle beam propagates into the material, interactions with the material will produce these secondary electrons and photons of lower energy. As these particles travel further they will in turn produce tertiary particles and so on. As the resulting particle shower propagates through the material, this process causes a 'build-up' of low energy particles which then deposit their energy into the material. The highest dose deposition will therefore be in a region inside the bulk of the material and not at the surface [7]. Examples of electron and photon showers demonstrate this in Figure 1.7. Beta particles are observed to lose energy through a continuous series of interactions, while photons interactions are observed as discreet events.

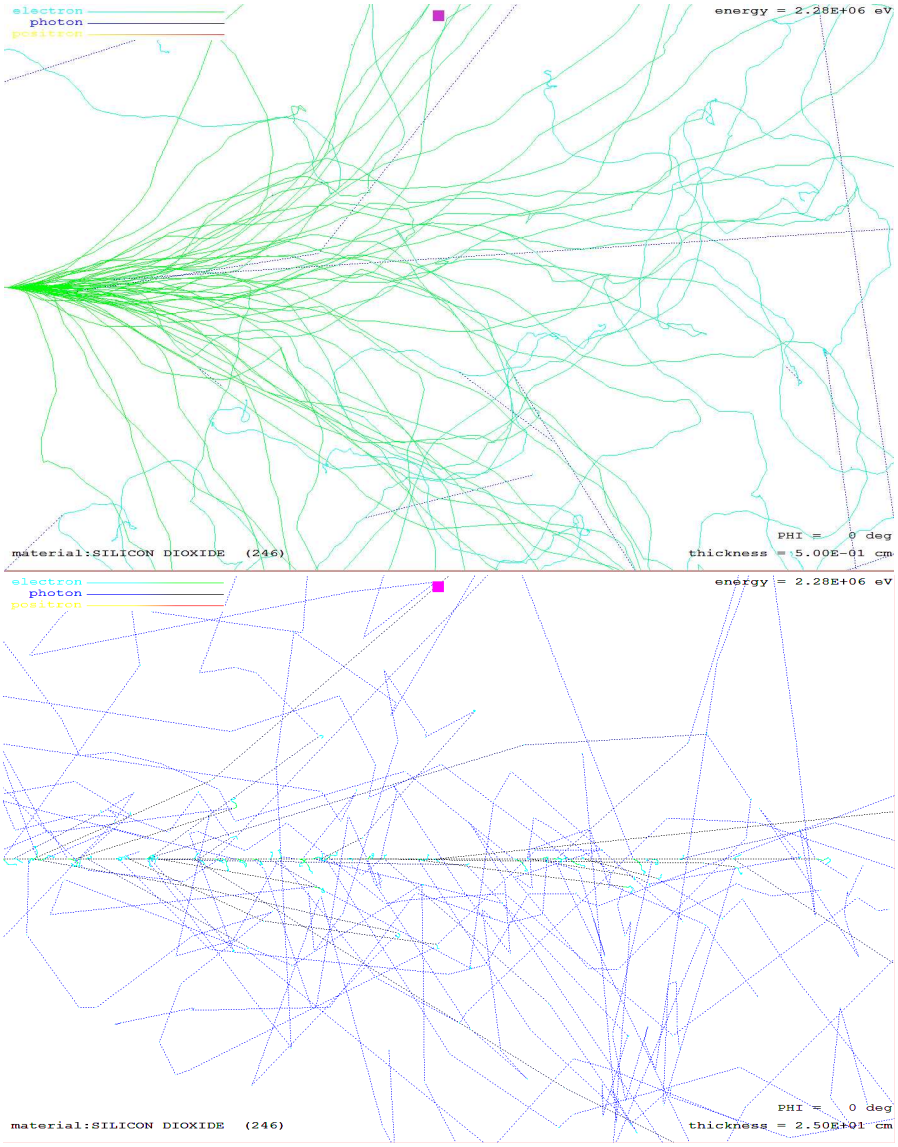

Figure 1.7: Electron (top) and photon (bottom) showers in silicon dioxide, each for 2.28 MeV primary energy. Data was simulated using PENELOPE, the process of which is explained in Section 1.5.

The processes by which high energy photons and electrons interact with matter is briefly summarised here, further information can be found from a number of sources [1,2,4,7].

1.4.1 Photon Interactions

The interaction of high energy photons with matter occurs through the following processes: each of which is shown in Figure 1.8.

Photoelectric Effect A photon, E, is absorbed by an atom and ionisation occurs. Electrons with high energy equal to the incident photon, E_e are then created and can be freed from the material. Characteristic emission, U, may be produced if out shell electrons replace the ejected electon.

Coherent (Rayleigh) Scattering Photons are scattered by bound electrons without excitation of the atom. Energies, E, of the incident and scattered photons are identical.

Incoherent (Compton) Scattering An incident photon, E, is scattered by an atomic electron, the scattered photon is of a lower energy, E', than the incident photon. The energy difference, E_e, is transferred to the electron.

Electron-Positron Pair Production An electron-positron pair forms when a high energy photon, E, interacts with a heavy particle, such as a nucleus. Interaction can also occur with an electron, known as 'triplet production'. Upon creation of an electron-positron pair, e^+ and e^-, the remaining energy, U, is imparted to the adjacent particle.

1.4.2 Electron and Positron Interactions

The interaction of electrons and positrons with matter occurs through the following processes, each process is shown in Figure 1.9.

Positron Annihilation Upon interacting with an electron, a positron will undergo electron-positron annihilation, producing a pair of photons. Although positrons are not used for irradiation in this project, positrons may still be produced due to pair production from high energy photons.

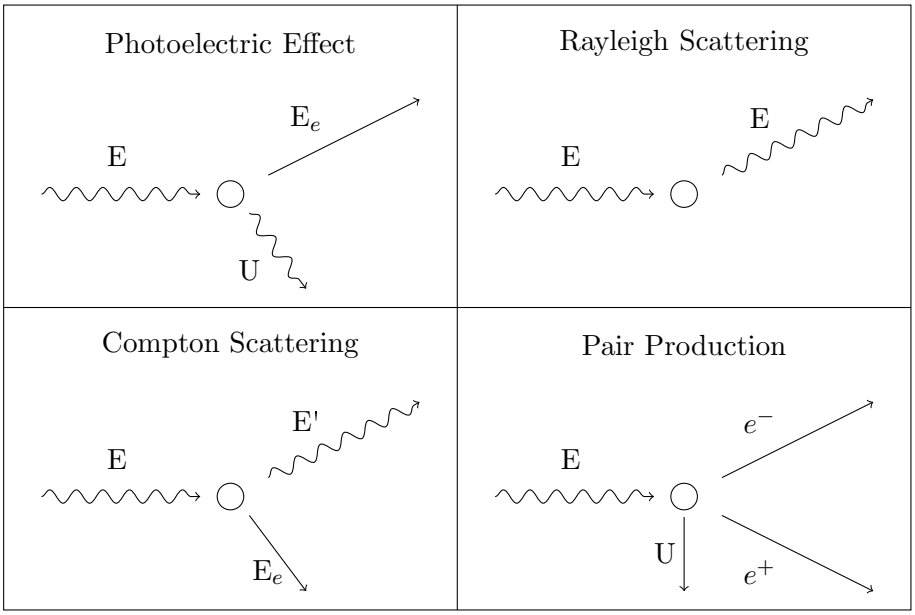

Figure 1.8: Interactions of photons with matter.

Elastic Collisions An electron interacts with an atom and is scattered with negligible loss of energy. The energies, E, of the incident and scattered electron are appreciably similar.

Inelastic Collisions An electron interactions with atoms which cause electronic excitations or ionisations. There is a difference in energy between the incident, E, and scattered electron, E', following the interaction, with the remaining energy, U, imparted to the atom. Interactions of this nature are the main energy loss mechanisms for medium and low energy particles.

bremsstrahlung Electrons undergoing acceleration in the field of a nucleus will emit X-rays, called bremsstrahlung or 'braking radiation'. The energy of the emitted photon, E_p, is the difference between that of the initial, E, and scattered, E', electron energies.

1.4.3 Radiation Sources

Radiation sources were used for many experiments reported in different chapters of this thesis, hence it is appropriate to give a summary of their basic characteristics here, further details of their usage in individual experiments will be described in these later chapters.

Beta Particle Sources $^{90}Sr/^{90}Y$ beta sources were used for all experiments evaluating the luminescence properties of the materials, as well as many experiments using

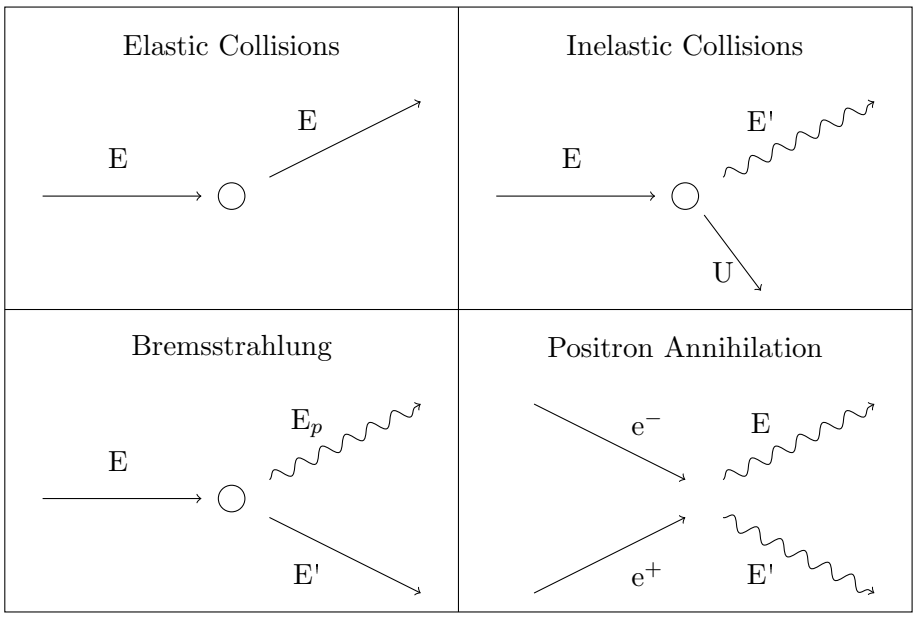

Figure 1.9: Interaction of electrons with matter.

optical fibres. These sources contain the strontium-90 radioisotope as an alloy in a silver foil mounted in a stainless steel holder, and are classed as 'sealed' sources. The beta irradiation is delivered from the 'active face', which is 15 mm in diameter. The strontium-90 isotope undergoes β^- decay into yttrium-90, with an energy of 0.546 MeV. Yttrium-90 subsequently undergoes β^- decay into zirconium-90 with an energy of 2.28 MeV. There is also a small proportion of photons emitted at 1.7 MeV. Table 1.1 summarises each ^{90}Sr/^{90}Y sealed source. Current activity of each source was calculated using the equation $A = A_0 exp[-0.693t/T_{1/2}]$ where the activity, A, of a source is calculated from the original Activity, A_0, using the time, t, since the source was fabricated and the half life of strontium-90 ($T_{1/2}$ = 28.8 years). The half-life of yttrium-90, 64 hours, is considered negligible in this calculation. A summary of the ^{90}Sr/^{90}Y sources is given in Table 1.1.

Table 1.1: ^{90}Sr/^{90}Y Radiation Sources Used for Optical Fibre OSL Experiments.

Name	Year of Purchase	Activity in Year of Fabrication (mCi)	Current Activity (mCi)	(MBq)
β20	1976	0.02	0.0082	0.3
β500	1976	0.5	0.205	7.58
β5	1976	5	2.05	75.85
β21	1976	21	8.62	318.94
β40	1985	40	20.4	754.8

X-ray Source While many experiments utilised beta sources, work was also performed to prove the optical fibres could also detect photon irradiation and hence experiments with optical fibres were also performed using X-ray irradiation. All X-ray

irradiations were performed using a Lorad LPX300 X-ray source in a facility operated by the DSTO[2]. The tube voltage ranges from 10 - 300 kV, filament current ranges from 0.1 - 10 mA and maximum operating power is 900 W. This maximum operating power requires a reduction of current if using high voltage, for example when using a voltage of 300 kV the maximum current is 3 mA. Off the tungsten target, the X-rays are produced as an elliptical beam with dimensions of 60° by 40°.

In X-ray tubes, photons are produced mainly due to bremsstrahlung, the X-ray emission spectra are therefore defined by the characteristics of bremsstrahlung emission in the target material [7]. Typically, X-ray emission will feature a broad spectrum of photon energies, decreasing in intensity up to the energy of the electrons accelerated across the tube potential. No photons are produced with energies above the energy of the electron beam. The emission spectrum will also feature prominent peaks corresponding to the characteristic K_α and K_β lines of the target material due to atomic de-excitation where electrons are ejected from inner-level shells of atoms within the target [2, 7]. A representation of a typical bremsstrahlung spectrum is shown in Figure 1.10, showing the broad bremsstrahlung spectrum with characteristic K_α and K_β lines. The table shows the energy of these characteristic lines for tungsten, the target material of the X-ray tube described above [82]. Due to the broad X-ray emission spectrum, experimental data is therefore reported with respect to the potential across the X-ray tube, and not the X-ray photon energy.

The total X-ray intensity during an exposure may be adjusted either by changing the exposure time, or by changing the filament current. The overall intensity of the X-ray beam may be described by multiplying the filament current (mA) by the irradiation time (s), to produce a value in mAs.

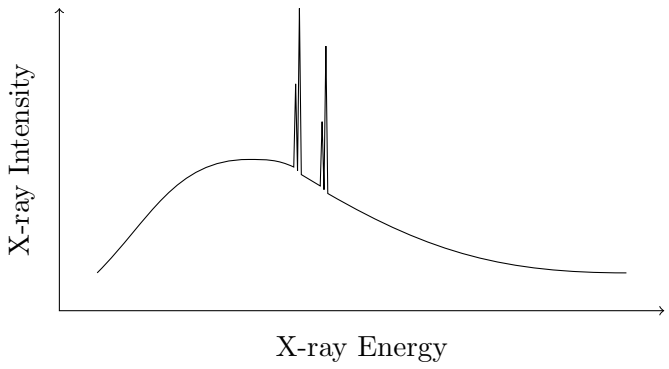

Peak	Energy (keV)
K_{α_1}	59.3
K_{α_2}	57.9
K_{β_1}	66.9
K_{β_3}	67.2

Figure 1.10: Representation of a typical bremsstrahlung spectrum. Table inset lists the energies of the K_α and K_β characteristic X-ray peaks for tungsten.

[2]Defence Science and Technology Organisation

1.5 Simulation of Energy Deposition

1.5.1 Motivation

Experimental work provides a wide variety of information on the behaviour of a material's response to radiation, however simulations may also be used to provide a deeper understanding of the processes occurring. Occasionally, obtaining information experimentally is impractical, or prone to large uncertainties. In these cases simulations may provide information which would otherwise be unobtainable. A precise measurement of the dose profile in a material, for example, is a useful measurement, but determining this profile experimentally is difficult. Simulations may be performed instead, and furthermore may provide a richer variety of results than could be obtained experimentally. Physically, there are constraints on the activity and particle energy of the available radiation sources used in experimental work. In contrast, a wide variety of different parameters may be used for simulations.

Simulations also need experimental validation, to ensure what is being simulated accurately reflects the real world. Experimental work can therefore be used to ensure simulations are running correctly. Areas where both experimental work and simulations can be performed are compared with each other, after which simulations can be run with parameters which are not accessible for experimental work.

Fabrication of glasses and optical fibres can be an expensive and time consuming process and simulations may be used to estimate the response of a material, which can be used to guide fabrication work. The dose deposition profile, mentioned previously, can be directly used as a guide for fabricating an optical fibre with the optimum diameter for detecting a certain type of radiation. Simulation of an optical fibre surrounded by different materials will give an indication of the dose absorption of an optical fibre when embedded or surrounded by these materials. In this way, simulations can be used to obtain a quick understanding of how an optical fibre may respond to different environments and radiation types, in order to guide further fabrication and experimental work.

1.5.2 Simulation Package and Theory (PENELOPE)

PENELOPE (**P**enetration and **ene**rgy **lo**ss of **p**ositrons and **e**lectrons) is a Monte Carlo simulation package used to calculate the transport of high-energy photons, electrons and positrons through matter [83]. A comprehensive guide to the simulation package is available and provides a thorough description of the physical processes it uses to perform simulations, as well as an explanation of the use of the package [84]. A brief

description of the important theory and notes on the usage of the package will also be given here.

1.5.3 Physical Processes Simulated by PENELOPE

PENELOPE simulates a high-energy electron, photon or positron interacting with matter. The interaction mechanisms simulated are those summarised in Section 1.4. The mean free path of a particle within a material is used to determine the distance travelled before an interaction is calculated. Once the particle has travelled this distance, selection of an interaction process is executed, followed by the continued propagation of the particle with its post-interaction energy. Secondary particles may be generated by interactions and, if of sufficient energy, the propagation and interactions of these particles are also simulated.

Each particle therefore travels through the material, depositing energy based on the above processes. Once the particle and all of it's daughter particles fall below a threshold energy, the simulation for that particle is completed. In order to build up the required statistics, many particles are simulated. Simulations performed for this project typically involved $10^6 - 10^8$ primary particles. Individual simulations are a compromise between computation time and the desired statistical precision. Certain simulations were run representing an optical fibre in an experimental environment. Due to the small volume of optical fibres, only a small fraction of the simulated particles interact with the active volume representing the fibre, leading to higher uncertainties, hence these simulations were performed with a greater number of primary particles, 10^8 particles in most cases. The uncertainties for these simulations are still higher compared with others, however future simulations may be performed with an even greater number of primary particles if improved statistics are required, although this would proportionally increase the calculation time for the simulation.

1.5.4 Abilities and limitations

PENELOPE is a package designed to simulate the transport of energy by electrons, positrons and photons through matter. It is not capable of simulating alpha particles, neutrons or other forms of ionising radiation. For these calculations other simulation packages, such as GEANT4, are suitable, but for someone new to the field, PENELOPE is a simpler, more intuitive simulation package to use than GEANT4 and other packages. Constructing simple simulations is straightforward and the ability to construct more complex geometries is also available.

A limitation is that below approximately 10 keV, computed results start to vary from

those observed experimentally. Hence PENELOPE should not be used for computation of dosage for energies below 10 keV.

1.6 Project Constraints and Opportunities

1.6.1 Glass Fabrication Facilities

Research in the initial stages of the project was constrained by the facilities and equipment available. Glass fabrication and processing facilities were only capable of working with soft glasses (such as lead silicate, fluoride phosphate and tellurite) and hence the available choice of materials was constrained to soft glasses. Materials such as silicates, while briefly investigated, were not considered as candidates for further research due to the lack of fibre fabrication equipment capable of working at the high temperatures these glasses required.

At a later stage in the project, facilities suitable for processing of silica glasses became available, this enabled exploration of new materials. Silica was found to be suitable for radiation sensing applications and the luminescence characterisation of this new material was guided by work previously performed on soft glass. This opened up new opportunities for the project with materials that have improved transmission loss and better mechanical properties and chemical stability, providing an important contrast and potential advance on the work done with soft glasses.

1.6.2 Detection Systems

Similar to the initial constraints found for the available glass and glass processing techniques, technological limitations to the luminescence detection system were also encountered. Low level light detection requires expensive and specialised equipment, and bialkali photomultiplier tubes (PMTs) are often used for this purpose. Bialkali PMTs are only usefully sensitive in the 200 to 550 nm wavelength region, hence luminescence emission is likewise constrained to this region, and the UV absorption edge of many different glass types narrows this region further. PMTs also require high voltage power supplies to operate, hence experiments are rarely portable. Due to this, experiments were initially constrained to materials and systems where luminescence occurs in the 350 to 550 nm region. This wavelength region corresponds with the peak efficiency of many PMTs and is longer than the UV absorption edge of several soft glasses.

The appearance of low noise-high sensitivity single photon avalanche diodes (SPADs) from approximately 2010 has enabled the detection of low-intensity signals using silicon. The detectable wavelength region is appreciably wider than that of most PMTs,

approximately 200 to 1000 nm, and the quantum efficiency is also generally higher. In addition, SPAD devices have low power requirements and are smaller and more portable than PMTs. The dark current in SPADs is also lower, typically 10 counts/s compared with an average 50 counts/s found in many uncooled bialkali PMTs. Therefore using SPADs for luminescence detection opens up a range of wavelength regions previously inaccessible when using a PMT, allowing a greater range of potential luminescence materials and dopants. The greater quantum efficiency and lower noise of SPAD devices also allows detection of fainter signals than previously possible with PMTs. An additional physical advantage of SPADs are their suitability for integration onto the end of a fibre as a single detection element.

The two factors mentioned above have had a considerable impact on the scope and direction of research. With the materials selection constrained to soft glass, and the emission and detection wavelengths confined to the 350 – 550 nm region, initial research was limited to materials which satisfied these conditions. At a later stage in the project, silica processing facilities became available, this allowed silica and silicate glasses to be seriously considered as potential materials suitable for further investigation. At a similar stage in the project, a SPAD device was also procured for detection of luminescence, this allowed investigation of materials and dopants which produce luminescence within the 300 – 1000 nm region. The use of a SPAD detector also made the experimental test bed for optical fibre measurements highly portable, allowing measurements to be performed in other facilities.

1.7 Comparison of Detectors

Experiments presented in this thesis are performed using two different types of optical detectors: photomultiplier tubes (PMTs) and single photon avalanche diodes (SPADs). PMTs have an established history of use for detection of low-intensity signals and have been used extensively for TL and OSL detection. Many experiments were performed using bialkali PMTs, as this was efficient for lab-based experiments and testing of new optical fibres. However, the long-term goal of this work is to create a system suitable for deployment in real-world applications, and for this purpose a PMT is bulky and requires a high voltage power supply, which makes PMTs unsuitable for many applications.

Another type of detector - a single photon avalanche diode (SPAD) - is an alternative detector offering comparable sensitivity to a PMT, but are small, lightweight and have low power requirements. They are a practical choice when considering real-world applications of the optical fibre sensor. Two SPAD devices were used for the experimental work presented in this thesis: a Micro Photon Devices PDM model and a Lasercompo-

nents COUNT®-blue model. The technical specifications of both these SPAD models are compared with the specifications of a bialkali PMT, shown in Table 1.2 and the quantum efficiencies shown in Figure 1.11.

The detection efficiency for these SPAD models is appreciably higher than that of many photomultiplier tubes. In addition, the dark current of SPADs are also lower: a 50 mm diameter PMT will operate with an average dark current of 40 - 50 counts/s while both the SPAD units shown here operate with a dark current of 8 - 10 counts/s. However, while SPAD detectors can have higher efficiency with lower dark current, the small size of the detector area requires careful focusing of the luminescence signal. The PMT has a detection area with a diameter of 50 mm, while SPAD units typically have a detector area of 50 – 100 μm^2. This affects the optical coupling of light from an optical fibre output onto the detector face. For a PMT it is a simple case of loosely focusing the light onto the PMT aperture, whereas when using a SPAD the light must be carefully focused and aligned

When comparing the two different SPAD models, the Lasercomponents SPAD is shown to have the highest sensitivity with comparably low dark noise and as such it was the device preferred for experimental work. All results in this thesis reported to be detected using a SPAD will have been performed using this Lasercomponents COUNT®-blue model.

Table 1.2: Comparison of specifications for an EMI 9235 QB photomultiplier tube and two SPADs, a Lasercomponents COUNT®-Blue and a Micro Photon Devices PDM.

Specification	**PMT**	**COUNT®-Blue**	**PDM**
Detector Area	15 cm^2	50 μm^2	50 μm^2
Dark Noise (counts/s)	50-60	10-20	10-20
Waveband (nm)	300-550	350 – 1100	350 – 1000
Peak Quantum Efficiency	30 %	70 %	50 %
Timing Resolution (ps)		1000	250
Dead Time (ns)		45	77
Operating Voltage (V)	1200	12	12
Dimensions (cm)	8 x 8 x 20	4 x 7 x 10	4 x 5 x 8

1.8 Thesis Overview

As has been outlined in this introductory chapter, the research presented here aims to produce an optical fibre capable of detecting ionising radiation by using the mechanism of optically stimulated luminescence intrinsically within the fibre. The following is a summary of each chapter presented in this thesis, and how the work therein helps to achieve this goal. An overview of the process used to take a material from an initial

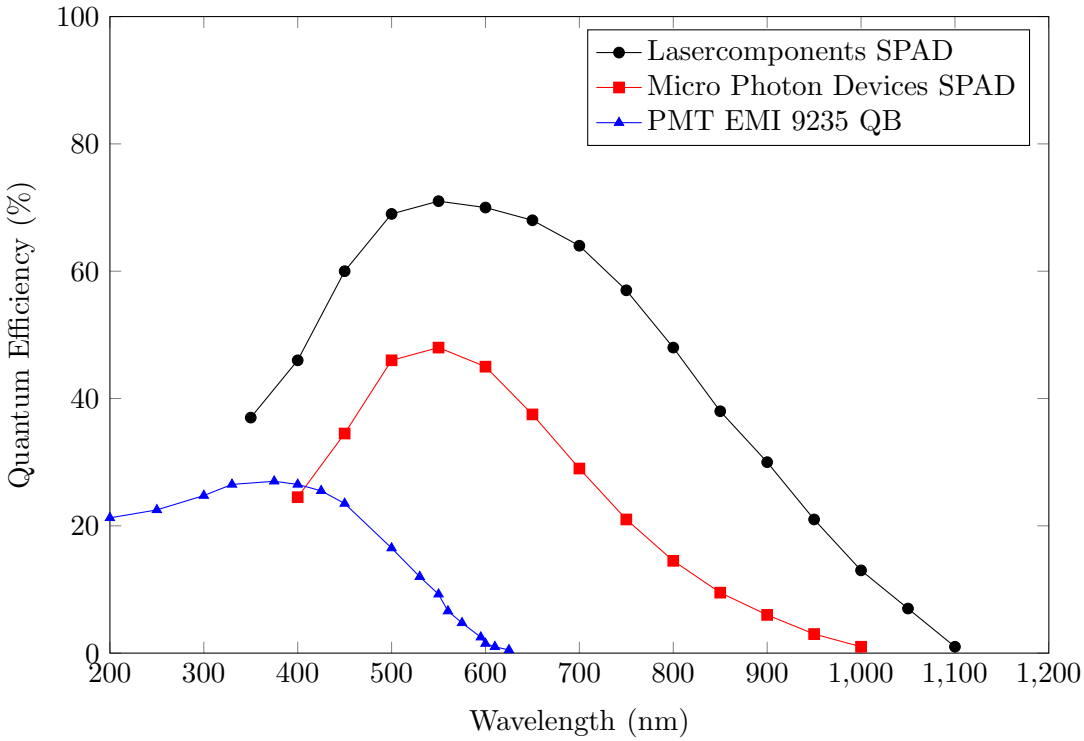

Figure 1.11: Quantum efficiency of a PMT (EMI 9235 QB) compared with two single photon avalanche diodes, Micro Photon Devices (MPD) and Lasercomponents (COUNT®-blue).

materials characterisation phase to a radiation-sensing optical fibre is given in Figure 1.12.

Materials Identification and Characterisation The second chapter in this thesis presents the work performed to determine a suitable glass material capable of producing an OSL response and also capable of fabrication into optical fibres. Fluoride phosphate glass was identified as the most promising candidate and this material was studied and work was done to further improve its dosimetry characteristics. While necessary to determine basic characteristics such as composition, spectroscopy and the OSL response, work in this area was pushed further in an attempt to gain a deeper understanding of the material and its luminescence characteristics.

Doping of Fluoride Phosphate Glasses Following the identification of fluoride phosphate glass as a suitable material, Chapter 3 presents the work performed to improve the radiation sensing performance of the material by doping the glass with rare earth and transition metal ions.

Fabrication Chapter 4 presents the process by which the fluoride phosphate glasses studied in Chapters 2 and 3 were fabricated into optical fibres. Fluoride phosphate glass is not widely used as an optical fibre material. For glass materials such as tel-

lurite, lead silicate, ZBLAN and most notably silica, the literature contains a variety of established methods, but for fabrication of fluoride phosphate optical fibres, the literature contains fewer resources. Work was therefore required to establish suitable parameters for turning this material into optical fibres of sufficient quality for use in radiation sensing measurements. The approach was primarily based on the established methods for fabricating optical fibres out of other soft glasses, such as tellurite and lead silicate.

Radiation Sensing Measurements with Optical Fibres Following fabrication of the glass into optical fibres, in Chapter 5 they were tested for their radiation sensing capabilities, firstly as a concept demonstration, then subsequently to aid improvement of the material properties and fabrication techniques. Testing the OSL response of small samples of material is straightforward using current instruments. Doing similar tests on optical fibres, however, requires a different approach. An experimental protocol by which fibres could be systematically tested needed to be created, this involved solving a number of problems relating to the usage of optical fibres and the measurement of the OSL signals.

Radiation Sensing Measurements using Silica Glass Following the work with fluoride phosphate glass, silica glass was considered as an alternative material for optical fibre radiation sensing. Chapter 6 presents the evaluation and characterisation of these glasses, followed by the fabrication of optical fibres and the testing of them in radiation sensing experiments.

Discussion and Conclusions Chapter 7 considers all the experimental work performed and draws conclusions about the effectiveness and suitability of the materials and methods for performing radiation dosimetry in real-world applications.

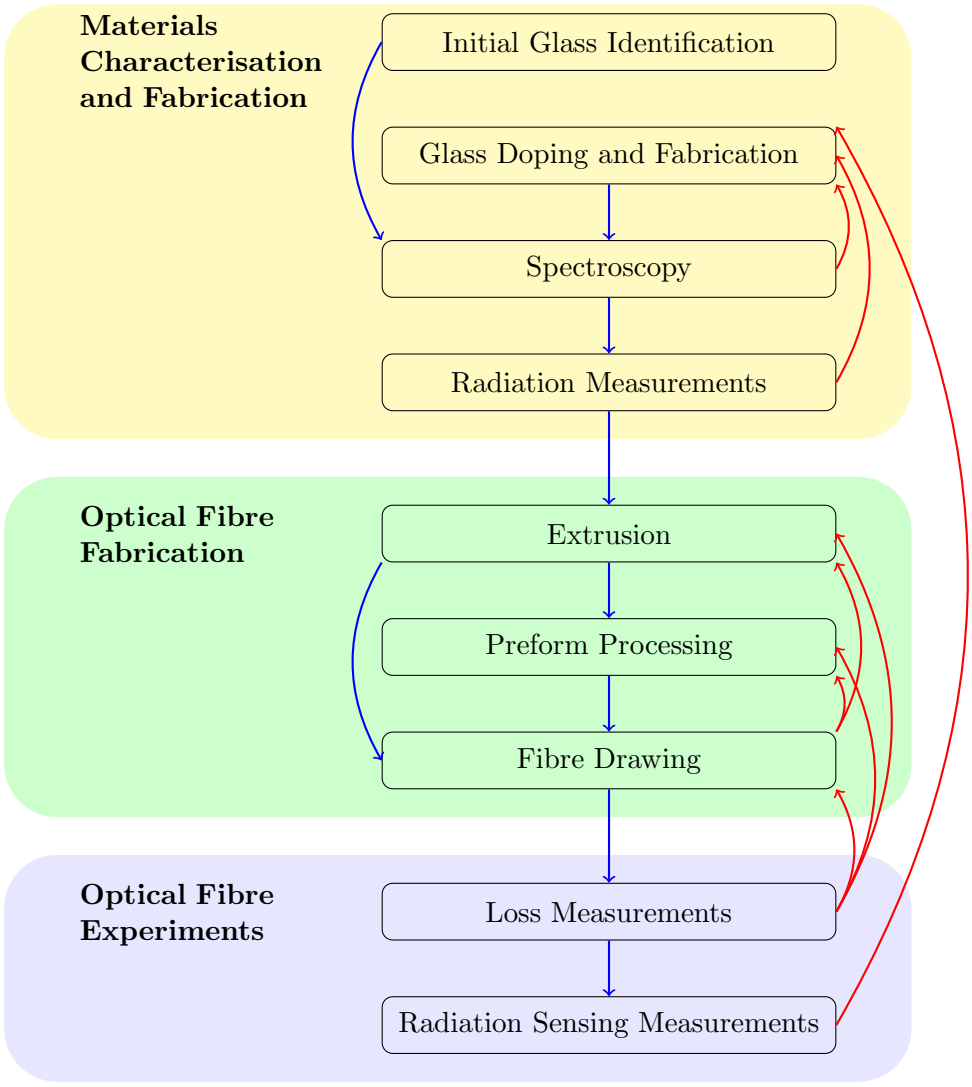

Figure 1.12: Overview of experimental process from the initial glass analysis through to radiation sensing measurements with optical fibres. Blue lines: chronological timeline of experiments. Red lines: experimental results used to guide analysis and fabrication of new materials and fibres.

Chapter 2

Identification and Characterisation of Fluoride Phosphate Glass

The fundamental requirement of the proposed radiation-sensing optical fibre is a glass material which has a measurable response to ionising radiation using the mechanism of optically stimulated luminescence. It was therefore necessary to firstly identify a material that produces a usable OSL response, then characterise it for both its optical and luminescence properties.

2.1 Initial Survey of Glass Characteristics

2.1.1 Glass Samples

An initial screening of glass samples was performed in order to identify suitable materials for further study. A selection of different glass types were tested. The selection criteria isolated glasses that could be fabricated into optical fibres and were transparent in wavelength regions applicable to OSL. Experiments were initially performed on bulk samples, as optical fibres were not a requirement at this stage of the work. Samples in their bulk form are cheaper to acquire, easier to process for experiments and a wider range of sample types are available. The types of glasses tested are listed:

- Fluoride Phosphates
- Phosphates
- Tellurites
- ZBLAN[1]
- Fluoro-aluminates
- Silicates
  - Lead silicates
  - Borosilicates
  - Soda lime silicates

The most important characterisation test to perform on glass samples was to measure their response to ionising radiation and to determine which glasses produce OSL. This process is explained in the following Section.

2.1.2 Screening for Optically Stimulated Luminescence

The instrument used for many of the experiments presented in this thesis is the Risø TL/OSL DA-20 Reader, an instrument designed for measuring the OSL and TL from small samples of material. This instrument comprises a calibrated $^{90}Sr/^{90}Y$ beta source for irradiations, diode arrays at 470 nm and 870 nm for optical stimulation of the sample, filters for isolation of the luminescence signal from the optical stimulation, and an Electrontubes 9235QB bialkali photomultiplier tube for detection of the luminescence. Further technical details and a diagram of the Risø Reader are provided in Appendix B.1.

Small samples of glass were initially cut from polished slides, however it was soon shown to be more efficient and representative to crush samples of the glass into grains with diameter between 250 and 350 µm, of which approximately 12 mg aliquots were prepared on sample holder discs. More details of the sample preparation for analysis

[1] **Z**rF_4–**B**aF_2–**L**aF_3–**A**lF_3–**N**aF

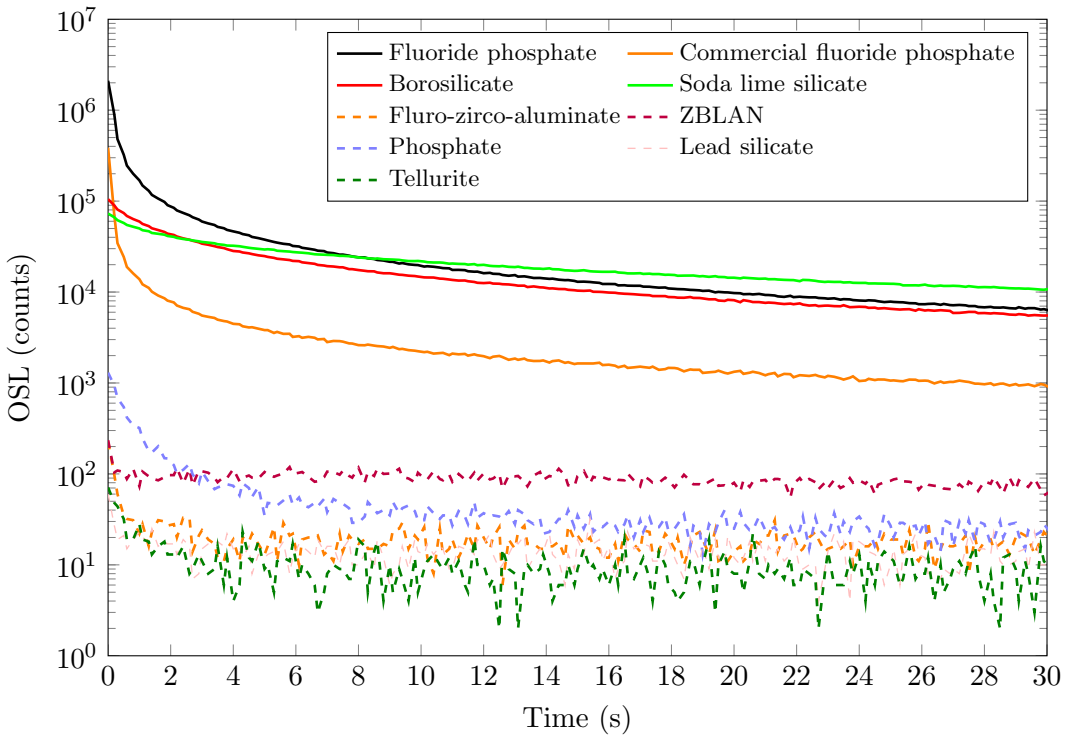

Figure 2.1: Example of an OSL response from a variety of the glass samples examined.

in the Risø Reader are also provided in Appendix B.1. Samples were tested using two different optical stimulation and filter combinations: the first used 470 nm stimulation with a HOYA U340 filter, allowing measurement of luminescence from 300 - 400 nm; the second combined 870 nm stimulation with a Schott BG39 filter, allowing measurement of luminescence from 350 - 600 nm.

The power of optical stimulation from the 870 nm diode array is 166 mW/cm^2; on a 5 mm diameter sample this is 32.5 mW. For the 470 nm diodes, the power at the sample position is 80 mW/cm^2; on a 5mm diameter sample this is 15.7 mW.

Of the glasses tested several showed an OSL response to ionising radiation, but only fluoride phosphates and silicates showed a high enough intensity for practical use. Fluoride phosphate glasses were observed to have very fast optical response: the signals were bleached out quickly within several seconds exposure to 470 nm photons, which equates to between 15 – 30 mJ of optical power. In comparison, silicate glasses were observed to have very slow response, bleaching of samples required longer illumination times, in the order of tens of seconds to minutes, requiring upward of 1000 - 2000 mJ of optical power to bleach. An example of an OSL response from each of these glass types is shown in Figure 2.1.

2.2 Fluoride-phosphate Glass

Of the glasses tested, fluoride phosphate was considered the most suitable for the aims of the project. It showed an OSL response and the fast rate of its untrapping allowed the material to be re-set to its pre-irradiated state quickly. It is also a soft glass, allowing extrusion and fibre fabrication at temperatures below 1000 ℃, unlike silica glasses which require higher temperatures. Fluoride phosphate glass is a low index, low dispersion, mid-IR transparent glass produced for optical applications, it also has good transmission into the UV.

2.2.1 Varieties of Fluoride Phosphate Samples

Several different fluoride phosphate glass samples were studied in their bulk form, either as crushed grains or polished slides. These samples were obtained from previous research projects, several samples were fabricated at the University of Jena[2], and several at the University of Southampton[3]. These samples varied in their composition, fabrication conditions and dopant ions, hence several samples of similar composition were also fabricated from different raw material sources. A summary of these samples is given in Table 2.1 and a more comprehensive guide of each sample is provided in Appendix A.2. Experiments performed on a representative selection of these samples will be presented.

Table 2.1: Representative selection of fluoride phosphate glass samples analysed for their luminescence behavior.

Sample Name	**Fabrication Environment**	**Source**
FP1	Oxidising	Commercial
FP1red	Reducing	Remelted In-house
FP2	Unknown	Commercial
FP3	Oxidising	In-house
FP4	Reducing	In-house
FP5	Oxidising	In-house
FP6	Reducing	In-house
FP7	Reducing	In-house

These samples of different fluoride phosphate glass were used for measurements studying the composition, spectroscopic and luminescence properties. For the remelting and fabrication of optical fibres, producing large quantities of fluoride phosphate glass was infeasible for the glass fabrication facilities available to the project. Fluoride phosphate glass was therefore sourced externally from Schott Glass Company, and is the sample

[2]Friedrich Schiller University of Jena, Jena, Thuringia, Germany
[3]University of Southampton, Southampton, United Kingdom

FP1 in Table 2.1, further information on this glass can be found in Appendix A.2.2. This glass was measured and observed to show an OSL response. Although the intensity of this OSL response was lower than for many other fluoride phosphate samples, it was used for all remelting and fabrication work due to its commercial availability in sufficient quantities for further experimental work.

2.3 Composition

2.3.1 Electron Microprobe

Information on the elemental composition of glass samples was required for performing simulations in PENELOPE, where the proportion of each element in the material needs to be known for correct calculation of radiation transport. It is also useful to know the glass composition in order to understand the results obtained in later experiments. While the batch composition of samples made in-house are known, a small amount of variation might occur due to evaporation of certain elements during the glass melting. The composition of commercially acquired samples was unknown. Several samples were therefore analysed with an electron microprobe to determine their composition.

Glasses were prepared for analysis by embedding into a resin disk, prepared by Pontifex & Associates [4], and coated with graphite. Samples were then analysed using a Cameca SX51 electron Microprobe[5], results are shown in Table 2.2, and in Figure 2.2.

An immediate observation from the results is the difference in fluoride and oxygen content in each glass: Samples FP1 (Schott N-FK51A) and FP2 (Schott PK52A), both commercial samples, have a higher oxygen to fluorine ratio than most other samples. Likewise, sample FP7 has a notably lower oxygen to fluorine ratio. This is of interest, as samples containing lower levels of oxygen to fluorine have been observed to produce a higher intensity OSL response. Also of interest is the presence of barium in commercially acquired samples, FP1 and FP2, which is not present in any in-house prepared glass. It is not clear if the barium content has any impact on either the optical transmission or the OSL response: acquisition and testing of samples containing varying proportions of barium might be necessary to establish any relationship. Calcium is also observed to be present at a slightly lower concentration in FP1 and FP2. Sample FP7 shows the most dissimilarity with other glasses, and the OSL response for this glass is observed to be lower than for many other fluoride phosphate glasses. Given the trend observed for the oxygen:fluorine ratio in other samples, this might be attributed to the comparatively high oxygen content in this sample.

[4] Pontifex and Associates Pty Ltd, 26 Kensington Rd, Adelaide, Australia.
[5] Adelaie Microscopy, Medical School North, University of Adelaide.

Table 2.2: Composition of several fluoride phosphate glasses as determined by analysis with an electron microprobe.

Element	Atomic Percentage (At %)					
	FP1	FP2	FP4	FP5	FP6	FP7
O	22.6	23.7	17.6	19.3	12.6	29.7
F	42.9	43.3	50.1	48.3	56.0	37.0
Na	0.1	0.1	0.0	0.0	0.0	0.0
Mg	2.4	2.5	2.8	2.8	2.8	2.6
Al	10.7	9.1	10.2	9.6	9.7	8.3
P	5.6	5.2	3.6	4.2	3.0	7.1
Ca	6.0	5.5	9.3	9.5	9.1	6.3
Sr	5.5	6.6	6.3	6.3	6.7	8.9
Ba	4.2	4.0	0.0	0.0	0.1	0.0

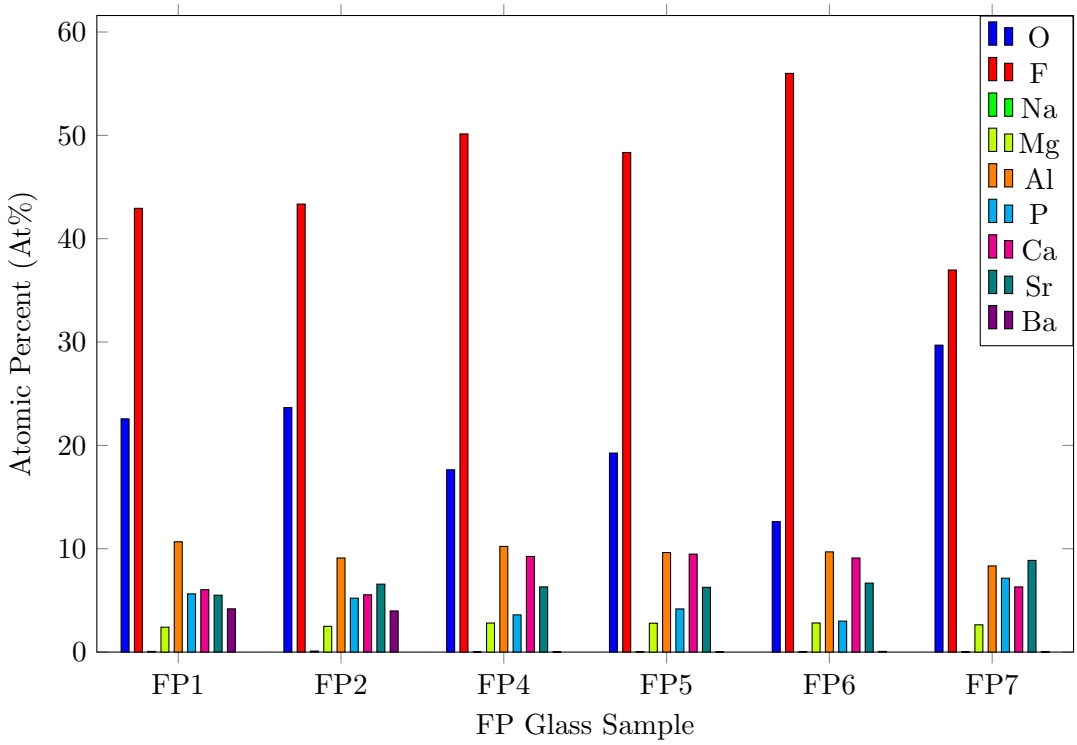

Figure 2.2: Composition of fluoride phosphate glasses as determined by an electron microprobe. Data was taken from multiple points on the glass surface for each sample.

2.3.2 ICP-MS/OES

Inductively coupled plasma mass spectroscopy/optical excitation spectroscopy (ICP-MS/OES) was used to identify and determine the concentrations of ions within the glasses, introduced in the form of impurities in the raw materials from which glasses were fabricated, and also possibly from the materials in which the glasses were processed (i.e. melting crucibles). These impurities act as 'pseudo-dopant' ions and may provide the radiative recombination paths that allow luminescence to occur. Identifying these impurity ions is potentially useful to try and explain why some samples emit luminescence at certain wavelengths, and why some samples have a higher OSL response.

Samples of glass were analysed by Genalysis[6]. Samples were prepared by cutting from bulk glass and polishing off any surface layers, in order to reduce the possibility of contamination from, for example, iron in the saw blade. Several samples of fluoride phosphate glass were analysed, results are shown in Table 2.3. The detection limit for each element shown in Table 2.3 is provided in Appendix A.3.

The results show copper ions in several samples, copper (I) in fluoride phosphate glass is known to emit in a peak centred at 400 nm [85–87]. Thermoluminescence emission spectroscopy, discussed further in Section 2.6.1, indicates emission from fluoride phosphate glass in a broad peak centred at 400 nm. This could therefore indicate the copper impurities in the glasses are providing radiative recombination centres. The presence of platinum in sample FP1 indicates it might have been melted in a platinum crucible, with some dissolution occurring into the glass.

2.4 Transmission Spectra and Photodarkening

The absorption spectra for several different fluoride phosphate glasses are shown in Figure 2.3. Transmission spectra of polished slides were taken with an Agilent Cary 5000 UV-Vis-NIR Spectrophotometer from 400 to 1200 nm in transmission mode, with background subtraction. For each slide, the thickness is measured in order to calculate the loss.

The absorption observed in the 200 - 350 region is due to metal ion impurities in the glass such as $Fe^{2+/3+}$, Fe^{2+} is known to absorb at 250 nm [87]. The intrinsic UV absorption edge is at approximately 200 nm, further into the UV than many other soft glasses, such as tellurite or lead-silicate, this can potentially be an advantage if stimulation or luminescence wavelengths in the UV are used in optical fibres. Improvement in

[6]Genalysis Laboratory Services - Intertek, 11 Senna Rd, Wingfield, Adelaide, Australia

Table 2.3: ICPMS/OES analysis of fluoride phosphate glass samples. The concentration, c (ppm), of impurity ions is shown.

FP1		**FP4**		**FP7**	
Element	c (ppm)	Element	c (ppm)	Element	c (ppm)
Pt	185	Cu	21	Zn	12
W	128	Ce	2.4	Ga	8.2
Zn	97	Ta	1.6	Cr	6
Ni	36	Co	1.1	Zr	4.4
As	17	W	1	Ni	4
Eu	11.89	Zr	1	W	3.7
Sb	10.78	Y	0.9	Sn	2.5
Co	9.2	Ag	0.8	Yb	2.5
Ti	9	Yb	0.56	Cd	2.1
Zr	5	Sb	0.51	Se	2
Cu	3	Hf	0.5	Y	1.24
In	2.45	Eu	0.28	Te	1
Ga	2.2	Ge	0.2	Co	0.9
Ta	2.1	Rb	0.2	Rb	0.79
Y	1.9	Pr	0.19	Sb	0.72
Au	1			La	0.59
Hf	0.5			Ta	0.42
Sm	0.43			Hf	0.33
Ge	0.3			Mo	0.3

the transmission in this region is dependant on the purity of the raw materials and the fabrication conditions. The research-grade samples (FP4 and FP6), for example, have lower loss and demonstrate the potential of fluoride phosphate glass as a high quality optical material suitable for optical fibre applications.

2.4.1 Effect of Photodarkening

Photodarkening induced by beta radiation was studied in fluoride phosphate glass. Polished slides of FP1 were exposed to the 20.4 mCi ^{90}Sr/^{90}Y beta source (β21) and the transmission spectra taken at intervals throughout the irradiation time, Figure 2.4 shows the spectra. The glass transmission decreases across the whole spectrum measured, but most noticeably in the 350 - 600 nm region. In particular, a broad absorption peak centred at 480 nm is observed.

These effects are similar to previous studies of fluoride phosphate glass, where glasses were exposed to UV radiation from a variety of sources such as mercury lamps and ArF- and KrF-excimer lasers [88–91]. The broadband reduction in transmission, with a broad peak centred in the 400 - 500 nm region, is observed in these previous studies. In some cases, formation of colour centres is attributed to ions present in the glass, either as impurities or dopants. For example, the oxidation of Fe^{2+} ions to Fe^{3+} is considered [88].

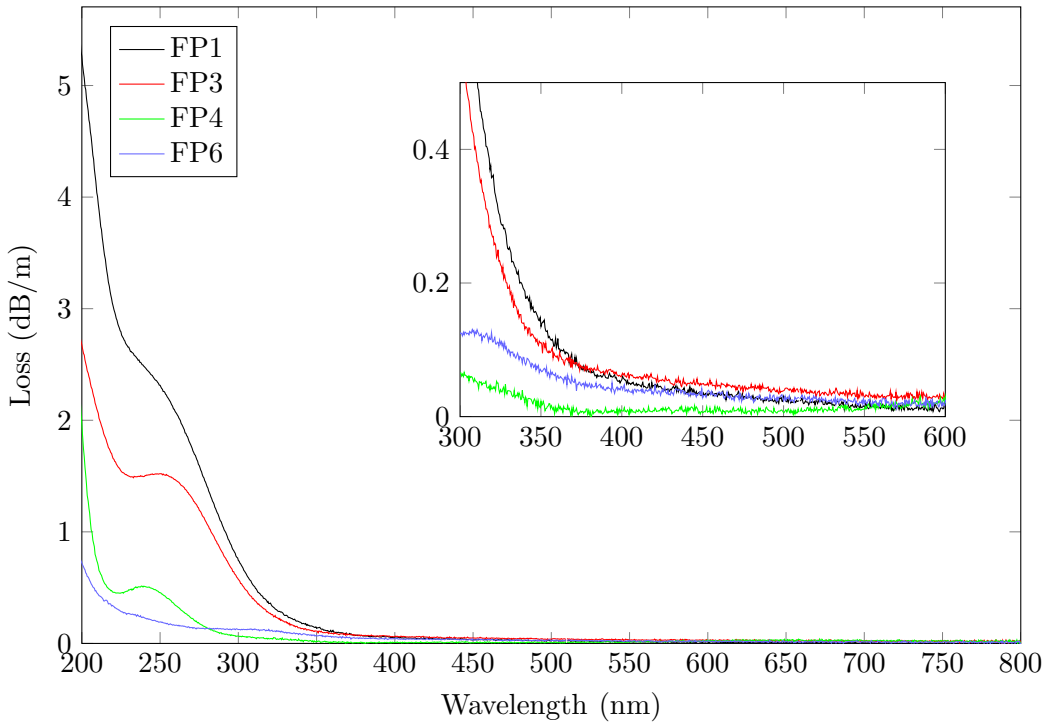

Figure 2.3: Transmission spectra of several different samples of FP glass, taken using 1 mm thick polished slides.

Colour centre formation occuring in phosphate groups is also proposed [89].

Following irradiation, colour centres remained in the glass for long periods of time but do show some fading. Figure 2.5 shows the spectrum immediately following irradiation and also after a period of three months. There is a slight reduction in absorption due to colour centres, presumably due to ambient temperature annealing; hence to determine if colour centres may be removed thermally, irradiated samples of glass were annealed at 200 ℃ for 2 hours, after which transmission spectra were again measured. As can be seen in Figure 2.5, the transmission spectrum is comparable to the unirradiated glass.

Depending on the dose environment of an optical fibre device, this radiation-induced photodarkening will potentially decrease the transmission quality of the optical fibres. As the main absorption peak is in the 300 - 600 nm wavelength range, centred at 480 nm, this directly impacts the wavelength regions of interest when using photomultiplier tubes or single photon avalanche diodes for detection of the OSL (refer to Section 1.7 for more information on these detectors). In low dose environments, this photodarkening will be negligible, but in high dose environments, or applications where a fibre may be placed in a low-dose environment for extended periods of time, the photodarkening will eventually compromise the quality of the detector. In this circumstance, it may be possible to heat-treat fibres between measurements in order to remove any photodarkening effects, however while possible for certain applications this approach would be impractical in many environments.

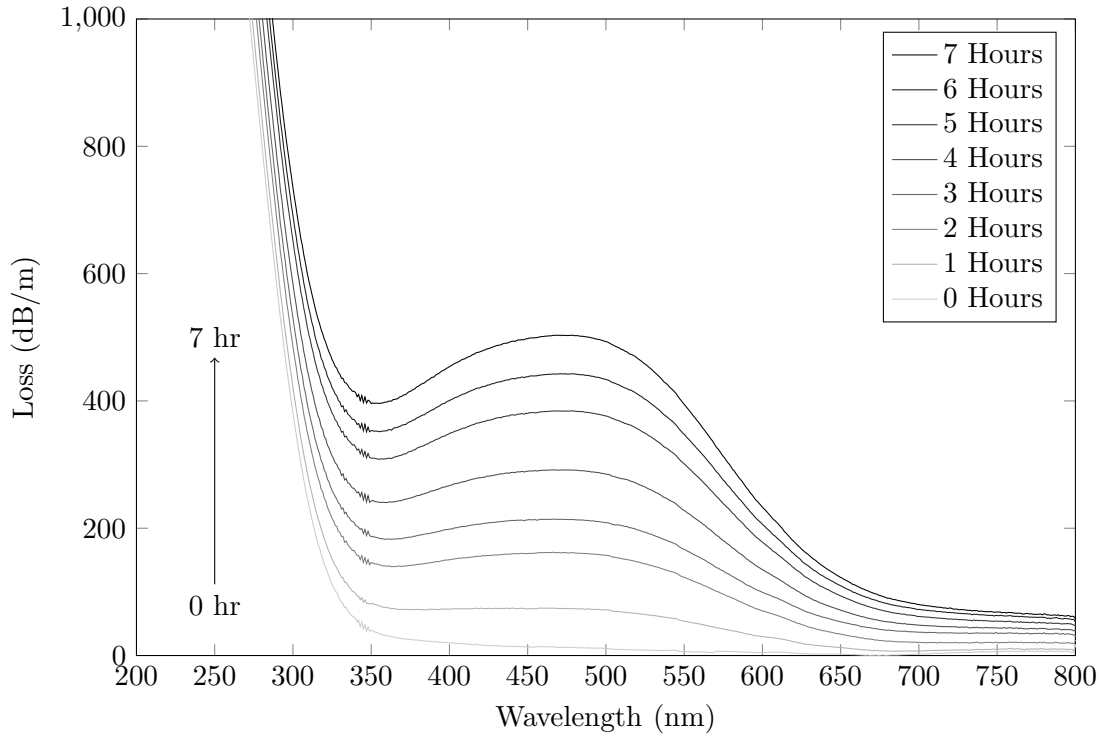

Figure 2.4: Photodarkening in Schott N-FK51A fluoride phosphate glass over 7 hours due to irradiation with a $^{90}Sr/^{90}Y$ Beta source.

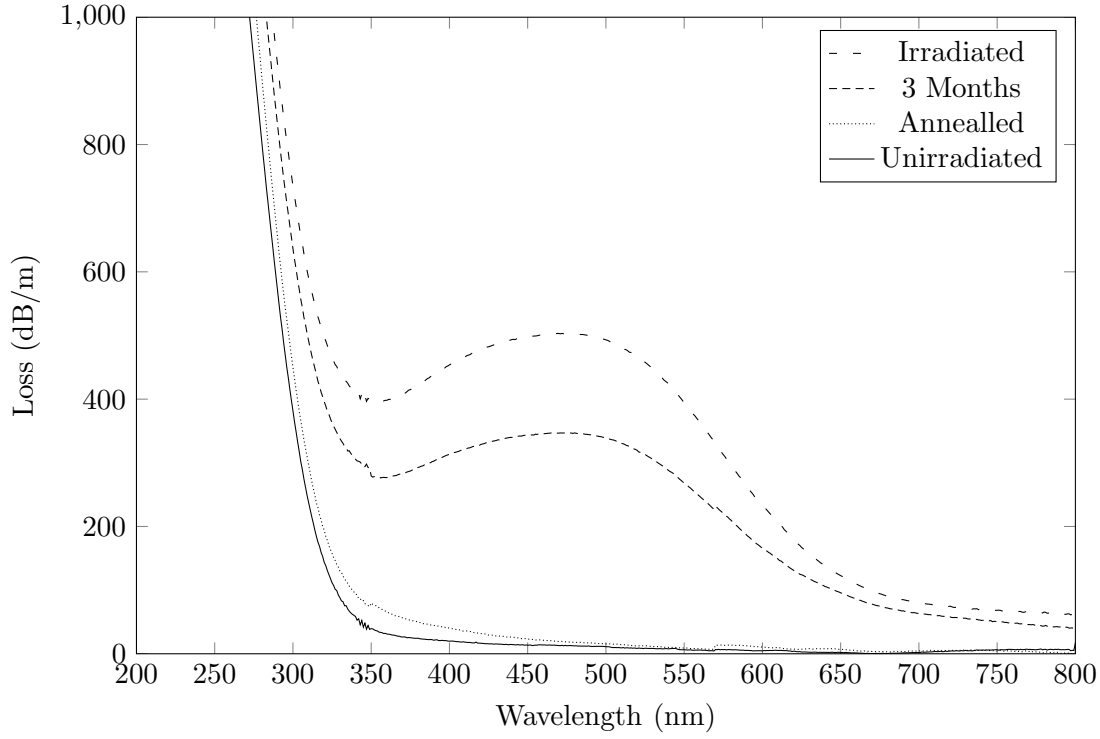

Figure 2.5: Annealing of colour centers by heat treatment at 200 ℃ for 2 hours.

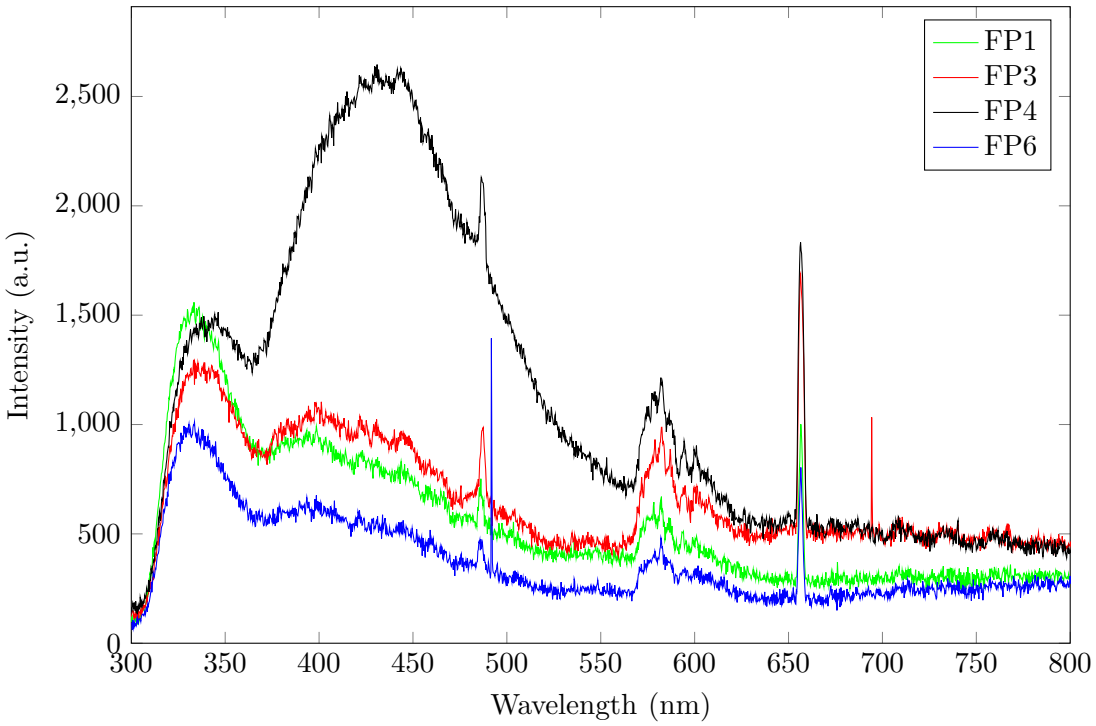

Figure 2.6: Emission spectra of several FP glass samples.

2.4.2 Emission Spectra

The emission spectra of fluoride phosphate glasses were also measured using a Princeton Instruments SpectraPro 2300i spectrofluorimeter[7]. Excitation in the UV is provided by a mercury lamp, and in the visible by an incandescent bulb; the specific wavelength is selected using diffraction grating monochromators, incident through an adjustable slit aperture. Fluorescence is collected and focused by a fused silica lens into a fibre guide leading to the detector module, which uses diffraction grating monochrometers and a peltier cooled CCD array to obtain a spectrum. Between the optical fibre coupling and the detector module a Schott WG320 nm long pass filter was used to suppress any scattered excitation photons.

For the FP glasses analysed, an excitation of 250 nm was used and results are shown in Figure 2.6. Sharp 'spikes' are occasionally observed in the spectra and are not due to fluorescence from the sample, they are are attributed to the interaction of cosmic radiation with the detector chip. Although the glass is undoped, slight fluorescence is observed at 440 and 580 nm. This could be due to impurity ions, discussed in Section 2.3.2, and is an indication of where luminescence emission may occur in the glass during OSL. Sample FP4 has the strongest emission at 440 nm, which is provisionally attributed to the higher concentration of Cu^{+} impurities present in this sample, as is shown in Table 2.3, which is known to emit in the 440 – 450 nm region.

[7]Princeton Instruments - Roper Scientific

2.5 Redox State of Fluoride Phosphate Glass

The opportunity existed to compare glasses that had been fabricated in ambient atmosphere, then remelted in a reducing environment. A reducing environment is produced using a glovebox with a nitrogen or argon atmosphere and a vitreous carbon crucible. When studying different samples of fluoride phosphate glass, a higher OSL response was observed in glasses that had been fabricated or remelted in a reducing environment. Table 2.4 summarises the OSL response of each glass. It can be seen that for each glass, the sample fabricated under reducing conditions has the higher OSL response.

Table 2.4: Effect of glass fabrication atmosphere on the OSL response of fluoride phosphate glasses

Sample	**Redox**	**OSL (counts/g/Gy)** $\times 10^6$	
		275 − 400 nm	**350 − 600 nm**
FP1	Oxidising	7.56	0.88
FP1red	Reducing	10.79	1.23

A reducing environment would result in a lower oxygen content in the glass, resulting in oxide vacancies in the glass lattice. These oxide vacancies may then act as additional electron traps, thereby allowing a greater population of trapped electrons to be created when the glass is exposed to radiation. The oxidation state of dopant ions within the glass are also affected by the environment, ions in the +2 or +3 state in ambient atmosphere can be reduced to their +1 or +2 state when subjected to a reducing atmosphere. This can therefore change the emission properties of the recombination centres in the glass, and hence affect the OSL response.

2.6 Luminescence Characterisation of Fluoride Phosphate Glass

Due to the quantity of glass needed for further experimental work with fluoride phosphate glass, the commercially available FP1 glass[8] was procured for all further doping, fabrication and OSL experiments presented in later chapters. While batches of fluoride phosphate glass could be manufactured in-house, there was the risk of batch-to-batch variation; procuring a larger quantity of FP1 glass provided a benchmark by which various doping and fabrication results could be compared.

[8]Schott N-FK51A fluoride phosphate glass.

2.6.1 Thermoluminescence Measurements

Thermoluminescence is an important technique for measuring the luminescence characteristics of a dosimetry material. From TL measurements it is possible to calculate trap depths, trap lifetimes and frequency factors. It may also yield information on the distribution of the energy levels of the trap.

Thermoluminescence

Samples were measured on the Risø OSL/TL DA-20 Reader described in Section 2.1. Measurements were made over the temperature range of 20-300 ℃ at a heating rate of 1 K/s under a nitrogen atmosphere, after samples were exposed to 1 Gy of beta radiation from the ^{90}Sr/^{90}Y beta source. Identical measurements were also performed on unirradiated samples to provide a background measurement, this was used to subtract the incandescence detected at temperatures approaching 300 ℃. TL results for FP1 and FP1red glasses are shown in Figure 2.7, the main TL peak (T_m) can be seen at 65 ℃, there is also a declining edge observed between 0 - 40 ℃. This result indicates a broad distribution of shallow traps within the material, all features are below 150 ℃. The decay observed from 0 - 40 ℃ indicates TL stimulated at room temperature from very shallow traps. The majority of this signal will have decayed out in the short time between irradiation and commencement of data collection.

The intensity of TL from the FP1 glass remelted in a reducing environment shows a higher TL intensity - this is attributed to the formation of extra traps due to oxide vacancies in the material from the reducing atmosphere. These redox conditions could also reduce transition metal or rare earth impurity ions, potentially yielding a higher intensity emission from these ions in the detectable waveband of the PMT. While this straightforward TL measurement indicates a shallow distribution of traps in the material, further testing using initial rise TL and TL emission spectroscopy provides more information on the material; this will be explained in the following two sections.

Initial Rise Thermoluminescence

While a conventional TL measurement provides an estimation of the trap depth at T_m, more detail can be obtained using the initial rise thermoluminescence method [8,80,92]. This method analyses the rising edge of the TL peaks in order to obtain information on the activation energies E of traps. To perform initial rise measurements, it is important for the TL peak to be clearly defined and separated from other TL peaks, however this is not a common occurrence in many materials. The 'fractional glow' initial rise method is therefore used in order to overcome this problem, where consecutive TL measurements

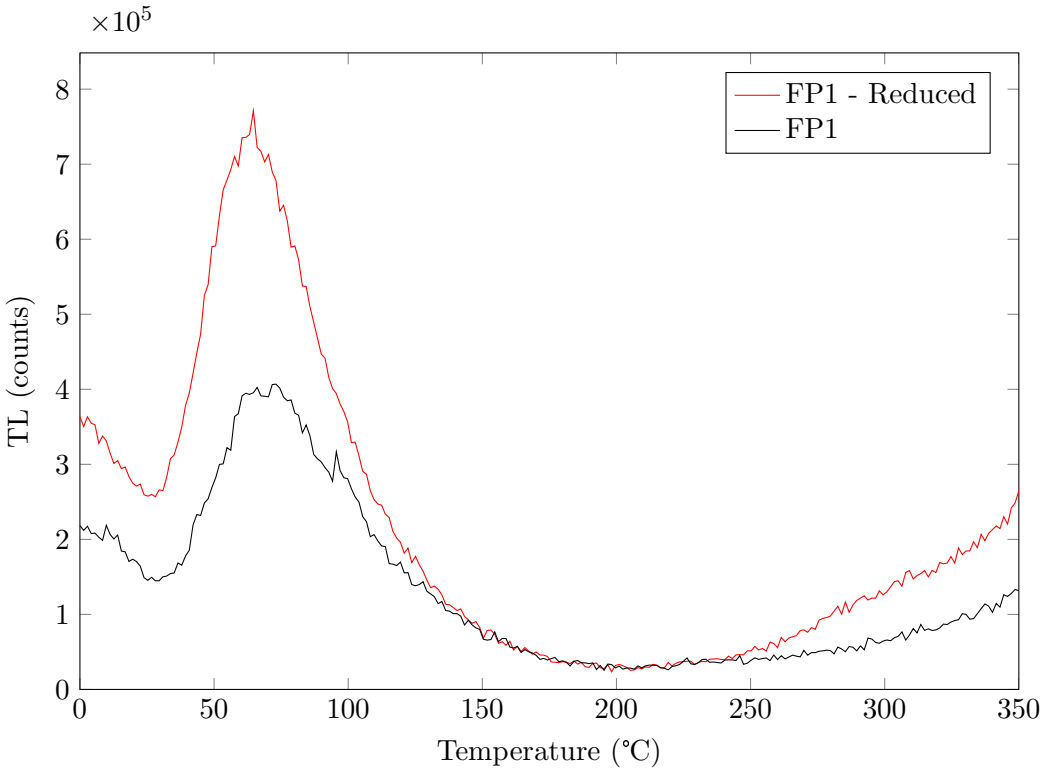

Figure 2.7: Thermoluminescence of FP1 glass melted in different redox conditions.

are performed in order to thermally isolate the trapped electrons responsible for each peak.

Following radiation exposure, TL is measured to a certain temperature, then cooled to room temperature. TL is again measured to a temperature slightly higher than the initial measurement and this process repeated up to the final temperature. For this study, this process was repeated at 20 K increments up to a temperature of 300 °C using a heating rate of 1 K/s. 300 °C is high enough to resolve the TL peak, without going to a temperature where incandescence introduces unnecessary background. The process was also performed with unirradiated samples to obtain background measurements. Initial rise data for sample FP1 is shown in Figure 2.8.

From this data, the activation energy can be calculated using the following relation:

$$I_t = c \times \exp\left[\frac{-E}{kT}\right] \tag{2.1}$$

Where I_t is the thermoluminescence intensity, c is a constant, E is the activation energy, k is Boltzmann's constant and T is the temperature. A plot of $ln(I)$ vs. $1/T$ over the initial rise region will yield a linear relationship with a slope of $-E/k$ from which the activation energy is calculated. Figure 2.9 shows a plot of $ln(I)$ vs. $1/T$ for T = 60 °C. Table 2.5 shows the activation energy values calculated.

The frequency factor, which is effectively the frequency with which a trapped electron

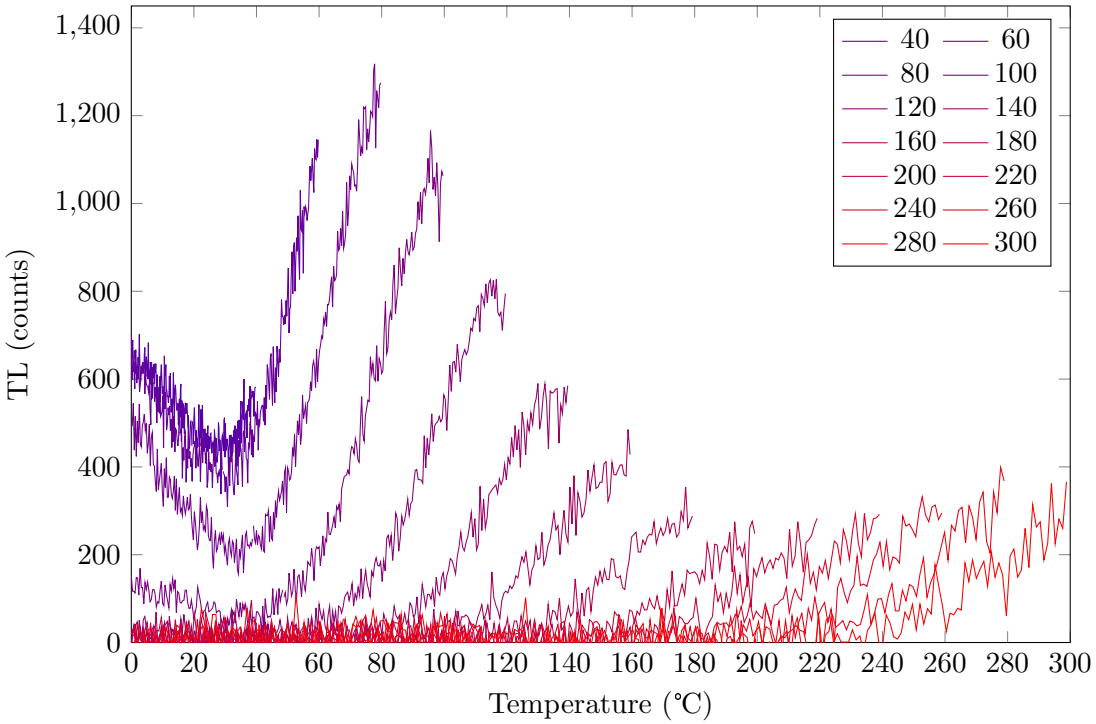

Figure 2.8: Initial rise thermoluminescence for Schott N-FK51A fluoride phosphate glass.

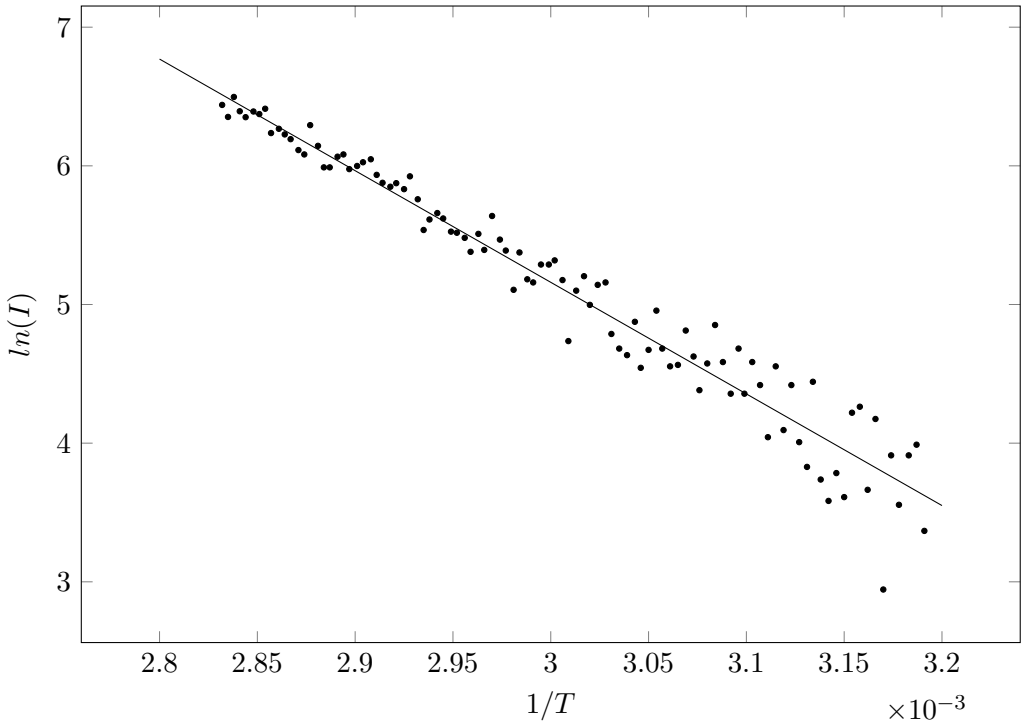

Figure 2.9: Calculation of the slope for $ln(I)$ vs. $1/T$, from which values for E, s and τ are extracted.

will attempt to escape its trap, is also calculated using the relation:

$$\frac{\beta E}{kT_m^2} = s \exp\left[\frac{-E}{kT_m}\right] \tag{2.2}$$

where s is the frequency factor, β is the heating rate and T_m is the maximum temperature of the thermoluminescence peak. Trap lifetimes, t, are calculated using the equation and along with the frequency factor are also shown in Table 2.5:

$$\tau = \frac{1}{s} \exp\left[\frac{-E}{kT}\right] \tag{2.3}$$

The data in Table 2.5 shows shallow trap energies, a distribution in the 0.5 – 0.65 eV range, and the resulting short lifetimes of these traps. This is consistent with the results seen in Sections 2.1 and 2.2, where the kinetics of OSL readout were observed to occur promptly, consistent with a population of shallow traps which are bleached promptly. The trap distribution in other materials often covers a deeper range of energies: the main dosimetry peaks in Al_2O_3:C, for example, have trap depths between 1 - 1.3 eV [93–96].

Table 2.5: Activation Energy (E), Frequency Factor (s) and Lifetimes at T = 293 K (τ) for FP1 glass using initial rise data.

T_m (°C)	E (eV)	s (s^{-1})	τ (s)
60	0.50 ± 0.039	1.9E6	200
80	0.63 ± 0.041	5.1E7	1200
100	0.69 ± 0.016	1.4E8	6300
120	0.76 ± 0.027	2.9E8	3.6E4

Thermoluminescence Emission Spectroscopy

The spectrum of the emitted luminescence is an important parameter; it is used to determine the most suitable detection wavebands. This in turn determines the choice of filters, detectors and optical stimulation wavelengths. Spectral information cannot be readily obtained on a Risø Reader, therefore a thermoluminescence emission spectrometer was used. Although no observable signal was measured using this technique on undoped samples of glass, TL emission spectroscopy was used successfully to analyse samples of doped FP glass, shown in Chapter 3. Therefore, for the sake of completeness, the method and the results will still be included in this section for undoped FP glass samples.

The thermoluminescence emission spectrometer [97, 98] uses an interferometer to ex-

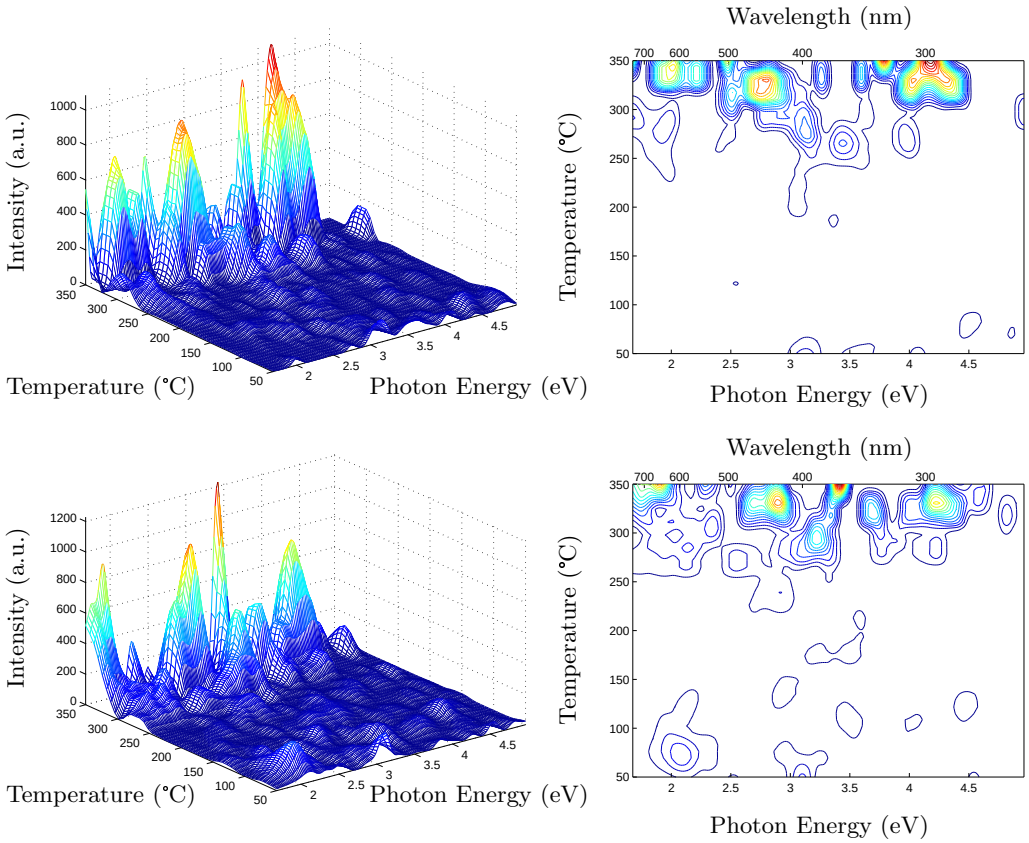

Figure 2.10: Thermoluminescence emission spectrum of undoped FP1 glass. Top = ambient melting conditions, bottom = reducing melting conditions.

tract spectral information from the luminescence signal throughout the heating process. Unlike a Risø Reader, it does not have a mounted irradiation source, hence samples are irradiated using a $^{90}Sr/^{90}Y$ beta source prior to each measurement. Due to this, the measurement process has a longer irradiation-to-measurement time than measurements performed in the Risø instrument, and hence the population of electrons in shallow traps may become depleted. From TL and initial rise TL measurements, the OSL from FP glass was shown to originate from mainly shallow traps. As a result of this, the only discernible signal from TL emission spectroscopy measurements are peaks caused by incandescence from the heating plate. Regardless, the data can be seen in Figure 2.10, where no TL emission peaks are observed. The features observed at approximately 300 °C are due to incandescence from the TL heating plate.

2.6.2 Optically stimulated luminescence

The initial screening of glasses for their OSL response was discussed in Section 2.1, however there were additional OSL measurements performed on several of the FP glasses listed in Table 2.1 to further characterise the materials and identify the most radiation-sensitive glasses for further study. As was shown previously, initial tests simply compared the OSL response of a wide variety of different materials under the

same conditions, experiments shown here attempt to provide more in-depth information on the luminescence characteristics of the selected materials.

Filters

The filtering of the luminescence signal from the stimulation light needs to be performed carefully, so as to maximise the number of detected photons while sufficiently suppressing the stimulation wavelength. Insufficient filtering of the stimulation wavelength leads to the luminescence signal being lost under the high background of scattered stimulation photons, which in a worst-case scenario, can lead to damage of sensitive detector elements.

Filters are selected for their transmission windows, suitable for the luminescence emission of the samples. Filters must also be selected which adequately block the scattered optical stimulation photons, this is due to the sensitivity of PMT and SPAD detectors, which can be easily damaged by over-exposure of photons. Interference filters can be custom-made to select a wavelength range, however they only attenuate off their passband by about 4 orders of magnitude, insufficient for blocking the tens of milliwatts typically used for optical stimulation during OSL measurements. Coloured glass filters can provide over 6 orders of magnitude rejection per millimeter of glass, so a sufficient thickness can be used in practice.

For stimulation at 470 nm, a HOYA U340 filter, 7 mm thick, offers a good UV transmission window in the 275 - 400 nm range and high suppression of scattered stimulation photons. For stimulation at 870 nm, a 3mm thick Schott BG39 is used, providing a window in the 350 - 600 nm range. Other filters, such as the Schott BG38, have wider transmission windows and are more on-band for various applications, but the suppression at the stimulation wavelength is not adequate, resulting in poor signal-to-noise ratio.

When performing OSL measurements with a 532 nm laser, Corning 7-59 filters were used due to their high transmission in the 350 - 450 nm waveband and strong suppression at 532 nm. In several later experiments a Schott BG3 filter was used, which has very similar transmission characteristics to the Corning 7-59 filter, was also coated with an interference filter designed to reject 532 nm. One disadvantage of the Corning 7-59 and Schott BG3 filters is the wide transmission window from 725 - 1200 nm, which allows scattered light in this waveband to reach the detector.

Reproducibly Complete Bleaching

The consistancy of an OSL response across a series of consecutive measurements is an important parameter and it has been studied previously in devices designed for medical applications [34, 60, 61, 63]. To test how efficiently the population of trapped electrons is optically stimulated out and removed ('zeroed' or 'bleached'), a number of OSL measurements were performed consecutively with minimal delay between each individual measurement. For each sample: one set of OSL measurements was performed using 5 s of optical stimulation and then again using 30 s of optical stimulation, in order to vary the amount of 'bleaching'[9] received by the sample between individual measurements. The 470 nm LED source in the Risø Reader provides 15.7 mW, and the 870 nm source provides 32.5 mW of power. Using the 470 nm LED stimulation, 78.4 mJ of energy is therefore incident on the sample over 5 s of optical stimulation, and 470.4 mJ over 30 s. Using the 870 nm LED stimulation, 162.7 mJ is incident over 5 s, and 976.2 mJ over 30 s. The intensity of the OSL signal is obtained by integrating the first 0.2 s of signal obtained during optical stimulation. The experiment was performed on samples FP1 and FP1red in both the 275 – 400 nm and 350 – 600 nm waveband, using the filter and stimulation wavelength combinations described in the previous Section. Results can be seen in Figure 2.11.

The FP1red glass sample demonstrates the 'memory' ('residual') effect a material may have when consecutive OSL measurements are performed, this indicates a fraction of the trapped population of electrons remains trapped once the measurement is complete. With each consecutive measurement more electrons accumulate in trapping centres and subsequently contribute to the signal detected in following measurements, this effect increases linearly with each measurement. This effect can be avoided by either (a) increasing the energy of the stimulation photons, thereby increasing the untrapping efficiency, or (b) increasing the stimulation time, allowing more time for electrons to become untrapped. In Figure 2.11 both of these scenarios are demonstrated. When using 870 nm stimulation the 'memory' effect is observed, however when using 470 nm photons for an equivalent time period, this effect is not observed and all electrons appear to be untrapped, or 'bleached'. For this same sample measured with 870 nm photons, 5 s of optical stimulation (162.7 J) is insufficient to bleach the sample, while 30 s (976.2 J) appears to untrap all electrons and no memory or residual dose effect is observed.

All other samples and measurement parameters indicate the FP1 glass is sufficiently bleached between measurements with just 5 s of optical stimulation, except for the case

[9] application of optical and/or thermal stimulation for the purposes of thoroughly removing a population of trapped electrons in a material.

of FP1red when using optical stimulation at 870 nm. FP glasses are therefore shown to be potentially useful in applications where back-to-back measurements need to be made without any variation in the OSL behavior.

Dose Dependence of OSL

The OSL response of fluoride phosphate glass was measured for samples FP1 and FP6 as a function of applied dose in the Risø Reader using stimulation at 470 nm and a HOYA U340 filter. For each reading, the radiation exposure time was increased, while optical stimulation was maintained at a consistent intensity and collection time. The luminescence signal was integrated and plotted with respect to the applied dose, results are shown in Figure 2.12. The data was fitted with both linear and exponential trend-lines, however both were found unsuitable for the entire data set. Between 0.1 and 2 Gy, the data follows a linear trend, after which the data is seen to follow a saturating exponential trend. The trend-lines are shown in Figure 2.12.

This could be explained by several factors. Firstly, the material has shallow electron traps and short trap lifetimes, this was also discussed further in Section 2.6.1, but it is sufficient to state the excited population has a lifetime on the order of tens of seconds to minutes. As a result, during the irradiation the trapped population is partially untrapping, hence the final OSL signal will not be as high as if all the charge had remained trapped. For longer irradiation times, this becomes more of an issue as ambient temperature untrapping drains an increasing proportion of the trapped charge, until dynamic equilibrium is reached and the signal intensity is seen to plateau at approximately 2 Gy, as shown by Figure 2.12.

This test is important for establishing the suitability of the material for dosimetry applications as a storage phosphor, since the material has an OSL response proportional to applied dose, once a calibration curve is established it could be used for quantitative measurements. If such a relationship did not exist, the usefulness of this glass as a dosimeter material would be limited.

Isothermal Decay of OSL

Isothermal decay, which is the depletion of a trapped population of electrons held at a constant temperature, is another method by which the properties of traps may be measured. Using isothermal decay, it is possible to make assumptions about the kinetic order of a luminescent material. Following the method outlined in McKeever [92], the decay of the excited population is measured with respect to time at a set temperature. Holding the temperature constant, several OSL measurements are performed on

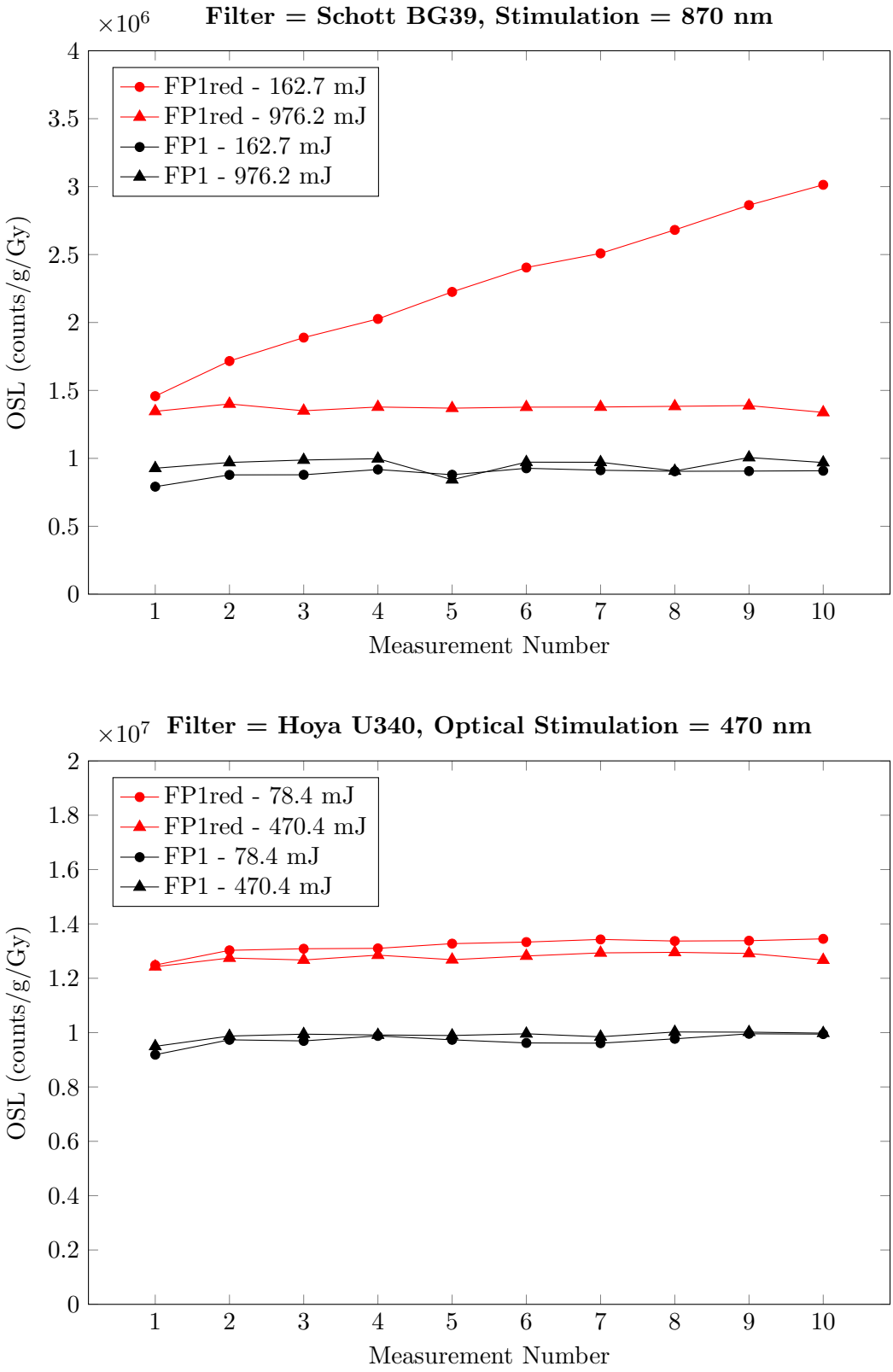

Figure 2.11: Complete bleaching of FP1 and FP1red glass in both the 275 - 400 nm and 350 - 600 nm wavebands, using 470 nm and 870 nm optical stimulation respectively. Results are given for different bleaching times between measurements, 5 s and 30 s, the optical power incident on each sample is shown in the legend. Lines are provided only as a guide for the eye.

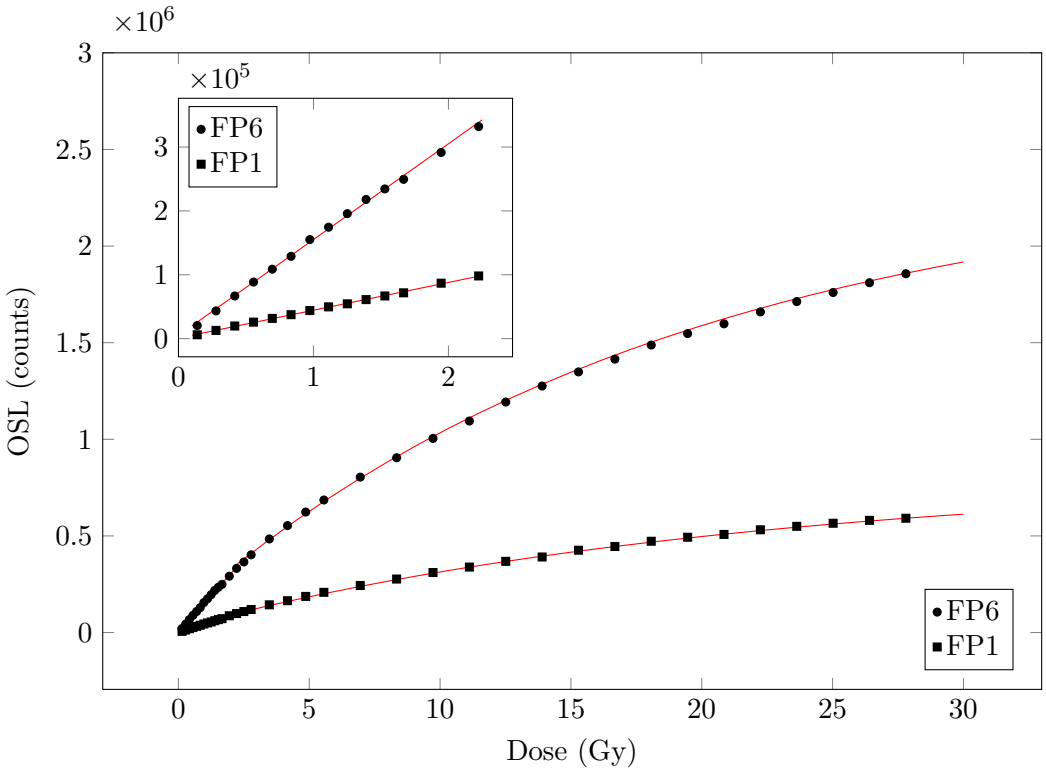

Figure 2.12: OSL signal of fluoride phosphate glass as a function of the applied dosage. Trendlines indicate a linear response from 0 - 2 Gy, and an exponential response from 2 - 30 Gy.

an irradiated sample with a delay time between each measurement. So as to avoid unnecessary depletion of the trapped population - short, low power, pulses of optical stimulation at 470 nm were used. From this, the size of the excited population after a certain amount of time is measured. Measurements were taken at 10, 17, 26, 42, 78, 184, 490 and 1496 s, values for time have been adjusted to account for the duty cycle times of components within the Risø instrument. This experiment was performed at ambient temperature, as well as 40, 50, 60, 70 and 80 ℃. In certain cases the kinetic order can be established by using Equation 2.4, derived in McKeever [92]:

$$(I/I_0)^{(1-b)/b} = 1 + n_0^{b-1}(b-1)s' \exp\left[\frac{-E}{kT}\right]t \tag{2.4}$$

where I is the intensity, I_0 is the initial intensity and b is the kinetic order of the decay.

In the case where a material has an exponential decay, a plot of $ln(I/I_0)$ vs. t will produce a linear relationship; where I is the intensity, I_0 is the initial intensity and t is time. Figure 2.13(a) shows FP1 glass does not produce a linear trend and does not have first order kinetics. For materials with higher order kinetics, a plot of $(I/I_0)^{(1-b)/b}$ vs. t can be used, substituting an appropriate value of b. This can be used to establish the kinetic order of the decay. This was attempted for second order kinetics ($b = 2$), and as indicated by Fig. 2.13(b), the relationship is not linear. The kinetic order was

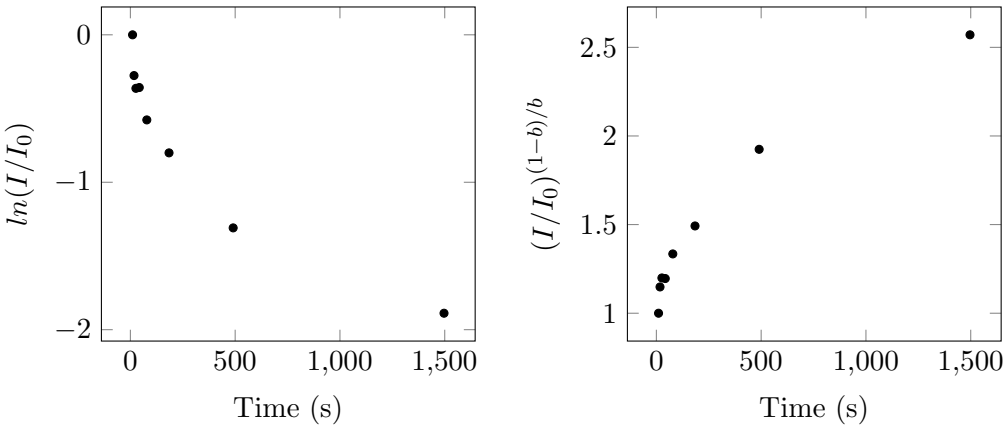

Figure 2.13: (a) $ln(I/I_0)$ vs. t and (b) $(I/I_0)^{(1-b)/b}$ vs. t. Data shown is for measurements taken at ambient temperature on FP1 glass.

not obtained for any value where $b \to \infty$, indicating we cannot assume any simple model such as de-trapping from a broad distribution of traps. It is also possible that a combination of re-trapping, tunnelling and a broad range of energy levels associated with a given defect, due to the amorphous structure of glass, all contribute to the complex behaviour observed.

Stimulation power

The OSL response with respect to the intensity of the optical stimulation was measured in the Risø Reader by varying the power output of the LED array. For the FP1 glass this was performed at 470 nm using a Hoya U340 filter; after 10 seconds of beta stimulation, the OSL response is then integrated over the first 0.2 s of optical stimulation. Measurements were repeated at a variety of optical stimulation powers, and between each measurement samples were glowed out for 300 s at 300 ℃ to ensure no residual trapped charge remained in the sample. The results are shown in Figure 2.14.

From 0.03 to approximately 0.8 mJ the OSL intensity is dependant on the stimulation power, however above approximately 1.6 mJ the intensity is sufficient to immediately stimulate most of the trapped population. A weaker optical stimulation could result in a slower decay rate of the OSL response, where the initial intensity is not high but the untrapping and luminescence occurs over a longer time period. This might not be a problem for an intense OSL response, but for a sample with a weaker intensity signal-to-noise might become a problem. Poor signal-to-noise in a low intensity sample can be partly overcome by detecting the signal over a fewer number of channels, enabling the signal to be integrated over a lower background. For an OSL response, this requires simultaneous untrapping of the majority of the trapped population, which would require an intense optical stimulation source. This result indicates experiments with optical

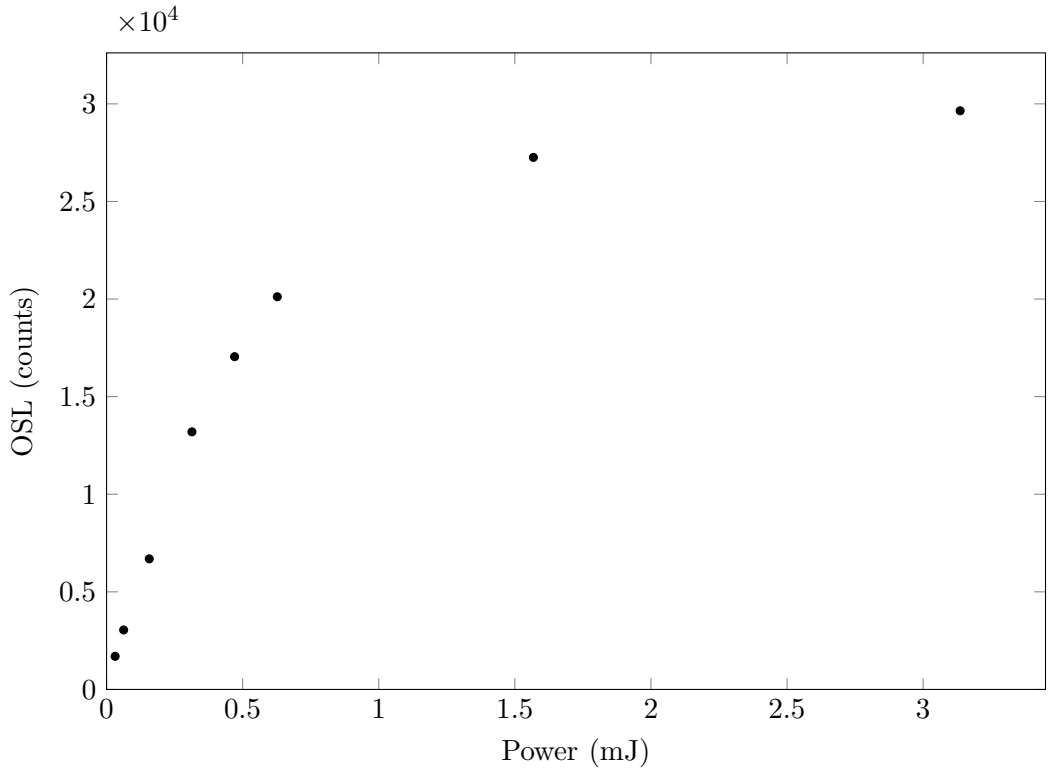

Figure 2.14: OSL with respect to the stimulation power of the diode arrays in the Risø Reader.

fibres will need to have a stimulation light source with sufficient power to immediately untrap the majority of the trapped population, a weak optical stimulation will not be able to take full advantage of the OSL output of the material without poor signal-to-noise affecting the result.

2.7 Simulations of Radiation Penetration and Dose Deposition

The behaviour of ionising radiation of various types and energies when interacting with matter is of fundamental importance to consider for dosimeter and radiation detecting applications. Understanding this behavior will allow the production of a device which best utilises the dose absorption properties of the material. Simulations and calculations were used to investigate how beta particles and photons would behave in various materials, such as how far they penetrate and where within the material energy is deposited. Due to the thin geometry of optical fibres, this becomes important for estimating the effectiveness of energy deposition from different particles over a range of energies.

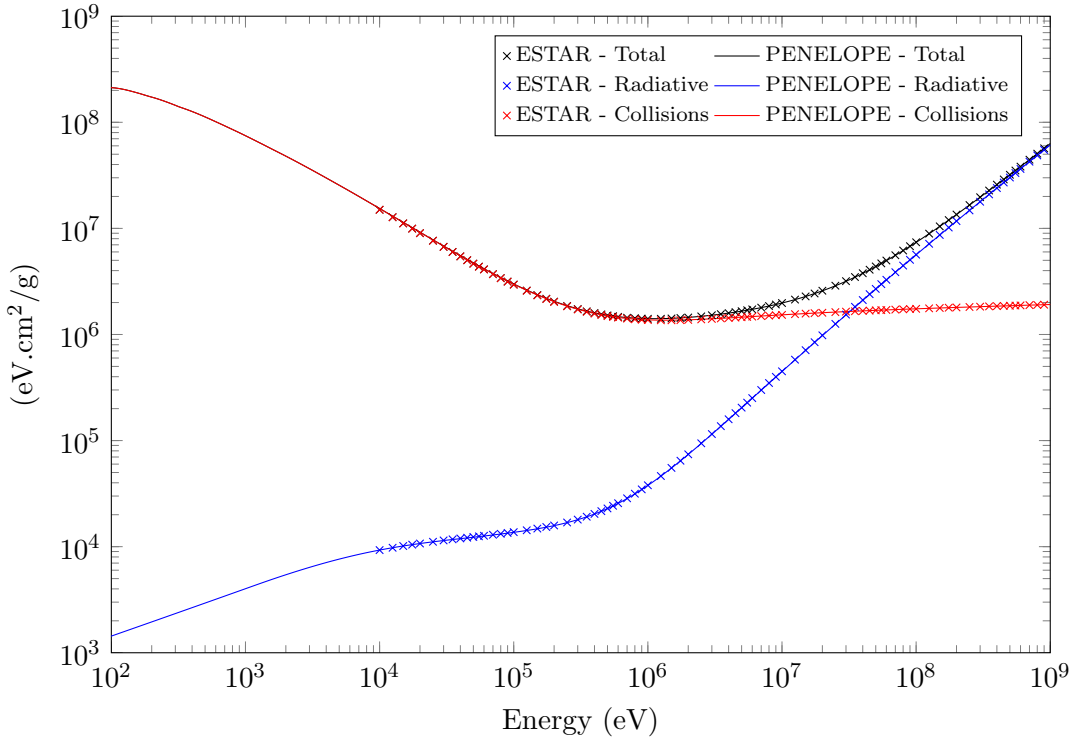

Figure 2.15: Stopping power of fluoride phosphate glass over a range of particle energies.

2.7.1 Stopping Power

The stopping power, a value describing the attenuation of the energy of a particle in a material due to physical interactions [2], was calculated for FP glass using the materials functionality of PENELOPE, and also compared with results calculated by the ESTAR tool provided by NIST. The calculated stopping powers are shown in Figure 2.15.

A more detailed suite of data is provided in Appendix A.5 showing the radiation interaction values for FP glass. Values such as the mean free path and attenuation coefficients for each energy loss mechanism are provided for both photons and electrons across a range of energies.

2.7.2 Energy Transfer

To estimate the transfer of energy per unit length of material, simulations were performed with PENELOPE considering FP glass plates of varying thickness. This measurement is similar to a linear energy transfer measurement, which describes the energy lost by a particle per unit length of the material [2,99]. Values of between 100 - 1000 µm were used, as these are the diameters of the glass fibres and 'canes' which are studied in Chapter 5. Electrons were simulated with primary energies of 2.28 MeV to match the energy of emission from ^{90}Sr/^{90}Y beta sources; photons were simulated with energies of 100 keV as an example of the energy range studied using the X-ray source. The energy

deposited in the glass material at different thicknesses is shown in Figure 2.16.

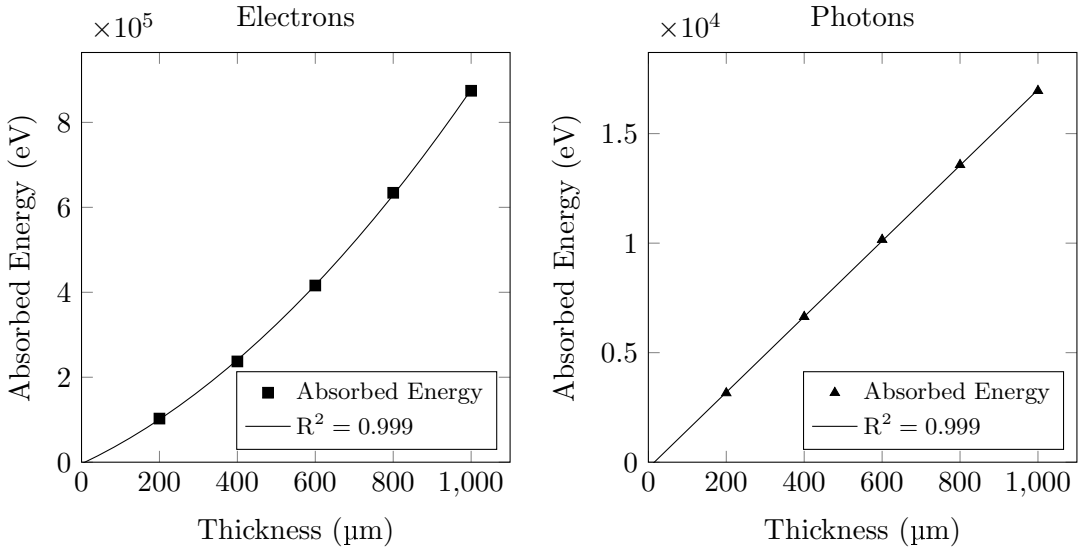

Figure 2.16: Simulated energy absorbed from a 2.28 MeV electron beam (left) and a 100 keV photon beam (right) by layers of FP glass with varying thickness.

For electrons, the energy deposition per unit length follows a polynomial trend between 0 and 1000 µm glass thicknesses, which is expected due to the dose pile-up caused by generation of secondary electrons [99], as discussed in Section 1.4. If this is approximated to a linear trend, the energy deposition over the 0 – 1000 µm range is approximately eV/µm. For photons, energy deposition from 100 keV photons is 17.3 eV/µm.

The data for the average energy of transmitted particles was also studied, simulations here show the data in the 0 - 1000 µm region, to match the width of fibres and canes used in later experiments, results are shown in Figure 2.17. For the sake of interest, simulations were also performed using greater glass thicknesses and the results are shown in Appendix D.2. For electrons, which lose energy over a series of interaction processes, this value was seen to decline quickly with increasing glass thickness, at 760 eV/µm. Photons, in contrast, tend to lose their energy as a result of individual interactions; so as expected, the energy of transmitted particles is very close to that of the original particle energy, 100 keV, and remains so for thicker layers of glass. For thicker glasses, as is seen in D.2, an abrupt decrease in transmitted particle energy is observed in glasses with thicknesses greater than 40 mm.

Energy transfer simulations indicate that over the dimensions of an optical fibre (160 – 300 µm), beta particles can be expected to interact strongly and deposit a higher fraction of their energy within the glass. X-ray photons, in comparison, deposit very little energy in these small volumes of material, indicating a high dose rate may be required to deposit sufficient energy into the material for a detectable OSL response. These

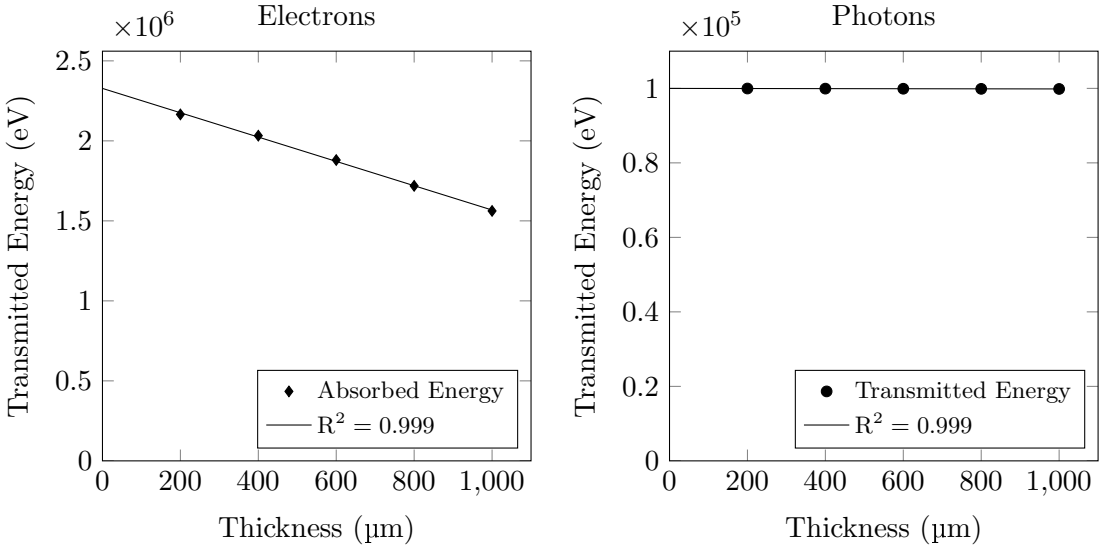

Figure 2.17: Simulated energy of transmitted primary particles from a 2.28 MeV electron beam (left) and a 100 keV photon beam (right) by layers of FP glass with varying thickness. Simulation was performed using PENELOPE.

results would be dependant on the particle energy and on the material surrounding the glass.

2.7.3 Range of Electrons

The range of electrons, R_e^{SP}, was calculated as per the method originally discussed by Katz [100]. This value simply indicates the maximum distance an electron with energy, E, may penetrate into the material[10] [4, 100]. This is therefore the minimum thickness required to completely attenuate electrons of this energy. This value relates to primary particles, and not to secondaries such as bremsstrahlung photons or secondary electrons. Equation (2.5) indicates the method used for each electron energy regime.

$$R_e^{SP}(kg/m^2) = \begin{cases} 4.12E^{1.265-0.0954ln(E)} & \text{when 10 keV} < E \leq 2.5 \text{ MeV} \\ 5.30E - 1.06 & \text{when } E > 2.5 \text{ MeV} \end{cases} \quad (2.5)$$

Using the case of 2.28 MeV beta particles, the appropriate equation gives a result of 10.95 kg/m^2, or 1.09 g/cm^2. We divide this by the density of FP glass, 3.68 g/cm^3, and come to a result of 2.98 mm. This is the maximum distance through FP glass that a 2.28 MeV electron may travel. For a thin sample of FP glass this means primary beta particles might travel through the material, this is addressed in the following Section 2.7.4. For radiation safety purposes, we can calculate the same value for lead shielding; using the density of lead, 11.34 g/cm^3, gives us a result of 0.96 mm. This is

[10]Note this value is not the distance of peak dose deposition, but rather the minimum thickness of material required to completely attenuate a beam of electron energy = E.

an unimportant result as in practice, each experiment involves the beta source incident directly upon the glass and a thick plate of aluminium, hence radiation shielding is more focused on attenuating the bremsstrahlung X-rays this produces, rather than the primary beta particles.

2.7.4 Dose Deposition Profiles

The dose deposition profiles for fluoride phosphate glass were simulated for both photons and beta particles using PENELOPE. The simulation uses a parallel, monoenergetic beam of particles at a variety of energies from 0.01 – 10 MeV incident on a plane slab of fluoride phosphate glass. The thickness of the glass is adjusted for each different primary particle energy to ensure all the energy from that particle is deposited within the glass slab. The dose deposition profiles are seen for beta particles in Figure 2.18, and for photons in Figure 2.19. Simulations were also run using an isotropically emitting radiation source, instead of a parallel source, the results are provided in Appendix D

The energy deposition observed for beta particles show the expected profiles, where the majority of the particle energy is deposited several microns into the material, after which the energy deposition rapidly drops off. The reason for this comes from the interaction of beta particles with matter, where many secondary electrons are produced, each of which will have further interactions with the material producing tertiary particles, and so on. This causes a pile-up of energy dissipating from the primary particle into many daughter particles which travel a short distance before losing their energy to the material. This is what causes an increasing energy deposition a short distance into the material, and the reason why the majority of the energy is not deposited in the surface layer.

The energy loss mechanisms for photons are slightly different, energy from the primary particle is generally deposited in one interaction and the energy deposition profile is therefore exponential.

To produce an efficient dosimeter, especially for low-dose applications, the material needs to absorb as much energy from each particle as possible. This may be achieved in principle by changing the material to one of higher density, or simply using a greater volume, but with an optical fibre device neither of these options is suitable. It is therefore important to understand the location and magnitude of dose deposition within the material, so optical fibres can be fabricated with geometries most suitable for maximum dose deposition. Consider beta particles: above an energy of 500 keV the maximum dose deposition is generally at a distance wider than the diameter of an optical fibre

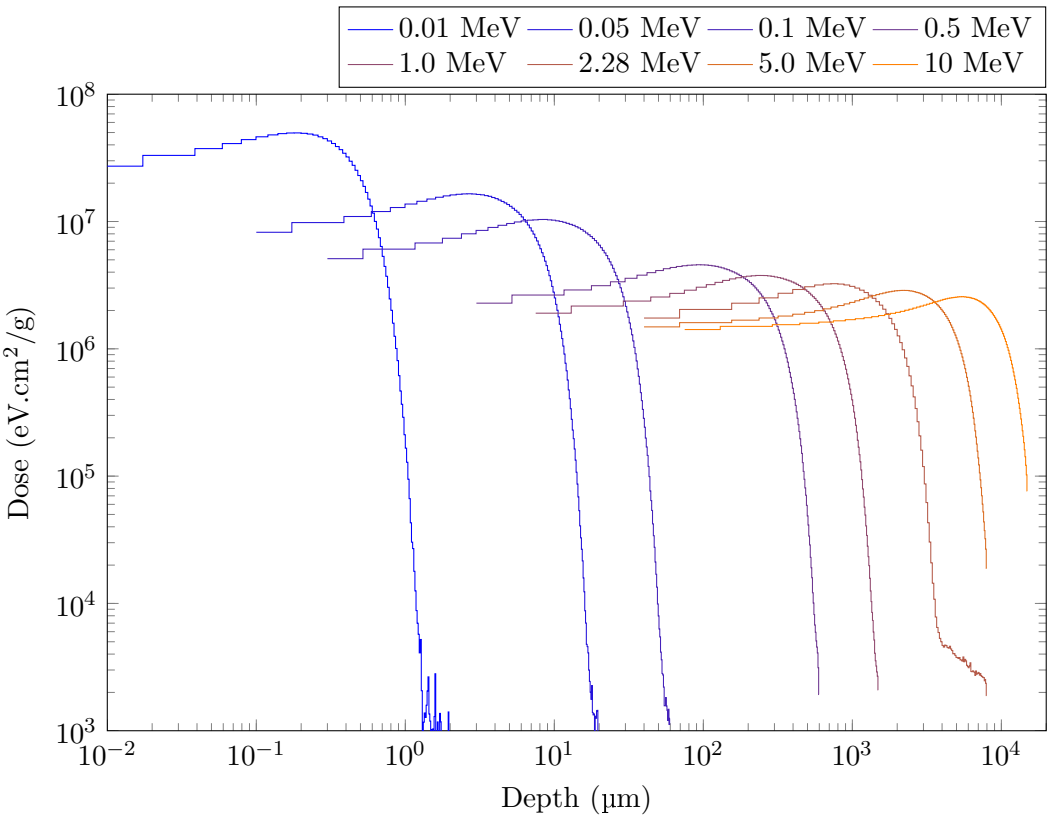

Figure 2.18: Dose deposition profile of a parallel electron beam into fluoride phosphate glass.

(160 µm). Fibres would therefore ideally be fabricated with the largest possible diameter. However for lower energy particles, the maximum dose deposition will occur at a value less than the thickness of an average optical fibre. The fibre would therefore need to be fabricated with a calculated diameter which would result in the maximum dose deposition occurring at the centre of the fibre, this would depend on the particle type and energy that the fibre is designed to detect.

2.8 Summary

Fluoride phosphate glass was identified as a suitable material due to its OSL production in response to dose. The optical and luminescence properties of the glass were studied and characterised, as well as certain information pertaining to radiation transport within the material. For the remainder of this thesis, the majority of the work presented will be performed with sample FP1, the commercially-acquired glass from Schott, due to its availability in large bulk quantities and the identified favourable characteristics. While FP1 has a slightly higher loss than other samples, such as samples FP3, FP4 and FP6, and a slightly lower OSL intensity, use of this commercially acquired glass removes the need to fabricate many small batches of new glass compositions. This removes any individual batch-to-batch variation of the glass and enables a consistent approach to doping experiments and optical fibre fabrication; in addition, it allowed

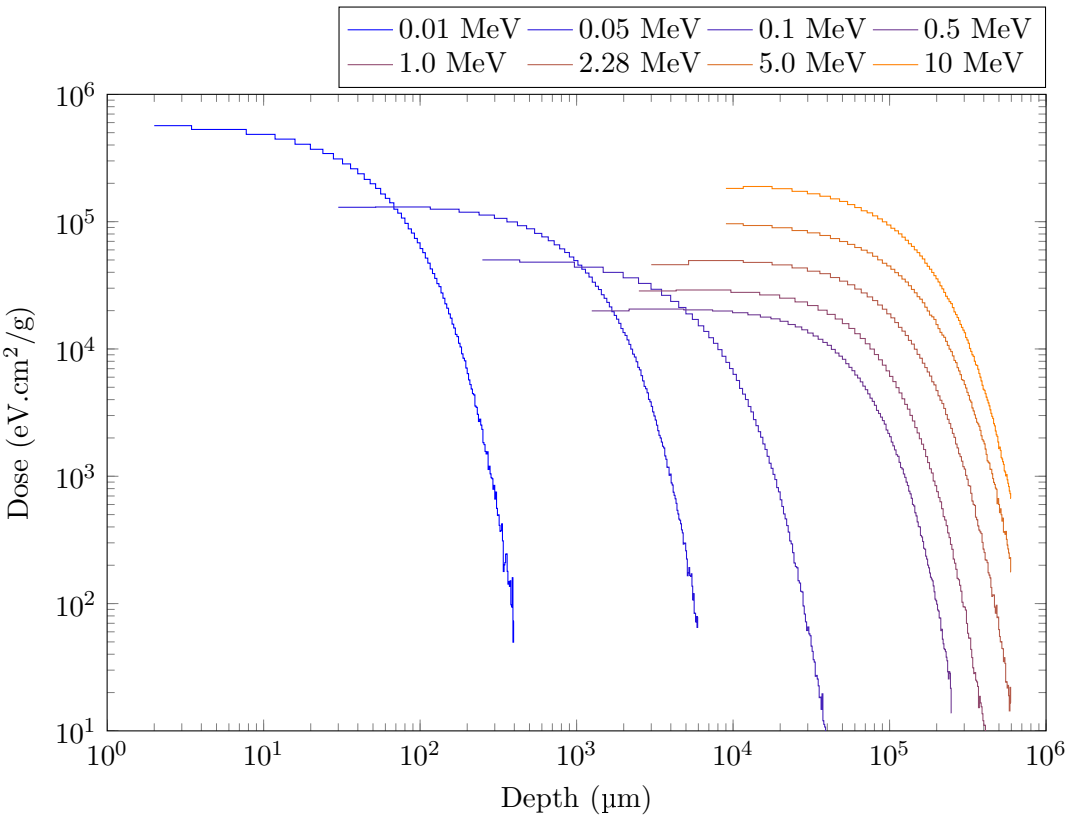

Figure 2.19: Dose deposition profile of a parallel photon beam into fluoride phosphate glass.

work to rapidly progress to fibre fabrication.

Chapter 3

Fabrication and Characterisation of Doped Fluoride Phosphate glass

As discussed in previous chapters, the recombination of electron-hole pairs during OSL production is affected by impurities in the glass. These impurities determine the emission wavelengths of the optically stimulated luminescence and can affect the structure of electron traps within the material. It is therefore possible to utilise some impurity ions present in the glass. However, more reliable and controllable results are achieved with active doping of the glass. This chapter presents the work done to produce a suitably doped FP glass for fabrication into a dosimetry fibre.

3.1 Choice of Dopant Ions

Several dopant ions were considered at different periods of time in the project. As was seen in Chapter 2 and will be presented later in Chapter 5, many experiments were performed using a bialkali photomultiplier tube, and as the peak quantum efficiency of such photomultiplier tubes is around the 400 nm region, it was therefore necessary to work with a material which emits luminescence in this wavelength region. One potential dopant is Cu^{+}, which has a broad emission peak centered at 450 nm, hence several glass samples doped with copper were fabricated and analysed.

Radiation detection measurements were also performed using a single photon avalanche diode (SPAD), the peak quantum efficiency of this detector is around the 550 nm region. Several possible dopant ions suitable for this waveband were therefore considered, including both Mn^{2+} and Tb^{3+}, which in FP glass are known to emit at wavelengths close to the peak efficiency of a SPAD. Mn^{2+} is known to emit a broad peak in the 550 - 650 nm region [101], and Tb^{3+} is known to emit with several peaks between 400 – 650 nm, with an intense peak at 550 nm [102, 103]. The compounds procured for doping were: copper (II) fluoride hydrate (99.999%), manganese (II) oxide (99.99%) and terbium (III-IV) oxide (99.99%).

It should also be noted that Ce^{3+} could be of use as a dopant ion if emission in the 350 – 450 nm region is required: strong emission in this region has been previously demonstrated for FP glasses doped with Ce^{3+} [104]. Doping of FP glass with Ce^{3+} was briefly attempted for this project, however due to the inability to homogenise the dopant ions into the glass it was abandoned in favour of work focusing on Tb^{3+} and Mn^{2+}. For work using a SPAD detector, emission in the 400 nm region is not optimal, hence dopants with an emission closer to the 500 – 600 nm region were preferred. In the future, however, if the 400 nm region becomes relevant for luminescence work, Ce^{3+} should be kept in mind as a potential candidate for doping FP glasses.

3.2 Fabrication of Doped Fluoride Phosphate Glasses

Depending on the dopant ion and the result desired, glass melting and doping was performed in either ambient or reducing atmospheres. This was primarily performed to control the oxidation state of the dopant ion. For example, when doping FP glass using CuO, ions may form in the +1 or +2 state, depending on the redox conditions of the glass melt; similarly manganese may exist in the +2 or +3 state. In general, reducing melting conditions were desired both for the resulting redox state of the dopant ions and the effect on the oxygen content in the glass; as such, many experiments were

performed under a reducing environment.

3.2.1 Oxidising Atmosphere

Samples of FP1 glass procured from Schott Glass Co. were cut up and placed in a platinum crucible, the dopant compound was added and the crucible placed inside the furnace. Samples were melted at 950, 1000 and 1050 ℃ for 1 to 3 hours. After dwelling in the furnace at temperature, samples were removed and swirled for approximately 20 s and then cast into a pre-heated graphite mould. Following the cast, samples were allowed to cool, before being placed into a separate furnace to anneal, where the temperature is increased to 450 ℃ and then cooled at a controlled rate of 0.1 ℃/s. The sample was then removed from the mould and post-annealed at 450 ℃ to remove any residual stress in the glass. The doped glass was then both cut into slides and polished for spectroscopy, and also crushed into 250 - 400 µm grains for analysis in the Risø Reader. Initial melting trials were performed at 950 ℃, but the glass was found to be too viscous for efficient casting, and a lot of glass remained in the crucible, therefore the temperature of remelts was raised to 1000 - 1050 ℃ for later experiments. Following each melting trial, the platinum crucible is cleaned of residual glass by etching in 32% HCl and polishing with sand.

3.2.2 Reducing Atmosphere

Samples of FP1 glass were cut and placed in a vitreous carbon crucible, which could be used due to the lack of oxygen in the controlled atmosphere of the glovebox. The carbon crucible is cleaned prior to use by submersing in methanol, which is then placed in an ultrasonic bath for 15 minutes to remove any loose carbon from the surface. The dopant compound was added and the crucible placed into a controlled atmosphere furnace, attached to the glovebox. Nitrogen was used to control the atmosphere and remove both oxygen and water. Samples were heated to 900 ℃ and allowed to dwell for 1-3 hours. After sufficient dwell time, the glass was removed and swirled for approximately 20 s, then allowed to cool slightly before being placed into a separate pre-heated furnace at 450 ℃ to anneal. Glass does not stick to vitreous carbon and cooled glass can easily be removed from the crucible, hence casting into a mould is not a necessary step as it is when using a platinum crucible; several samples therefore were not cast but allowed to cool in the crucible. To produce a doped glass with a certain geometry, such as for spectroscopy or for fibre fabrication, the melt was cast into a pre-heated polished brass mould with the appropriate dimensions. All casts were done inside the glovebox in a reducing atmosphere. Cooled samples were removed and post annealed at 450 ℃ in an ambient atmosphere to remove any residual stress in the glass. Finally, the glass was

then cut into slides and polished for spectroscopy, and also crushed into 250 - 400 µm grains for analysis in the Risø Reader.

Pictures showing the furnaces, glovebox, crucibles and moulds used for both oxidising and reducing atmosphere melts can be seen in Appendix B.2.

3.2.3 Sample Summary

A number of glass samples were produced for each dopant ion, using both ambient and reducing environments. Representative samples for each dopant under both oxidising and reducing conditions were chosen to demonstrate the results acquired, a summary is provided in Table 3.1.

Table 3.1: Representative selection of doped fluoride phosphate glass samples. Atmosphere refers to the conditions in which the glass was melted: the label 'ox' corresponds to an ambient atmosphere containing oxygen; the 'red' label corresponds to a controlled glovebox atmosphere purged with nitrogen, creating reducing conditions.

Sample Name	**Dopant**	**Atmosphere**	**Concentration (ppm wt)**
FP1-ox	undoped	oxidising	N/A
FP1-red	undoped	reducing	N/A
Cu-ox-60	copper	oxidising	60
Cu-red-60	copper	reducing	60
Cu-red-500	copper	reducing	500
Mn-ox	manganese	oxidising	2749
Mn-red	manganese	reducing	2749
Tb-ox	terbium	oxidising	7200
Tb-red	terbium	reducing	7200

3.3 Spectroscopy

Emission spectra were obtained using the Princeton Instruments Spectroflurometer as described in Section 2.4.2. Spectra were taken from bulk samples of doped glass. Excitation was provided by a mercury lamp with the excitation wavelength isolated using a diffraction grating monochrometor. FP glass doped with Tb^{3+} is optimally excited at 355 nm, it was therefore possible to also obtain emission spectra for Tb^{3+}-doped samples using stimulation from a frequency-tripled YAG laser. Absorption spectra were obtained using the Agilent Cary 5000 UV-Vis-NIR spectrophotometer under the same experimental conditions as described in Section 2.4.

3.3.1 Copper

The emission spectra of fluoride phosphate glasses melted under ambient and reducing atmospheres are shown in Figure 3.1. In the sample melted under reducing conditions the expected peak at 450 nm is observed, due to the presence of Cu^{+}. Samples melted under ambient conditions show no observable emission peaks, indicating the majority of the ions exist as Cu^{2+}.

The absorption spectra are shown in Figure 3.2. For Cu^{2+}. Literature indicates absorption peaks at 240 and 800 nm [86], these peaks are observed from the sample melted in an ambient atmosphere. The 240 nm peak is also observed for the sample melted under reducing conditions, indicating a proportion of ions remaining in the Cu^{2+} state. The reduced sample shows the indication of a peak at 180 nm, indicating the presence of Cu^{+} ions [86]. The decrease in intensity of the 240 and 800 nm absorption peaks and the increase of the 180 nm peak, indicates the reduction of Cu^{2+} to Cu^{+}.

3.3.2 Manganese

The emission and absorption spectra of manganese doped fluoride phosphate glass can be seen in Figures 3.3 and 3.4, respectively. The emission and absorption peaks are in accord with the literature for Mn^{2+}-doped FP glass [101, 105]. The higher emission intensity from Mn-red suggests a higher proportion of ions in the +2 state using the reducing fabrication conditions, under oxidising conditions a higher proportion of ions exist in the +3 state. The absorption observed in the 200 - 300 nm region for samples fabricated in oxidising conditions suggests absoprption is due to ions when they are in a higher oxidation state. This could also be due to impurities in the glass, such as $Fe^{2+/3+}$, and not just the manganese ions.

3.3.3 Terbium

The emission and absorption spectra agree with the literature [102, 103, 106], and can be seen in Figures 3.5 and 3.6, respectively. The Tb^{3+} $4f^{8} \rightarrow 4^{7}5d$ transition at 215 nm, shown also in previous literature [102, 106, 107], shifts the UV absorption edge of the glass to a slightly longer wavelength and no transmission is seen at wavelengths below 230 nm. The absorption peaks observed between 300 and 400 nm are also described previously in the literature for Tb^{3+} doped fluoride phosphate glass [106]. Terbium in fluoride phosphate glass exists as Tb^{3+} for glasses remelted under both ambient and reducing atmospheres. Radiation exposure can cause the formation of Tb^{4+}, which has been previously shown to absorb at 415 nm [106], however, no such peaks were observed here.

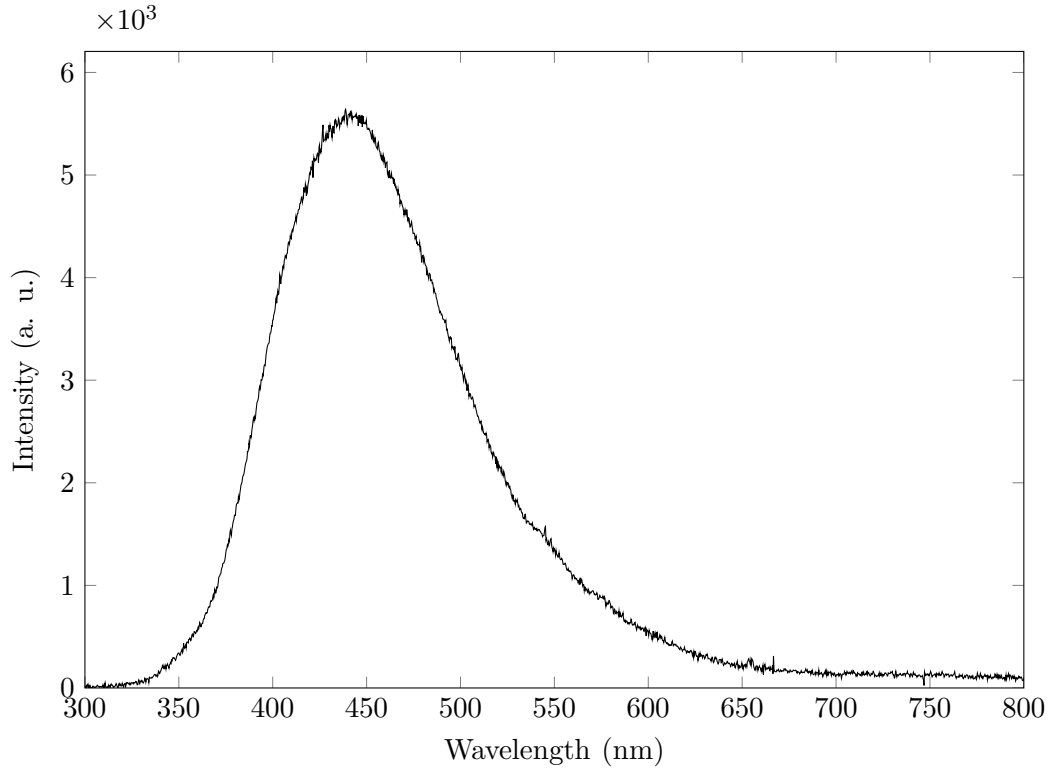

Figure 3.1: Emission spectra of sample Cu-red-60 under a reducing environment, copper concentration is 60 ppmwt.

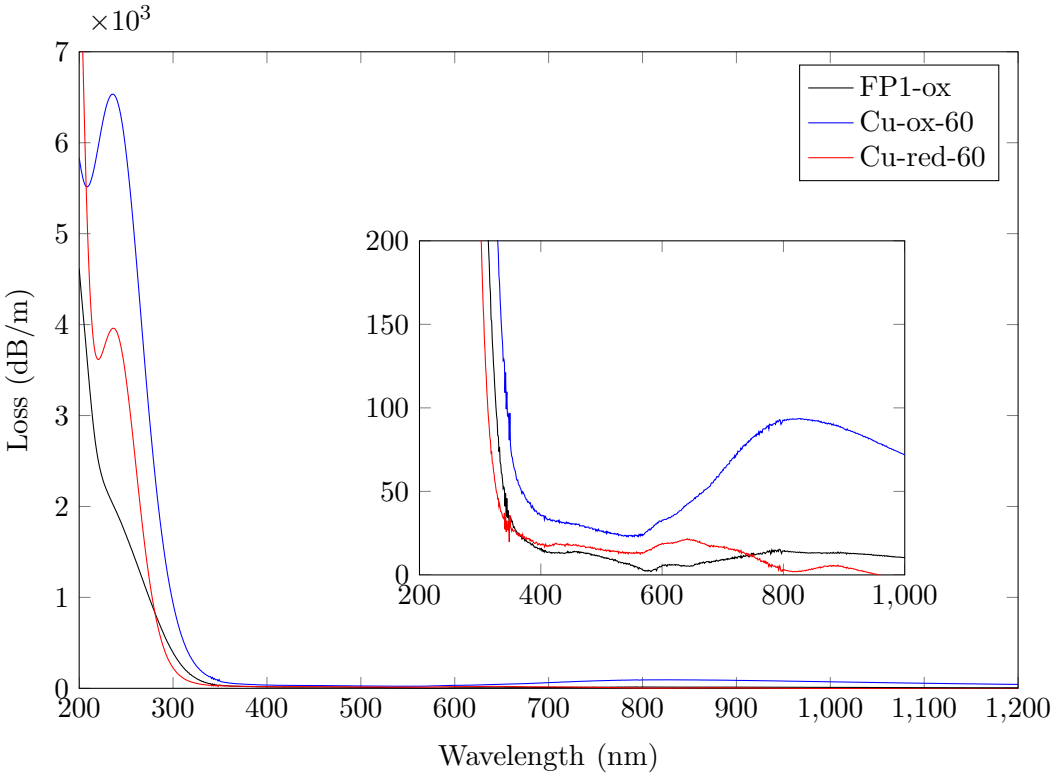

Figure 3.2: Absorption spectra of FP1 glass doped with copper ions and melted under ambient and reducing atmospheres.

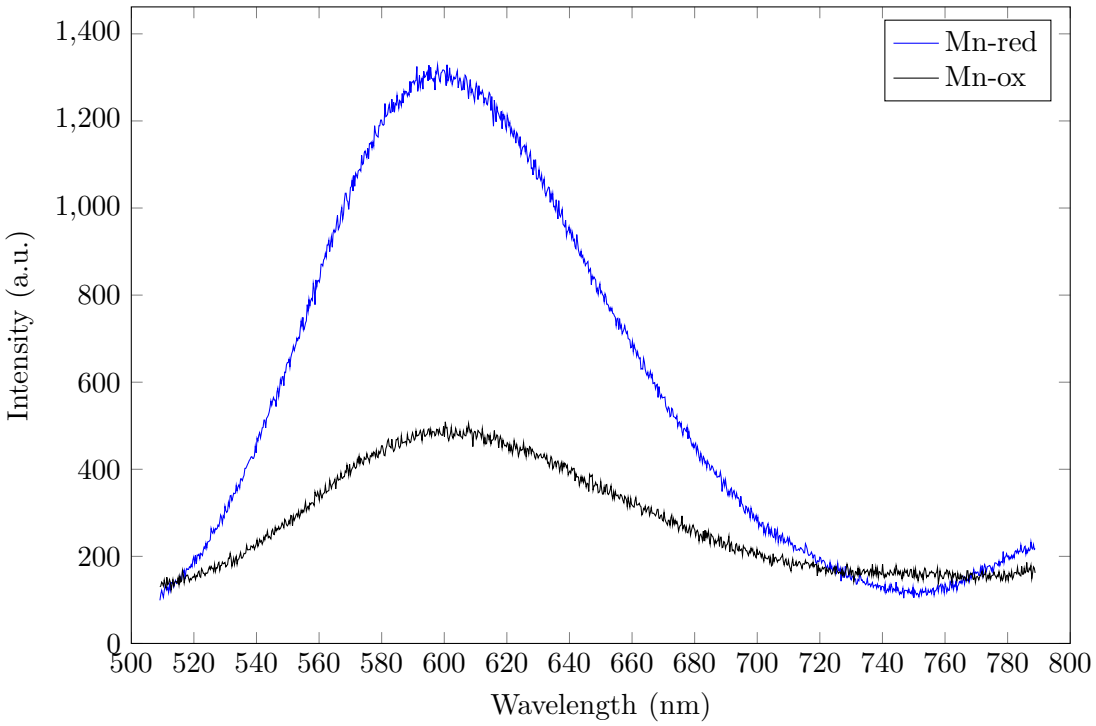

Figure 3.3: Emission spectra of FP1 glass doped with manganese.

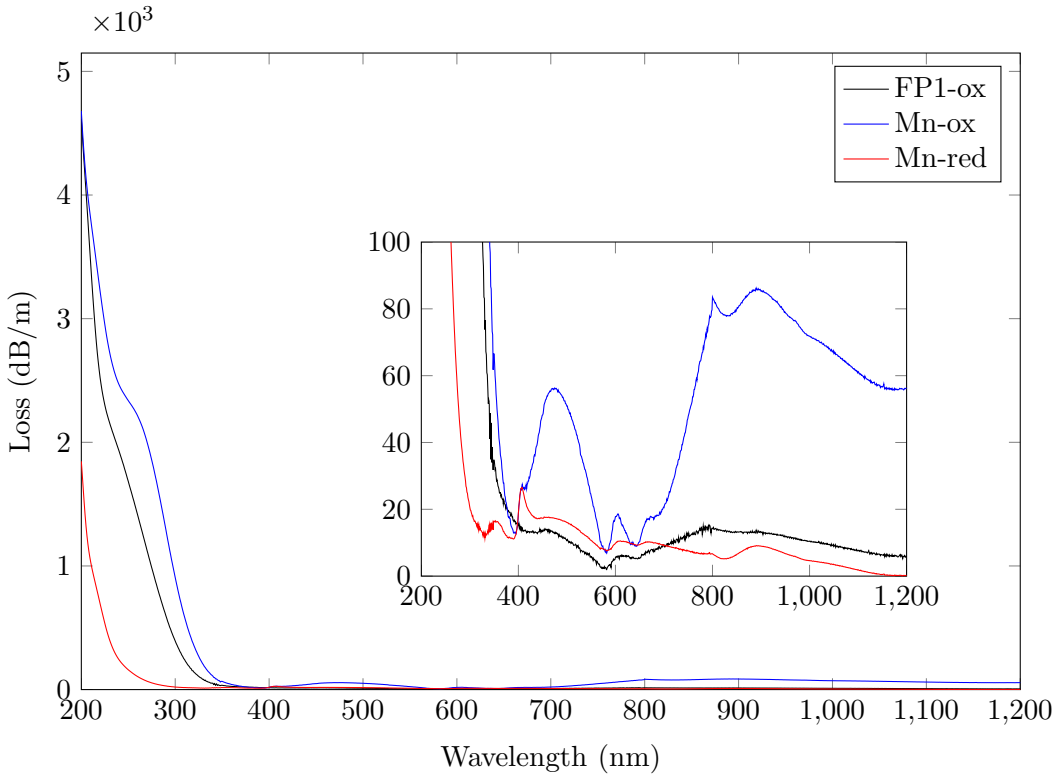

Figure 3.4: Absorption spectra of FP1 glass doped with manganese and melted under ambient and reducing atmospheres.

The expected emission peaks for Tb^{3+} are observed and fall within a suitable wavelength range for use with a SPAD optically filtered by a 3 mm thick Schott BG39 filter. Emission peaks have been attributed to transitions based on a previous study of Tb^{3+} ions in fluoride phosphate glass [103].

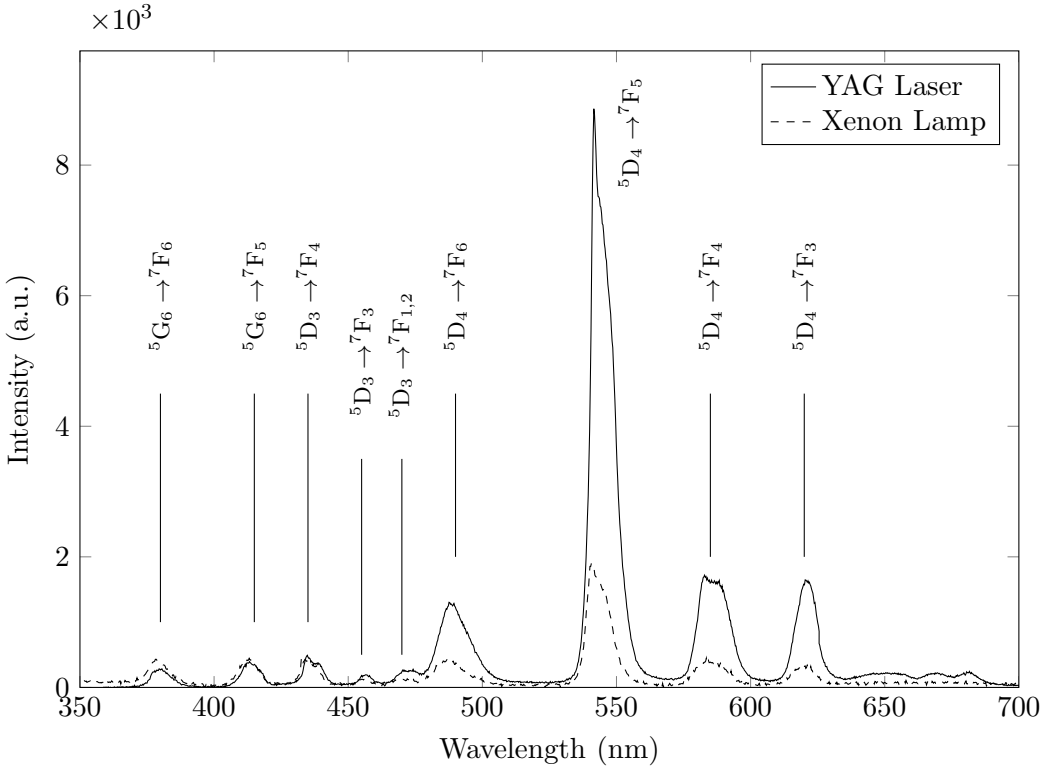

Figure 3.5: Emission spectra of sample Tb-red. Excitation at 355 nm with a mercury lamp and a frequency tripled YAG laser..

3.3.4 Radioluminescence Spectra

Emission spectra indicate the wavelengths at which OSL might occur, but due to the difference in stimulation mechanism, the OSL spectra and emission spectra should not be assumed to be identical. During fluorescence measurements, electrons are only excited to higher energy levels and emit during return to the ground state. However with OSL, electrons may be removed completely from the atom and trapped at delocalised defects, from where they are free to move through the conduction band. Due to the low number of photons emitted during OSL, measuring a spectrum of OSL emission is not experimentally feasible with the apparatus available, due to poor signal-to-noise. RL, however, is a closer analog to OSL emission than fluorescence emission. Unlike OSL, RL measurements can be integrated over the time period required to achieve good signal-to-noise.

RL emission measurements were performed on the Princeton Instruments Spectrofluorometer, used previously for fluorescence emission measurements as follows. An un-

mounted, sealed, $^{90}Sr/^{90}Y$-beta source was inserted into the sample chamber through an access port and held in place with a custom made mount. The face of the source was positioned up against one face of the glass, and RL focused and collected into the optical fibre from the opposite face. A diagram is shown in Figure 3.7. Interference was observed in the detector chip during initial measurements and was attributed to bremsstrahlung emanating from the irradiation of glass samples and the surrounding sample chamber. The sample chamber was therefore separated some distance from rest of the instrument, possible due to the optical fibre signal cable, and surrounded by lead sheeting. Subsequent measurements showed only background noise, indicating sufficient shielding of the equipment.

The RL spectra obtained from samples of glass, both undoped and doped with Cu^{+}, Tb^{3+}, Mn^{2+}, are similar to the emission spectra for each sample as is shown in Figure 3.8. The OSL emission is therefore reasonably assumed to be similar to the emission spectra of these other phenomena.

3.4 Optically and Thermally Stimulated Luminescence Measurements

TL emission spectroscopy and OSL measurements were performed on the doped glass samples. Most luminescence tests were performed using the Risø OSL/TL DA-20 Reader, in which case samples were crushed and mounted onto discs as per the method described in Section 2.6.

TL measurements were made using a heating rate of 1 K/s, and were performed between room temperature to 300 ℃, background measurements were performed for each sample in order to subtract the incandescence from the heating plate observed at higher temperatures.

TL emission spectroscopy was performed using the 3DTL emission spectrometer, the method used for experiments is as described in Section 2.6.1. Due to slight differences in thermal contact and heating efficiency, the TL peaks from TL emission spectroscopy are observed at slightly higher temperatures.

OSL measurements were also performed as described previously in Section 2.6.2. Optical stimulation wavelengths and filter combinations were also identical, using the 470 nm LED stimulation with a HOYA U340 filter, and 870 nm LED stimulation with a Schott BG39 filter, all optical stimulations occur for 5 s. The OSL intensity is normalised for mass in order to account for any small variation in mass between samples and is therefore reported as counts/g/Gy. For ease of comparison between samples,

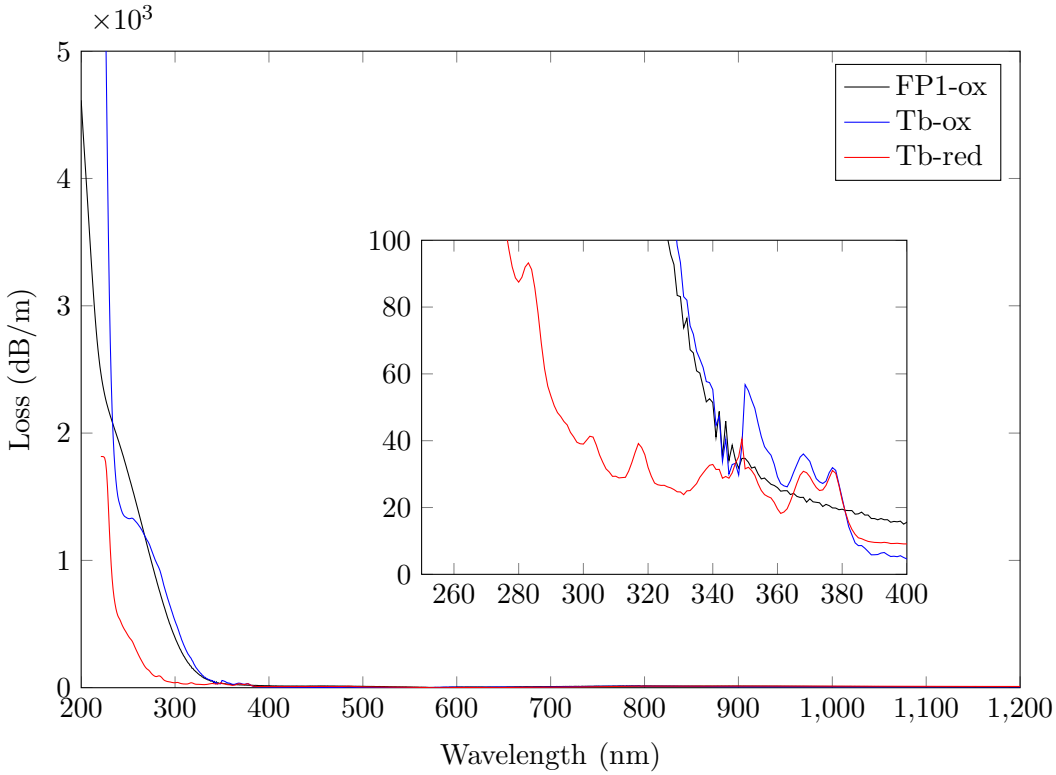

Figure 3.6: Absorption spectra of FP1 glass doped with Tb^{3+} and melted under ambient and reducing atmospheres.

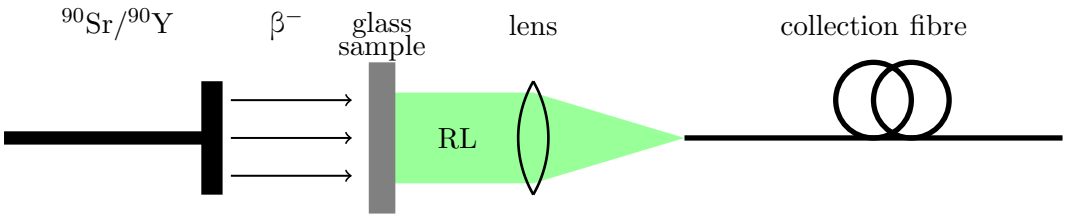

Figure 3.7: Experimental setup for measuring the spectra of RL from bulk glass samples.

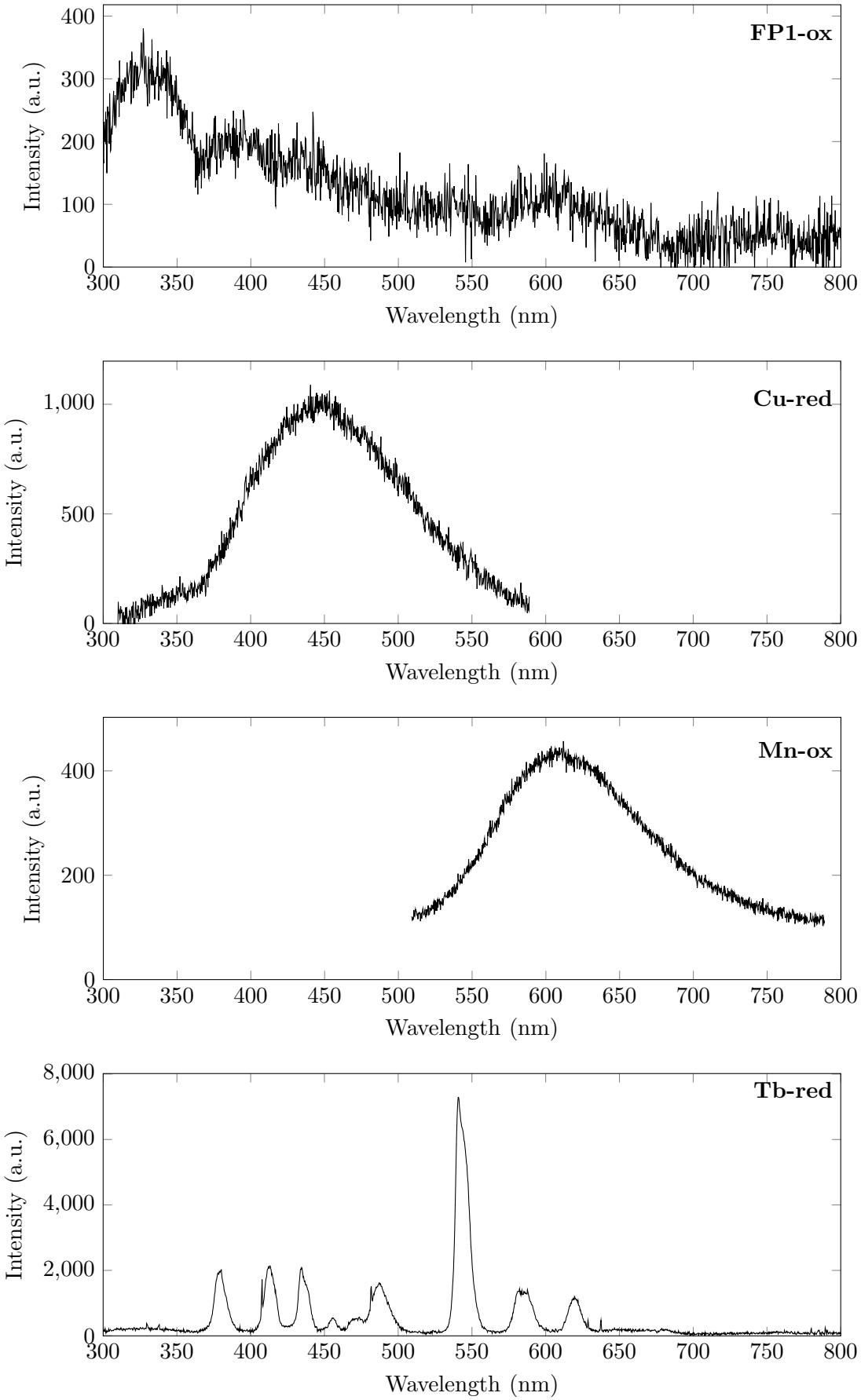

Figure 3.8: RL spectra of Schott N-FK51A fluoride phosphate glass. Excitation with a 320 MBq $^{90}Sr/^{90}Y$ beta source, described in Section 5.1.

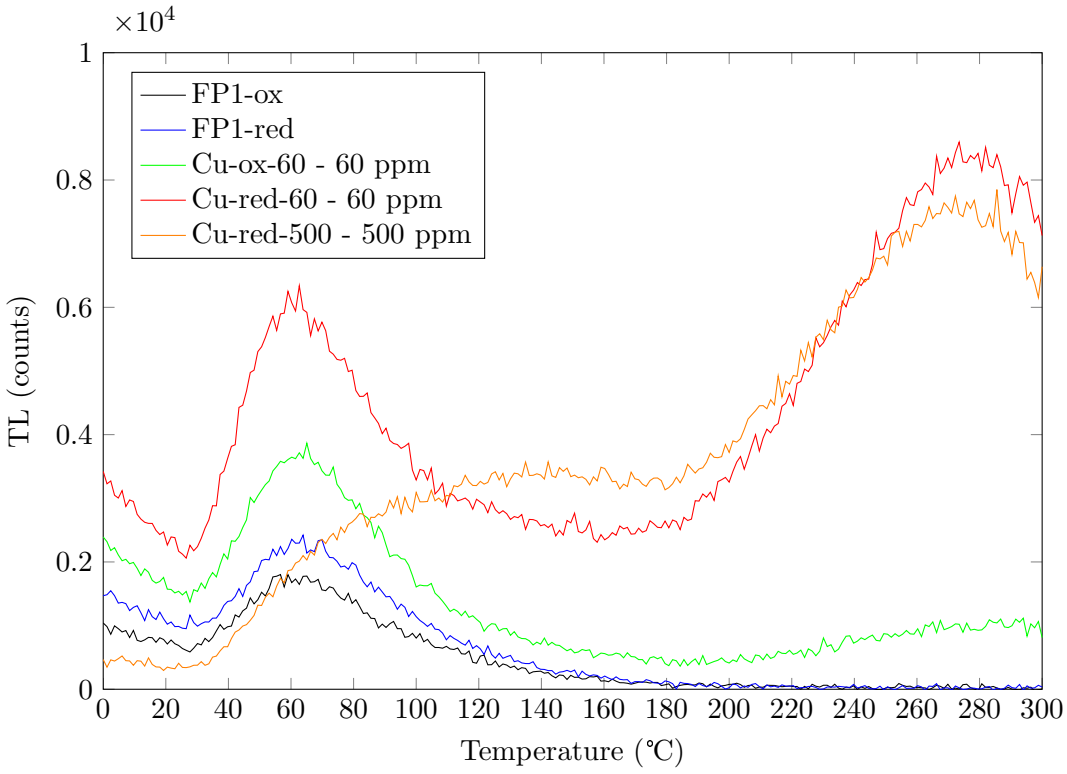

Figure 3.9: TL spectra of fluoride phosphate glasses doped with copper under ambient and reducing atmospheres.

data are presented on logarithmic plots.

3.4.1 Copper

Thermoluminescence TL was performed on the samples using the Risø Reader with a heating rate of 1 K/s and a HOYA U340 filter to isolate copper emission. Results show that in addition to the 60 ℃ peak seen in the undoped glass, an additional broad peak appears at 280 ℃, seen in Figure 3.9. This peak is present in samples melted under both ambient and reducing environments, however the intensity of this peak is much higher for the reduced samples, as can be seen by comparing the two 60 ppm samples in Figure 3.9. This indicates that the 280 ℃ glow peak is most likely due to Cu^{+} ions, rather than Cu^{2+} ions.

At higher dopant concentrations, the 60 ℃ peak is observed to shift to 140 ℃, as can be seen for the sample doped with 500 ppm Cu^{+} in Figure 3.9. At these higher concentrations, the structure allowing shallow traps at 60 ℃ is no longer possible, new traps with different energies might be forming.

Thermoluminescence Emission Spectroscopy Previously in Section 2.6.1 undoped samples of FP glass were analysed by TL emission spectrocopy, but no observable signal was measured. In comparison, Cu^{+}-doped samples show an intense response

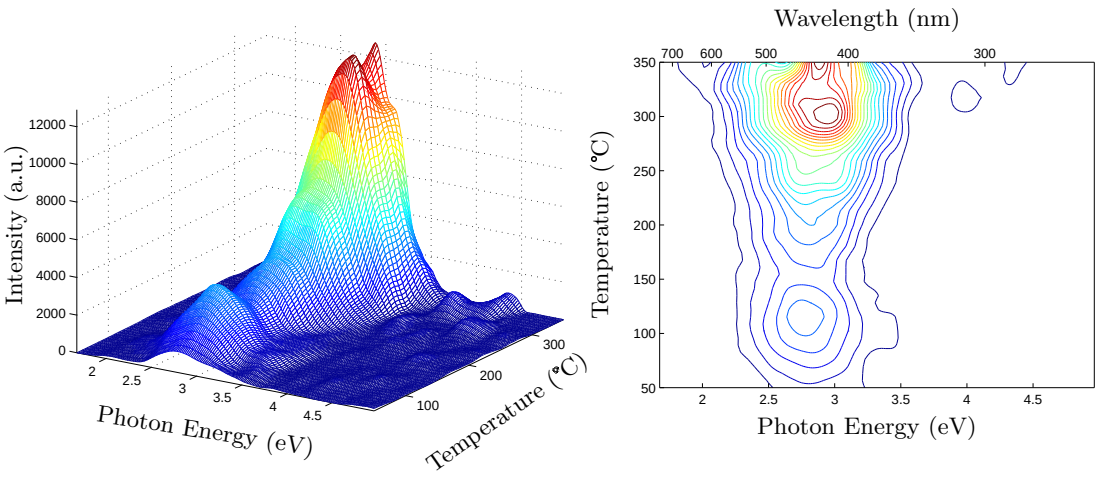

Figure 3.10: Thermoluminescence emission spectrum of sample Cu-red, 3D and intensity contour plots.

and TL emission peaks at 120 ℃ and 300 ℃ are visible, shown in Figure 3.10. Due to the heating rate of 5 K/s used here, peaks appear at a slightly higher temperature than the TL results observed when using a 1 K/s heating rate in the Risø Reader. The emission occurs at 450 nm which is expected from the fluorescence measurements shown previously.

Optically Stimulated Luminescence The addition of copper ions to the FP1 glass appears to increase the OSL response, especially in the 350 – 600 nm wavelength region, shown in Figure 3.11. The increase is attributed to the emission from Cu^{+} ions, which have a broad peak centered at 400 nm. This is consistent with a reducing atmosphere producing a higher proportion of copper in the +1 state, and samples remelted in the reducing environment are observed to have the highest OSL response. Ions in the +1 state may possibly also act as hole traps, hence a greater proportion of Cu^{+} would enable a higher number of trapped holes.

For samples fabricated under reducing conditions, the OSL response was measured as a function of concentration, results are shown in Figure 3.12. An increase in the OSL response is observed between concentrations of 0 – 100 ppm Cu^{+}, above which the OSL is observed to decrease. The increase in OSL signal up to approximately 100 ppm, followed by a decrease in intensity, could be related to the observations made on the TL measurements of these same Cu^{+}-doped glasses. The TL of the 60 ppm sample has a peak at 60 ℃ and 280 ℃, whereas in the 500 ppm sample this 60 ℃ peak is not observed and a new peak at 140 ℃ has formed. The combination of these results suggests a change in the glass lattice structure above approximately 100 pm, where instead of acting as isolate luminescence centres, adjacent ions might interact and cause quenching. They might also begin to effect the energy level structure of the

glass and the electron trapping centres.

3.4.2 Manganese

Thermoluminescence The TL emission for Mn^{2+}-doped FP glass is shown in Figure 3.13. TL experiments show the formation of deeper traps in the manganese doped samples when compared with the undoped glass. Initial rise TL analysis was also performed on the glass using the same method described in Section 2.6.1, and Table 3.2 shows the calculated values of trap depth (E), frequency factor (s) and lifetime (τ).

Table 3.2: Activation energy (E), frequency factor (s) and lifetimes at T = 293 K (τ) of sample Mn-ox.

T_m (℃)	E (eV)	s (s^{-1})	τ (s)
40	0.4 ± 0.17	5.89E+01	2.49E+05
60	0.5 ± 0.10	2.25E+02	5.00E+06
80	0.6 ± 0.05	9.32E+02	1.01E+07
100	0.7 ± 0.07	5.12E+03	4.95E+07
120	0.7 ± 0.07	3.53E+04	2.50E+08
140	0.8 ± 0.11	2.57E+05	7.85E+08
160	0.9 ± 0.12	2.63E+06	3.83E+09
180	1.0 ± 0.21	3.56E+07	2.11E+10
200	1.1 ± 0.04	2.72E+08	2.76E+10
220	1.2 ± 0.07	5.60E+09	1.66E+11
240	1.4 ± 0.12	1.71E+11	1.24E+12
260	1.4 ± 0.15	5.38E+11	3.26E+11
280	1.4 ± 0.15	4.60E+12	3.55E+11
300	1.5 ± 0.09	3.20E+13	3.02E+11

Thermoluminescence Emission Spectroscopy TL emission spectra for the manganese doped glass, shown in Figure 3.14, show the expected emission centered at 600 nm. The data does, however, show some discrepancy with the TL peaks observed in the Risø Reader, where the 340 ℃ peak is observed to have a much higher intensity than the broad peak centered at 110 ℃. In the 3DTL emission spectrometer, these peak intensities remain far more consistent through the temperature range.

Optically Stimulated Luminescence Manganese doped FP glass was previously shown to have intense TL emission peaks, but in comparison to its TL, this same glass has a very low OSL intensity. As can be seen in Figure 3.15, in both the 275 – 400 nm and 350 – 600 nm wavelength regions manganese doped glasses have comparable OSL responses to the undoped FP1 glass. It is possible the OSL emission is occurring primarily off-band from the filters used during OSL measurements, as the emission peak

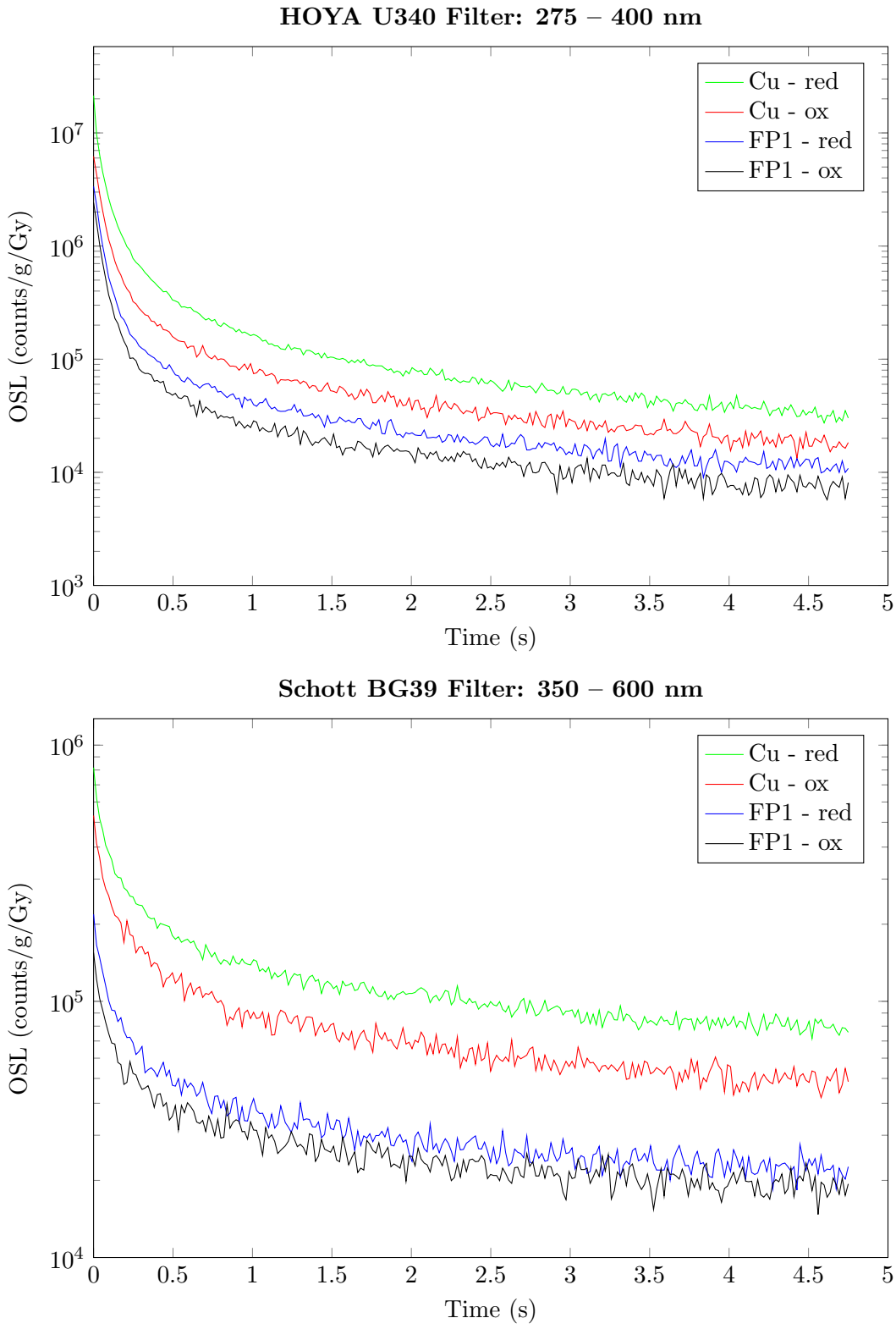

Figure 3.11: OSL shine-down trace for copper doped FP glass compared with undoped glass, produced under both oxidising and reducing conditions. Copper concentration is 60 ppmwt for each doped sample. Above: OSL detected using 470 nm optical stimulation and a HOYA U340 filter. Bottom: OSL detected using 870 nm optical stimulation and a Schott BG39 filter.

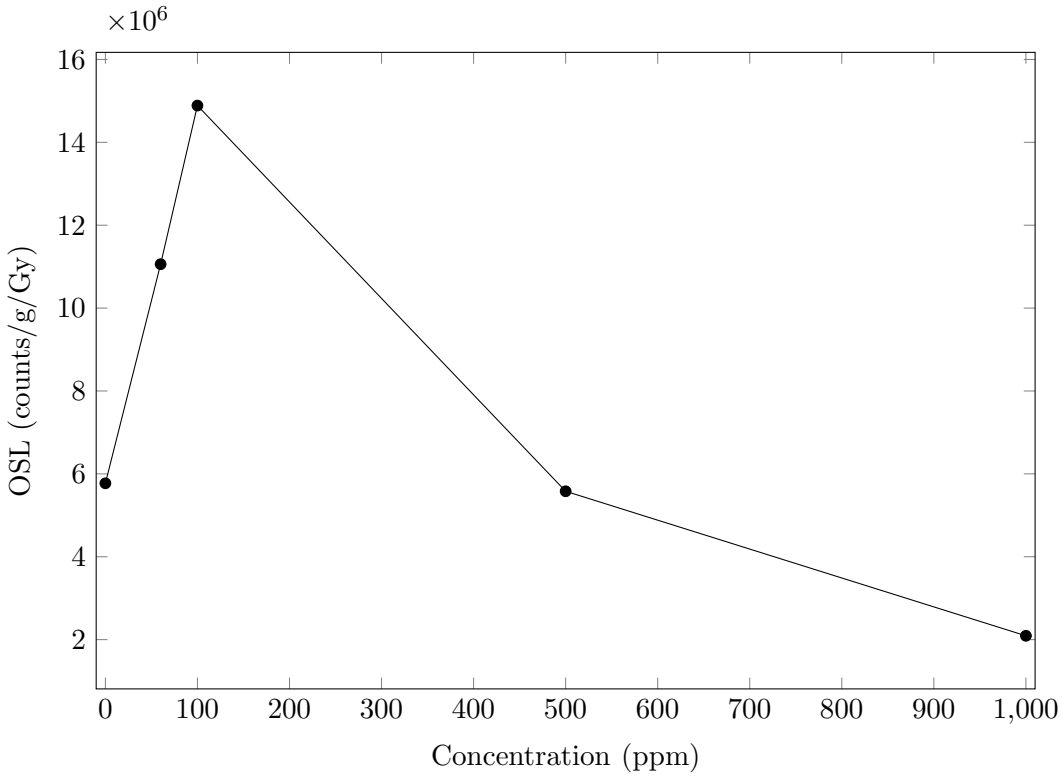

Figure 3.12: Integrated OSL counts from FP1 glass doped with Cu^{+} under a reducing environment. Lines are included only as a guide for the eye.

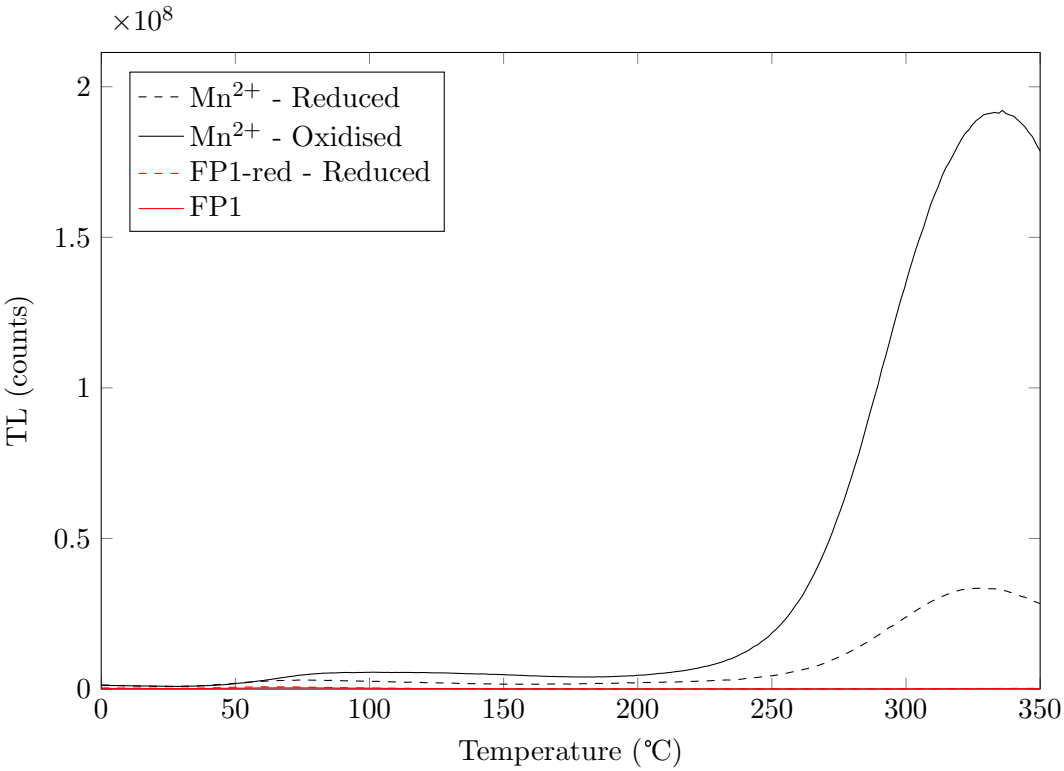

Figure 3.13: TL emission of Mn^{2+} doped FP glass.

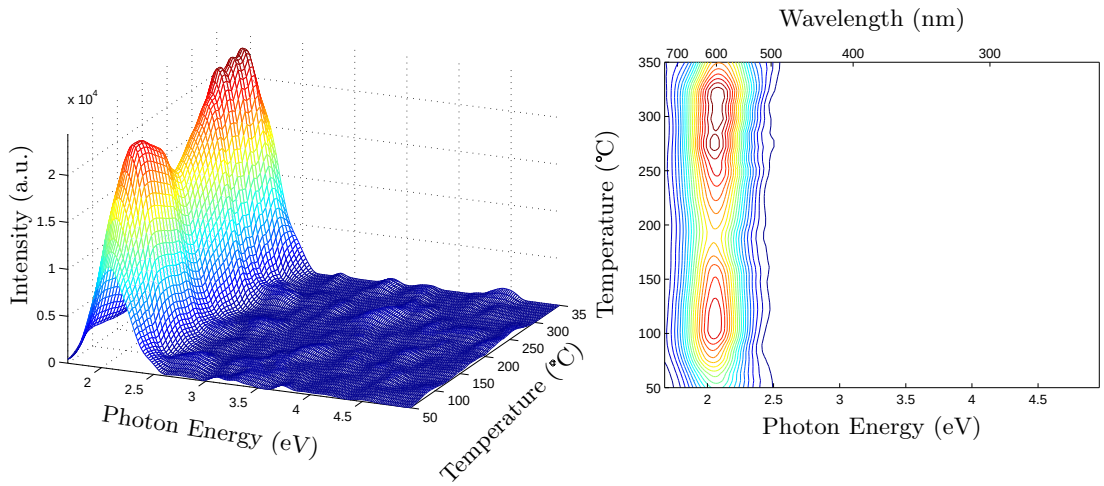

Figure 3.14: Thermoluminescence emission spectrum of sample Mn-ox, shown as both 3D and intensity-contour plots to highlight the dominance of 600 nm Mn^{2+} emission.

is centered at 600 nm, however a small tail of this peak is expected to overlap with the BG39 filter waveband. A proportion of the OSL should therefore be detectable, however it is obviously not sufficient to provide a suitably intense, detectable OSL response.

3.4.3 Terbium

Thermoluminescence TL experiments show that, like Mn^{2+} and Cu^{+}, Tb^{3+} doping produces an additional deeper electron trap in the material, shown by the occurrence of higher temperature TL peaks in Figure 3.16. Intense peaks were observed at 90 ℃ and 310 ℃, the 90 ℃ peak obscures the 60 ℃ TL peak observed in undoped glass. Initial rise TL was also performed for terbium doped glass, the results are shown in Table 3.3.

Thermoluminescence Emission Spectroscopy TL emission spectra were obtained for the terbium doped FP glass, results are shown in Figure 3.17. Several of the expected emission peaks from previous emission measurements were observed, in particular the 550, 490, 440, 420 and 380 nm peaks. Due to the resolution of the instrument, the 440 and 420 nm peaks appear as one broad peak and the 590 peak also appears as a small shoulder on the 550 nm peak.

Optically Stimulated Luminescence The OSL from terbium doped glasses shows improvement over undoped glasses for samples fabricated under both oxidising and reducing conditions in the 350 – 600 nm region, as seen in Figure 3.18. The series of emission peaks from 375 nm to 620 nm, shown in Section 3.3, provide emission overlap-

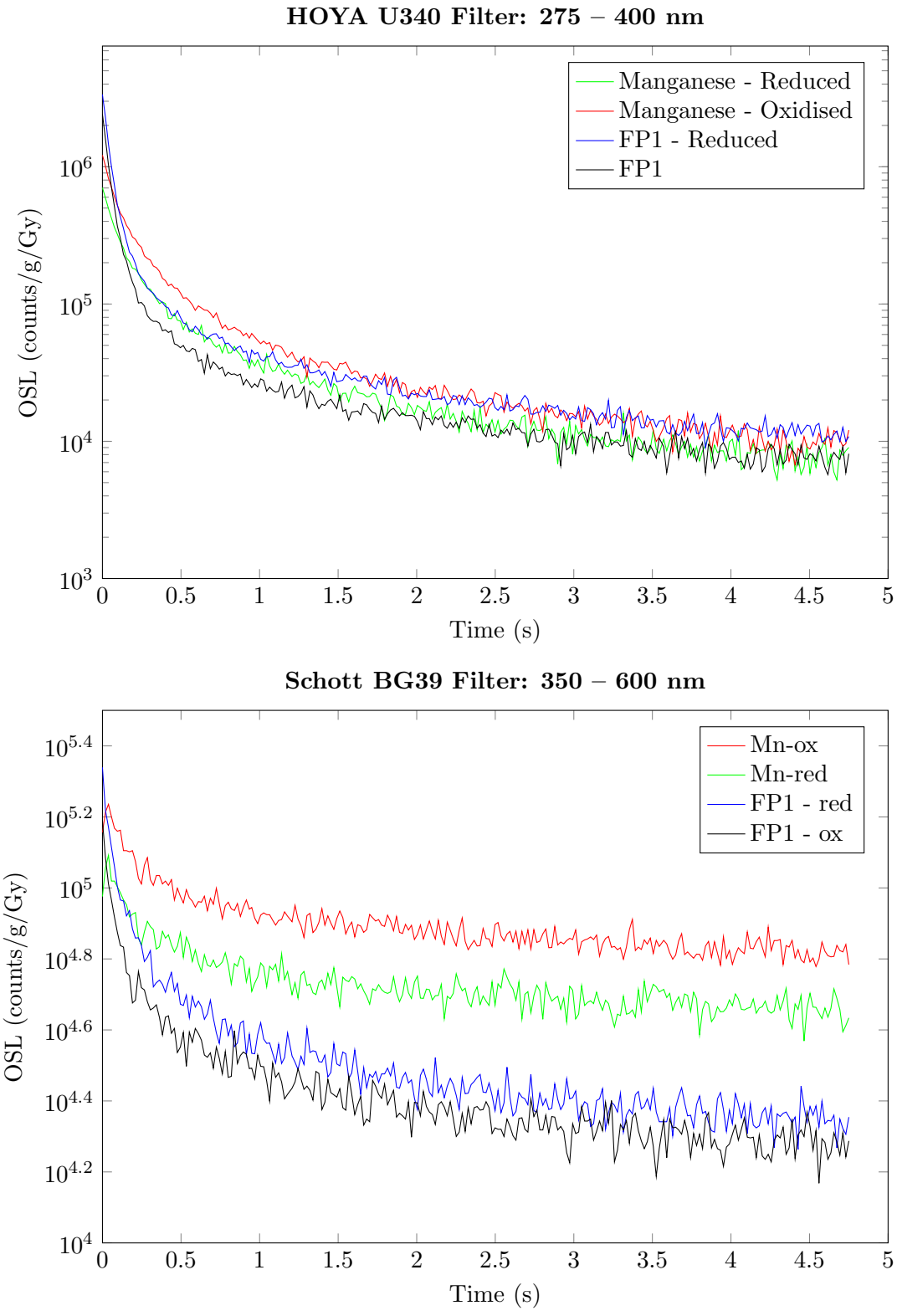

Figure 3.15: OSL shine-down trace for manganese doped FP glass compared with undoped glass, produced under both oxidising and reducing conditions. Manganese concentration is 2749 ppmwt for each doped sample. Above: OSL detected using 470 nm optical stimulation and a HOYA U340 filter. Bottom: OSL detected using 870 nm optical stimulation and a Schott BG39 filter.

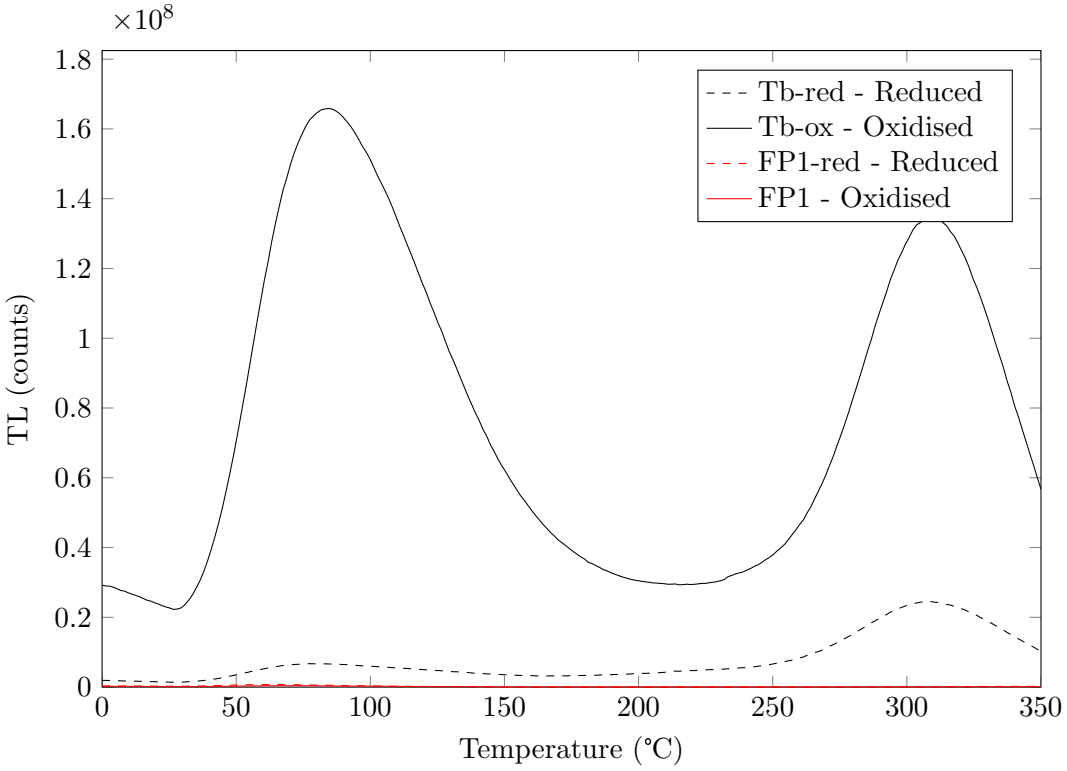

Figure 3.16: TL emission of Tb^{3+}-doped FP glass.

Table 3.3: Activation energy (E), frequency factor (s) and lifetimes at T = 293 K (τ) of sample Tb-red.

T_m (°C)	E (eV)	s (s^{-1})	τ (s)
60	0.53 ± 0.06	2.25E+02	5.03E+06
80	0.62 ± 0.05	1.13E+03	3.86E+07
100	0.72 ± 0.04	7.52E+03	2.90E+08
120	0.82 ± 0.07	6.59E+04	2.19E+09
140	0.87 ± 0.08	3.79E+05	2.35E+09
160	0.95 ± 0.07	3.45E+06	7.23E+09
180	1.00 ± 0.19	2.09E+07	7.12E+09
200	1.18 ± 0.11	8.99E+08	2.34E+11
220	1.21 ± 0.16	4.56E+09	1.19E+11
240	1.36 ± 0.22	1.70E+11	1.23E+12
260	1.41 ± 0.06	1.60E+12	1.36E+12
280	1.41 ± 0.13	4.43E+12	3.39E+11
300	1.45 ± 0.11	2.88E+13	2.69E+11

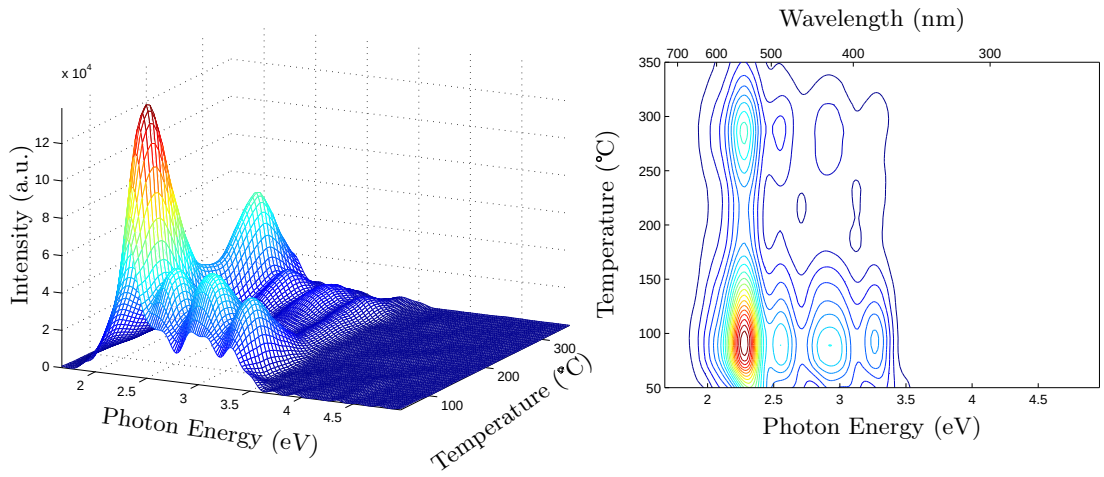

Figure 3.17: Thermoluminescence emission spectrum of sample Tb - red, 3D and intensity contour plots. The series of peaks seen for fluorescence and scintillation measurements are also clearly visible in the 400 – 600 nm region.

ping neatly with the 350 – 600 nm waveband of the Schott BG39 filter. Terbium doped glass fabricated in an oxidising environment is observed to have two orders of magnitude improvement over undoped FP glass, and an order of magnitude improvement over terbium doped glass fabricated in reducing conditions. The oxidising conditions may facilitate the formation of terbium ions in the +3 state, which produces the emission peaks observed in Section 3.3.

The OSL emission of oxidised terbium doped glass in the 275 – 400 nm region, is higher than for the undoped glass, however the kinetics of the OSL emission are observed to be slightly slower than for undoped samples. This could be due to the creation of deeper traps, seen in the TL measurements, producing a component of the OSL signal with a longer lifetime. This might increase the bleaching time necessary between measurements to reset the material and remove the entire population of trapped electrons. This was tested using a similar method to that described in Section 2.6.2, using sample Tb-ox: where several OSL measurements are performed on the sample with a certain bleaching time in between each measurement. As can be seen in Figure 3.19, 5 s of optical stimulation at 870 nm (162.7 mJ of energy incident upon the sample) is not sufficient to 're-set' the material following an irradiation, seen by the increasing intensity of each consecutive OSL measurement. When the bleaching time is increased to 100 s (1627 mJ of energy incident upon the sample), the material appears to be sufficiently bleached, and no cumulative storing of trapped charge is observed in consecutive OSL measurements.

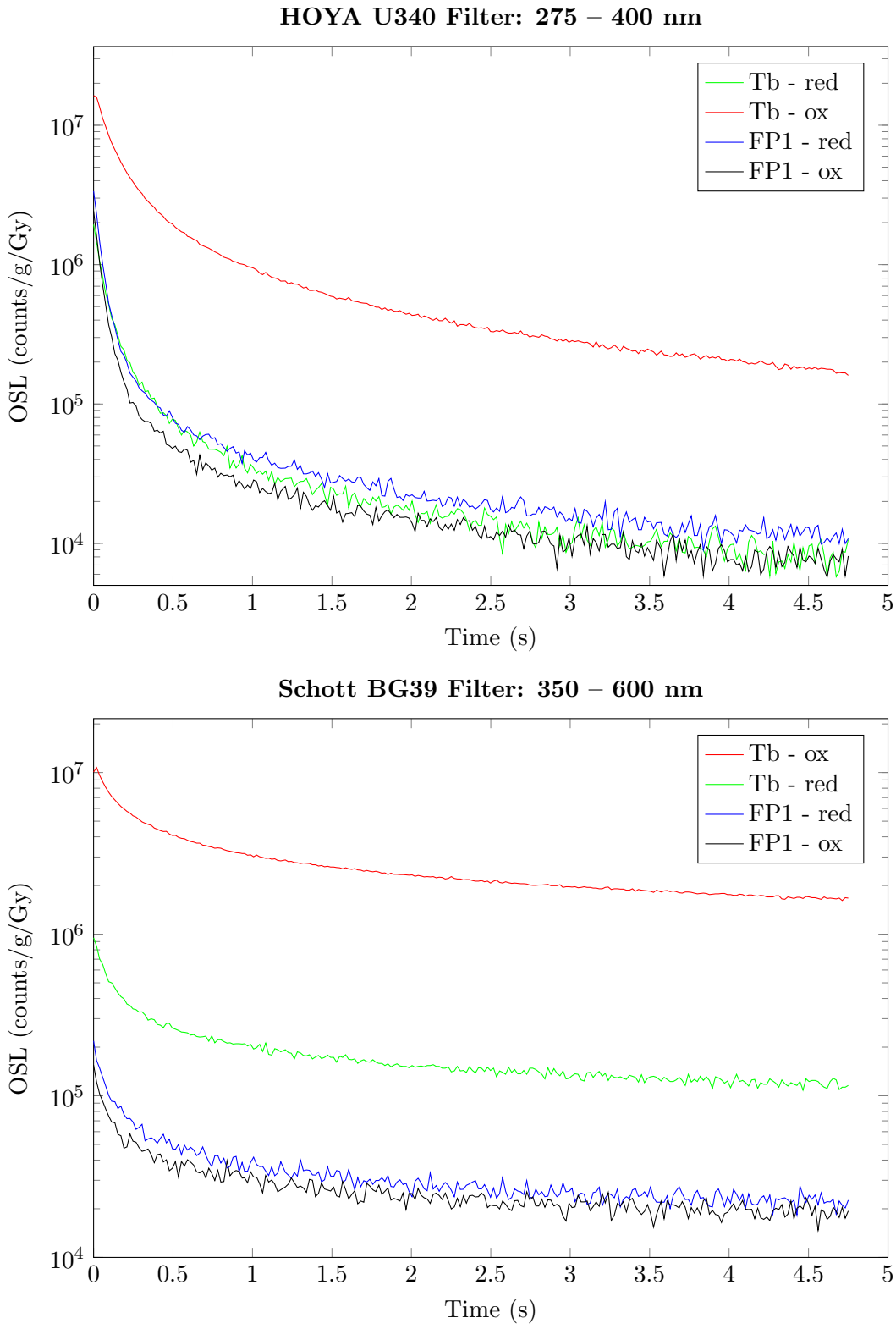

Figure 3.18: OSL shine-down trace for terbium doped FP glass compared with undoped glass, produced under both oxidising and reducing conditions. Terbium concentration is 7200 ppmwt for each doped sample. Above: OSL detected using 470 nm optical stimulation and a HOYA U340 filter. Bottom: OSL detected using 870 nm optical stimulation and a Schott BG39 filter.

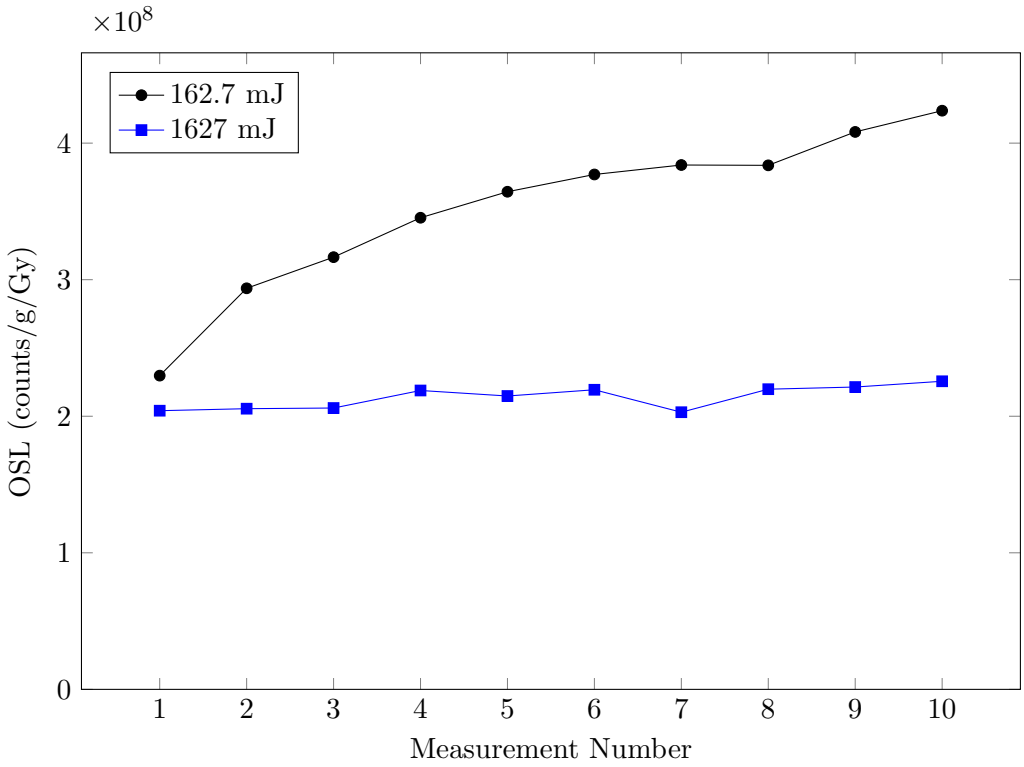

Figure 3.19: Reproducibility of sample Tb-ox glass with different 'bleaching' periods between individual OSL measurements. One set of measurements is taken using 5 s (167.2 mJ) of optical stimulation at 870 nm and the other with 100 s (1672 mJ). Measurements were taken using a Schott BG39 filter. Lines are included only as a guide for the eye.

3.4.4 Summary

TL results indicate the addition of Cu^{+}, Mn^{2+} and Tb^{3+} ions into the glass produces extra traps, which are deeper than those found in undoped glass. For Cu^{+} a 280 °C TL peak is produced, and at concentrations above approximately 500 ppmwt the 60 °C peak decreases and a new broad peak appears centered at 140 °C. Addition of Mn^{2+} was found to produce additional intense TL peaks at 140 °C and 280 °C, with energies of 0.83 ± 1.1 eV and 1.4 ± 0.15 eV respectively. Addition of Tb^{3+} was also observed to produce an additional TL peak at 240 °C, with an energy of 1.3 ± 0.21 eV.

OSL measurements indicate an increase in intensity when doping with Cu^{+} and Tb^{3+}, however despite the intense TL peaks, doping with Mn^{2+} is found to be ineffective. Samples doped with terbium were observed to have the greatest increase in OSL intensity, and the emission spectrum is ideal for use with a Schott BG39 filter. To compare each material, the OSL results for each sample were integrated for 0.2 s and normalised for mass, the results are summarised in Table 3.4 and Figure 3.20.

Table 3.4: OSL response of doped and undoped FP1 glass, fabricated under both oxidising and reducing conditions, integrated from 0 - 0.2 s. 275 – 400 nm indicates OSL in this wavelength region, achieved using a HOYA U340 filter and 470 nm stimulation. 350 – 600 nm indicates emission in this wavelength region achieved with a Schott BG39 filter and 870 nm stimulation.

Sample	**Dopant**	**Redox**	**OSL (counts/g/Gy)** $\times 10^5$	
			275 – 400	**350 – 600**
FP1 - Ox	Undoped	Ox	75.6	8.8
FP1 - Red	Undoped	Red	107.3	12.3
Cu - Ox	Copper	Ox	226.1	30.1
Cu - Red	Copper	Red	548.2	40.7
Mn - Ox	Manganese	Ox	69.1	13.2
Mn - Red	Manganese	Red	38.7	10.0
Tb - Ox	Terbium	Ox	1007	812.3
Tb - Red	Terbium	Red	77.4	60.3

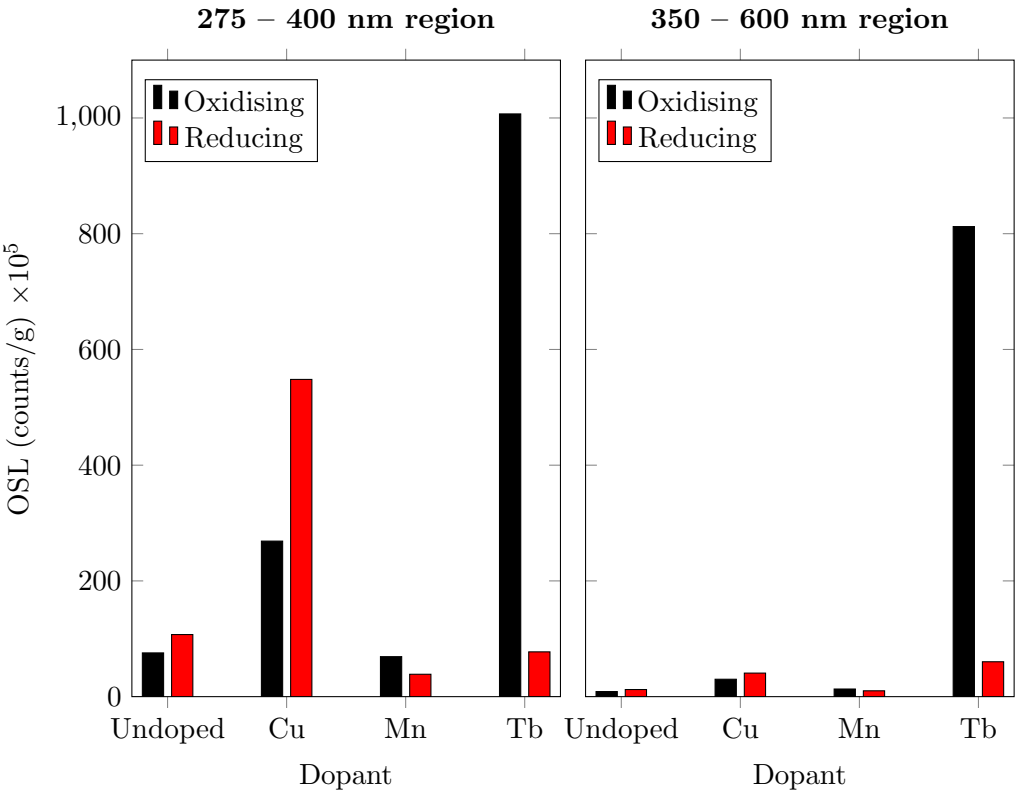

Figure 3.20: Plot of the OSL data provided in Table 3.4, shown for both 275 – 400 and 350 – 600 nm wavelength regions. Results shown for samples fabricated under both oxidising and reducing conditions.

3.5 Anomalous Fading

3.5.1 Theory

Many TL and OSL materials exhibit anomalous fading of the population of trapped electrons at ambient temperatures, this is defined as the fading of signal from traps deeper than are accessible by phonons at ambient temperatures. This fading therefore occurs by a different mechanism than straightforward thermal or optical stimulation (i.e. photon or phonon absorption). As an example, Figure 3.21 shows the anomalous fading from a sample of undoped, Mn^{2+}-doped and Tb^{3+}-doped FP glass. A TL measurement was performed immediately after irradiation, then another TL measurement performed with a delay of one hour between irradiation and heating. The difference between the two TL spectra has also been plotted. Significant fading of the 60 ℃ peak is observed for each sample, which is expected due to the shallow depth of this trap, however significant fading is also observed above this temperature, from the 40 - 60 ℃ region up to 300 ℃. At higher temperatures there is insufficient thermal energy to excite electrons from these deeper traps, demonstrating the movement of charge out of traps by alternative processes.

Different theories have been proposed to account for this fading. Tunnelling between electron traps and recombinations has been proposed, whereby an electron in a trap may tunnel through to an adjacent recombination centre. This model relies on electron traps and recombination centres being physically close to one another. One potential method to test this theory is to have samples doped with varying concentrations. Samples with a higher concentration will theoretically have traps and recombination centres closer to each other, and therefore the tunnelling probability will be higher. This could be measured by looking at the decay over time of this anomalous fading and seeing if the fading rate changes, a potential experiment which could be performed in the future if a variety of glasses doped with a number of different concentrations are produced.

3.5.2 Experiment to Detect and Observe Anomalous Fading

The anomalous fading in several samples was studied by measuring the light emitted from samples following irradiation. Samples were given a pre-heat in order to remove any weakly-trapped charge that might become untrapped by conventional thermal effects at ambient temperature, subsequently any light detected would be due to anomalous fading processes. Samples of glass were prepared on discs as for measurement in the Risø Reader. Each sample was irradiated for 60 seconds, followed by a pre-heat up to 160 ℃ at 5 ℃/s in the Risø Reader. Following irradiation and pre-heating,

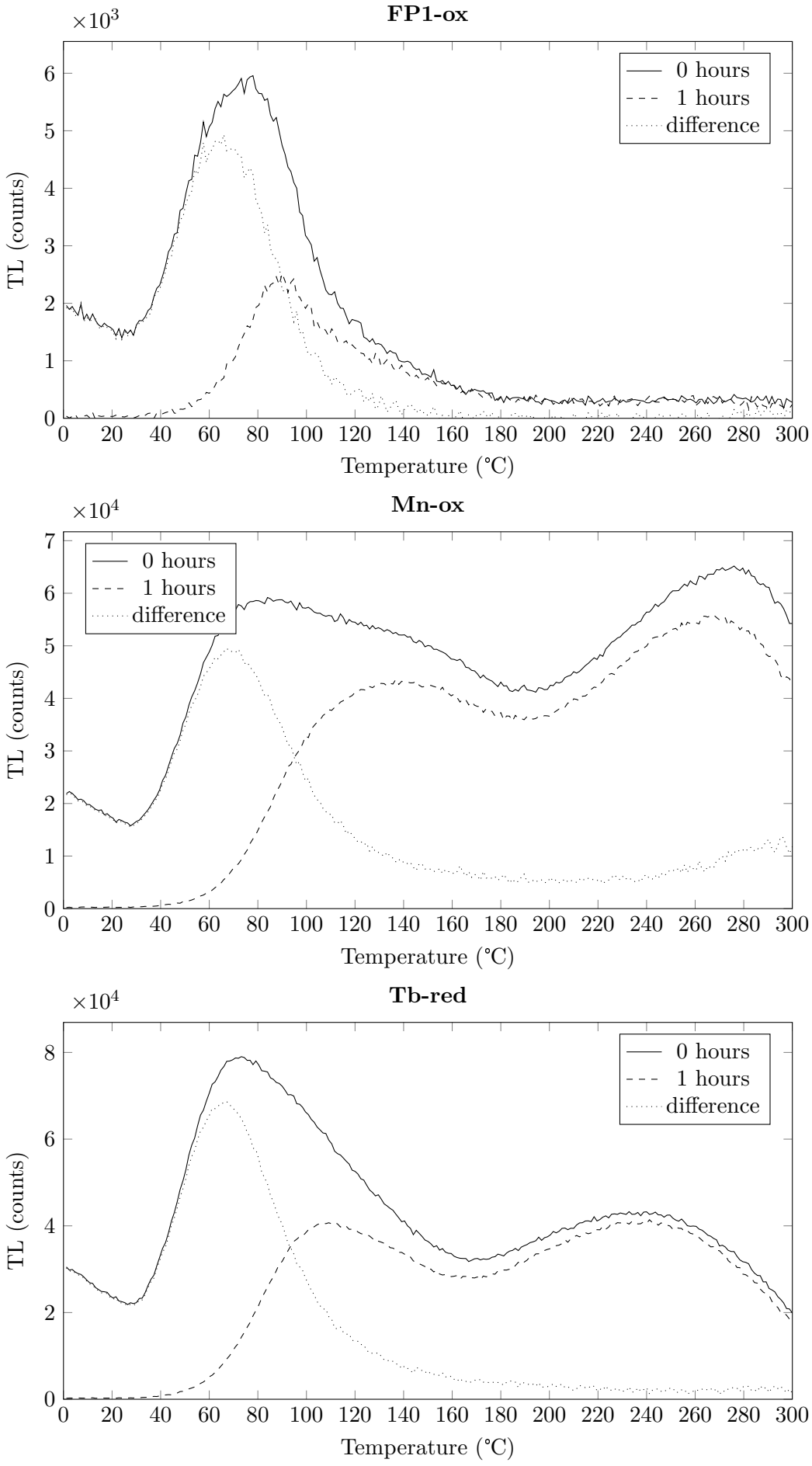

Figure 3.21: Anomalous fading of undoped and doped FP glasses following a one hour pause after irradiation.

samples were removed and placed into the chamber of a single aliquot reader, which contains an EMI 9635 QB PMT and collection optics enabling near 2π collection efficiency off the sample [108]. The reader has optical and thermal stimulation capabilities, however for the measurements described here no stimulation was applied to samples. The luminescence of the sample was recorded over several hours, with time intervals of 30 seconds. No optical or thermal stimulation was applied to samples, hence any luminescence occurring is due to anomalous processes.

To confirm results, further experiments were then performed with a preheat temperature of 230 ℃. This is because following a 160 ℃ preheat a small percentage of charge may still exist in traps thermally stimulable at room temperature; a preheat to 230 ℃ further ensures no charge remains in these traps.

3.5.3 Results

The Mn^{2+} and Tb^{3+} samples produced bright signals, however luminescence measured from Cu^{+} samples was faint. An example of the luminescence signal observed is shown in Figure 3.22, from a Mn^{2+}-doped glass preheated to 230 ℃. This sample was chosen as an example because, as shown in Figure 3.21, this sample exhibits the most significant fractional fading above 230 ℃. Figure 3.22 shows that the glass is producing luminescence, even following a preheat to 230 ℃ and with no stimulation sources.

For luminescence caused purely by a tunnelling process, we might expect a 1/t relationship, however this does not fit the data taken for any of the doped glasses. It is possible the luminescence measured is due to phosphorescence, which would not be affected by pre-heating the sample. Phosphorescence decay may be multi-exponential depending on the relaxation mechanism, and therefore cannot be ruled out due to the shape of the decay curve. A third order exponential function, for example, fits the data as is shown in 3.22, indicating several different decay components and lifetimes. This explanation, however, does not fully account for the charge we see lost as shown in Figure 3.21. We cannot assume the charge lost here relaxes via a radiative pathway, or a pathway that emits luminescence in the wavelength range detected by the PMT.

The mechanism of the fading observed in these samples is therefore not trivial to identify using any simple measurement method. What we can conclude from these limited observations is the unreliability of signals from these deep traps in doped FP glasses; the population of trapped electrons cannot be expected to remain constant even when the sample is kept isolated from optical and thermal stimulations. From earlier observations it is clear the low-temperature, shallow trap signals are depleted at ambient (room) temperature within tens of minutes in this glass. If the possible future

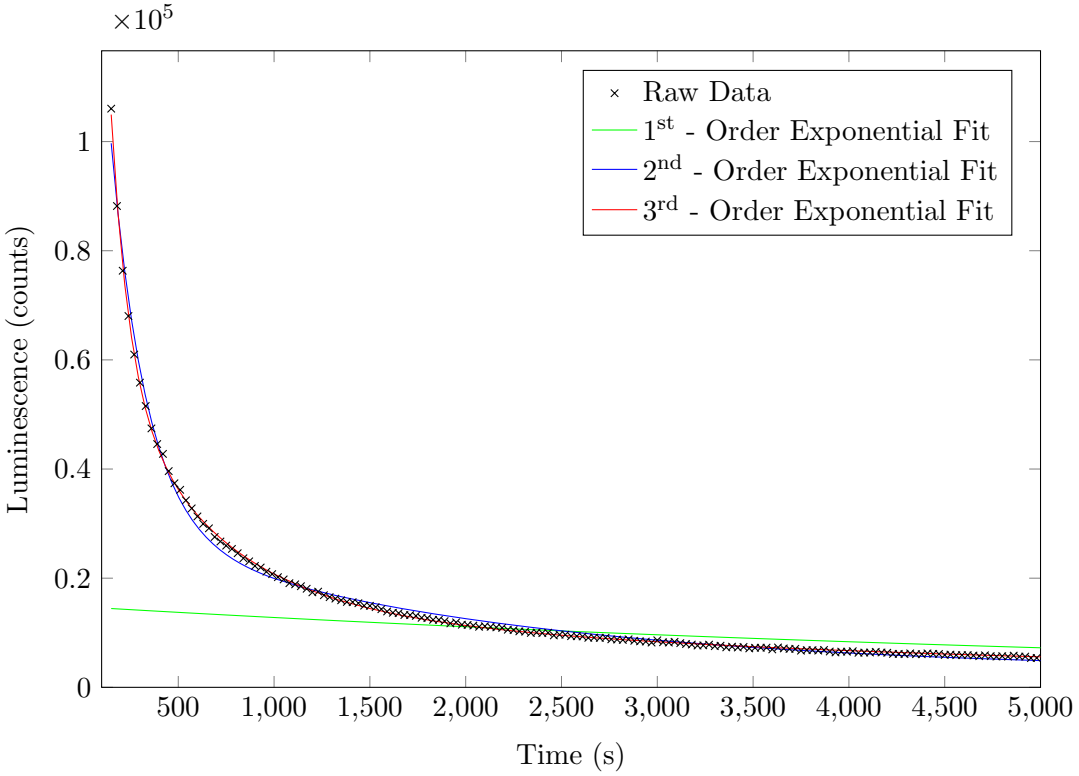

Figure 3.22: Luminescence from sample Mn-ox, following irradiation and pre-heat to 230 ℃. Sample receives no stimulation during data collection; the sample was held at ambient temperature for this measurement.

aim of doping with Tb^{3+}, Mn^{2+} or Cu^{+} is to create a suite of deeper traps with which to utilise longer lifetimes, this may instead lead to an unreliable material poorly suited to the task, if no further characterisation analysis is performed.

However, a major advantage to the fading of deeper traps is related to the advantages already stated for FP glasses; that being the easy bleaching and re-setting of the material for repeated measurements. If deeper traps are also depleting of their own accord at ambient temperature, the buildup of trapped charge, seen as residual dose, between measurements will be less of a problem. The difference in lifetime and depletion mechanism between shallow and deep traps should, however, still be considered carefully.

3.6 Summary of Dopant Properties

When performing TL measurements, Mn^{2+}-doped FP had a brighter signal than Tb^{3+}-doped FP due to the intense 280 ℃ peak. The most intense peak in Tb^{3+}-doped FP occurs at 100 ℃, with a smaller peak at 260 ℃, due to the requirement for optical stimulation of electrons from their traps this makes Tb^{3+}-doped FP a better candidate for OSL measurements than Mn^{2+}-doped FP. A low stimulation photon energy such as 852 nm (1.45 eV) will not excite electrons from the deeper traps found in Mn^{2+}-doped

FP as efficiently, whereas it would be better able to excite electrons from the shallower traps found in Tb^{3+}-doped FP.

As well as the trap structure, the emission wavelengths are also considered. The emission of Tb^{3+}-doped FP glass is an appropriate match for the transmission window of a Schott BG39 filter, shown in Figure 3.23. The emission of Mn^{2+}-doped FP, however, is significantly blocked by this same filter at wavelengths longer than 600 nm.

Fading measurements also showed that while Mn^{2+}-doped glass has a more intense 280 ℃ TL peak, it is prone to more severe fading than the Tb^{3+}-doped FP. Considering each of these parameters, Tb^{3+}-doped FP glass was determined to be the best option for producing doped FP optical fibres.

Cu^{+}-doping is considered useful if luminescence is desired in the 400 nm region, such as when using a PMT for detection, however due to the majority of work being performed with a SPAD, Tb^{3+}-doping was deemed more suitable.

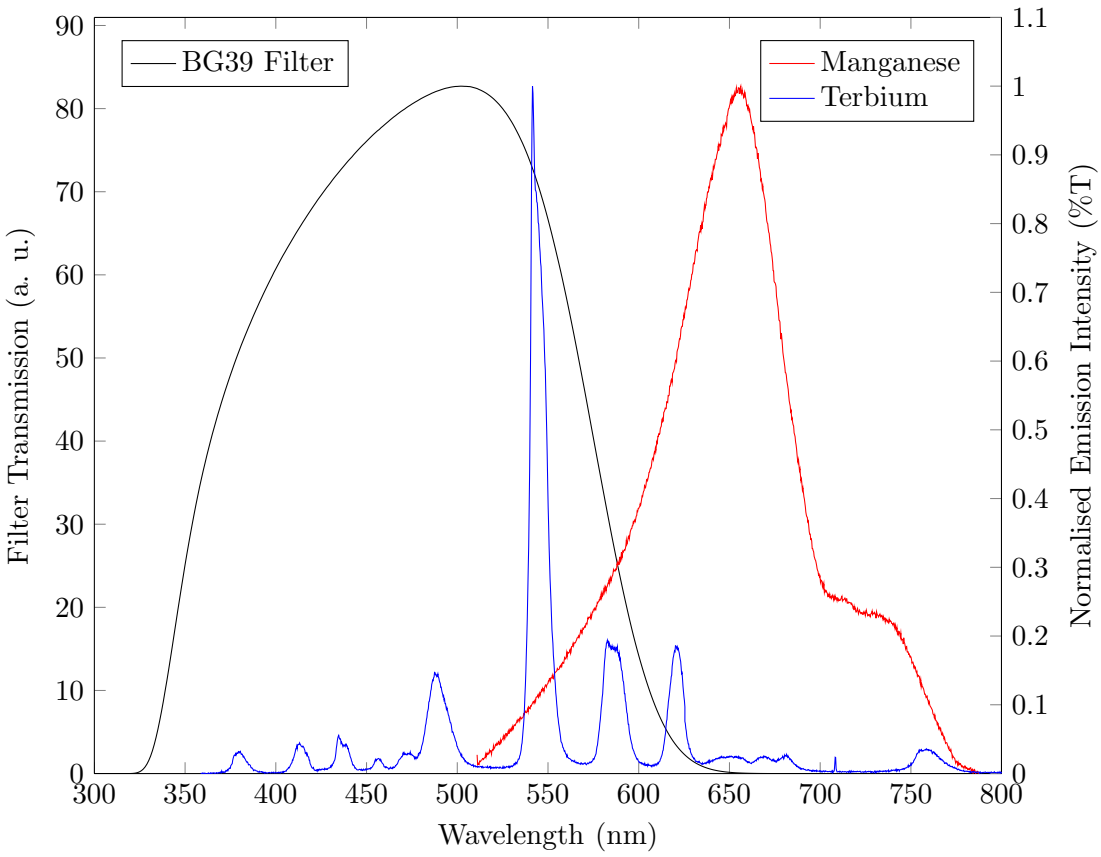

Figure 3.23: Emission spectra of Mn^{2+} and Tb^{3+}-doped FP1 glass compared with the transmission spectrum for a 3 mm thick Schott BG39 filter.

Chapter 4

Fabrication of Fluoride Phosphate Optical Fibres

In the previous chapters, fluoride phosphate glass was studied and determined to be a suitable material for the proposed fibre dosimeter. This chapter presents the work undertaken to turn this material into an optical fibre of suitable quality for radiation sensing measurements.

The fabrication process contains three main steps: extrusion of the glass into a preform, preparation of the preform for fibre drawing, then the fibre drawing itself. For simplicity, the structure of the chapter will follow these three main fabrication steps, and as such will not follow a strict chronological order. For example, the results obtained from early fibre drawing experiments will be referred to in the extrusion and preform treatment sections.

The results indicating fibre quality, the loss measurements, will be presented at the end of the chapter following all relevant explanations of the processes leading to these results.

4.1 Introduction

4.1.1 State-of-the-Art

Very little exists in the literature with regard to fluoride phosphate optical fibres, but several studies have demonstrated successful fabrication of fibres from this material [89,109,110]. For example, step index fibre preforms were fabricated using the rotational casting method and the optical fibres drawn from this had a loss of 0.1 dB/m.

4.1.2 Glass Material

To begin fabrication of fluoride phosphate optical fibres, larger quantities of sample FP1, Schott N-FK51A fluoride phosphate glass, were obtained. They were procured as 30 mm diameter rods, the appropriate diameter for extrusion, then cut into 70 mm lengths, weighing approximately 180 g, and finally polished.

Following the work demonstrated in Chapter 3, where FP1 glass was doped with various ions, FP1 glass doped with Tb^{3+} ions was produced here in sufficient quantities for optical fibre fabrication. The fabrication process of these Tb^{3+}-doped glasses is similar to that described in Chapter 3, and the further steps to process this glass into optical fibres will also be discussed later in this chapter.

4.1.3 Fibre Geometry

Due to the nature of the sensing device, that being one where the glass itself is the sensing component, the diameter and length of the optical fibre directly influences the sensitivity of the resulting device to ionising radiation. While there are advantages to step index optical fibre designs, the guided modes do not extend far beyond the core and the cladding glass just provides a stable environment. The ideal case is therefore to have a large-core fibre, where the guided modes interact with a large cross section of the glass material. The ideal fibre design for this case is a bare (unstructured) fibre, where the entire unit acts as a highly multi-mode core with an air cladding, which allows the entire glass cross-section to contribute as a sensing component. Optical fibres with this unstructured geometry were therefore fabricated primarily with a diameter of 160 µm, and a number of optical fibres were also fabricated with diameters ranging between 200 and 1000 µm.

4.2 Extrusion

Fabrication of optical fibre preforms was done using the extrusion method, with cast billets of FP1 glass. Another potential method is to melt the glass and cast into a preform geometry, however casting long preforms without bubbles is not trivial [111]. The extrusion method can also enable the production of microstructured geometries in the preform. In addition, extruded surfaces are fire-polished and usually require little post-processing of the surface before fibre drawing. This was found to be untrue for FP glass, however, as will be explained in later Sections. Extrusion was therefore used for preform fabrication; this method has also been used previously for fabrication of fluoride phosphate glass fibres [109]. A diagram of the extrusion process is shown in Figure 4.1, and a picture showing the extrusion machine is supplied in Appendix B.3, Figure B.4. During extrusion trials, a number of variables were adjusted. Due to expense, not all variables could be tested individually. A summary of the parameters used for each extrusion trial can be found in Appendix C.1.

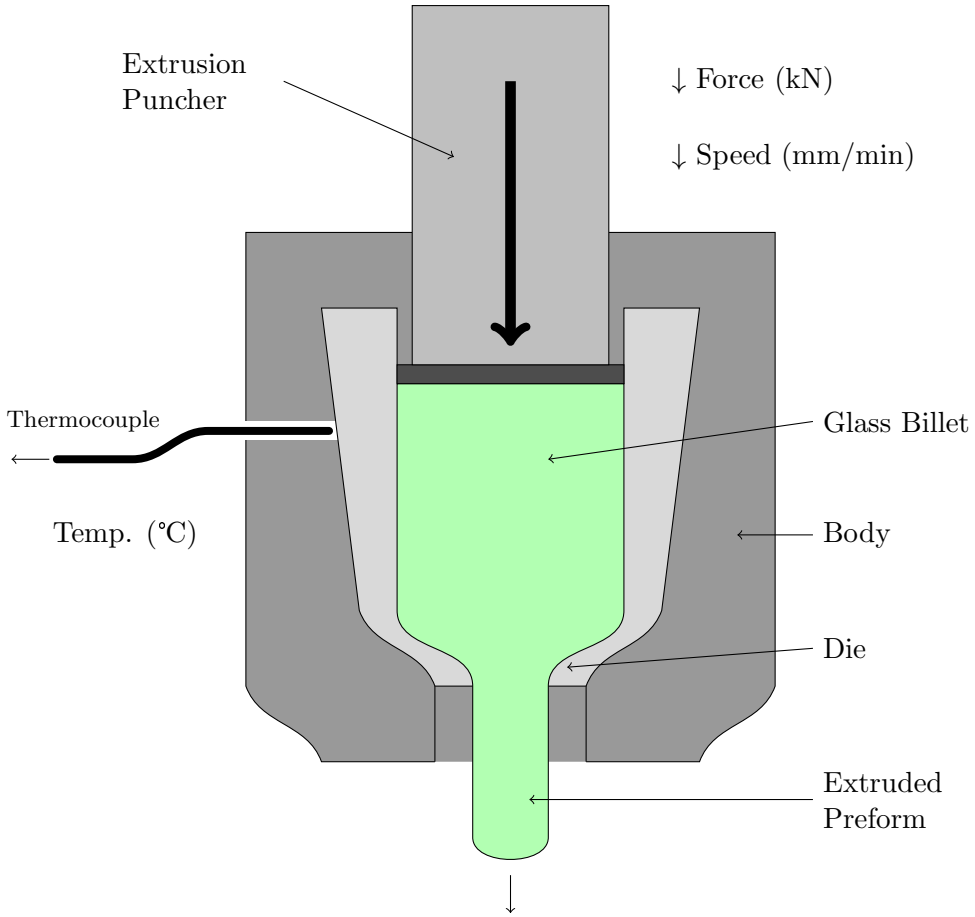

Figure 4.1: Cross-section of the extrusion process. This diagram shows only the inner section of the setup, surrounding the body is a furnace, which is controlled using feedback from the thermocouple. The puncher enters through the top of the furnace, and the extruded preform exists through the bottom.

4.2.1 Die Materials

Stainless steel was the first die material trialled, as it has been used successfully for the extrusion of other soft glasses such as bismuth, lead silicate, tellurite and others [111–114]. Stainless steel can be susceptible to chemical reactions with elements within the glass, leading to a preform with very poor surface quality. As it contains fluoride, fluoride phosphate glass has the potential for chemical interaction with stainless steel, facilitated by the extrusion temperatures of above 500 ℃. Extrusion trials performed using stainless steel had poor surface quality, containing many small crystalline defects and striations, which were attributed to the interaction of the glass with the stainless steel.

Graphite is an alternative when an inert die material is required, as it does not react with fluoride, unlike stainless steel. However, it cannot be used in atmospheres containing oxygen at temperatures higher than approximately 500 ℃, above which it may combust. Due to this, when extruding through graphite, the temperature used was 500 ℃. Preforms extruded through graphite were free of the crystalline defects observed on preforms extruded through stainless steel, which is explained by graphite being the more inert material, but they were observed to have striations running along the length. This is due in part to the higher force required for extrusion at lower temperature and is addressed further in Section 4.2.2.

From the experiments using stainless steel and graphite, it was established the die material needed to be inert and withstand temperatures above 525 ℃. A machinable ceramic, Macor® by Corning Inc., was found to be a suitable material as it is chemically inert, has low thermal expansion, can be machined into die parts using standard methods, and withstands temperatures up to 800 ℃. Preforms extruded through Macor® still had a number of crystalline defects, but were free of the striations observed on the surface of previous trials. Macor® was found to be the most suitable material for extrusion when no further processing was performed on a preform before fibre drawing. However as will be shown in later sections, the surface layer of preforms were eventually routinely removed before fibre drawing. Due to this, the effect of the die material on the preform surface was no longer an issue and extrusions were performed with stainless steel for the latest fibre trials.

4.2.2 Extrusion Force, Speed and Temperature

For an extrusion of glass the force, speed and temperature parameters are directly related [115], and each parameter has certain considerations which need to be addressed when choosing an appropriate value:

Force This is the force with which the machine will press down upon the softened glass billet in order to press it through the die; it is a dynamic variable which varies in order to keep the extrusion speed constant. A value of approximately 5 kN is suitable. However if the extrusion force is too high, the resulting preform may have striations or other defects on its surface.

Speed The speed at which the softened glass is pressed through the die - a static variable which is kept consistent by variation in the extrusion force. The extrusion speed (the speed at which the extrusion puncher is pushed downwards[1]) is generally in the order of millimeters per minute, values of between 0.05 mm/min and 0.2 mm/min are used depending on the type of glass being processed [112, 113]. Preforms extruded at fast speeds may be susceptible to surface damage, hence slower extrusion speeds are generally desired. If extruding long preforms, however, slow speeds can lead to an extrusion running over multiple days. The speed used can therefore become a compromise between surface quality and operating time. The extrusion speed is dependant on the viscosity of the glass, and is therefore dependant on the force.

Temperature The temperature at which the extrusion process occurs must be sufficient to soften the glass such that it may be pressed through the extrusion die, but not so high the glass softens and flows under its own weight. The temperature must also not be above a temperature at which chemical changes occur within the glass or between the glass and the die material, both of which can cause crystallisation. Furthermore, the temperature can also affect the die material itself, for example graphite must not be used above approximately 500 ℃, otherwise combustion may occur. In contrast to this, the temperature must not be too low, otherwise unacceptably high forces are required to push the glass through the die, which can lead to damage of the resulting preform surface.

The effect of extrusion speed and force on the preform quality is demonstrated in Figure 4.2, where the extrusion speed was reduced from 0.2 mm/min to 0.1 mm/min. The image is of the preform surface under magnification; to the left is the section of preform extruded at 0.2 mm/min; to the right is the section after the speed was reduced to 0.1 mm/min.

The values of force, speed and temperature were therefore adjusted over several extrusion trials in order to determine suitable values. For example, the temperature chosen for the first extrusion trial (Appendix C.1 - E1) was 515 ℃, the softening point ($T_{7.6}$) of Schott N-FK51A FP glass is 527 ℃ [116]. The force required for extrusion at this temperature was therefore high and many defects were observed on the preform sur-

[1] This is different to the speed at which the extruded preform exits the die.

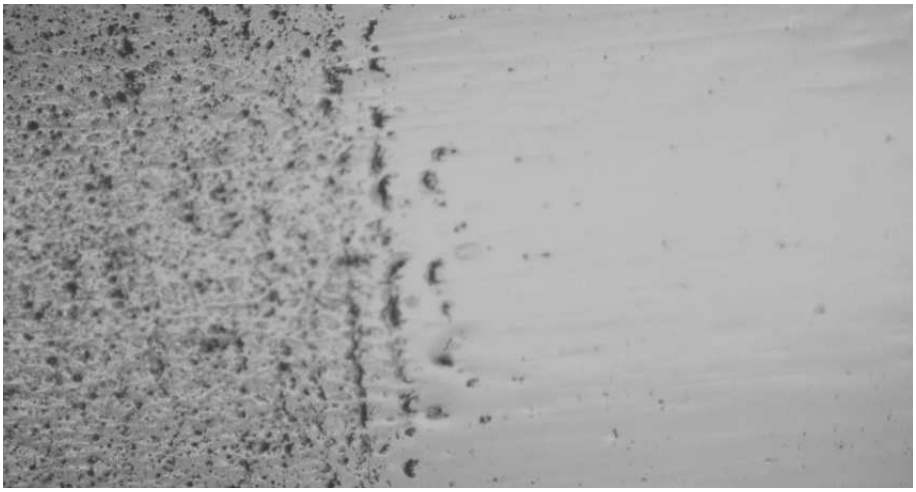

Figure 4.2: Preform surface quality following extrusion through Macor® at 525 ℃ at speeds of (left) 0.2 mm/min and (right) 0.1 mm/min.

face. A subsequent extrusion used a higher temperature of 525 ℃ in order to reduce the force required (Appendix C.1 - E2). The resulting preform still had a poor surface quality, and so slower extrusion speeds and different die materials were trialled (Appendix C.1 - E3). This process was continued, where a variety of different speeds and temperatures were trialled, along with the use of different die materials. Values were chosen which kept the force at acceptable levels, never exceeding 5 kN. A set of values were eventually determined which produced preforms of acceptable quality for fibre drawing: temperature = 525 ℃, speed = 0.05 mm/min, force = 1.5 - 2.5 kN. Using these parameters, the extrusion process would take approximately 25 hours for a 70 mm glass billet. These values were subsequently used for all extrusion trials E8 to E13 as seen in Appendix C.1.

4.2.3 Limit on Extrusion Temperature

The upper temperature limit of fluoride phosphate glass, above which the surface will show crystallisation, was tested on polished glass samples. Samples were heated in a furnace in ambient atmosphere to a certain temperature and allowed to dwell for 1 hour before being cooled. The surface of the sample was then observed for any changes. This process was then repeated several times, increasing the temperature with each measurement. In the furnace environment, surface changes were observed to occur at 525 ℃, Figure 4.3 shows the glass surface before and after heating to 525 ℃.

As is shown here crystalisation can occur at 525 ℃ in a furnace, however extrusions were still performed at this temperature in the extrusion machine. Preforms extruded at this temperature did not shown the surface effects observed in Figure 4.3, possibly due to the atmosphere present during extrusion.

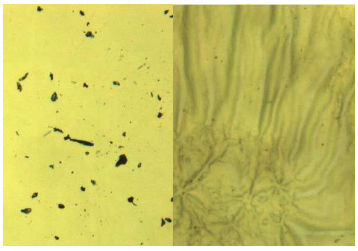

Figure 4.3: Effect on FP1 glass of heating to 525 ℃ in a furnace. Left: unheated sample of FP1 glass, right: FP1 glass following heating to 525 ℃.

4.2.4 Atmosphere

Chemical reactions between the glass and the environment were reduced by using appropriate die materials and a reasonable extrusion temperature. To further reduce any oxidation of the glass, a nitrogen atmosphere was used for all extrusions beginning at Extrusion Trial 4, a flow rate of 1 l/min was used. The nitrogen flow also served to create a consistent atmosphere throughout the extrusion, unaffected by temperature, humidity and other external atmospheric fluctuations.

Although nitrogen was used to control the atmosphere, an atmosphere completely free of oxygen was not possible, so a small amount of oxidation may still occur during the extrusion process. Furthermore, graphite die cannot be used above 500 ℃ due to the risk of combustion with this small quantity of oxygen.

4.3 Preform Treatment

Following extrusion, preforms required further preparation before the fibre drawing stage. Several observations, described later in Section 4.4.2, led to the conclusion that there was a thin surface layer on the preforms of slightly different composition to the bulk glass. This may be related to the changes observed on the surface of glasses heated to 525 ℃ observed in Figure 4.3. Surface treatment of preforms prior to fibre drawing has been shown to be effective for various types of glass [117, 118], and this section presents several methods by which this surface layer was analysed and the subsequent treatment of preforms to remove this layer.

4.3.1 Energy Dispersive X-ray Spectroscopy

The preforms were tested using energy dispersive X-ray spectroscopy (EDX) to determine if there was a compositional difference between the surface of the extruded preform (as-extruded) and the surface of the same preform with this surface removed by polishing (polished). Measurements were performed on a Philips XL20 Scanning

Electron Microscope[2], using EDX mode. During EDX measurements the sampling depth is of the order of micrometers, results are therefore expected to depict the composition of just the surface layer, without sampling from the bulk material underneath. Results show an increased presence of oxygen and decreased level of fluorine compared to all other elements, seen in Figure 4.4. This is assumed to occur during the extrusion process, where both out-gassing of fluorine and oxidation could be occurring at the elevated temperature. This would change the structure and properties of the as-extruded surface layer with respect to the polished layer. EDX was also performed to determine the composition of the crystalline defects on the surface. Results indicated these defects have the same composition as the as-extruded glass.

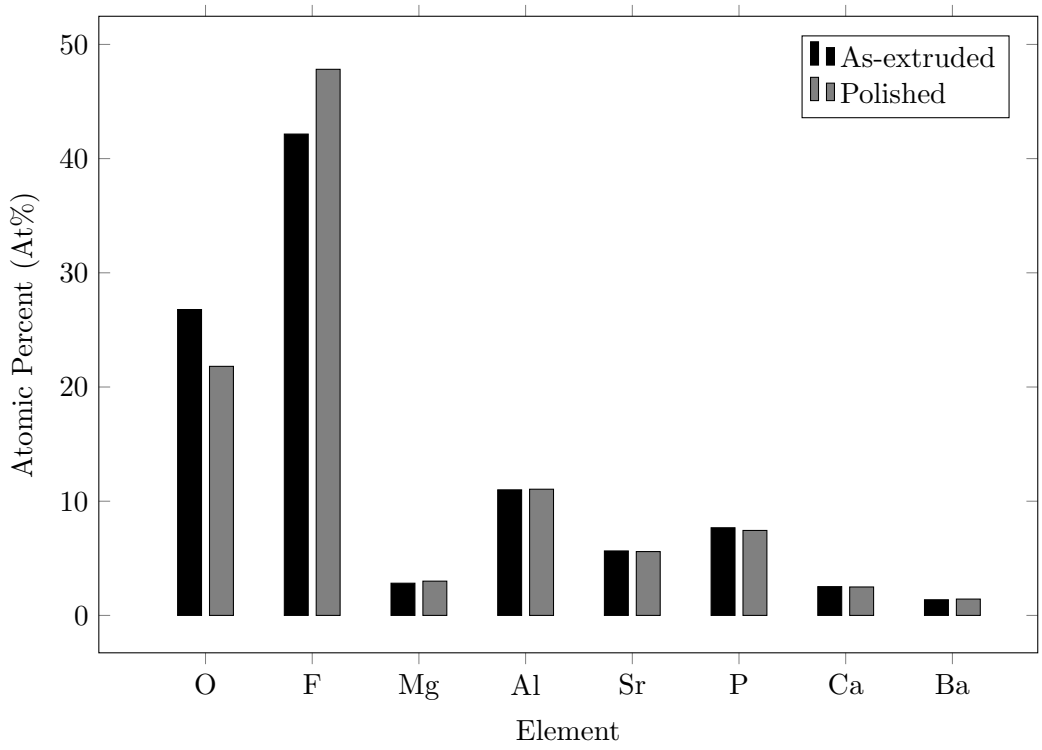

Figure 4.4: Composition of optical fibre preform surface compared with the bulk material, measured using the scanning electron microscope on EDX mode.

4.3.2 Optical Profiling

To further understand the structure of the preform surfaces, an optical profiler was used to obtain 3D information, as well as to provide a value for the surface roughness. A Bruker Contour GT-K Optical Profiler was used for measurements using both vertical scanning interferometry (VSI) and phase sensitive interferometry (PSI) methods. Measurements were taken of the preform surfaces, and the values for surface roughness (Sa) and average roughness (Ra) measured. Due to the curvature of the preforms, the data were corrected by subtracting the cylindrical curvature of the preform. In several

[2]Adelaide Microscopy, Medical School North, University of Adelaide

cases, noise caused by vibration was removed using a Fourier filter to subtract these distortions.

Results, shown in Figure 4.5, indicate the structure of striations and point defects, first discussed in Section 4.2. The defects occur both as point defects, such as where crystallisation might have occurred, and also commonly as long striations of defects. Optical profiler results were used to determine the effectiveness of surface treatments used to improve the preform quality. This will be discussed in Sections 4.3.3 and 4.3.4.

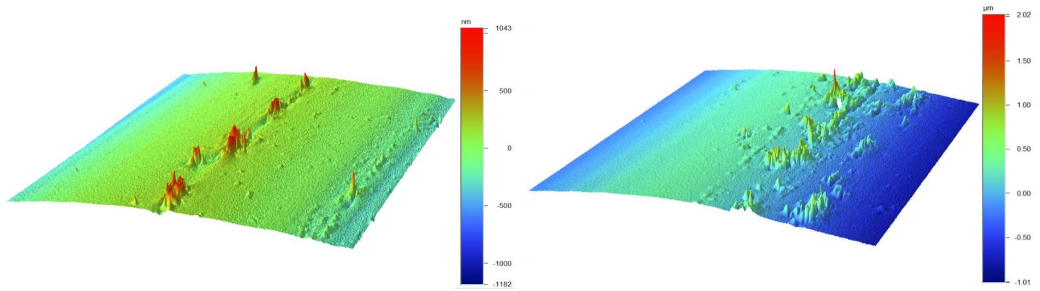

Figure 4.5: Examples of surface defects taken using the Optical Profiler using VSI mode. Note the colour-coded height scales can change significantly, based on the scale of the surface measured.

4.3.3 Chemical Etching

Surface analysis indicated extruded preforms had poor surface quality, even after optimising the extrusion conditions through die material, temperature, speed and force. Crystalline defects and the formation of a surface layer resulted in poor fibre quality, this surface layer therefore needed to be removed prior to fibre drawing. The first approach to remove the surface layer was to use chemical etching: etching has been shown previously to increase the surface quality of various glasses, including those containing fluoride and phosphate [118–120].

No previous studies were found on the etching of fluoride phosphate glasses, however etching has been done on ZBLAN and fluoro-aluminate glasses [118–120]. One study showed a solution containing $AlCl_3$ and HCl was an effective etchant for fluoroaluminate glass [118]; this was therefore tested, along with solutions containing only $AlCl_3$ or HCl. Solutions containing $ZrOCl_2$ and HCl are also effective for etching ZBLAN glasses [120,121], and were also tested. Studying the product test data for FP1 glass indicates fluoride phosphate glass is slightly susceptible to etching by triphosphates [116], therefore triphosphate solutions were also trialled. A summary of the etchant solutions is given here:

- HCl
- $AlCl_3$• HCl
- KOH
- NaOH
- ZrOCl
- HCl • ZrOCl
- HNO_3
- H_2SO_4

The majority of the solutions trialled were ineffective, however solutions of HCl and $AlCl_3$• HCl were observed to have an effect when heated. Samples of glass were therefore prepared with the same shape and mass, 5 x 5 x 2 mm ensuring the surface area was consistent at 90 mm^2. These samples were then etched in a variety of solutions containing different concentrations of HCl and $AlCl_3$• HCl. Solutions were heated to 80 ℃, and the samples weighed periodically. The weight of the glass is plotted with respect to time, an example is shown in Figure 4.6, and the etching rate is calculated from the slope. The etching rate of each solution is shown in Table 4.1. The solution containing 0.6 M $AlCl_3$ in 1M HCl was found to be the most efficient.

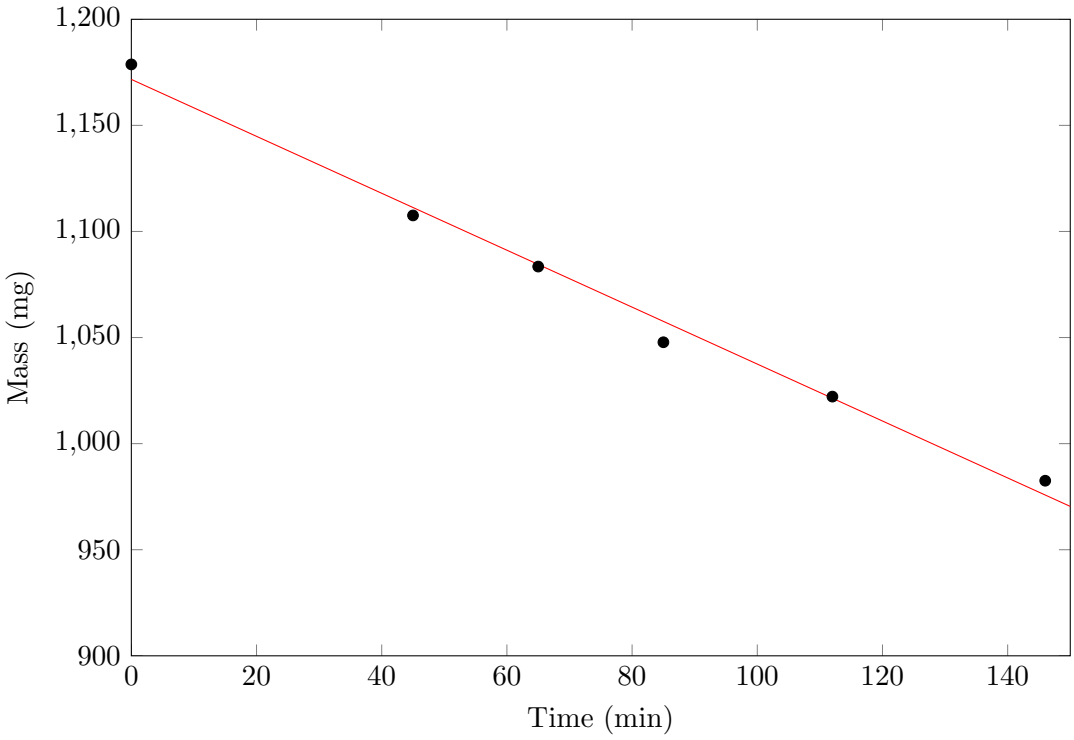

Figure 4.6: Etching efficiency of fluoride phosphate glass by 0.6 M $AlCl_3$ in 1M HCl, etching efficiency in mg/min is calculated from the slope.

While a solution of 0.6 M $AlCl_3$ • 1M HCl was found to have a faster etch rate than other solutions tested, the time required for any significant mass removal from a preform was still impractically high. In addition, although preforms were continuously rotated during the etching process, the resulting surfaces did not have a smooth surface. As can be seen from Figure 4.7, showing an etched preform, material has been etched away from specific sites on the surface, producing smooth holes.

Table 4.1: Summary of solutions trialled for etching of fluoride phosphate glass

Solution	*Concentration* (M)	*EtchRate* (mg/min)
$AlCl_3 \bullet HCl$	$0.2:1$	1.17 ± 0.02
$AlCl_3 \bullet HCl$	$0.4:1$	1.32 ± 0.04
$AlCl_3 \bullet HCl$	$0.6:1$	1.34 ± 0.06
$AlCl_3 \bullet HCl$	$0.8:1$	1.09 ± 0.05
$AlCl_3 \bullet HCl$	$1:1$	0.02 ± 0.01
$AlCl_3$	1	0.07 ± 0.01
HCl	1	0.83 ± 0.04
HCl	8	0.67 ± 0.02

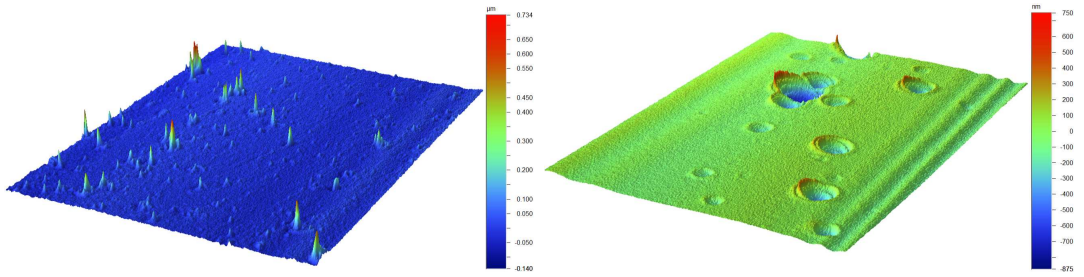

Figure 4.7: Surface profile of a fluoride phosphate preform showing (a) unetched and (b) etched surfaces.

A variety of both acidic and alkaline solutions were tested, and while some were more optimal than others, an efficient solution could not be identified. The etch rate in all cases was not sufficient to remove the necessary amount of material from the preform surface in a practical time period, even when etching at elevated temperatures. As a result of this study, fluoride phosphate glass was concluded to be resistive to usefully controllable etching. Etching was therefore deemed inappropriate for preparation of high-quality preforms in favour of mechanical polishing, discussed in the next Section 4.3.4

4.3.4 Mechanical Polishing

After chemical etching was found to be a slow and ineffective method of improving the surface quality of preforms, mechanical polishing was attempted. As the preform should ideally remain as smooth as possible the aim was to remove the surface layer from the preform without increasing the surface roughness.

Based on results obtained from the optical profiler, most defects were in the size range of 10 - 100 nm. Therefore colloidal silica, with an average particle size of 40 nm, was an appropriate choice for polishing, and has been used previously on indium fluoride glasses [122, 123]. Polishing for a short period (5 min) was found to be sufficient to remove many defects from the surface, but the fibre drawn from this briefly-polished preform was still found to be of poor quality. It was eventually determined that the

entire surface layer had an effect on the final quality of optical fibres.

Based on observations of the neck-down region of the preform remains, which contained significant corrugations, and considering the EDX results shown in Section 4.3.1, it was obvious the slightly different composition of this surface layer affects the fibre drawing process. The higher oxygen content causes a slight difference in the thermal properties between the surface and bulk layers of the glass, which causes a fracturing of the surface during the fibre drawing stage, resulting in defects which are drawn down onto the fibre surface. The solution to this problem was simply to remove not just the small defects on the preform surface, but to remove an entire layer from the surface of the preform.

This was achieved by polishing preforms for a longer period of time in order to remove a sufficient amount of material from the surface. To illustrate the process, measurements were taken of the surface using the optical profiler at different stages of the polishing process and can be seen in Figure 4.8. Initially (after 5 mins) the surface roughness is mildly improved by removing small defects introduced from the extrusion stage. When removal of the actual surface layer begins, the surface becomes very rough, followed by a gradual smoothing as this layer is removed entirely. This can be seen in Figure 4.9 where the surface roughness (Sa) is plotted against polishing time. It is interesting to note that the surface roughness before and after polishing is very similar; apart from clusters of defects, the surface of the as-extruded preforms is reasonably smooth, however the composition of this surface layer is different. Following polishing, both these clusters of defects and the compositionally different surface layer are removed to produce a very smooth preform ready for fibre fabrication.

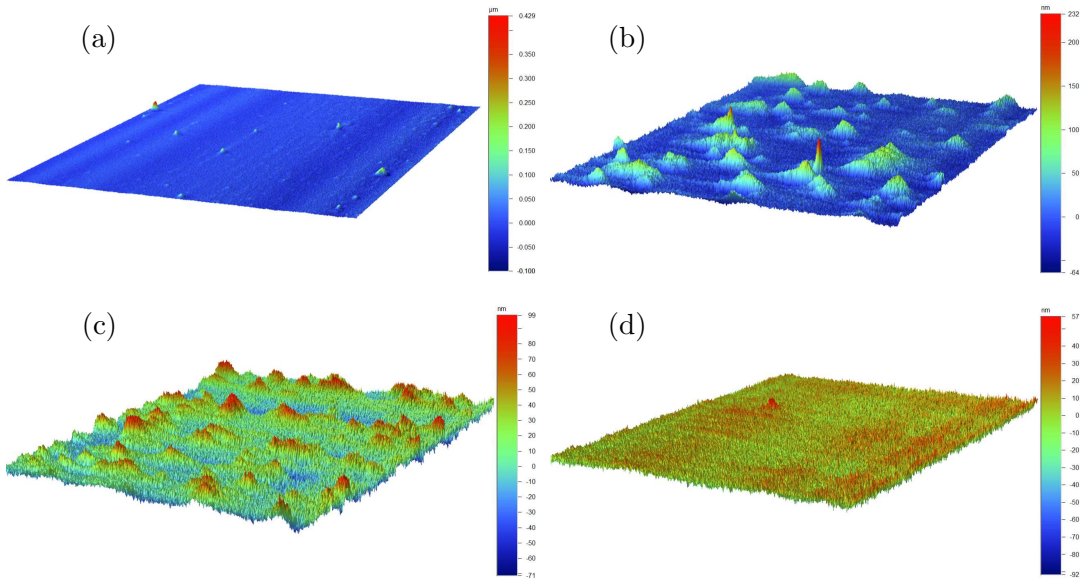

Figure 4.8: Surface of preform throughout the polishing process. Time = (a) 0 min (b) 10 min (c) 30 min (d) 90 min

The quality of optical fibres drawn from preforms with the surface layer removed im-

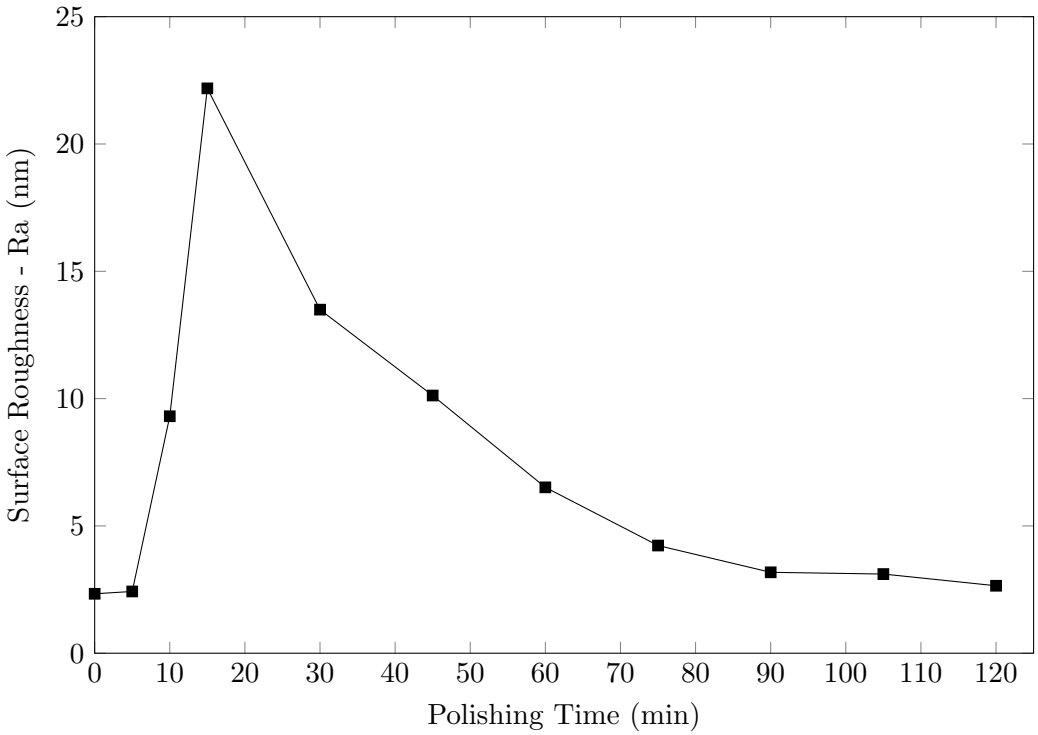

Figure 4.9: Surface roughness with respect to the polishing time of an FP preform surface with colloidal silica. Lines are included only as a guide for the eye.

proved significantly. Fibres had better transmission and were mechanically stronger. The fibre drawing itself was more stable, diameter fluctuation was reduced and draw tension was consistent. Preform remains were also observed following fibre drawing and the neck-down regions discussed in Section 4.4.2 showed significantly less corrugations, as is shown in Figure 4.10. This resulted in fewer defects being drawn down onto the surface of the optical fibres.

The softening of the glass at the beginning of the fibre draw was also more consistent and controllable using polished preforms. On unprocessed preforms, the preform would require a long heating period, followed by an abrupt drop. On polished preforms, the temperature could be reduced, softening occurred more quickly and the drop was slow and smooth. This is consistent with a compositionally different outer layer which requires a higher temperature to soften. The inside bulk glass is softened and the preform held in place by this outer layer, once this then softens there is nothing to hold it up and the drop occurs abruptly. With this layer removed, the preform heats more evenly and the drop is therefore slower and smoother, and occurs at a lower temperature.

Following the successful improvement of fibre quality by polishing this surface layer off, the use of Macor® as the extrusion die material was potentially no longer required. As the Macor® only had an influence on the surface quality of the preform, which was then polished off, it therefore had no influence on the final fibre quality. The

possibility of using stainless steel, a cheaper and more readily available die material, for extrusions was once again considered. An extrusion was therefore again performed using stainless steel, and the surface layer polished away using the same method as for previous preforms. The resulting loss of the fibre is compared with a previous fibre fabricated using Macor® in Figure 4.14. The resulting optical fibre was found to have similar loss, indicating extrusions can be performed with stainless steel dies to produce quality preforms so long as the surface layer is subsequently removed.

4.4 Fibre Fabrication

4.4.1 Fibre Characterisation

Characterisation of fibres will be explained first, as it is the metric used to guide fibre fabrication and to compare the results of different fabrication conditions. The main characterisation process applied to all fibres was loss measurement, performed using the cut-back method [77]. Using a broadband white light source, the attenuation of power at each wavelength is measured with an optical spectrum analyser. For the majority of measurements an incandescent bulb was used as a broadband source, however for certain low quality fibres this did not provide sufficient power to achieve a measurement. In these cases, a supercontinuum white light source was used. The supercontinuum source provides higher power than the incandescent bulb, however the output power is not as stable, and hence results are more uncertain. All fibres were measured at wavelengths between 400 - 1600 nm. The initial power was compared with the power after a series of cutbacks, and the loss calculated according to the relation:

$$\alpha(dB/m) = \frac{10.log_{10}(\frac{I_0}{I})}{l} \tag{4.1}$$

Where α is the loss, I_0 is the initial intensity, I is the cutback intensity, and l is the fibre length.

4.4.2 Fibre Drawing

Following fabrication of preforms, they were drawn into optical fibres. A summary of the drawing process is provided in Appendix B.4, as well as a picture of the fibre drawing tower in Figure B.5. As discussed in the introduction, fibres were drawn with a bare structure[3], where the majority of fibre fabricated had an external diameter of 160 µm.

[3]This is a fibre with no structure across its cross-section. It is also refered to as 'unstructured fibre', 'single index fibre' or 'un-clad fibre'.

Following fibre fabrication, optical fibres were measured to determine their transmission quality: this will be discussed in Section 4.4.1. A summary of the parameters used for all the fibre drawing trials is provided in Appendix C.2.

Heating of the glass preform in the draw tower is performed using a radio frequency furnace, where a radio frequency field induces heating in a cylindrical graphite or stainless steel susceptor. Due to the glass containing fluorine, many fibre drawing trials used a graphite susceptor, as any out-gassing of fluorine can corrode the stainless steel susceptors that are used for other glass materials.

Fibre Drawing Speed and Feed Rate Optical fibre quality is primarily dependant on preform quality, as is evident from the results observed before and after preform treatment; however minor improvement in fibre quality was also observed following adjustment to the fibre drawing speed and preform feed rate. The preform feed rate is the speed at which the preform is fed into the hot zone of the susceptor during the fibre drawing process. The fibre draw speed is the speed at which the optical fibre product is drawn down and spooled.

The diameter of an optical fibre is determined by these parameters. As the draw speed increases softened glass is drawn down out of the hot zone more quickly, resulting in less material being drawn into the fibre, this therefore produces a fibre with thinner diameter. Likewise, decreasing the draw speed slows the rate at which glass is removed from the hot zone, resulting in a fibre with a larger diameter.

To produce an optical fibre of a certain diameter, the preform feed rate is therefore set at a constant value and the draw speed adjusted until the specified fibre diameter is achieved. Increasing the feed rate will increase the speed at which material moves into the hot zone and is softened, thus requiring an increase in draw speed in order to maintain the specified fibre diameter.

The preform feed rate, and subsequently the overall fibre drawing speed, was adjusted in several fibre drawing trials; the details of each fibre drawing trial can be found in Appendix C.2. Diameter stability during the drawing process was improved with faster feed rates, however the drawback is the increase in draw tension, which makes fibres more liable to breakage during drawing [124]. It is also possible this is correlated with the decrease in glass temperature which occurs at higher feed rates, which might improve the diameter stability. Faster feed-rates might also affect the neck-down length, the distance over which the 10 mm diameter preform is reduced to a 160 µm fibre.

Temperature Another variable in the fibre drawing process was the drawing temperature. This parameter was highly dependant on the preform quality. For initial trials,

the temperature required to soften the glass to the point where it will drop under it's own weight was higher than the temperature required to continue the fibre drawing process; this temperature difference was generally between 5 - 15 ℃. For example, fibre trial F3 required a temperature of 760 ℃ to achieve a drop, but optimum drawing conditions were achieved when the temperature was decreased to 745 ℃. This was attributed to the surface layer discussed in Section 4.3. When this layer was removed, the drop was found to occur at approximately 750 ℃, and the downwards movement of the drop was considerably slower and more controllable.

Neck-down Surface Corrugation After fibre drawing was complete, the preform remains were inspected. On the neck-down section, the region in which the 10 mm preform reduces down to the fibre diameter, a corrugated pattern on the surface of the glass was observed. This was attributed to the compositional difference of this surface layer compared to the bulk glass, which was discussed in in Section 4.3. Figure 4.10 shows an image of the neck-down region with a corrugated structure, the 3D structure of this region is also shown using an optical profiler in Figure 4.11. This corrugated structure has been observed previously in fluoroaluminate glass fibres [125] and fluoroindate glass fibres [111], and was attributed to crystallisation due to oxygen during fibre drawing [111, 126]. Striations and imperfections on the fibre surface could be attributed to these deformities being drawn down onto the fibre.

This corrugation pattern is most likely formed due to the softening of the bulk glass beneath the surface layer, which is subsequently drawn down into the fibre: the surface layer would therefore become stressed and fracture into the surface structure observed. This might explain the behavior discussed previously, where for untreated preforms a higher temperature was required to achieve a drop, i.e. the surface layer might prevent the drop from occurring until the bulk glass is sufficiently softened to cause the surface layer to break, causing a rapid drop. When removed, there is nothing to prevent the glass from evenly softening, resulting in a smooth, controlled drop.

4.5 Summary of Optical Fibre Quality

In this chapter, the parameters important to fabrication of optical fibres have been discussed. Fibre loss measurements are presented here to demonstrate the effect of the improvements made to the fabrication process. The loss of various fibres made through the duration of this project are shown in Figure 4.12, this figure shows the overall improvement in fibre quality as improvements were made to the fabrication process. Several fibre trials are not shown (F1, F2, F5, F6, F10, F14), either due to poor quality

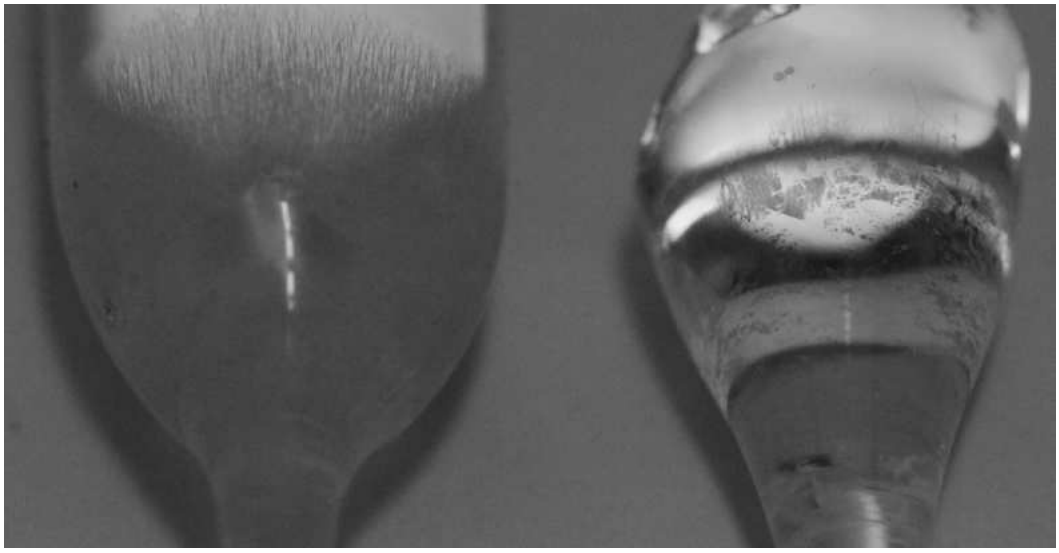

Figure 4.10: Comparison of neckdown region between (a) unpolished and (b) polished preforms. All other fabrication conditions were constant.

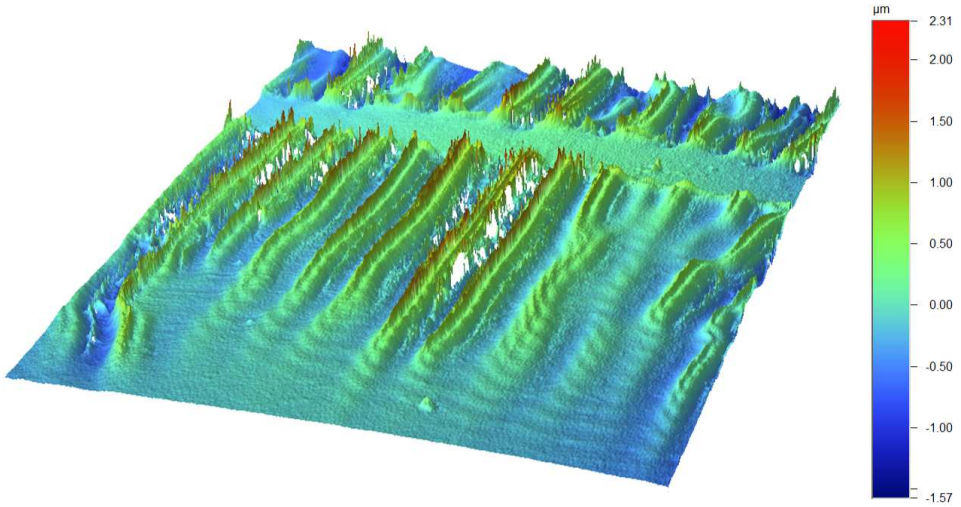

Figure 4.11: Neckdown region of fluoride phosphate fibre preform remains imaged with an optical profiler. The surface layer has been drawn into a corrugated structure. The fibre drawing direction is in line with the corrugations and toward the bottom of the figure.

where a loss measurement was not possible, or due to a pull failure where no optical fibre product was obtained. Data with high uncertainties can also be observed, particularly for the first few trials (F3, F4, F7 and F8), where a supercontinuum laser was used as the broadband light source. As mentioned previously, this laser has more fluctuations in power than the incandescent bulb used for later measurements; this appears as noise in the measured loss. The loss at 550 nm of a selection of fibres is shown in Figure 4.13.

In initial fabrication trials, the extrusion parameters such as speed, force and temperature were the main variables considered, later fabrication trials still have some adjustment in temperature and speed, and also some variables are adjusted during the fibre drawing process. The final fabrication trials all use similar extrusion conditions, improvements are instead made to the preforms prior to fibre drawing, in the form of polishing. In Figure 4.14 the effect of polishing preforms to remove the surface layer can be observed. Removal of the surface layer allowed use of stainless steel as an extrusion die material, a cheaper, more efficient alternative to the Macor® previously used.

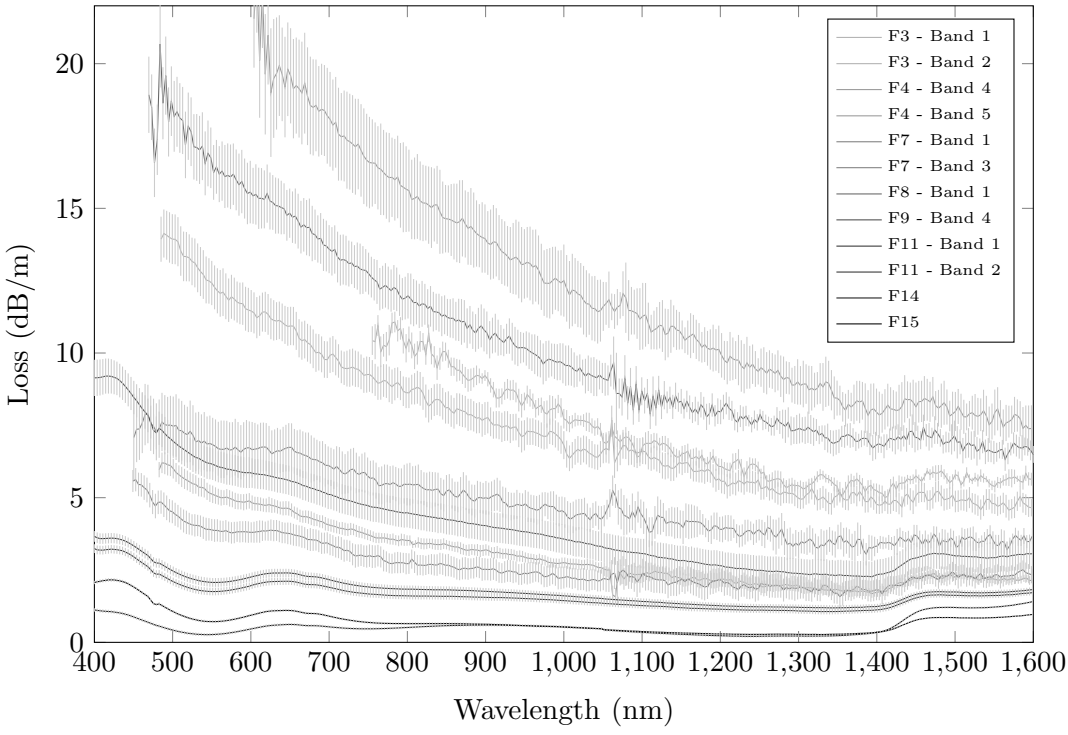

Figure 4.12: Loss in undoped fluoride phosphate optical fibres.

4.6 Doped Fluoride Phosphate Optical Fibres

Following studies of the spectroscopic and luminescent properties of doped fluoride phosphate glasses, optical fibres were fabricated from Tb^{3+}-doped FP1 glass using the improvements in optical fibre fabrication methods presented in this chapter. Tb^{3+}-

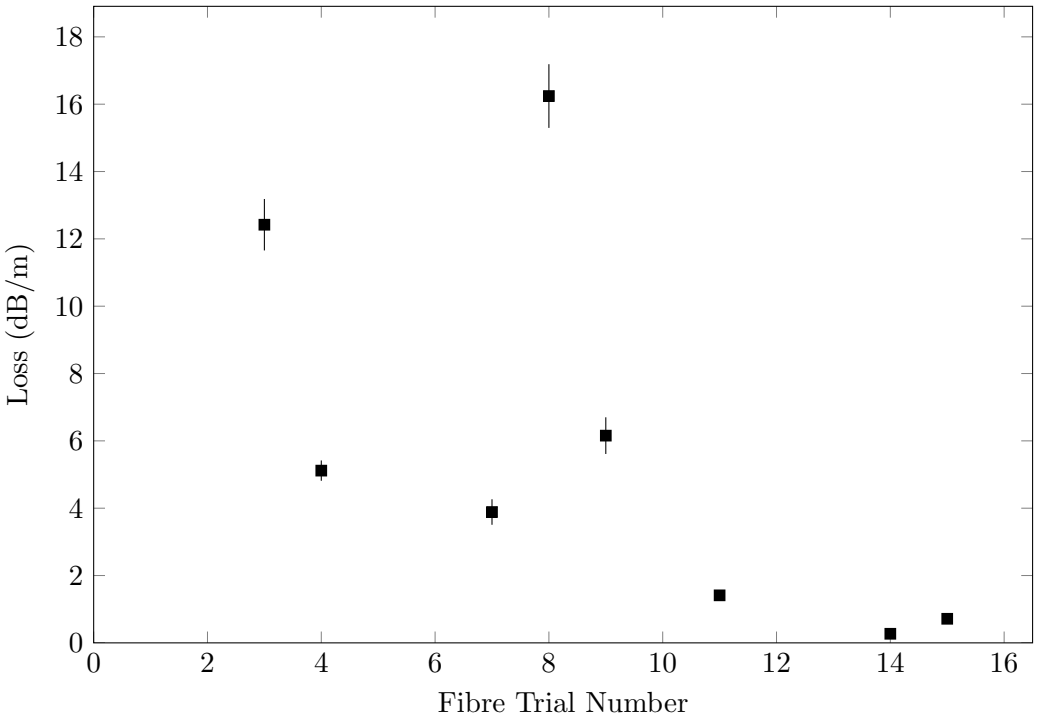

Figure 4.13: Loss of selected undoped FP1 optical fibres at 550 nm. Polishing of fibre preforms was commenced for fibre trial F11. Due to high loss or fibre pull failure, not every fibre trial result can be shown. In two cases (F12 and F13)) preforms were drawn down into canes, not fibres, hence no loss result is shown.

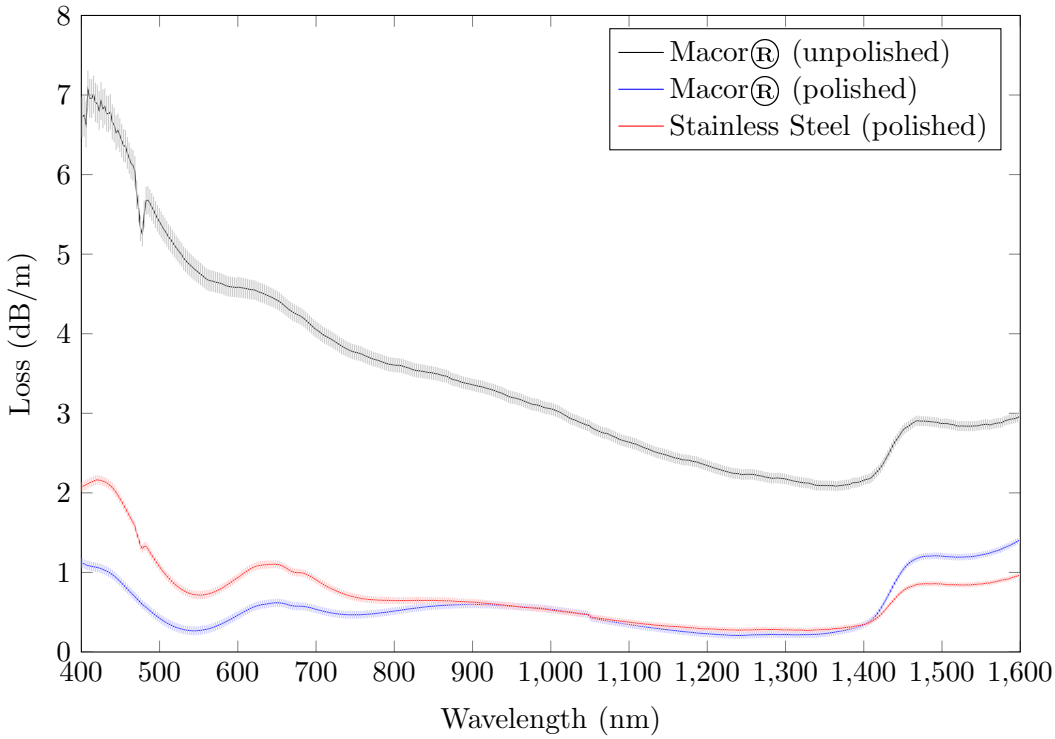

Figure 4.14: Loss of fluoride phosphate optical fibres fabricated from polished preforms extruded through Macor® and stainless steel.

doped FP1 billets were fabricated using the method outlined in Section 3.2.2. To produce optical fibre preforms, a minimum of 100 ml (370 g) of glass is required, hence the doping was done in larger volumes than used previously. Two glasses were fabricated (samples TBRM2a and TBRM3a) in order to obtain a variety of fibre and 'cane' diameters, one glass billet was used for cane drawing, and the other used for fibre drawing. Both glasses were fabricated under reducing conditions in a vitreous carbon crucible, with a concentration of 7200 ppmwt (10×10^{19} ions/cm^3), the same concentration as was used for experiments shown in Chapter 3. The doped glasses were cast into brass moulds of 30 mm diameter to produce two billets, which were then polished ready for the extrusion step; billets can be seen in Figure 4.15. Using the method described in Section 4.2, the billets were fabricated into bare preforms and prepared for fibre and cane drawing. One of the doped preforms was drawn down into canes with diameters of 400, 600, 800 and 1000 µm, the second preform was drawn into fibres with diameters of 160, 200 and 250 µm.

Loss measurements were performed on doped glasses using the method described in Section 4.4.1, the results are shown in Figure 4.16. The transmission quality of the Tb^{3+}-doped fibre (F19) is poorer than the best quality undoped fibre (F15) by approximately 9 dB/m at 550 nm, the main emission peak of Tb^{3+} in FP glass. The absorption measurements shown in Section 3.3.3 show no significant absorption at this wavelength, so the poor transmission quality of the fibres cannot be attributed to absorption by the dopant ions. A possible explanation is the formation of crystalline defects on the surface or in the bulk of the material, caused by the introduction of terbium ions. It is also possible the extra oxygen content introduced by the Tb_4O_7 has an effect on crystal formation, however this is unlikely to be the case as the samples were fabricated in an oxygen-free, reducing environment, which would reduce the oxygen content.

To test whether introduction of Tb^{3+} into the glass contributed significantly to the poor loss, another fibre was produced with an order of magnitude lower concentration of Tb^{3+} ions. If introduction of terbium was causing the high loss, then this second fibre would be expected to have a lower loss. Fabrication of another doped fibre was attempted with a Tb^{3+} concentration an order of magnitude lower, at 720 ppmwt (1×10^{19} ions/cm^3). The methods for glass melting, polishing, extrusion, preform preparation and fibre drawing were identical to those described previously for the initial doped glass fibre. During polishing of the glass billet, several bubbles and black impurities were again observed. Bubbles were probably introduced into the glass during casting of the 30 mm billet from the crucible. Following fibre drawing, loss measurements show this fibre (F18) has poorer transmission than the preceding fibre, despite the lower concentration, seen in Figure 4.16.

Another variable which could increase the loss is carbon impurities introduced into the glass from the vitreous carbon crucible in which the glasses were melted, small particles of carbon can come off the crucible interior and act as scattering centres in the final glass material. Fibres were inspected under a microscope and many small impurities were observed, examples are shown in Figure 4.17. Black crystalline defects might be due to incomplete homogenisation of the dopant compound, Tb_4O_7, or crystal growth around un-dissolved crystals of Tb_4O_7, but it is also likely they are due to these carbon impurities introduced from the crucible.

Following this result, another fibre was therefore drawn using Tb^{3+}-doped glass fabricated in a platinum crucible in ambient conditions, in order to avoid introduction of carbon into the glass. This glass was prepared using the same method outlined in Section 3.2.1, using a Tb^{3+} concentration of 7200 ppmwt (10×10^{19} ions/cm^3). Extrusion, polishing and fibre drawing steps were all identical to the previous fibre fabrication trials. This fibre (F19) shows significant improvement, with a loss at 550 nm approximately 3 dB/m higher when compared to undoped glass, and approximately 8 dB/m lower when compared to the previous Tb^{3+}-doped fibres. This result indicates carbon impurities are likely to be the cause of high loss in glasses melted in vitreous carbon crucibles, however the addition of Tb^{3+} when using a platinum crucible still causes a small increase in loss. One further test which could be explored is to remelt a glass without the addition of dopants; it could be the remelting process, even when using a platinum crucible and not a vitreous carbon crucible, is introducing impurities into the glass which effect the fibre loss.

An interesting observation to note was the slight increase in the softening and melting temperature of the Tb^{3+}-doped glasses, recorded during the extrusion and fibre drawing steps. For extrusion, an increase of 5 ℃ from 525 - 530 ℃ was required, and during fibre drawing an increase of 50 ℃ from 765 - 800 ℃ was required for the fibre drop and subsequent draw. This is attributed to the addition of Tb_4O_7 slightly changing the thermal properties of the FP glass.

4.7 Fibre Jacketing

For real-world applications, optical fibres require jacketing to protect them both from physical damage and inadvertent ambient optical stimulation. All fibres drawn for experimental purposes did not have jacketing, therefore simulations were performed to predict the behavior of energy deposition if a coating were to be applied to the fibres.

Using PENELOPE, a 160 µm thick slab of FP glass was constructed with a layer of PVC plastic directly adjacent, between the glass and the particle source. PVC was chosen

Figure 4.15: Tb^{3+}-doped FP glass billet, polished in preparation for extrusion. Tb^{3+}-concentration is 7200 ppmwt, billet mass is 102.6 g.

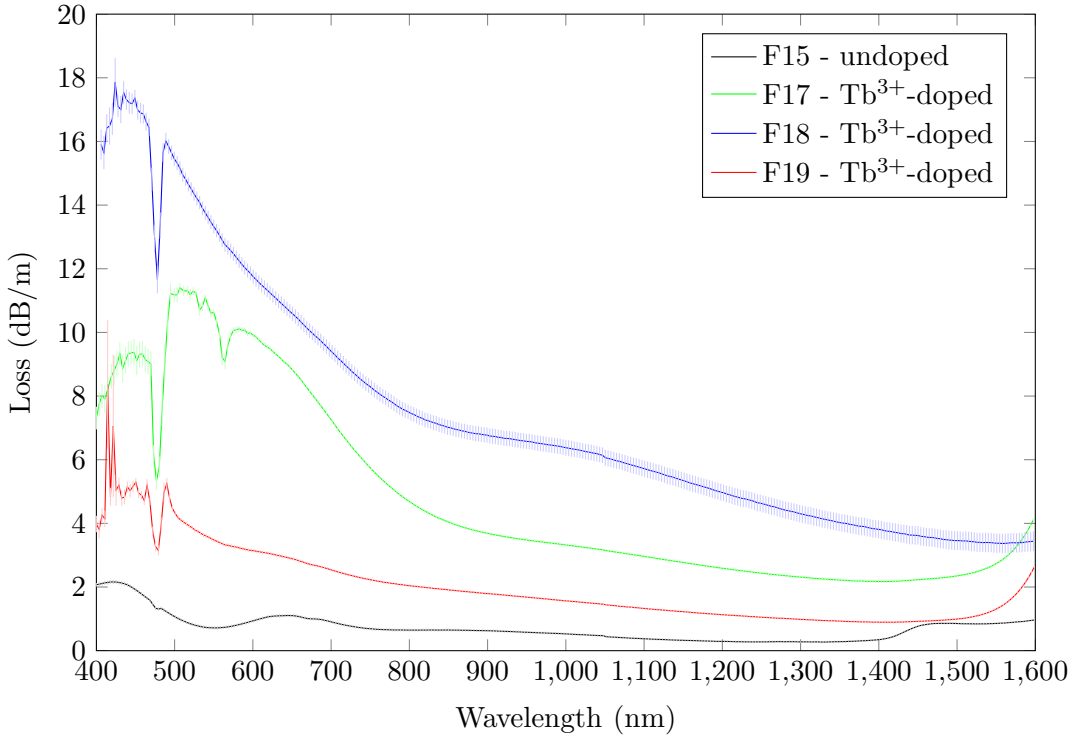

Figure 4.16: Comparison of loss in undoped and Tb^{3+}-doped fluoride phosphate optical fibres. Optical fibres were fabricated from glasses melted in both oxidising and reducing atmospheric conditions. F15: Undoped, F17: Tb^{3+}-doped 7200 ppmwt reducing atmosphere, F18: Tb^{3+}-doped 720 ppmwt reducing atmosphere, F19: Tb^{3+}-doped 7200 ppmwt oxidising atmosphere

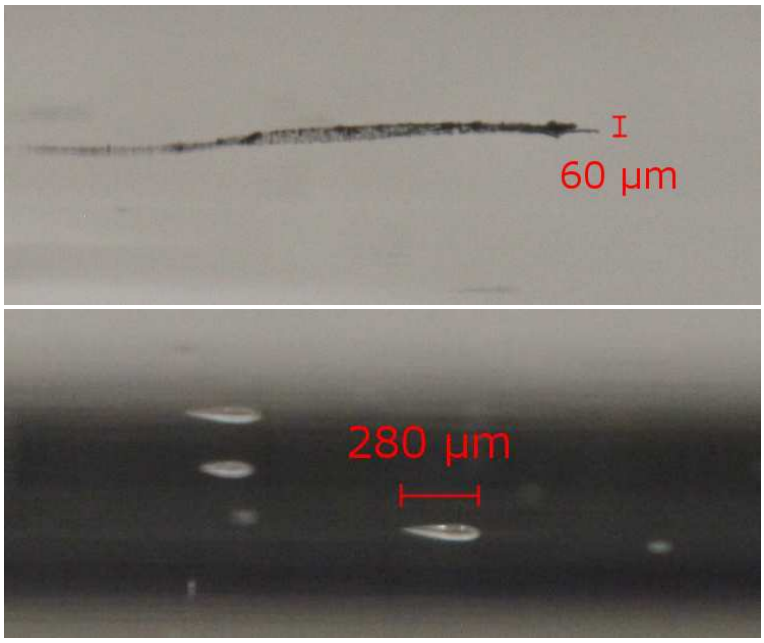

Figure 4.17: Crystalline and bubble defects in Tb^{3+}-doped FP preform (E17). Several lines of black crystalline defects were observed to reach lengths of approximately 5 - 10 mm.

as it is sometimes used as part of the jacketing on optical fibres; simulations could also be performed using a UV-curable acrylate polymer, which is also used for fibre coating, but the composition of this material would need to be studied first. Therefore, for these simulations PVC acts as an analogue for other plastic jacketing materials. Simulations were run for varying thicknesses of the PVC layer to demonstrate how the energy deposition within the FP glass layer is affected, using both photons and electrons with an energy of 2.28 MeV. The results are shown in Figure 4.18.

As can be expected from observing the energy-deposition profiles shown in Section 2.7.4, the energy deposited into the FP glass layer increases as the PVC layer thickness increases. This is due to the dose pile-up as the primary particles interact with the material in the PVC layer, creating secondary electrons which then go on to deposit their energy in the glass layer. As can be expected, this effect is much more pronounced for beta particles than for photons, which at 2.28 MeV travel through the thin 160 µm glass layer without significant interaction or energy deposition.

These results indicate jacketing of optical fibres will not be detrimental to their radiation-detecting function, and in fact might help to increase the sensitivity by facilitating secondary-electron pile-up and increasing the total energy absorbed by the optical fibre.

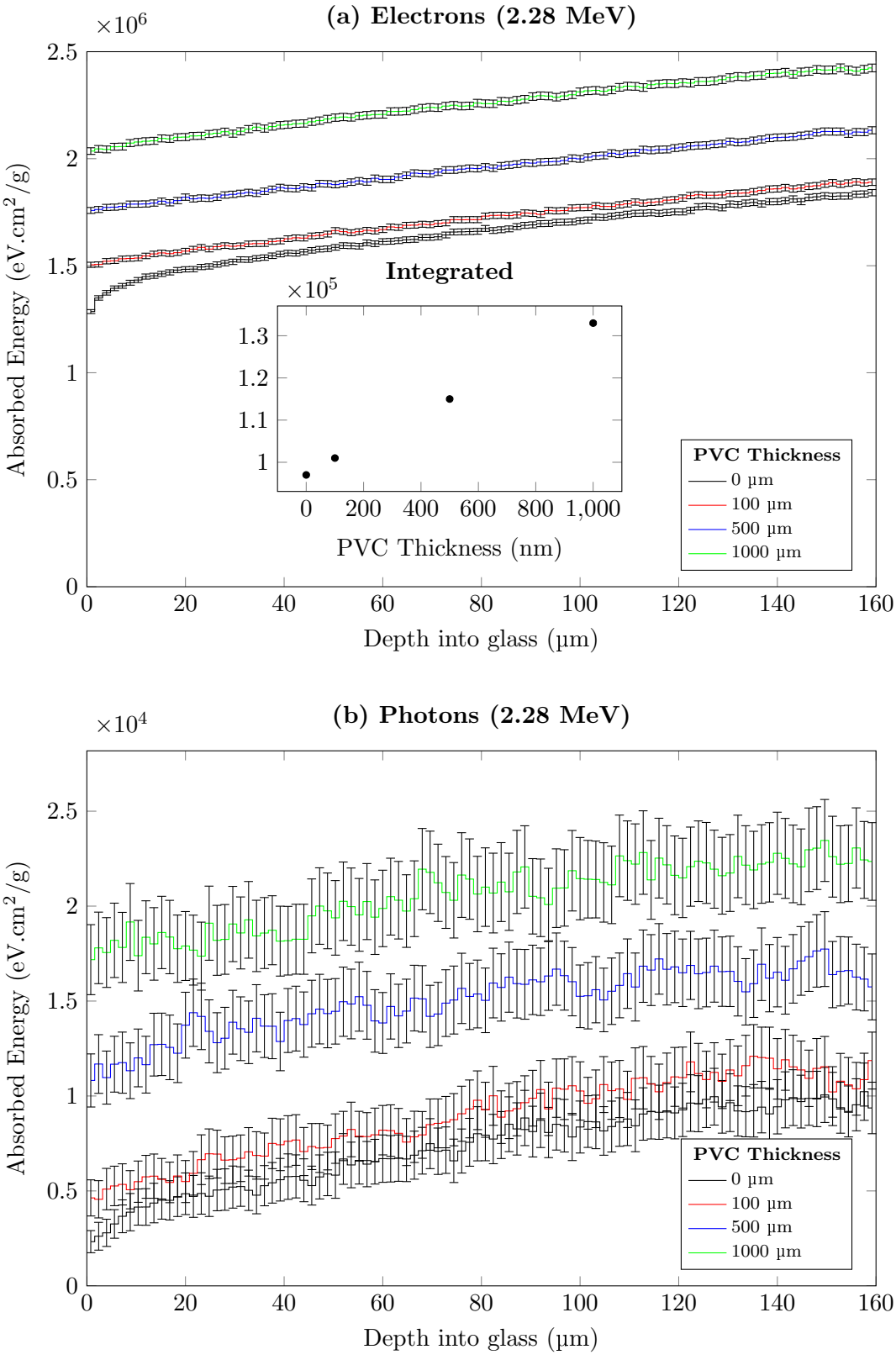

Figure 4.18: Absorbed energy comparison of (a) 2.28 MeV beta particles and (b) 2.28 MeV photons within a 160 µm thick slab of FP glass with PVC layers of varying thickness.

4.8 Summary

Initially, fabrication of fluoride phosphate glass into optical fibres produced very poor results; fibres had high loss and were fragile and the loss was from 5 - 20 dB/m. Improvements made to the extrusion, preform treatment and fibre drawing steps eventually allowed the fabrication of higher quality fibres, with low loss from 0.5 - 1 dBm and better mechanical strength. In addition, building upon the work of Chapter 3, Tb^{3+}-doped FP fibres were fabricated, the quality of which were improved upon to produce doped fibres with reasonably low loss at 2 - 4 dB/m. These fibres, both doped and undoped, were then used in the radiation sensing experiments which will be described in the next chapter.

Chapter 5

Detection of Optically Stimulated Luminescence in Optical Fibres

Previous chapters demonstrated the luminescence properties of fluoride phosphate glass and how it could be fabricated into optical fibres. This chapter describes taking these optical fibres and using them in radiation-sensing experiments. The development of an experimental testbed for fibre measurements is described and dosimetry measurements are performed using a variety of different detector, wavelength and irradiation regimes.

5.1 Dose Deposition and Radiation Considerations

5.1.1 Radiation Safety

For safety purposes, shielding of people and equipment from the radiation sources was carefully considered. Depending on the type of experiment performed, different arrangements of shielding materials were constructed. The main points considered for radiation shielding will briefly be described here.

When using $^{90}Sr/^{90}Y$ sources bremsstrahlung is produced, as has been previously described in Section 1.4, where the energy of the bremsstrahlung radiation is related to the mean atomic number, Z, of the material. For low Z materials such as aluminium, low energy X-rays are produced, which are easily absorbed by lead sheeting. For high Z materials such as lead, higher energy X-rays are produced, which require more extensive shielding to completely block.

Considering this, radiation shielding for each experiment was designed such that beta particles would first interact with low Z materials (FP glass and aluminium) to create a shower of low energy X-rays. These X-rays were then absorbed by lead sheeting placed around the perimeter of each experiment. For each new experimental configuration, the shielding was tested with a hand-held radiation meter to ensure no leakage of radiation. The areas in which a person would stand in order to operate the experiment were double-checked from various angles both above and below the table-top and confirmed in all cases to be less than 5 µSv/hr.

The aluminium fibre holder designed to keep fibres neatly held in place serves both as part of the radiation shielding described above, but also as a means to increase the dose absorbed by the glass, as will be explained in the following Section 5.1.2.

For experiments performed using the X-ray source, radiation shielding did not need to be erected for personal safety, as all people are removed from the irradiation room before exposure. The nature of the X-ray beam, however, posed a risk to equipment. When working with a $^{90}Sr/^{90}Y$ beta source, the radiation field is confined to a small area using lead shielding. As previously mentioned, for X-ray experiments ionising radiation is incident as a broad cone on the experimental setup and consequently irradiation of test-bed components was unavoidable. As a precaution to minimise exposure, components such as the laser sources and SPAD were therefore positioned on the optical table outside the primary X-ray beam to avoid any potential damage. Further to this, components were protected with lead sheeting of sufficient thickness to attenuate 300 keV X-rays. The background signal measured by the SPAD during irradiation was monitored. No change in the signal was observed, allowing us to assume that these pre-

cautions were sufficient to ensure the X-ray irradiation is not affecting the behaviour of the SPAD.

5.1.2 Dose Deposition Profiles

The dose deposition profile of ionising radiation into fluoride phosphate glass was shown in Section 2.7 for photons and electrons at various energies. The experiments presented in this chapter primarily use the 2.28 MeV beta particles produced by $^{90}Sr/^{90}Y$ beta sources to irradiate glass fibres with diameters in the range of 160 – 1000 µm. As can be seen from earlier results (Figure 2.18), electrons with an energy of 2.28 MeV deposit a large proportion of their energy at depths greater than 1000 µm.

In addition to this the $^{90}Sr/^{90}Y$ beta sources emit isotropically and only a small fraction of the total number of particles will be directly incident upon the thin fibres and canes. As such, a large proportion of dose to the glass will be due to secondary electrons and bremsstrahlung generated within the aluminium fibre holder. This can be seen in the simulation results shown in Figure 5.1, where the dose depositions from an electron beam incident on thin wafers of FP glass (160 µm and 1 mm thick) were simulated with and without a layer (3 cm) of aluminium behind the glass, simulations were performed using PENELOPE. For both 160 µm and 1 mm glass simulations, the absorbed dose is higher when a layer of aluminium is present. This can be attributed to secondary electrons and bremsstrahlung radiation produced within the aluminium and radiated in the backwards direction into the glass. As can be intuitively expected, there is a greater contribution of dose from the side of the glass directly next to the aluminium layer. If we integrate the total dose absorbed in the glass, we find for the 160 µm thick layer a 17.5 % increase with the aluminium backing. For the 1 mm thick glass layer, this same value is 9.6 %.

The simulations shown here consider the layer of aluminium behind the glass, which to a certain extent describes the physical case of a fibre laying on an aluminium holder. In actual experiments, the fibre is laying within a groove in the aluminium plate, and on each side the aluminium is directly exposed to the $^{90}Sr/^{90}Y$ beta source without any glass in between. We can therefore assume the actual physical fraction of dose deposited to the glass due to secondary electron and bremsstrahlung radiation in the aluminium holder is higher than is suggested by the simulations.

5.1.3 Calculation of Dose Deposition in Fibres

The dose absorbed by optical fibres in the experimental setup used for OSL measurements was approximated by using the Risø Reader, which is calibrated to give a known

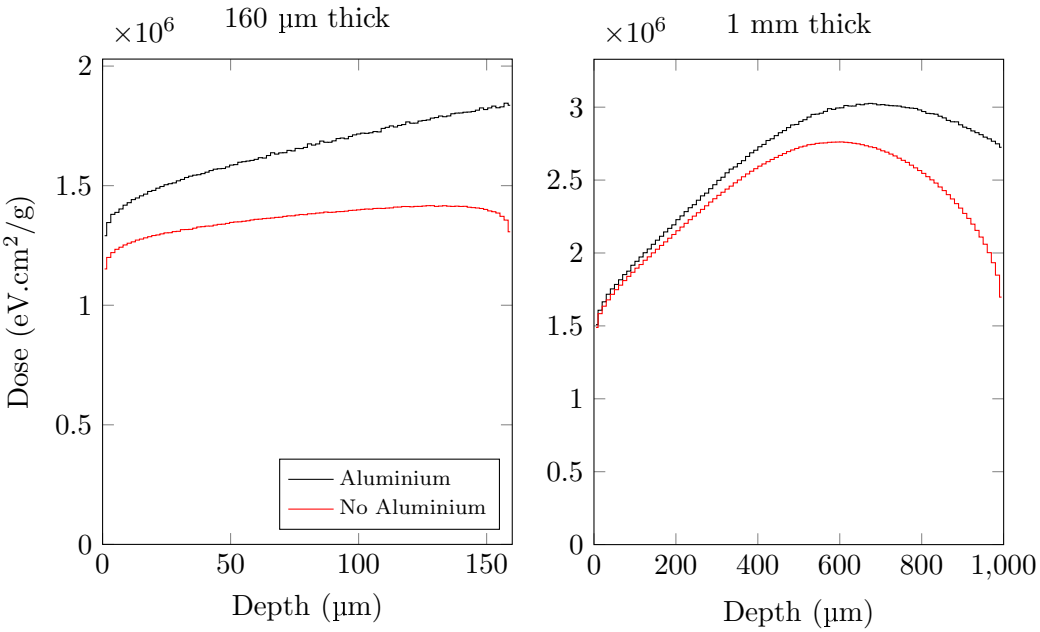

Figure 5.1: Dose comparison in a 160 µm thick slab of FP glass with and without an aluminium backing.

dosage in Gy/s to 200 µm grains of quartz from the ^{90}Sr/^{90}Y beta source mounted on the instrument. Since the optical fibres are in the 160 – 200 µm diameter range, this calibration can be used to approximate the dose absorbed by the fibres in the experimental setup. To do this, the TL light sum from a sample irradiated in the experimental setup is compared with a calibration curve from the same sample irradiated at varying dosages in the Risø Reader. This process requires several steps:

Irradiation in experimental setup A 7.5 mm length of Tb^{3+}-doped FP1 optical fibre was placed in the fibre holder of the experimental setup, this was the longest length capable of fitting in a sample holder in the Risø Reader. The fibre was irradiated using the 'β40' ^{90}Sr/^{90}Y beta source for 10 seconds under darkroom conditions, then taken out of the fibre holder and placed in a light-tight sample holder. The sample was then placed in the Risø Reader and the TL measured to 350 ℃ at a heating rate of 1 K/s after a pre-heat to 100 ℃ to remove any signal from the 60 ℃ peak. The 240 ℃ TL peak was then integrated, the intensity of this peak was $1.46 \pm 0.04 \times 10^5$ counts.

Establishing a calibration curve This same fibre sample was then thermally bleached by heating again to 350 ℃ to ensure there were no residual dose from trapped electrons. The sample was then irradiated for 1 second using the ^{90}Sr/^{90}Y beta source mounted in the Risø Reader, after which the TL was measured to 350 ℃ at a heating rate of 1 K/s after a pre-heat to 100 ℃, exactly the same as was done to the sample following irradiation in the experimental setup. Following this TL measurement, the sample was again heated to ensure no trapped charge

remains. This same procedure was then repeated for irradiation periods of 2, 5, 10, 15, 20 and 30 seconds. The intensity of the 240 ℃ TL peak was integrated for each measurement and plotted, a fit is applied in order to obtain the calibration curve, shown in Figure 5.2.

The result from irradiation in the experiment setup ($1.46 \pm 0.04 \times 10^5$ counts) was then compared to the calibration curve to establish the equivalence between the dose rate in the Risø Reader and the experimental setup: a 10 second irradiation on the experimental setup was found to be equivalent to an 11.6 second irradiation in the Risø Reader, a ratio of 1:1.16.

Mass stopping power correction Since the dose rate in the Risø reader is calibrated for quartz (SiO_2) and the fibres are made from FP glass, a correction factor based on the mass stopping powers of each material needed to be applied. The composition of FP1 glass was previously determined with the use of an electron microprobe, shown in Section 2.3.1, the composition along with the mass stopping power and molecular weight of each element is shown in Table 5.1. The total mass stopping power of the material was calculated according to Equation (5.1) [127], where $\left(\frac{\delta E}{\delta x}\right)_T$ represents the total stopping power, n the atomic percentage of the element, N, in the material, Mn the molecular weight of element and $\left(\frac{\delta E}{\delta x}\right)$ the stopping power of the element. The stopping power calculated for FP1 glass was therefore $\left(\frac{\delta E}{\delta x}\right)_T = 1.5173$ MeV.cm^2/g, for silicon dioxide the stopping power is 1.6 MeV.cm^2/g, giving a ratio between the two of 1.0545. The dose rate to SiO_2 in the Risø Reader was 0.111 ± 0.004 Gy/s, applying this stopping power correction factor the dose rate to FP1 glass was 0.105 ± 0.004 Gy/s.

Table 5.1: Composition of FP1 glass, the molecular weight and stopping power of each element is listed along with the atomic percentage of the element in the material.

Element	**Atomic Percent (At %)**	**Molecular Weight (g/mol)**	**Stopping Power (MeV.cm^2/g)**
O	22.6	16.00	1.72
F	42.9	19.00	1.604
Na	0.1	22.99	1.563
Mg	2.4	24.31	1.592
Al	10.7	26.98	1.535
P	5.6	30.97	1.539
Ca	6.0	40.08	1.603
Sr	5.5	87.62	1.383
Ba	4.2	137.33	1.32

$$\left(\frac{\delta E}{\delta x}\right)_T = \frac{\sum_A^N nMn \left(\frac{\delta E}{\delta x}\right)_N}{\sum_A^N nMn} \tag{5.1}$$

Calculation of the experimental dose rate Using the dose deposition ratio between the experimental setup and the Risø Reader, and applying the mass stopping power correction, the dose deposited to an optical fibre in the fibre holder of the experimental setup was therefore calculated to be 0.122 ± 0.004 Gy/s.

This same method of calculating dose rate was initially attempted using undoped FP1 glass, but as the only TL peak in undoped FP1 glass is at 60 ℃, this was considered unreliable, due to the lifetime of electrons of these shallow traps, which are more likely to be thermally stimulated out at ambient temperature, causing rapid loss of luminescence after irradiation. Due to the time delay between irradiating the sample in the experimental setup and measuring the TL in the Risø Reader, a non-negligible amount of fading would have occured. After fibres were fabricated using Tb^{3+}-doped FP1 glass, this dose calibration process was repeated using the significantly more stable 240 ℃ peak in the Tb^{3+}-doped glass.

Some experiments presented later in this chapter use glass 'canes', with diameters up to 1 mm, and not fibres. This dose calibration method, while a reasonable approximation for 160 – 200 µm diameter fibres, cannot be reasonably approximated to the 1 mm diameter of these glass canes due to the difference in geometry and the difference in the dose deposition profile this causes. As such, for experiments using glass canes, the exposure time of irradiation, and not the dose, is used to report results.

5.2 Detectors, Optical Stimulation and Filters

Previous chapters have mentioned the detection wavebands, optical stimulation wavelengths and filters used for OSl measurements, and provided results for each of these regimes. This Section will summarise the process by which the detector type, optical stimulation and filters were chosen for OSL measurements with optical fibres.

5.2.1 Detection with a PMT

Initial experiments with a PMT detector used a 15 mW 532 nm diode pumped laser as the stimulation light source. Of the available light sources for fibre experiments, this was the most suitable due to its power and wavelength being reasonably close matches to the 470 nm stimulation used in the Risø Reader. In later experiments a 473 nm laser

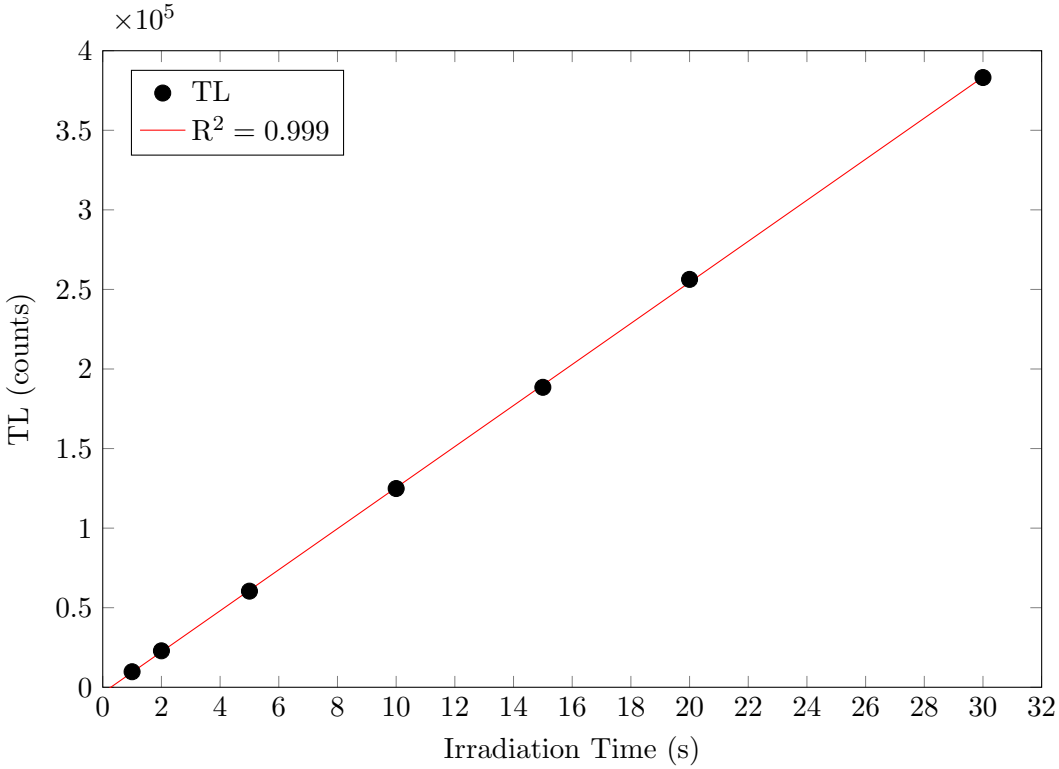

Figure 5.2: TL Calibration curve of dose delivered to a 7.5 mm Tb^{3+}-doped FP1 fibre section.

became available, however 532 nm remained the most suitable wavelength due to the filter options available. To assist in the input coupling of the stimulation laser into the fibre, and to separate the luminescence signal from the optical stimulation, a dichroic mirror with an edge at 505 nm was used; the spectrum can be seen in Figure 5.3. This enables reflection of the 532 nm stimulation light into the beam path at a 90° angle, and transmission of the luminescence signal centered at 400 nm.

When stimulating with 473 nm, a HOYA U340 filter is the most appropriate for isolation of luminescence, however this transmits in the window shown by Figure 5.4, which is slightly off-band of the luminescence emission from the undoped FP1 glass. In contrast, scattered stimulation photons at 532 nm can be efficiently blocked by a Corning 7-59 or a Schott BG3 filter, the transmission window of which is closer to the luminescence emission of the glass. For many experiments Corning 7-59 filters were used; however, in later experiments Schott BG3 filters with interference coatings designed to reject the stimulation laser wavelengths were used. The transmission spectra of both filters are similar, as is shown by Figure 5.4. When using Corning 7-59 filters, a stack of filters with a total thickness of 8 mm was required for adequate blocking of the scattered stimulation photons at 532 nm, however when using a coated BG3 only one 3 mm thick filter was required for adequate attenuation. For each experiment in this chapter using a PMT the filter(s) will be noted: several experiments use the Corning 7-59, while others use a Schott BG3. In each case they essentially serve the same purpose and the only difference is a slightly better detection efficiency when using a Schott BG3.

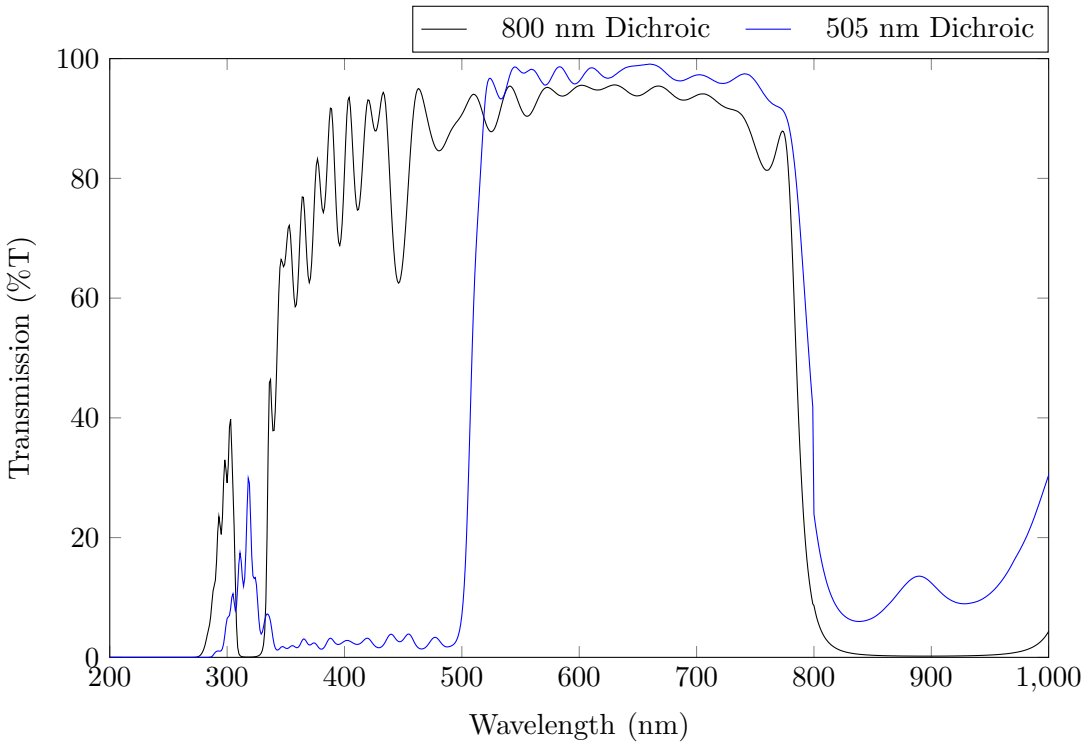

Figure 5.3: Transmission spectra of dichroic filters used for isolation of the luminescence signal from the optical stimulation. Note that for the 800 nm dichroic, the stimulation laser is reflected and the luminescence signal is transmitted through to the detector; for the 505 nm dichroic, the stimulation laser is transmitted and the luminescence signal is reflected toward the detector.

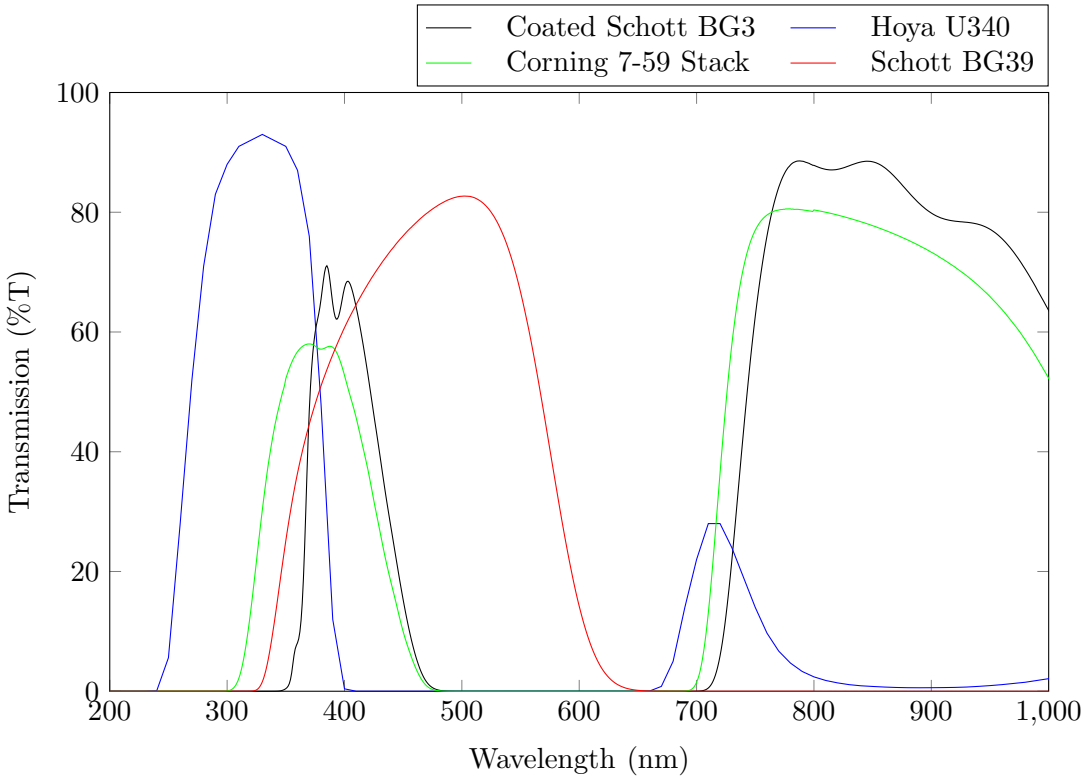

Figure 5.4: Transmission spectra of individual coloured glass filters used in the Risø Reader and for OSL tests on the experimental test-bed. The Schott BG3 filter is 3 mm thick, the Hoya U340 is 7.5 mm thick, the Corning 7-59 is a stack of 3 mm and 4 mm filters totalling 7 mm in thickness, the necessary thickness to adequately suppress scattered photons at 532 nm. For suppression of scattered photons at 852 nm, a BG39 filter 3mm thick is sufficient.

5.2.2 Detection with a SPAD

Experiments were also performed using a SPAD for detection of luminescence. The quantum efficiency of the SPAD is equal to that of the bialkali PMT at blue-violet wavelengths, but it is also able to detect out to 1000 nm, with a peak efficiency at 550–600 nm. This is a critical advantage if the luminescence emission falls in the 550 to 1000 nm region, which is effectively off-band and undetectable with a PMT.

Luminescence in the 350 - 450 nm region

Performing experiments in the 350 - 450 nm waveband is possible with the SPAD using a 532 nm laser for optical stimulation, however the sensitivity of this detector up to 1000 nm requires the use of extra filters. As is seen in Figure 5.4 the Corning 7-59 and Schott BG3 filters have a pass band window in the near IR starting at 750 nm. When using a PMT detector this is not a problem, as they are not sensitive beyond 650 nm. SPAD detectors, due to their sensitivity out to 1100 nm, are affected by this IR transmission window. As a result, when using only a Schott BG3 filter with a SPAD very high background counts are detected, this also becomes a safely issue for the SPAD detector, which can be damaged by over-exposure of photons.

Determination of the spectra of the light penetrating through to the detector was performed by measuring the system with an optical spectrum analyser (OSA). An experiment was set up similar to that used for detection of OSL, however no radiation source was used, and the OSA was placed in the position of the SPAD. A variety of stimulation sources and filter combinations were then tested to determine the source of the scattered light, and which combination of filters might be best to attenuate this while still efficiently transmitting the luminescence wavelengths.

Each individual laser was first tested without any glass or filters, this was done to determine any emission harmonics, and the line-width of emission. The results are shown in Figure 5.5, where it is apparent each laser does not emit only at the specified wavelength. For example the 532 nm laser has the expected emission at 1064 nm and the 852 nm laser has a significant shoulder of approximately 25 nm either side of the main emission peak.

Several combinations of filters were then tested to determine the most appropriate combination to attenuate scattered photons. To attenuate photons in the 700 - 1200 nm region, a short pass interference filter with a cut-off at 700 nm was tested with the Schott BG3 filter. The transmission of the interference filter is shown in Figure 5.6, and the transmission of the composite stack is shown in Figure 5.7. As is shown by each of these figures, windows at 920 and 1000 nm still exist through which optical

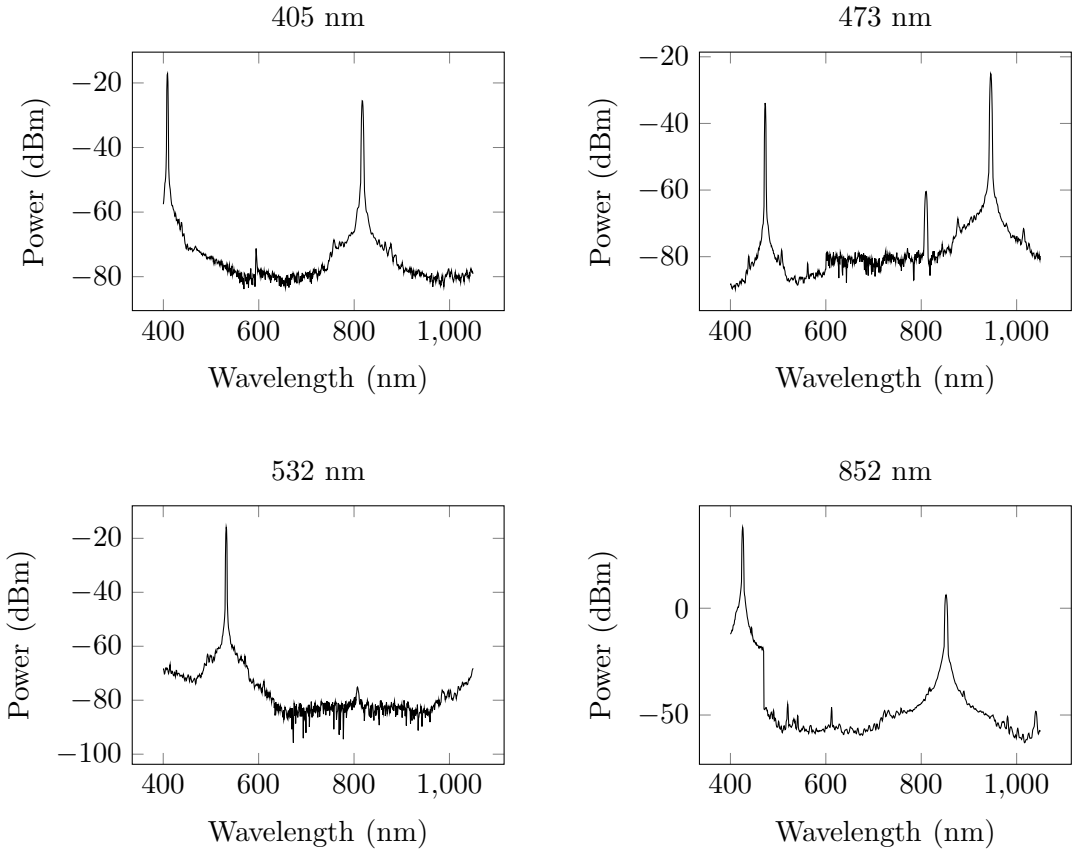

Figure 5.5: Output spectra of the lasers used for OSL measurements in optical fibres.

noise can penetrate to the detector. Another short-pass interference filter, with an edge at 800 nm (shown in Figure 5.6), was added to the filter stack in an attempt to attenuate wavelengths above 800 nm. The transmission of the composite stack is shown in Figure 5.7, and only a small window at 710 nm is present. A small window also exists at 1040 nm, however as is shown in Figure 5.7, this window is in a region of low quantum efficiency even for the SPAD. When this composite filter was tested with the 532 nm laser and SPAD, significant background counts were still measured, indicating the small window centred at 710 nm still transmitted an unacceptable level of scattered photons.

The Schott BG39 filter transmission spectrum, shown in Figure 5.6, has strong attenuation at wavelengths longer than 700 nm and was therefore tried in combination with a Schott BG3 to attenuate wavelengths longer than 700 nm. The transmission of this composite filter is shown in Figure 5.7. Although the BG39 attenuates part of the desired transmission window of the Corning 7-59 filter, it is very effective in suppressing the 700-1200 nm window. When experiments were performed with the SPAD at 532 nm, there was negligible background noise detected: complete blocking of the scattered 532 nm photons was achieved, with a transmission window centred at 400 nm having a peak transmission of 40%.

Although the composite filter, comprised of the BG3 and short pass interference filters, provided a larger transmission window at around 400 nm, it was insufficient to attenuate the background noise of scattered stimulation photons. It was concluded that the composite filter comprised of the BG3 and BG39 filters was the most appropriate choice, despite the smaller transmission window around 400 nm, due to its ability to completely suppress the stimulation wavelength, and was therefore the most suitable filter combination for attenuation of stimulation wavelengths in the 500 - 700 nm region and transmission of emissions in the 400 nm region. The dichroic mirror used to assist input of the optical stimulation at 532 nm is the same 505 nm dichroic filter used previously.

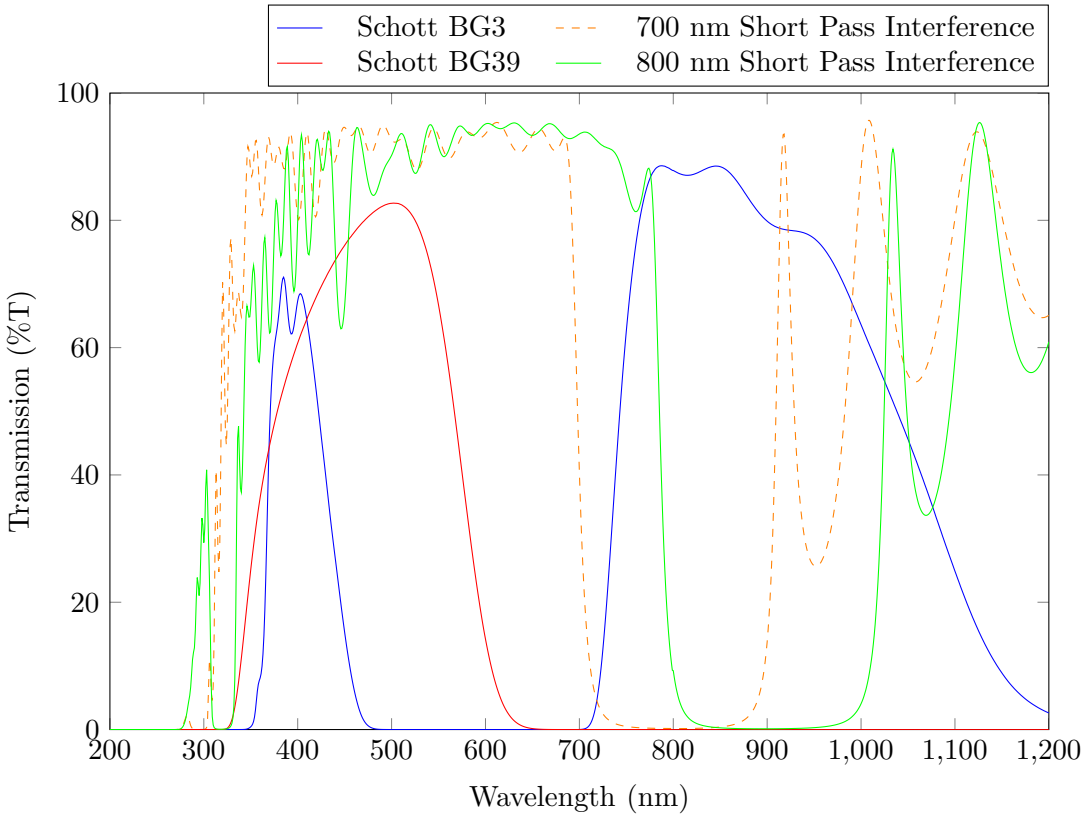

Figure 5.6: Transmission spectra of the individual coloured glass (3 mm thick) and interference filters used for OSL measurements.

5.2.3 Luminescence in the 350 - 600 nm region

To take advantage of the wide wavelength range over which the SPAD is sensitive, experiments were also performed using the 350 - 600 nm waveband. This use of the 350 - 600 nm region was also a significant factor in the decision to introduce Tb^{3+} ions into the FP1 glass, due to the intense emission peaks in this waveband. A suitable laser and filter combination was found to be a 100 mW, 852 nm diode-pumped laser in conjunction with a 3 mm Schott BG39 band-pass filter. While band pass filters exist in

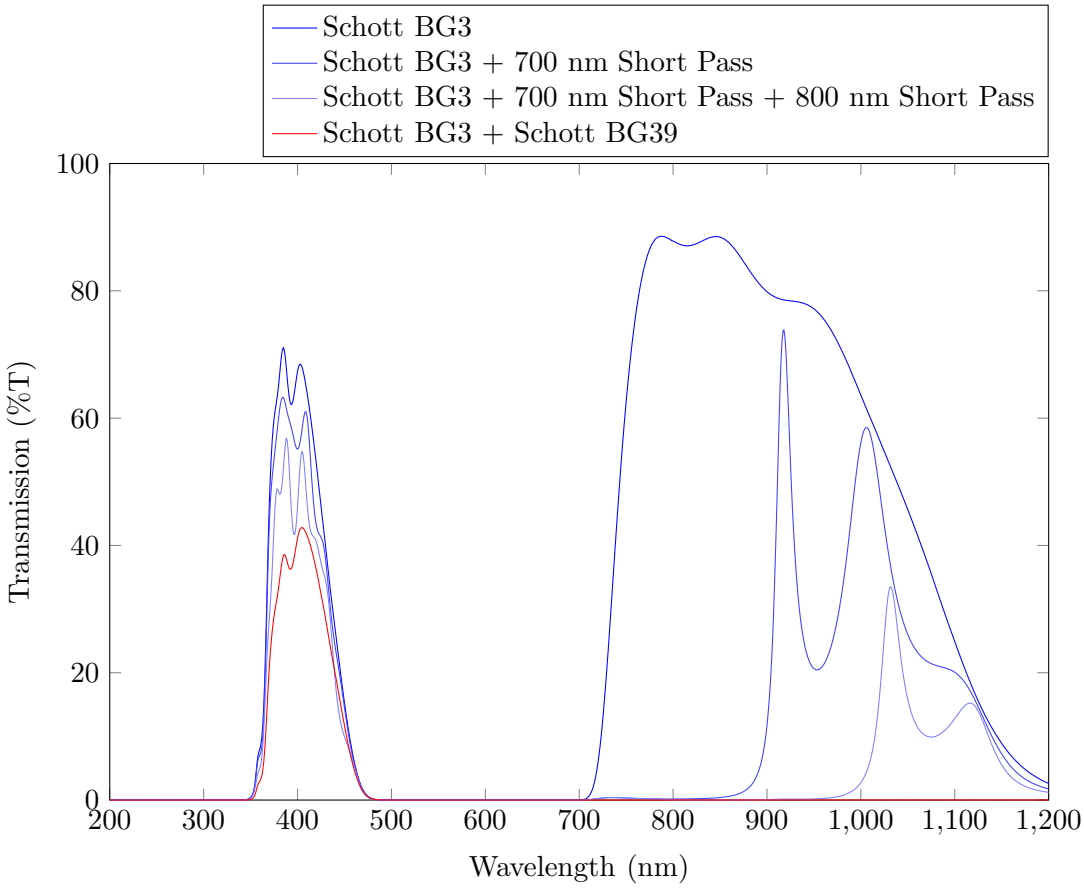

Figure 5.7: Suppression of the 700 - 1100 nm transmission window with composite filters. Composite filters are constructed by stacking a BG39 filter with 700 and 800 nm short pass interference filters, and also separately with a Schott BG39 filter. The Schott BG3 and BG39 filters are both 3 mm thick.

this waveband with wider transmission windows, and would better take advantage of the detection waveband of the SPAD, their suppression in the IR is not sufficient to block scattered photons from the stimulation laser. The Schott BG39 is therefore a suitable choice due to its reasonable transmission window from 350 – 600 nm and its efficient attenuation of 852 nm photons. This difference in transmission is 6 orders of magnitude for a 3.8 mm thick filter. An alternative is to use a lower-intensity optical stimulation, perhaps allowing the use of other filters; however due to the lower untrapping efficiency of photons at 852 nm, a reasonably intense optical stimulation is desired. A similar stimulation wavelength and filter combination is also used in the Risø Reader, where a Schott BG39 filter is used in conjunction with 870 nm LEDs, allowing predictions to be made between the behavior of glasses analysed in the Risø Reader and fibres tested using the SPAD. A dichroic mirror with an edge at 800 nm was used to input the optical stimulation into the beam path, and transmit the luminescence signal, the spectrum can be seen in Figure 5.3.

5.3 Development of an Experimental Test-Bed

In Chapter 2 the OSL properties of fluoride phosphate glass were established. Next, a method of detecting OSL from optical fibres needed to be established in order to perform radiation sensing experiments and provide proof-of-concept demonstration. Using bulk samples it was possible to perform a variety of OSL measurements on various glasses; in comparison, detecting OSL in optical fibres has several challenges which will be addressed in this Section.

Initial attempts to measure OSL in optical fibres were performed during the first fluoride phosphate optical fibre trials discussed in Chapter 4. As can be seen from Figure 4.12, the loss of these optical fibres is high and this resulted in difficulties when trying to measure an OSL signal from the fibres. Part of this Section therefore deals with the methods used to obtain a measurable signal. Later experiments were able to utilise optical fibres of better quality, following work done concurrently on improving the fabrication process. These later experiments benefited both from improvements in fibre quality, and improvements in the method used to measure OSL in the fibres.

This Section will provide details on the methods used to improve the signal-to-noise ratio in order to detect an OSL signal. Several example results will be provided to demonstrate the effect of several parameters, and later Sections will then provide OSL results taken using the experimental testbed which will be described here.

5.3.1 Differences Between Bulk and Fibre Measurements

Most experiments with bulk glass were performed using the Risø Reader, but this apparatus cannot accommodate lengths of optical fibres. A list detailing the main differences between the two systems is provided here:

Optical coupling The Risø Reader was used for most bulk measurements, and it is designed to efficiently collect light from a sample presented as a 7 mm diameter circular target and direct this onto the photomultiplier tube. For fibres, only photons captured by the guided modes of the fibre are transmitted to the detector.

Housing The Risø Reader is completely light-tight, whereas fibre experiments are exposed to ambient light and require light-tight housing customised for each experiment. The long length of fibres can make this awkward.

Stimulation geometry The Risø Reader illumination is delivered from circular LED modules which illuminate the sample from all sides. For optical fibres, they can either be excited from the sides, or by coupling light into the fibre. Stimulation from the sides is undesirable due to the complexity of setting up a diode array along the length of the fibre, and for fibres that might potentially be jacketed or in a light tight environment. Stimulation by coupling into the fibre is more efficient and would be the method required if using a jacketed fibre in a real-world application.

Collected fraction Luminescence is emitted in 4π. In the Risø Reader, the collection angle off the face of the sample is approximately 0.4 steradians, refer to Appendix B.1. In a fibre, it is the fraction coupled into the guided modes of the fibre. If collection is only possible at one end of the fibre, it will be half this value.

Fragility For sample presentation in the Risø Reader, small grains are stuck to a steel disc using silicon oil, resulting in a relatively robust sample which is easy to handle. Optical fibres made from fluoride phosphate glass can be fragile and susceptible to fracture if handled improperly.

Irradiated mass On a Risø Reader sample disc, approximately 12-14 mg of glass can be used. The irradiated mass of a 160 µm optical fibre is approximately 0.75 mg when irradiating with a $^{90}Sr/^{90}Y$ beta source (approximately 6.25% of that used in the Risø Reader). For X-ray experiments, the irradiated mass is approximately 65 mg (approximately 540% of that used in the Risø Reader).

Source shielding The $^{90}Sr/^{90}Y$ beta source in the Risø Reader is fully shielded and pneumatically operated. For fibre experiments, the $^{90}Sr/^{90}Y$ is not completely shielded and must be operated by hand. When using the X-ray source, irradiation

is operated remotely, but the room is inaccessible during irradiation.

Light sources The Risø Reader has two diode modules, enabling optical stimulation only at 470 and 870 nm. Laser sources at 405, 473, 532, 640 and 852 nm are available for optical fibre experiments, with the option of using other light sources as required.

Due to the differences described above, performing fibre measurements was not as simple as using the same light sources and filters, and substituting a fibre for the bulk glass. The following sections will describe how the various issues were overcome in order to perform OSL measurements in optical fibres.

5.3.2 Signal Detection and Integration

The experiments presented in this chapter used both PMTs and SPADs for detection of the luminescence, in each case the signal output by the detector is a TTL pulse, meaning the same data collection system could be used with each detector. The detector (PMT or SPAD) was connected to an Ortec Photon Counting Card. Initially bin times of 10 and 100 ms were used, however after initial measurements, all OSL results reported in this thesis used bin times of 1 ms. Exceptions to this are several of the results taken when improving and optimising the experimental test-bed in Section 5.3.3.

To obtain an OSL measurement first the data collection was started, optical stimulation was then applied to the sample for a several seconds, after which data collection was stopped. Data was collected with a timing of 1 ms per channel. The data was then integrated from the onset of the OSL signal for 0.2 seconds, this value remained consistant for all measurements. A background was then established, while the optical stimulation was still active, by averaging over 1 second following depletion of the OSL signal; this background is then subtracted from the integrated OSL signal.

5.3.3 Improvements in Signal-to-Noise Ratio

As the experimental test-bed was first developed at an early stage in the project most of the work was done using the PMT: the SPAD had not yet been acquired. Demonstrations of the signal-to-noise improvements were all obtained using the 532 nm laser with the Corning 7-59 filter and a bialkali PMT, using the undoped FP1 optical fibres and canes fabricated in earlier trials. Improvements made to the test bed were later re-arranged to accommodate the use of a SPAD.

Increasing Signal Intensity (bundles)

Experiments in the Risø Reader typically used 12 mg of material, whereas the mass of a 160 µm optical fibre section beneath a radiation source with an active face of 78 mm^2 is 0.75 mg. The total luminescence intensity is a function of irradiated mass, and as shown, the irradiated mass in an optical fibre is lower than that used for bulk measurements. This can be overcome by stacking a number of optical fibres into a 'bundle', this will increase the mass of glass beneath the radiation source, and hence increase the measured luminescence light sum.

Measurements were performed using bundles of fibres: lengths of fibre trial F11 were stacked together and then coiled such that both ends of each fibre were sitting adjacent as part of the same bundle. One fibre end was selected from the bundle and coupled to a 405 nm laser, this was done to produce a 'guide' signal within the bundle, which enabled the optics to be focused and aligned at the luminescence signal wavelength. This is shown in Figure 5.8.

The beam diameter of the stimulation laser is <1 mm, while the diameter of the fibre bundle was approximately 4.5 mm radius, therefore a beam expander was used to increase the beam diameter such that each fibre had light incident on it and so coupled into it. During setup of the optical stimulation, the output of the guide fibre was monitored with a power meter, and hence the power in each fibre measured and optimised. During stimulation, each fibre was stimulated by approximately 78 µW. Due to the bundle coiled around on itself at both end faces, the stimulation input and luminescence output occurred along the same optical path, hence a dichroic mirror was used to isolate the luminescence signal from the stimulation light. This dichroic also helped attenuate scattered stimulation photons.

When measurements were performed on these bundles, an OSL response was observed for the first time from FP glass optical fibres, previously no OSL response was measurable. Figure 5.9 shows the OSL intensity increasing with the number of fibres in the bundle, this result demonstrates FP glass fibres can produce an observable OSL response. To determine the minimum number of optical fibres necessary to observe an OSL response, fibres were removed one at a time from the bundle, and OSL measurements performed at each step. The result can be shown in Figure 5.10. Since the fibres could not be completely extracted from the experiment, as this would upset the optical alignment, fibres were culled from the experiment by cutting them at the output end, removing them from the system optically rather than physically. Although the luminescence could not be measured from these culled fibres, they may have still had an impact on the dose profile during irradiation, as inactive fibres on the top of the bundle may affect the dose buildup in fibres below. The alternative, to remove fi-

bres completely, would have altered the optical alignment between each measurement, hence simply culling each fibre from its optical alignment was deemed a less disruptive method and to have a smaller effect on reproducibility of results, and removed the need to re-establish the optical alignment for every measurement.

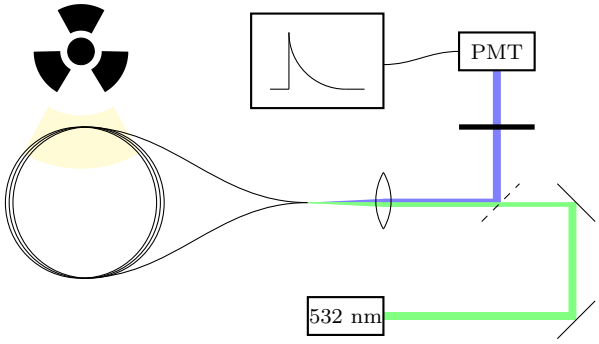

Figure 5.8: Experimental setup for the detection of OSL from a coiled fibre bundle with a PMT, the optical stimulation at 532 nm is shown in green, luminescence is shown in violet.

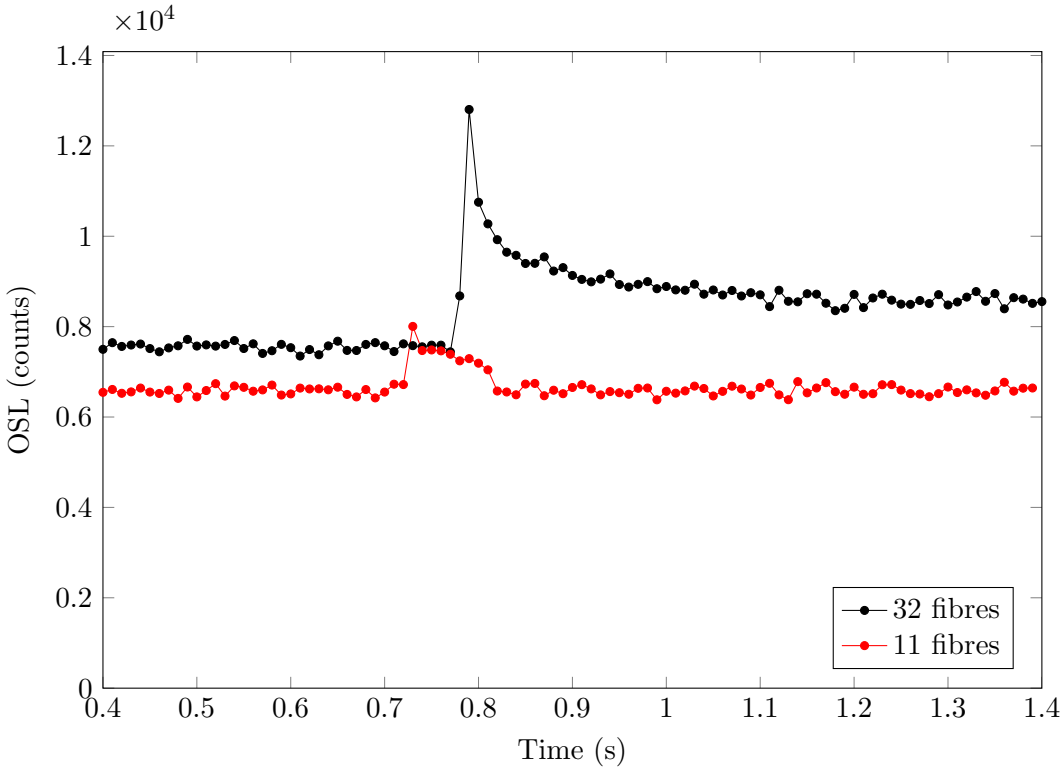

Figure 5.9: OSL response from bundles of 160 µm diameter FP optical fibres, increasing the number of fibres in the bundle increases the OSL intensity. No observable OSL was measured from a single fibre at this stage. The shutter for optical stimulation was operated manually, hence OSL is observed at slightly different times from the onset of data acquisition. Lines are included only to assist in distinguishing the data.

Housing of the Optical Fibre Test Bed

Experiments with free-space optics are open to the environment and are affected by ambient light. When measuring low intensity luminescence with highly sensitive de-

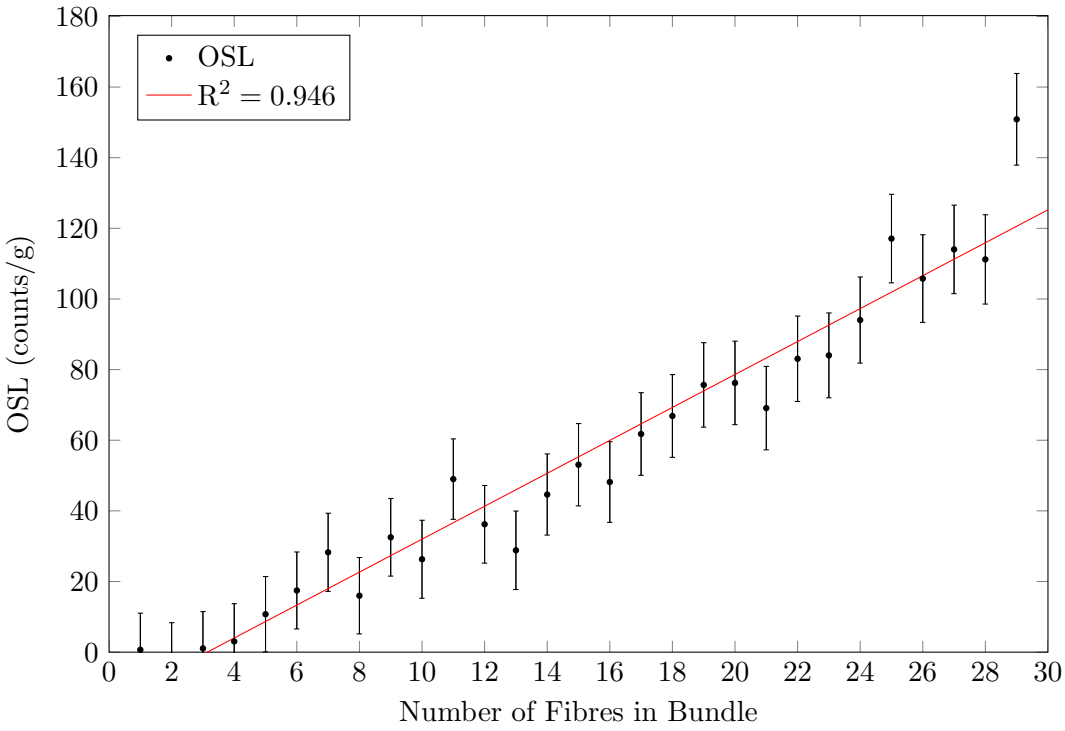

Figure 5.10: OSL signal from a fibre bundle. Each measurement is taken with a different number of total fibres in the bundle.

tectors, this ambient light can be enough to obscure the signal. One method to solve this problem is to put the entire experiment in a light-tight housing, however this is impractical for experimental work, where optical alignments need to be continuously performed and access to the radiation source is necessary while taking measurements. Therefore, it is very helpful to only put the section of the experiment between the fibre output and the detector sensor in a light tight housing. This allows unobstructed interaction with the rest of the experiment during measurements. One problem with this method is the optical fibres are open to stimulation from any ambient light during measurements, potentially releasing trapped charge prematurely during radiation exposure. Therefore the laboratory is operated under blackout conditions during measurements to reduce this unwanted stimulation.

Early experiments were taken using a housing surrounding the detector face of the photomultiplier tube, but were open on one face to allow room for fibres and optics. This reduced the signal-to-noise to a certain extent, but results were still impacted by ambient light. Later experiments utilised custom made blackened aluminium boxes. The detector sensor in these boxes is completely isolated from external light sources and the only light entering is passed through a window over which the filter is placed. Even using this housing, the light levels in the laboratory had to be kept to a minimum, as small amounts of light were still leaking through the housing. Given the low intensity of the OSL, only a small amount of scattered light was enough to obscure the luminescence signal.

Using these methods and taking these precautions, the background counts during experiments could be reduced to almost dark-count levels for each detector (PMT = 35 counts/s, SPAD = 10 counts/s), as is shown in Figure 5.11. This allowed the optimum signal-to-noise levels to be reached.

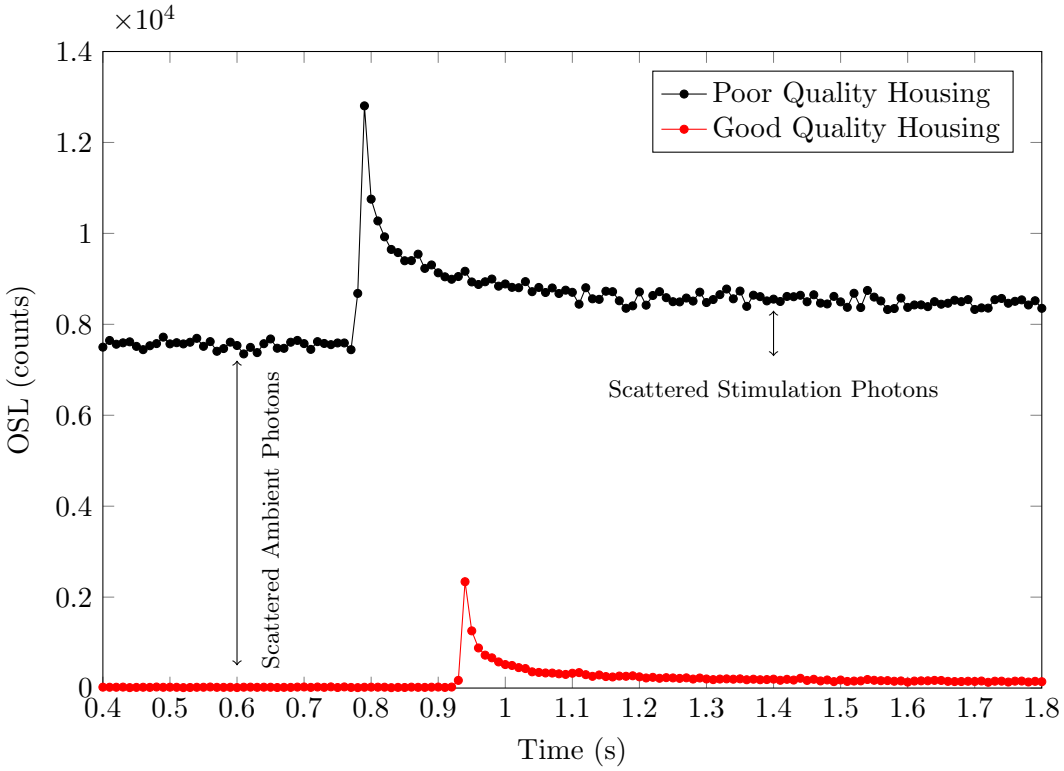

Figure 5.11: Isolation of the detector from scattered photons decreases the background noise; scattered photons are due to both ambient light sources and the laser optical stimulation. In addition, performing experiments in black-out conditions reduces the background further. Data was taken from two different optical fibres, therefore light sums should not be directly compared, the data serves as a demonstration of background counts.

Irradiation Sequence

It is possible to interrogate an optical fibre for an OSL response while it is being irradiated, however due to RL the OSL signal then sits on top of an already increased count rate, making it less distinctive. For all OSL measurements, the irradiation source was therefore removed from the fibre before the OSL measurement. An example of this process is shown using data from measurements taken with a fibre bundle made from trial F11, shown in Figure 5.12, where the initial period has a high intensity due to RL, after which the beta source is removed at 1.6 s and the measured intensity drops to dark-count levels. Stimulation with the laser promptly follows, producing the OSL spike observed at 2.5 s, which quickly decays down to background levels.

The slightly higher back intensity observed from 2.5 to 4 s is due to scattered photons from the stimulation laser, indicating an insufficient filter thickness was used for this

measurement, due to using only one 4 mm Corning 7-59, and not the stack of 2 x 4 mm filters subsequently used.

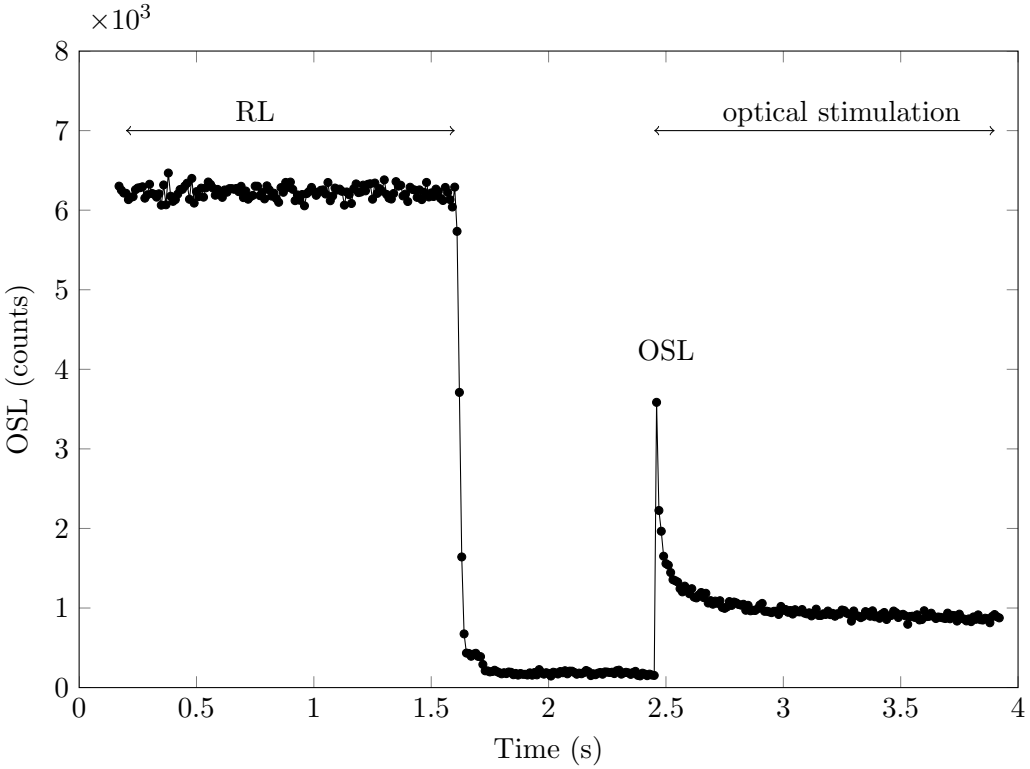

Figure 5.12: RL and OSL signals from a bundle of FP1 optical fibres, each of which are marked on the plot. Irradiation is from a $^{90}Sr/^{90}Y$ beta source, optical stimulation at 532 nm, detection with an EMI 9635 QA PMT using a 4 mm Corning 7-59 filter.

Fibre Holder

For bulk measurements, holding the glass in the Risø Reader is a simple case of attaching approximately 100 – 200 µm sized grains onto a steel disc using silicon oil. When using optical fibres, holding the optical fibres in place is more complex, as they need to be in a holder capable of supporting a shielded radiation source weighing approximately 2 kg. This holder also needs to be of a suitable material for radiation attenuation: aluminium is a perfect candidate due to its low atomic number. Due to this, the beta radiation absorbed will be converted to a shower of soft X-rays, which is easily absorbed by a few millimetres of lead. With this aluminium-lead combination, experiments can be set up quite safely for the user. For simple single fibre and cane measurements, an aluminium block with a v-groove is sufficient. However, in experiments where a fibre coiled several times beneath the radiation source is desired, the holder needs to be more complex. A fibre holder was devised with the design shown in Figure 5.13: it has a depressed track into which the fibre is placed, it can be coiled at several different radii (depending on the fragility of the fibre), and has two output sections where the fibre is then placed into standard commercial optical stages. A cover plate is placed on top, which both

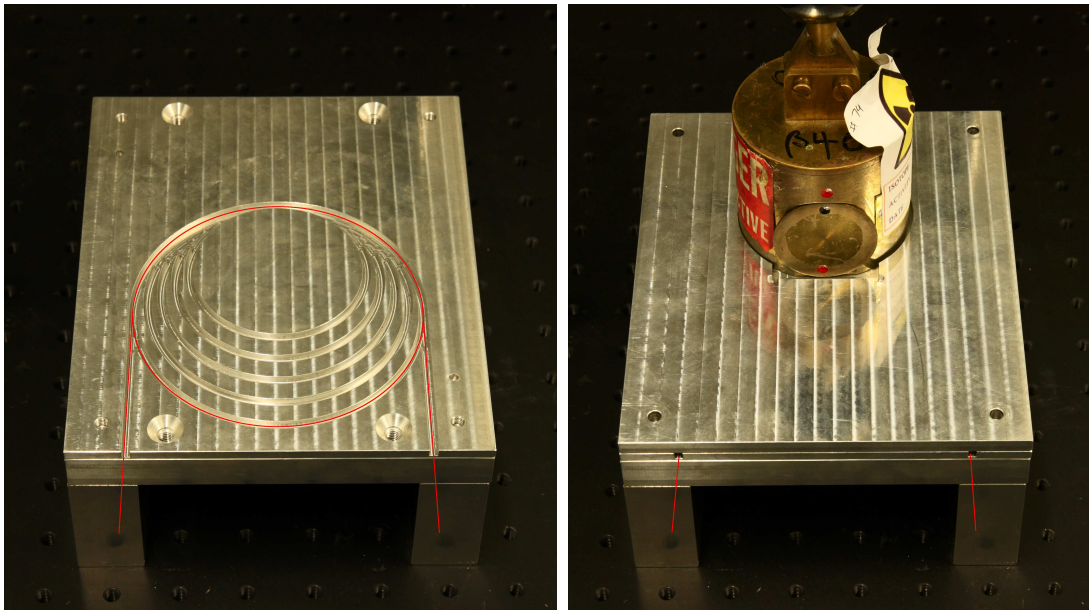

Figure 5.13: Sample holder designed to hold an optical fibre coiled in a near light-tight environment underneath a $^{90}Sr/^{90}Y$ beta source. It is machined from aluminium in order to provide a material with low Z number for conversion of beta particles into low-energy bremsstrahlung emission. Red lines indicate the position of a fibre in the holder without the cover plate (left), and the holder is also shown with its cover plate and the beta source in position (right).

holds the fibres down in the track and creates a light-tight environment to ensure there is no premature optical stimulation of the fibre from the ambient environment. The radiation source is then placed into the lid in the depression shown, directly above the coiled fibre. During experiments using the X-ray source, the entire fibre holder is placed in the X-ray beam. The lid may remain on or off depending on the desired experimental conditions.

Improving Bundle Configuration with 'Canes'

The construction of fibre bundles to increase the signal-to-noise allowed successful measurements of OSL in the glass, but they are impractical in several ways. Mechanically, they are fragile and difficult to construct and the fibre ends are difficult to align in the same plane, making optical coupling inefficient; furthermore, uniform coupling of the optical stimulation into each fibre is not possible. Therefore, to insert a larger mass of glass into the beta irradiation beam, for several experiments optical fibre bundles were replaced by canes fabricated from FP1 glass. These canes were essentially identical to the optical fibres in all ways except diameter: the fibres were drawn to 160 µm in diameter and the canes from 200 to 1100 µm in diameter. The main advantage of performing measurements on the canes is the efficient optical coupling. Using bundles, the end faces of each fibre could not be aligned properly, hence the focal point of each was at a different position, but as is shown in Figure 5.14, this is not a problem when using a cane. However, the flexibility of canes, especially those from 500 – 1100 µm

in diameter, is very low and they cannot be coiled into the fibre holder. Therefore for measurements using canes, a simple length of aluminium plate with a v-groove was attached to a post, providing a robust stand to hold the cane safely beneath the radiation source.

Measurements using canes were performed by coupling the stimulating light into one end of the cane and detecting the luminescence signal from the opposite end, as is shown in Figure 5.15. Initially, the cane diameter was chosen such that its cross sectional volume beneath the radiation source matched that of the sum of the cross sectional volumes of all the fibres in the bundle. As a result, the irradiated mass in each experiment was equivalent. Canes were also fabricated at a variety of diameters in order to determine the OSL response as a function of the cane/fibre dimensions, this will be shown in Section 5.4.3.

The OSL result obtained when using a glass cane (fibre trial F12) is shown in Figure 5.16 compared with a result taken when using a fibre bundle. To compare these results, the data needed to be normalised for the bin time used in each measurement, 100 ms was used for the bundle and 1 ms for the cane.

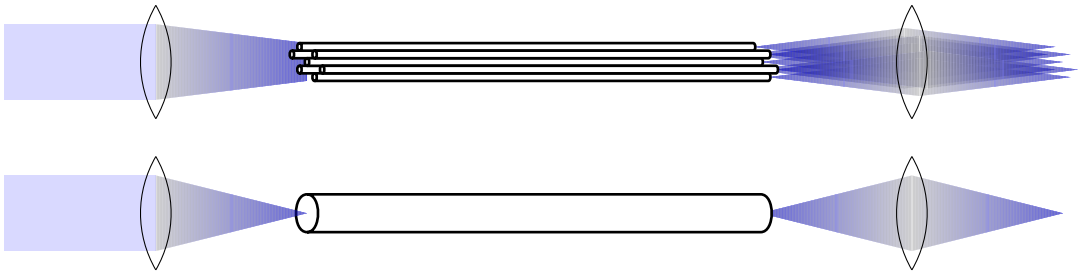

Figure 5.14: Schematic representation of the set-up for a fibre bundle and a cane.

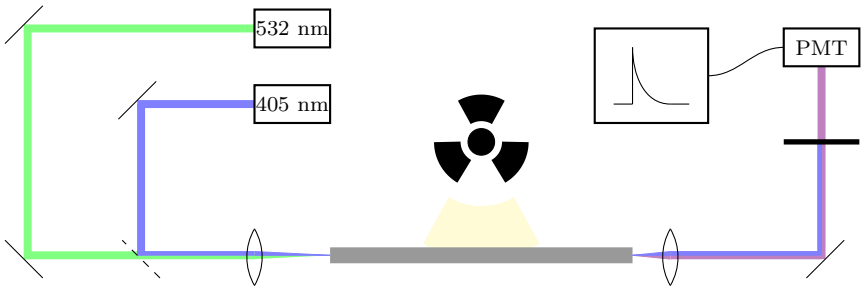

Figure 5.15: Experimental setup for the detection of OSL from glass canes using a PMT. The optical stimulation at 532 nm is shown in green, luminescence is shown in violet, the 405 nm laser used to assist optical alignment is shown in blue.

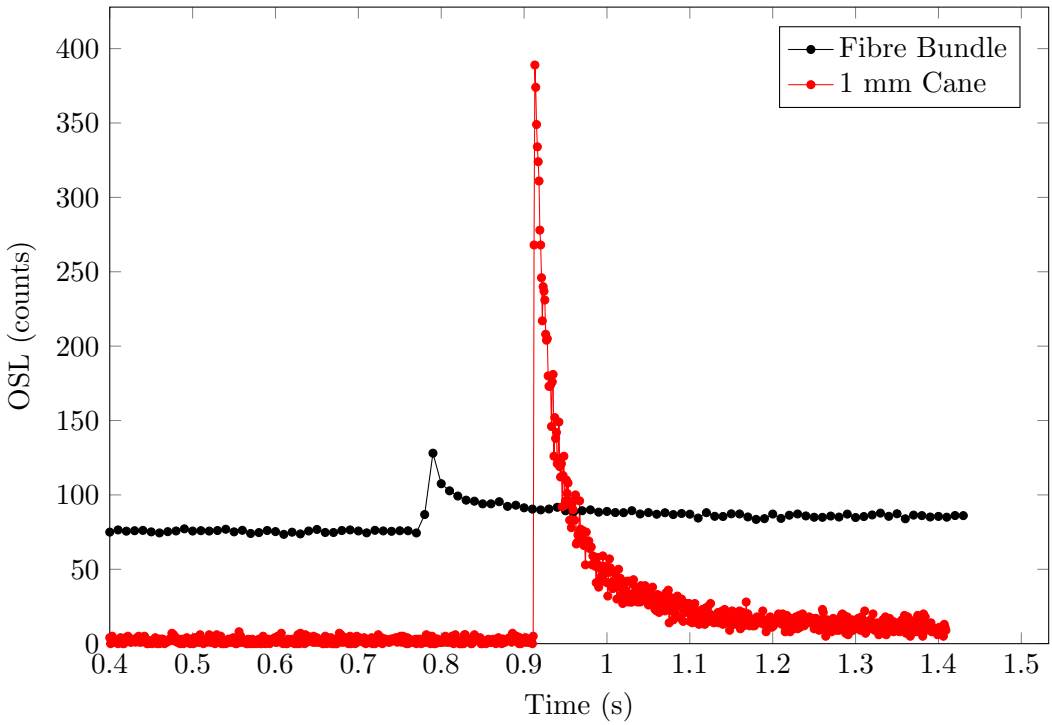

Figure 5.16: OSL response from a 1 mm FP cane compared with a bundle of 32, 160 µm diameter FP fibres. In order to compare the results here, data has been normalised for the bin time of data collection: a 100 ms bin time was used for the bundle, 1 ms was used for the cane.

5.3.4 Optical Alignment

For measurements using a PMT, the output of the fibre could be roughly focused onto the detection surface of the PMT, hence careful alignment was not necessary. Measurements using SPAD detectors required more precise focusing due to the small detector diameter, in this case 50 µm. Some initial experiments using the SPAD were unsuccessful due to inaccurate focusing of the luminescence output onto the small detector area. Due to the low intensity and transient nature of an OSL signal, integration over an extended length of time is not possible, hence collection and focusing of the OSL signal needs to be optimised.

Focusing of the fibre output onto the SPAD was therefore performed before each set of measurements. A laser with an emission wavelength roughly equivalent to the OSL signal wavelength was coupled into the opposite end of the fibre. This guide laser signal is then output from the fibre at the SPAD end, collimated using an Edmund Optics 4x objective, passed through the dichroic mirror and the filter(s) and onto the SPAD detector chip. The laser is of an appropriate wavelength to pass through both the dichroic mirror and the filter. The output objective is on a micrometer stage to allow positioning of the beam in x and y coordinates to align it with the SPAD detector. Following this, the beam is finally focused down onto the detector face using an Edmund Optics 10x objective placed on another micrometer stage between the filter

and the SPAD.

The guide laser is attenuated by many orders of magnitude with neutral density filters, then the detector powered on. Due to the sensitivity of SPAD devices, a signal intensity above approximately 10^6 counts/s can damage the detector, hence the requirement to attenuate the laser signal. The optics are then given a final adjustment by observing the count rate detected by the SPAD while optimising the position of the 10x input objective. This setup is shown in Figure 5.17

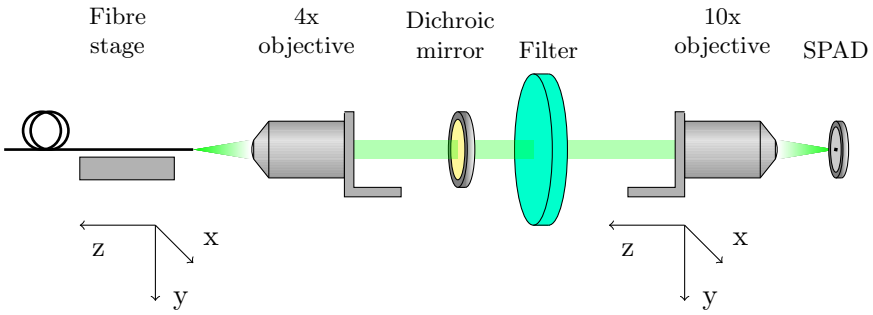

Figure 5.17: Alignment control of fibre output onto the 50 µm SPAD detector chip.

A 10x optic was chosen for coupling into the SPAD due to its focal distance; 40x and 60x objectives, while perhaps better able to focus the beam down to the detector chip, were not able to be placed close enough for the focal point to be in the same plane as the detector face. A variety of lenses were trialled for this purpose, at f=19, 20, 35, 40, 50.2, and objectives at 4x, 20x, 40x and 60x, and of these the 10x objective was found to produce the best results.

Although the fibre output was carefully focused onto the SPAD detector area, it is evident a substantial loss of signal still occurred for all experiments with the SPAD. When comparing experiments performed with the PMT and SPAD unit, measurements performed with a SPAD generally have lower signal intensities. Due to the higher quantum efficiency of the SPAD units, this result is not intuitive, but the ease with which the fibre output is collected by a PMT compared with the careful focusing required for detection using a SPAD explains the difference in signal intensity measured with each detector.

For future work in this area, it would be useful to optimise the method by which the signal is collected and focused onto the detector area. A mostly fibre coupled system could replace the free-space optics used in experiments, reducing the need for continuous alignment of optics due to instrument drift, however fibre coupling losses would also need to be considered. SPAD units with fibre pigtails are available commercially, optimised for use with optical fibres, but integrating optical filters into the system would be an issue.

5.4 OSL Measurements

Once an experimental test-bed was designed and a method established to obtain an OSL response, experiments were performed to study the capability and limits of this OSL from fibres. Measurements were initially performed using undoped fibres and canes, mostly using a PMT for luminescence detection, and the experimental configurations for measurements of canes and fibre bundles are shown in Figures 5.15 and 5.8 respectively.

5.4.1 Stimulation Power

The OSL response with respect to the power of the optical stimulation was measured in Section 2.6.2 for bulk FP glass. A similar experiment was performed using an FP cane (fibre trial F12). A 532 nm laser source with variable power output was used for stimulation, the power reported in the data is the power output from the cane, measured by a photo meter prior to each OSL measurement. Following measurement of the power output, a standard OSL measurement is performed using a photomultiplier for luminescence detection and 2 x 4 mm Corning 7-59 filters to reject stimulation photons. The OSL is integrated over the first 0.2 s of stimulation and plotted with respect to stimulation power, the result is shown in Figure 5.18.

The result shows a similar trend to that shown in Section 2.6.2, where a certain threshold stimulation power is required to rapidly excite the majority of the population of trapped electrons. This result also tells us that above this threshold power, a more intense stimulation source is unnecessary. This is important when considering the filtering of the luminescence signal from the scattered optical stimulation; a high intensity stimulation source will require a thicker filter to sufficiently attenuate, which in turn will additionally attenuate the luminescence signal. It is therefore necessary to choose a stimulation source of sufficient intensity to adequately excite the population of trapped electrons, but not so intense that sufficient filtering to reject the scattered stimulation light becomes difficult.

5.4.2 OSL with respect to dose

The OSL response of FP glass with respect to exposure time was demonstrated previously in Section 2.6.2: here is shown the same experiment performed on a 1 mm diameter cane (fibre trial F12). The experimental setup was as shown in Figure 5.15, with stimulation at 532 nm, isolation of the luminescence using a Schott BG3 filter and detection with a PMT. For each OSL measurement, the cane was exposed to irradiation from the $^{90}Sr/^{90}Y$ beta source for varying lengths of time and each value for exposure

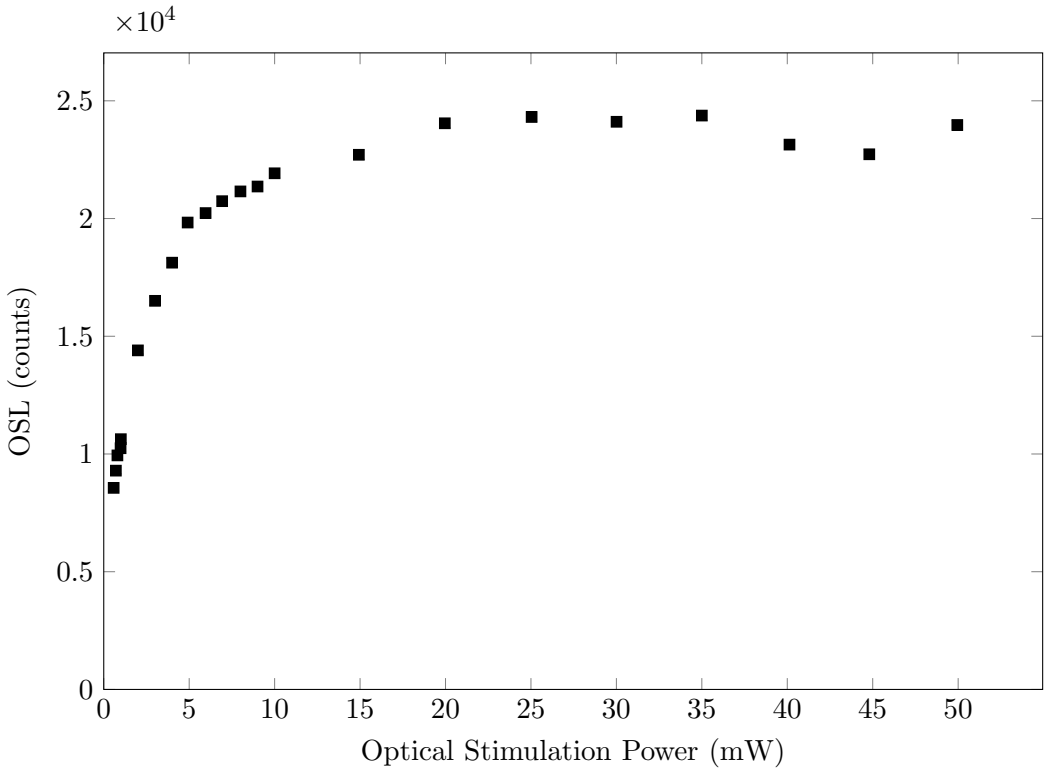

Figure 5.18: OSL in FP glass with respect to stimulation laser power at 532 nm.

time was repeated five times in order to improve the statistics. The OSL response with respect to radiation exposure time is shown in Figure 5.19.

There is an increase in OSL intensity with respect to dose, however it reaches a saturation level. This may be a dynamic equilibrium between trap filling and trap emptying due to the short lifetime of the excited population, as was demonstrated in Section 2.6. During irradiation, the already-trapped electrons might decay back to the ground state, an effect which would become more significant for longer irradiation times as the trapped charge population builds up.

Following this result, an experiment was performed using radiation sources with different activities. The same experimental setup was used, however the irradiation time was kept constant at 120 s. The dose received by the fibre was therefore a function of the source activity, the result can be seen in Figure 5.20. A similar result to that seen in Figure 5.19 is observed, where the response follows an exponential trend. This exponential trend is therefore not only due to the equilibrium between trap filling and trap emptying which was discussed previously, otherwise the response would be linear when the exposure time is kept constant. This result suggests the glass has a limited capacity to store charge in an excited state, perhaps due to a limit of trapping centres which become full beyond a certain absorbed dose.

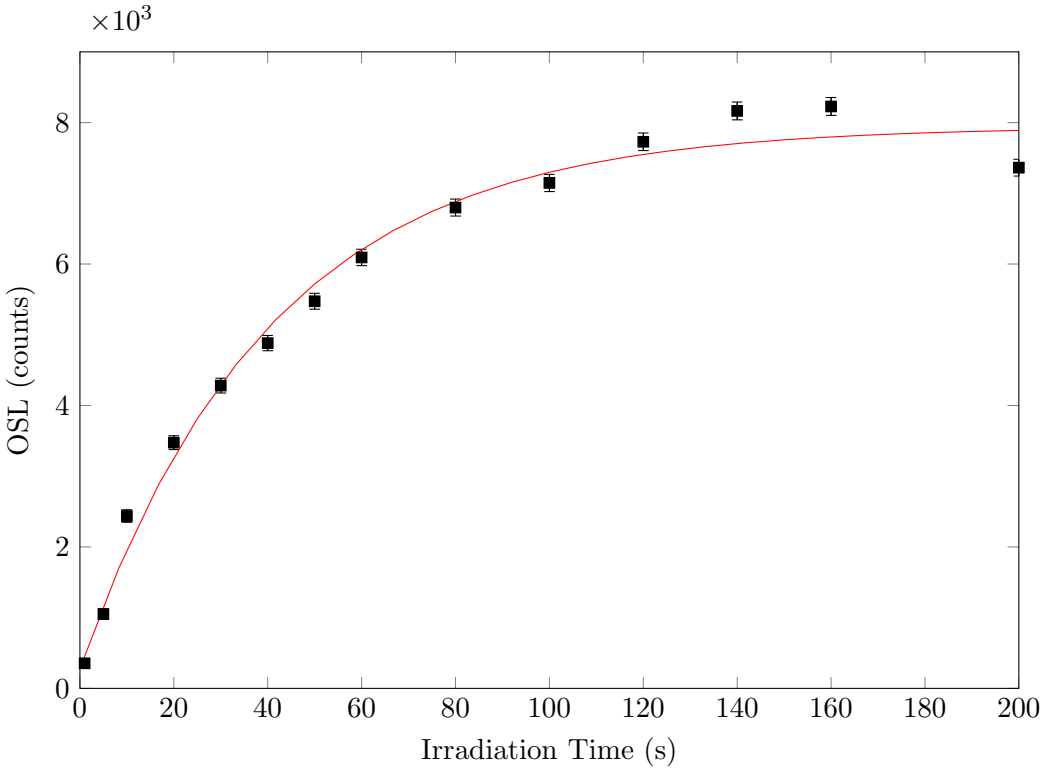

Figure 5.19: OSL response of FP1 glass cane with respect to $^{90}Sr/^{90}Y$ exposure time.

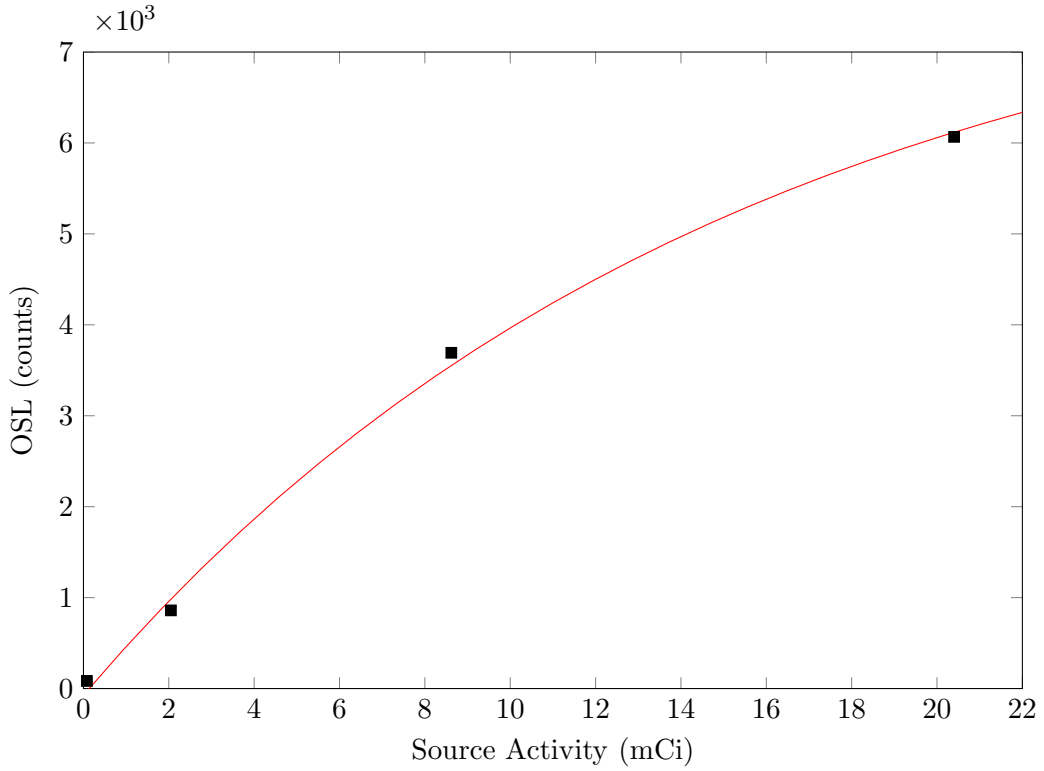

Figure 5.20: OSL response of FP1 glass cane with respect to activity of the $^{90}Sr/^{90}Y$ beta source.

5.4.3 Minimum Fibre Size and Mass

The minimum size of the optical fibre required to observe an OSL response was initially quite large. Measurement needed to be done with a cane in order to record a 'single element measurement', for a 1 mm cane, this is an irradiated mass of approximately 35 mg. Improvements in fabrication enabled smaller canes and fibres to eventually be used. A series of fibres and canes were fabricated with varying diameters (fibre trials F13 and F14). OSL measurements were performed using 532 nm stimulation and 2 x 4 mm Corning 7-59 filters, with a PMT for detection.

The result of the OSL response as a function of cane diameter is shown in Figure 5.21, in the 200 – 300 µm diameter range the canes have sufficient flexibility to be considered to be optical fibres. The intensity of the OSL response in this experiment is a function of the irradiated volume, we therefore expect a polynomial trend with respect to the cane diameter, which is shown in Figure 5.21. The data shows significant uncertainty between 400 and 800 µm diameter canes. This is attributed to the cleave quality. Fibres with small diameters can be cleaved using fibre cleaving instruments, enabling good reproducibility. Canes, however, are cleaved by hand with a ceramic blade, leading to higher uncertainty. For larger diameter canes, however, any defects from the cleave affect a lesser fraction of the total cleave surface, hence for increasing cane thickness, uncertainty introduced from the cleave will decrease. This leads to the region of higher uncertainty being the between large fibres and the small canes.

The fibre with a 160 µm diameter shows an observable OSL response, indicating measurements are achievable using a single fibre. At this diameter, the dose absorbed by the fibre is 14.6 ± 0.5 Gy. The detection of this signal, which was not previously possible, is attributed to the improvement in optical fibre quality that is discussed in Chapter 4.

5.4.4 Summary

In this Section several different examples of OSL measurements have been demonstrated. Overall, experiments have demonstrated the capability of FP optical fibres to perform sensing of ionising radiation using OSL, however most experiments lack sufficient signal intensity to be meaningful in real-world applications. The experimental setup used for measurements shown here generally had the radiation source positioned near the fibre end, at a position of approximately 10 cm, as is shown in Figure 5.22. This mitigated the effects of transmission loss in the fibre, and enabled detection of a small luminescence signal, however a more intense OSL signal was desired, and this prompted the work presented previously in Chapter 3.

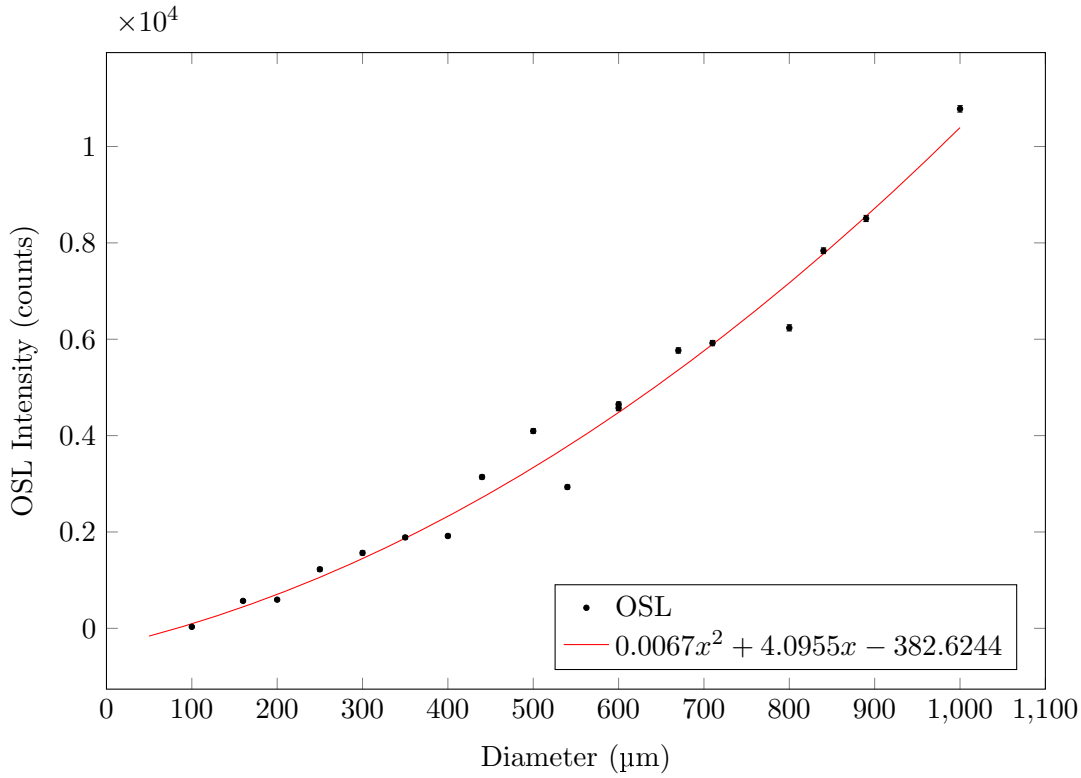

Figure 5.21: OSL response of canes with respect to diameter. Dose was approximately 14.5 ± 0.5 Gy.

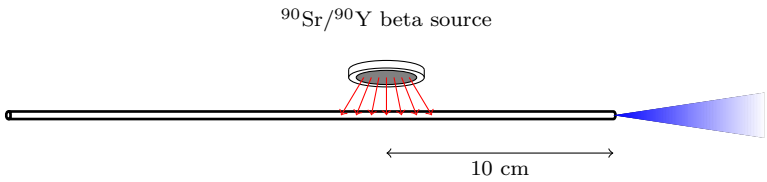

Figure 5.22: Experimental setup for the detection of OSL from a single optical fibre using a SPAD.

5.5 OSL Measurements on Tb^{3+}-Doped Optical Fibres

All experiments shown thus far were performed using canes and fibres fabricated from undoped FP1 glass, and although successful OSL results were obtained, the signal intensity was generally insufficient for any practical real-world usage. Most results were obtained using canes in order to improve the signal-to-noise, which while valuable for demonstrating proof-of-concept, are not sufficient to satisfy the main goal of the project: the development of an OSL-active optical *fibre*. Achievement of this main goal became possible following the work presented in Chapter 3, where the OSL intensity of the material was improved, and optical fibres were subsequently fabricated from this material. These optical fibres, doped with Tb^{3+}, were capable of producing an OSL response intense enough for measurement with a single length of fibre, without needing to use canes or bundles to obtain the necessary signal-to-noise ratio.

As was shown in Chapter 4, 3 sets of Tb^{3+}-doped optical fibres were fabricated, the first two (F17 and F18) using a reducing melting atmosphere and different concentrations of Tb^{3+}, and the third (F19) using an oxidising melting atmosphere. Along with F17, canes of thicker diameter were also fabricated out of a glass fabricated under identical conditions. Due to the poor transmission quality of fibre F18, it was not used extensively for OSL measurements, most tests were done using fibres F17 and F19. Different OSL measurements were performed on each set of fibres and are shown in the following sections.

5.5.1 OSL Tests on Tb^{3+}-Doped Fibre Melted in Reducing Atmosphere

OSL as a Function of Fibre Size A series of fibres and canes with varying diameters were fabricated (trials F16 and F17), and OSL tests performed similar to the experiment demonstrated in Section 5.4.3. The experiment performed here uses a SPAD for detection of the luminescence, and the experimental setup used is the one shown in Figure 5.23, using the 852 nm laser for optical stimulation and a Schott BG39 filter to isolate the OSL signal. The $^{90}Sr/^{90}Y$ beta source was set up close to the output end of the fibre, a distance of 90 mm, to avoid excessive attenuation of the OSL signal. For each measurement the irradiation time was two minutes, for fibres in the 160 - 200 µm range the absorbed dose was therefore approximately 14.6 ± 0.5 Gy. The results can be seen in Figure 5.24.

An OSL response was detected in fibres of 160 and 200 µm diameter, indicating the material is sensitive enough to allow single-fibre detection, giving proof-of-concept for the measurement of OSL in fibres using the SPAD detector. When using undoped FP1

fibres in this exact setup no OSL response was measurable, indicating the improvement of the glass material was indeed necessary for the system to work.

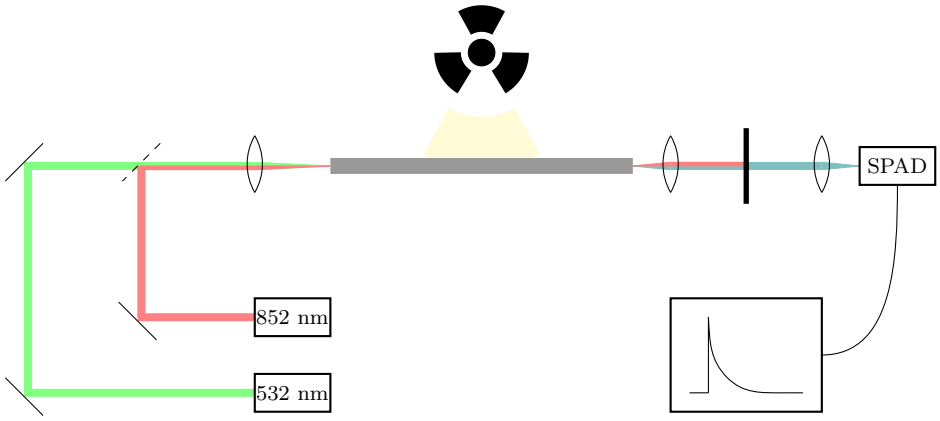

Figure 5.23: Experimental setup for the detection of OSL from glass canes using a SPAD. Optical stimulation at 852 nm is shown in red, luminescence is shown in teal, the 532 nm laser used to assist optical alignment of the system is shown in green.

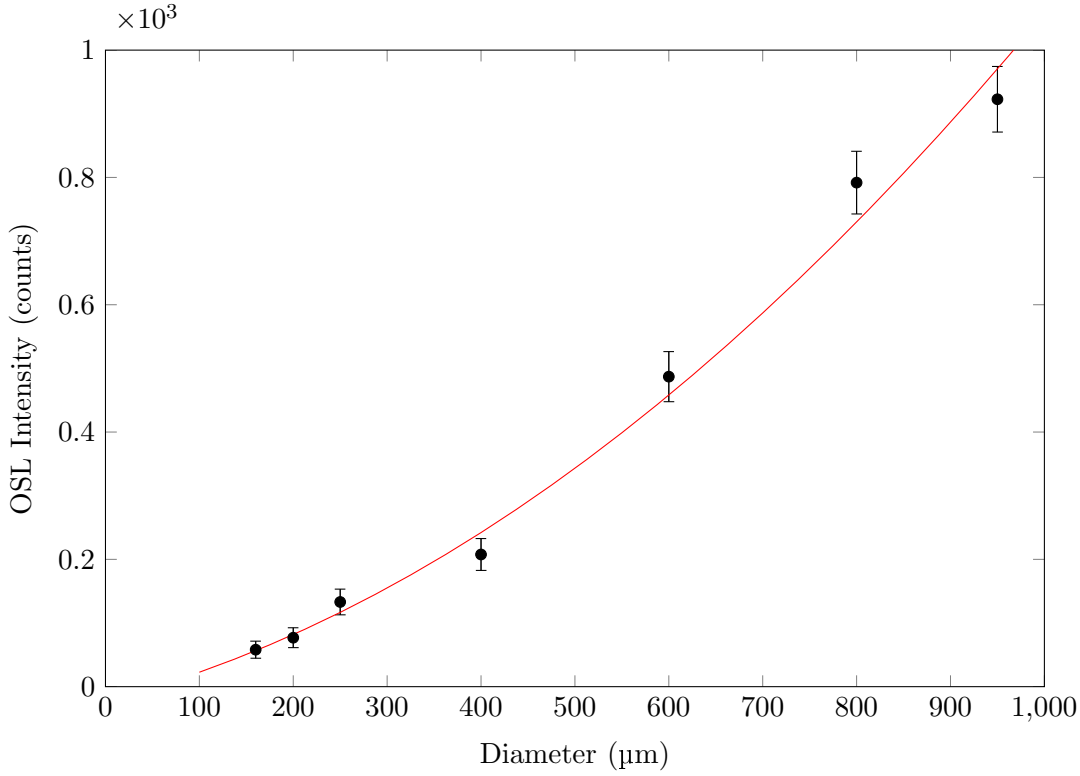

Figure 5.24: OSL response of Tb^{3+}-doped fibres/canes with respect to diameter. Detection was by a SPAD optically filtered by a 3 mm Schott BG39 filter. Dose was approximately 14.6 ± 0.5 Gy.

OSL as a Function of Position Along the Fibre Due to the high loss of this fibre, shown in Chapter 4, the OSL signal was not expected to propagate a long distance down the fibres or canes. An experiment was performed to demonstrate this: a 1 mm diameter, 800 mm long doped cane (F16) was set up as per Figure 5.23. The cane was then irradiated several times using the $^{90}Sr/^{90}Y$ beta source at varying positions along

the cane. The experiment commenced at the furthest distance from the output of the cane so as to avoid the effects of photodarkening and irradiation was performed for 120 s for each measurement to ensure good signal-to-noise. Following each measurement, the radiation source was moved closer to the output end of the cane and the measurement repeated; the result is shown in Figure 5.25.

The OSL response in the Tb^{3+}-doped glass is seen to decrease significantly as the distance between irradiation and cane output is increased, this is attributed to the high loss of the Tb^{3+}-doped fibres and canes (10 dB/m), shown in Figure 4.16, use of lengths greater than 1 m would not be possible. The high loss of these doped glasses has been demonstrated in comparison to undoped FP1 glass, and this measurement shows the effect of this severe loss on OSL signals when using the material in radiation-detection measurements.

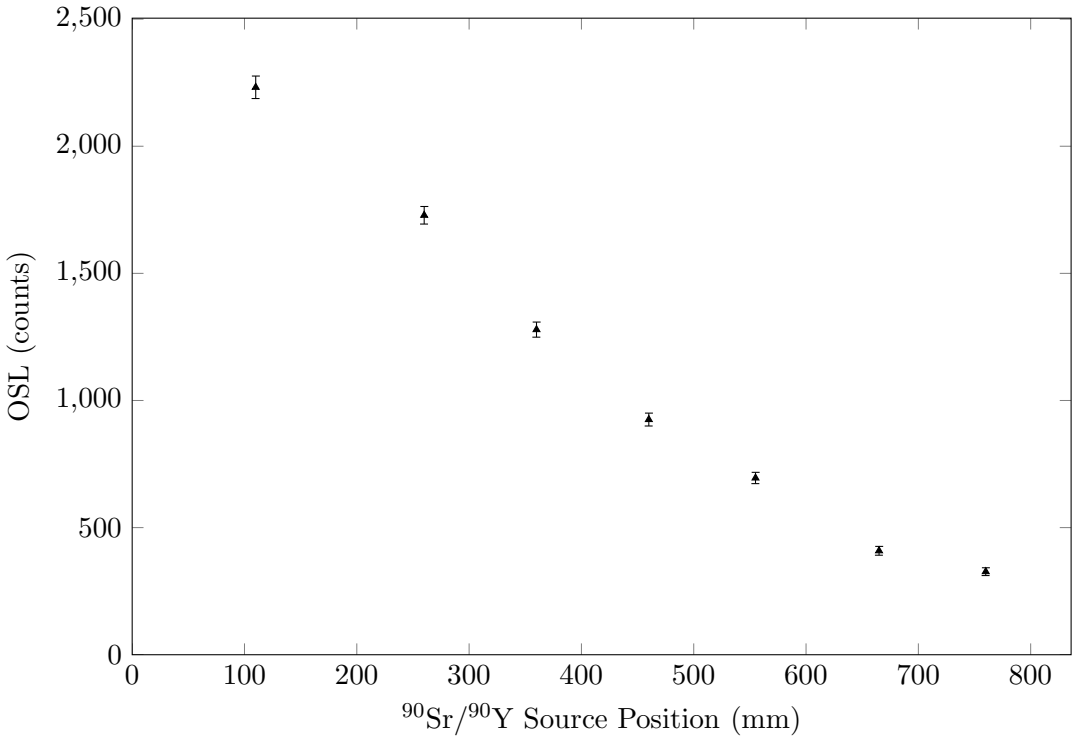

Figure 5.25: Normalised OSL measurements with respect to the position of the ^{90}Sr/^{90}Y radiation source along glass canes measured from the cane output, cane diameter is 1000 µmu. Measurements were taken in the 350 – 600 nm wavelength region using a Schott BG39 filter and optical stimulation at 852 nm.

5.5.2 OSL Tests on Tb^{3+}-Doped Fibre Melted in Oxidising Atmosphere

OSL as a Function of Position Along the Fibre The Tb^{3+}-doped fibre, melted under oxidising atmosphere (F19), was drawn into a set of bands with diameters of 160, 200 and 250 µm. The same experiment shown in the previous Section, where the

OSL intensity is measured as a function of the $^{90}Sr/^{90}Y$ beta source position along the optical fibre, was also performed for each fibre diameter. The experimental setup used is shown in Figure 5.26, and the experimental method is identical to that described previously. The results are shown in Figure 5.27.

Detection of OSL was again possible using single fibres and for this glass the fabrication of canes with larger diameters was not necessary to obtain good signal-to-noise. Compared to the previous Tb^{3+}-doped fibres, (F17 and F18) this fibre has much lower loss (3 - 4 dB/m), shown in Figure 4.16, and OSL. Extrapolating the OSL intensity trend, detection using much longer lengths of fibre should be possible, this is discussed in the next Section.

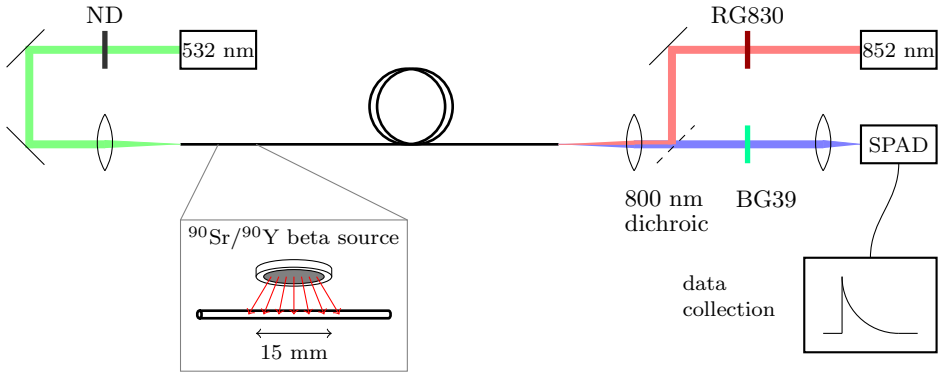

Figure 5.26: Experimental setup for the detection of OSL from a single optical fibre using a SPAD.

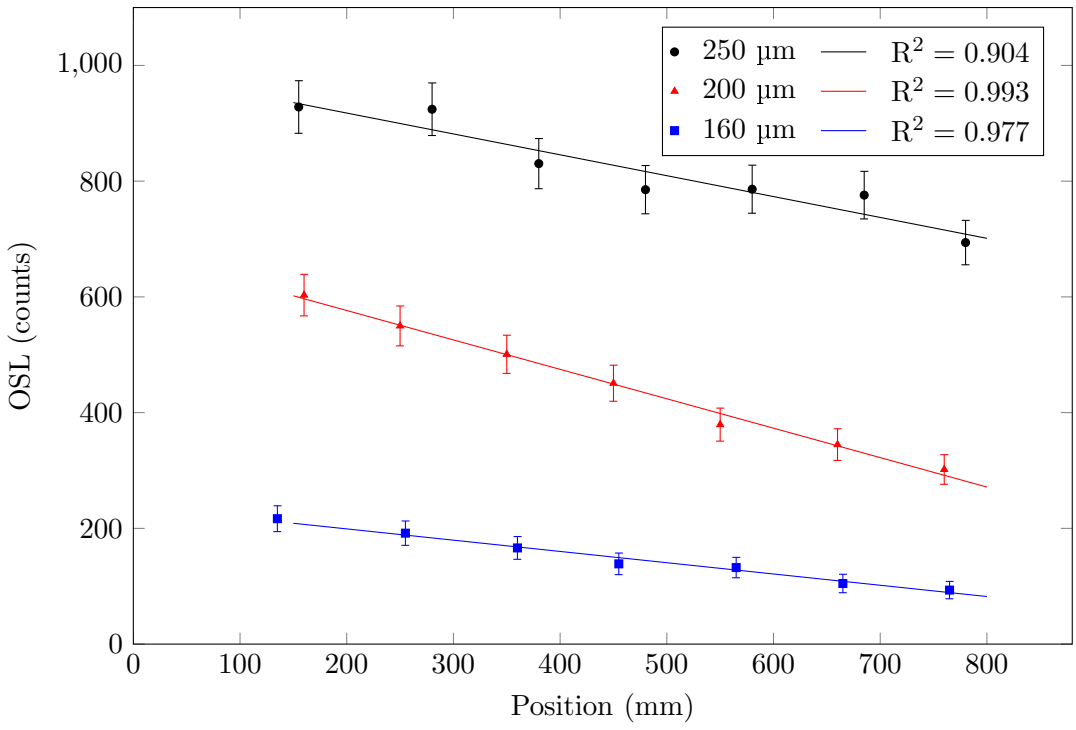

Figure 5.27: Normalised OSL measurements with respect to the position of the $^{90}Sr/^{90}Y$ radiation source along glass canes measured from the fibre output. Measurements were taken in the 350 – 600 nm wavelength region using a Schott BG39 filter and optical stimulation at 852 nm.

Maximum Fibre Length The range down the fibre at which OSL measurements could still be performed was tested for fibres of each diameter: 160, 200 and 250 µm, using irradiation from the $^{90}Sr/^{90}Y$ beta source and a dosage of 14.6 ± 0.5 Gy (120 s irradiation time). The RL measured during the irradiation was also recorded, results are shown in Table 5.2. In general, fibres with larger diameters have more intense OSL signals, due to the greater irradiated mass of material. However, fibre cleave quality and optical alignment cannot be exactly replicated for each length of fibre tested, even when the careful alignment process is performed. For this reason, thicker fibres occasionally had a lower intensity OSL response than fibres with a smaller diameter, as can be seen in Table 5.2.

Results indicate successful OSL measurements using far longer lengths of optical fibre than was previously achievable with both undoped glass fibres and fibres fabricated from terbium doped glass produced in reducing environments. An important point to highlight is the small irradiation area on the optical fibre, shown in Figure 5.26, where only 15 mm of fibre receives a dose - a small fraction of the total fibre length. In applications where the radiation field is spread over a wider area, more fibre would become exposed and the OSL intensity proportionally higher for a given dose rate.

A more intense OSL response is detected in the 350 - 600 nm waveband, presumably due to the wider detection band and the intense 550 nm emission peak from Tb^{3+}. This enabled the use of longer fibre lengths than for tests performed in the 350 - 450 nm waveband.

An interesting observation is the ratio of RL to OSL in each different waveband. If we consider the 350 - 450 nm region, using 532 nm stimulation and the BG3/BG39 filter stack, the RL in counts/second is consistently lower than the OSL intensity, a ratio of approximately 1:1.5. For the 350 - 650 nm waveband, using 852 nm stimulation and a BG39 filter, the RL is consistently higher than the OSL, a ratio of approximately 1:0.2. This could indicate luminescence due to OSL might be occurring by a different recombination path than RL. A possibility is that due to the immediate recombination of electron-hole pairs during RL, the emission spectrum is more closely related to that observed for fluorescence measurements. During OSL, however, where the electrons are trapped at defect sites, the recombination pathway following optical stimulation might be different, potentially resulting in a different emission spectrum.

5.5.3 Summary

The results shown in this Section, particularly those results taken from the oxidised Tb^{3+}-doped fibre (F19), are essentially a proof-of-concept for the main goal of this

Table 5.2: Distance along a Tb^{3+}-doped fibre at which an OSL signal is measurable using an absorbed dose of 14.6 ± 0.5 Gy from a $^{90}Sr/^{90}Y$ beta source. Measurements were performed using both wavelength regimes: stimulation at 532 nm using a Schott BG3-BG39 filter stack and stimulation at 852 nm using a Schott BG39 filter.

Fibre	Distance (m)	RL (counts/s)	OSL (counts)
350 - 450 nm waveband. 532 nm stimulation - BG3/BG39 filter stack			
160 µm	1.9	59.0 ± 7.7	102.9 ± 28.4
200 µm	0.98	61.0 ± 7.8	89.7 ± 17.9
250µm	1.9	64.0 ± 8.0	88.4 ± 26.9
350 - 600 nm waveband. 852 nm stimulation - BG39 filter			
160 µm	1.5	458 ± 21.4	148.5 ± 20.7
200 µm	2.6	164 ± 12.8	44.1 ± 13.0
250µm	2.4	221 ± 14.9	37.5 ± 12.9

project: OSL measurements performed intrinsically in an optical fibre. Previous Sections demonstrate OSL results from short lengths of fibre, or from canes with large diameters, but none of those results indicated a real-world application would be viable. The results shown here indicate OSL measurements can be consistently taken using appreciable lengths of optical fibre, as is depicted in Figure 5.28, with suitable sensitivity for real-world usage. Compared with previous measurments with undoped glass, as is shown in Section 5.4 and depicted in Figure 5.22, this is a significant improvement.

This work shows that FP glass doped with Tb^{3+} under an oxidising environment is the most suitable candidate, and should be the subject of further study. The loss of this optical fibre (F19) is still high compared to undoped glass, but this could be improved by optimising the fabrication procedure and dopant concentration to achieve a compromise between loss and OSL sensitivity. Longer lengths of fibre and higher OSL intensities would then be available, further improving the system.

It has also been shown that measurements can be taken using both the 350 - 450 nm (852 nm stimulation - BG39 filter) and the 350 - 600 nm wavebands (532 nm stimulation - BG3/BG39 filter stack). While more intense signals were detected using the 350 - 600 nm waveband, the flexibility exists to use either regime, depending on the resources and requirements of the desired application.

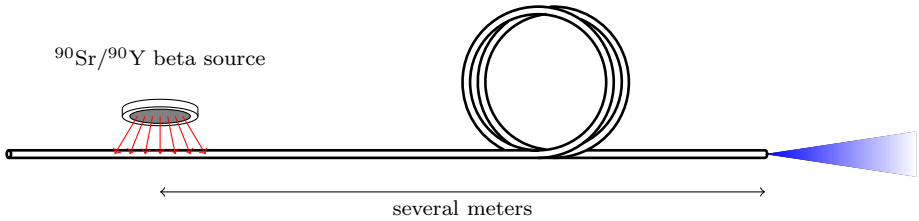

Figure 5.28: Experimental setup for the detection of OSL from a single optical fibre using a SPAD.

5.6 Detection of X-rays

Up to this point in the experimental work, irradiation of samples was performed using the $^{90}Sr/^{90}Y$ beta sources summarised in Section 1.4.3. Access to an X-ray source was now obtained in order to test the performance of optical fibres under exposure to photon radiation. As shown in Section 1.4, electrons and photons interact with matter by different mechanisms, therefore it was important to investigate if glasses behaved differently after irradiation with X-rays rather than beta particles. Experiments were performed using a Lorad LPX-300 X-ray source, a brief summary of the X-ray source was given in Section 1.4.3.

5.6.1 Experimental Setup

Optical Fibres At the time of X-ray measurements being performed, fibre F19 had not yet been fabricated and all tests were performed using fibre F17. While the sensitivity and transmission loss of this fibre is not as good, very promising OSL results were still obtained. If tests were to be performed again using the better quality fibre, it is assumed the OSL response would be more intense for each experiment.

Measurements were generally performed several times on one length of fibre due to uncertainties introduced when changing the fibre in the experiment. Variables include the cleave quality, input coupling of the stimulation laser, and coupling of the signal onto the SPAD. In addition, each length of optical fibre may have a slightly different optical quality due to the impurities potentially introduced during the fabrication process.

Fibre Position Fibre coils were positioned at approximately half the beam angle, as shown in Figure 5.29. Although the intensity per unit area will be greater closer to the source, this would take the fibres closer to the edge of the X-ray beam, where there might be greater inconsistency in the beam intensity. This position was chosen to compromise between the two, where the fibres were positioned at approximately 10° from the centre axis of the beam; the source-to-fibre distance was 295 mm.

X-ray Beam Profile Tests were performed to evaluate the intensity profile of the beam, due to the divergence (40° by 60°) it might have been possible the intensity varied with respect to the angle from the centre. Small (5 mm diameter) Al_2O_3:C dosimeter chips were positioned at various points under the beam and irradiated. The thermoluminescence signal and background of each chip was then measured using the Risø Reader and the 220 ℃ peak integrated. In order to compare the intensity of the response from each chip, a calibration curve is established for each chip by measuring

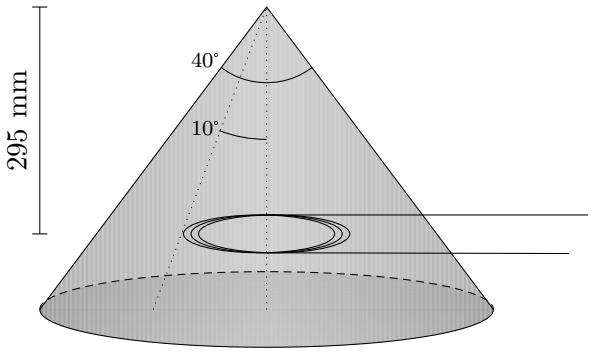

Figure 5.29: Schematic representation showing the X-ray beam divergence and the position of the fibre coil in the X-ray beam.

the TL response of each chip as a function of applied dose in the Risø Reader. The signal acquired from X-ray irradiation is then compared with the calibration curve to establish the dose absorbed, an example is given in Figure 5.30. The resulting beam profile is shown in Figure 5.31; there is some large variation observed on the outer-most Al_2O_3:C chips, at the edge of the beam. Most chips in the inner beam region report a similar beam intensity, with the exception of two chips which show a much higher intensity. This could be due to anomalous readings for these particular Al_2O_3:C chips.

The beam was also imaged using an X-ray imaging plate, shown in Figure 5.32. From these measurements the beam profile was observed to be acceptably uniform within the area where optical fibres were irradiated.

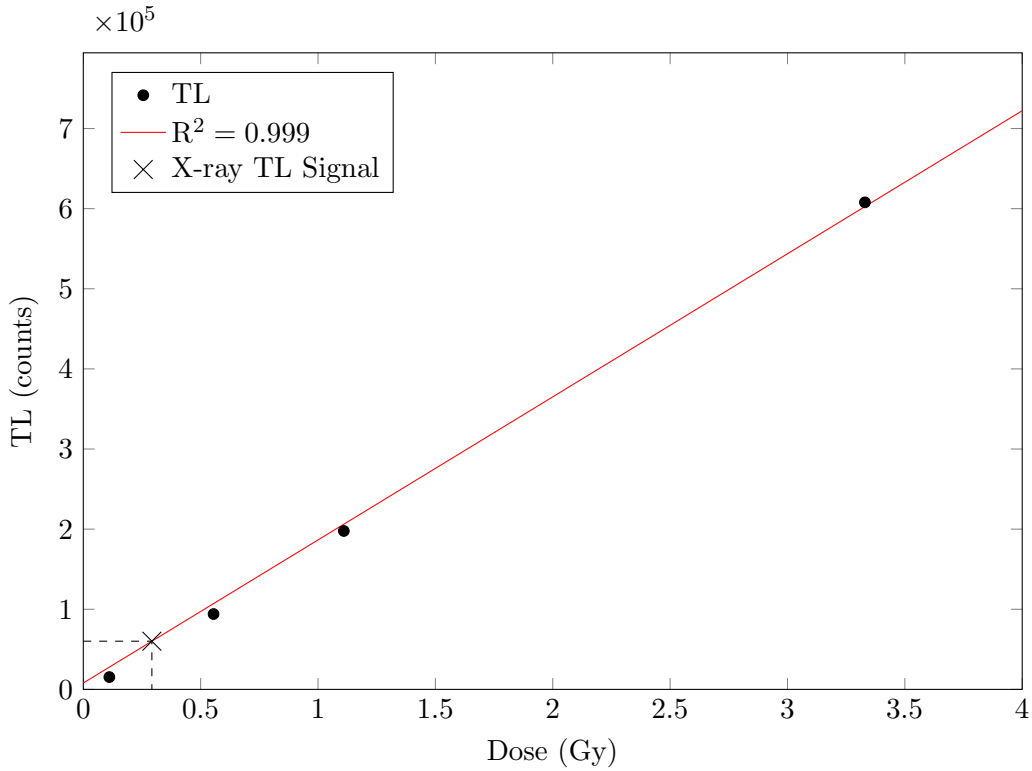

Figure 5.30: Example of a TL calibration curve of dose delivered to an Al_2O_3:C dosimeter chip in order to calculate an equivalent dose.

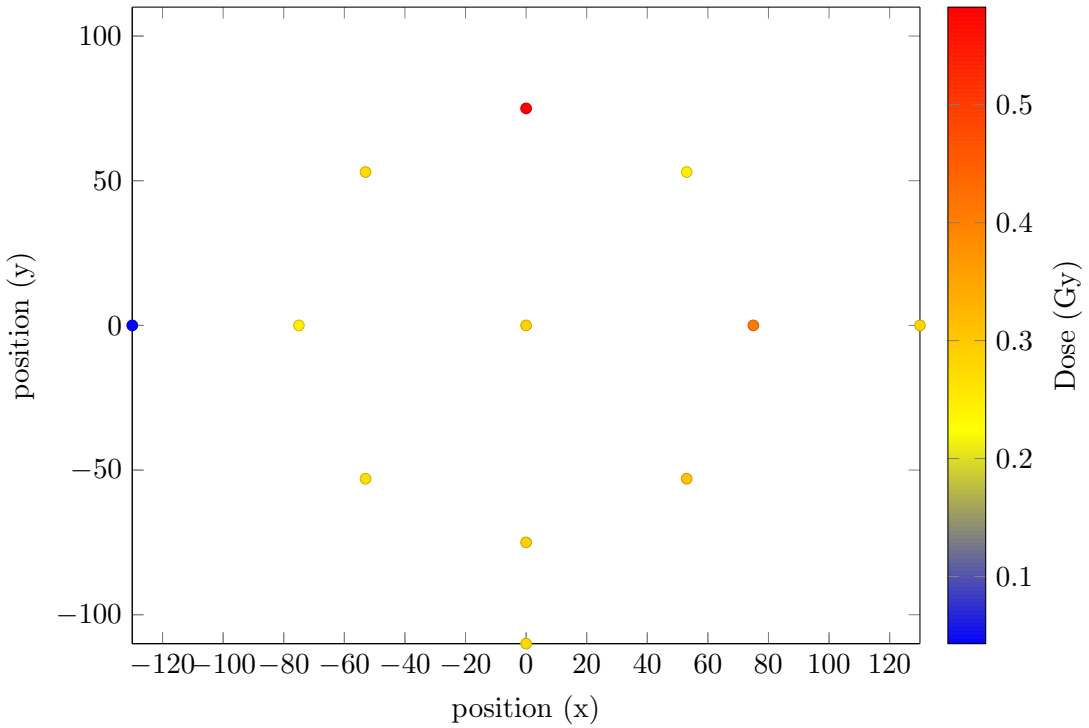

Figure 5.31: X-ray Beam profile obtained from placing Al_2O_3:C dosimeter crystals at certain x, y positions in the X-ray beam. The dose absorbed by each chip is then calculated from the TL intensity, normalised for the TL response of each individual chip.

OSL Detection The OSL capture and detection setup is similar to that shown in Figure 5.26, using the following equipment: optical stimulation was performed with a 100 mW 852 nm laser, the intensity measured at the fibre output was approximately 25 mW, filtration of luminescence from the optical stimulation was done with a 3 mm Schott BG39 filter and luminescence was detected with the Lasercomponents SPAD. Measurements were taken on 160 µm fibres, and lengths of approximately 870 mm were used, corresponding to an irradiated volume of 17.5 mm^3 and an irradiated mass of 65 mg. For most measurements, irradiation times of 60 s were used; to vary the total X-ray intensity for an exposure, the filament current was adjusted.

5.6.2 Results

Photodarkening

When performing initial experiments on fibres, both the OSL and RL response was seen to decrease after prolonged exposure. This was attributed to photodarkening: as discussed in Section 2.4.1, it affects a broad wavelength range centred at 475 nm. The

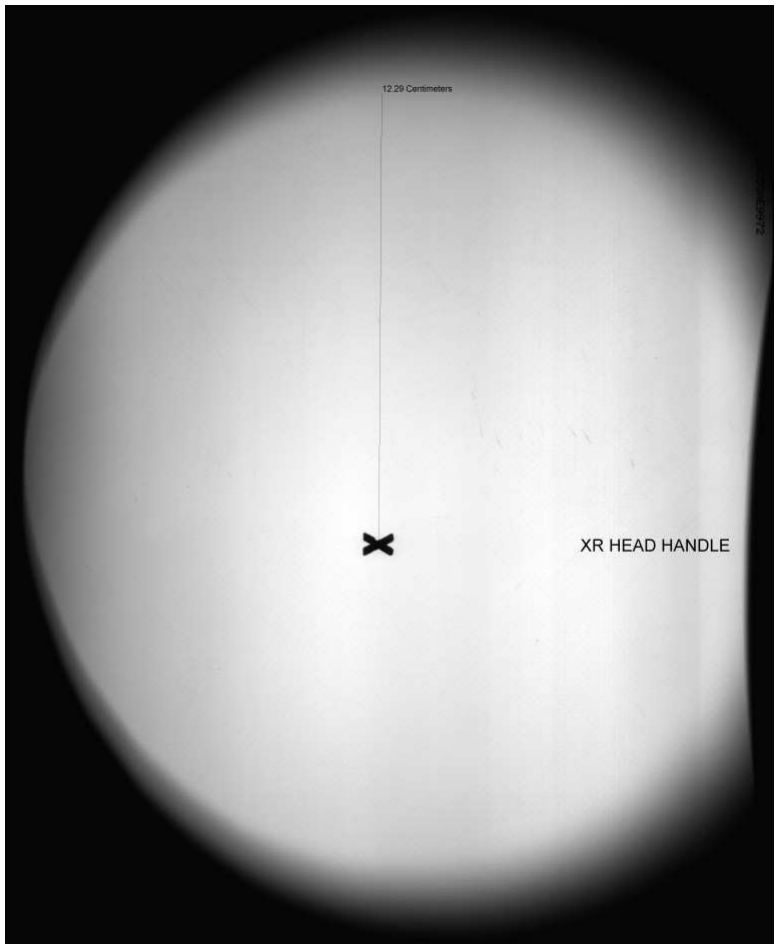

Figure 5.32: X-ray imaging plate exposed to the X-ray beam in order to visualise the beam intensity profile. Beam attenuation is observed on the right hand side due to the X-ray Head handle. No significant fluctuation of beam intensity is observed in the central area where optical fibres are positioned.

effects of photodarkening were not noticeable in previous measurements performed with $^{90}Sr/^{90}Y$ beta sources, which might be attributed to the method of exposure. When using the beta source, the irradiated portion of the fibre is 12 mm in length, this leaves the remainder of the fibre unirradiated and hence free of photodarkening. A signal produced in this short irradiated section could therefore travel along the remaining fibre length without attenuation due to photodarkening. In contrast, with the X-ray experiments the whole fibre is irradiated, hence a luminescence signal produced in any one fibre section will therefore travel along photodarkened fibre for the majority of the remaining length. The effects of photodarkening are therefore much more obvious and significant during X-ray experiments.

The effect of photodarkening could be observed in real time by monitoring the intensity of a laser signal coupled through the fibre, it could also be observed by measuring the RL intensity. A 532 nm laser was coupled into a length of fibre and attenuated with neutral density filters to an intensity safe for detection using the SPAD. Irradiation was performed at a tube potential of 300 kV with a filament current of 3 mA, with data collection occurring throughout the exposure period. Figure 5.33 shows the signal intensity from the fibre output with respect to time. Initially, a constant signal of 1200 counts/s is observed from the 532 nm laser. When radiation exposure begins, a RL component is added bringing the intensity to 4600 counts/s. As the exposure continues, the intensity gradually decreases. When the exposure is finished (in Figure 5.33 this is seen at 95 seconds) only a very low signal from the laser was observed at 20 counts/s. This value is only slightly above the background of approximately 10 counts/s and demonstrates a serious optical attenuation effect created by the irradiation.

Although photodarkening appears to significantly attenuate the transmission of the OSL signal, faint signals are still detected from fibres subjected to a large amount of irradiation. This signal is most likely from the section of fibre closest to the output end, where the effects of photodarkening will be not be enough to completely attenuate the OSL signal. Photodarkening by high-dose irradiation is therefore seen to be a significant factor to consider in applications of FP fibres in high dose environments.

Beam Intensity

OSL measurements were taken as a function of beam intensity at two different tube potentials, 100 and 300 kV. The beam intensity, in milliamp seconds (mAs), was changed by adjusting the filament current while using a constant exposure time of 60 s. Results can be seen in Figure 5.34.

The trend observed in Figure 5.34 is similar to that observed for measurements per-

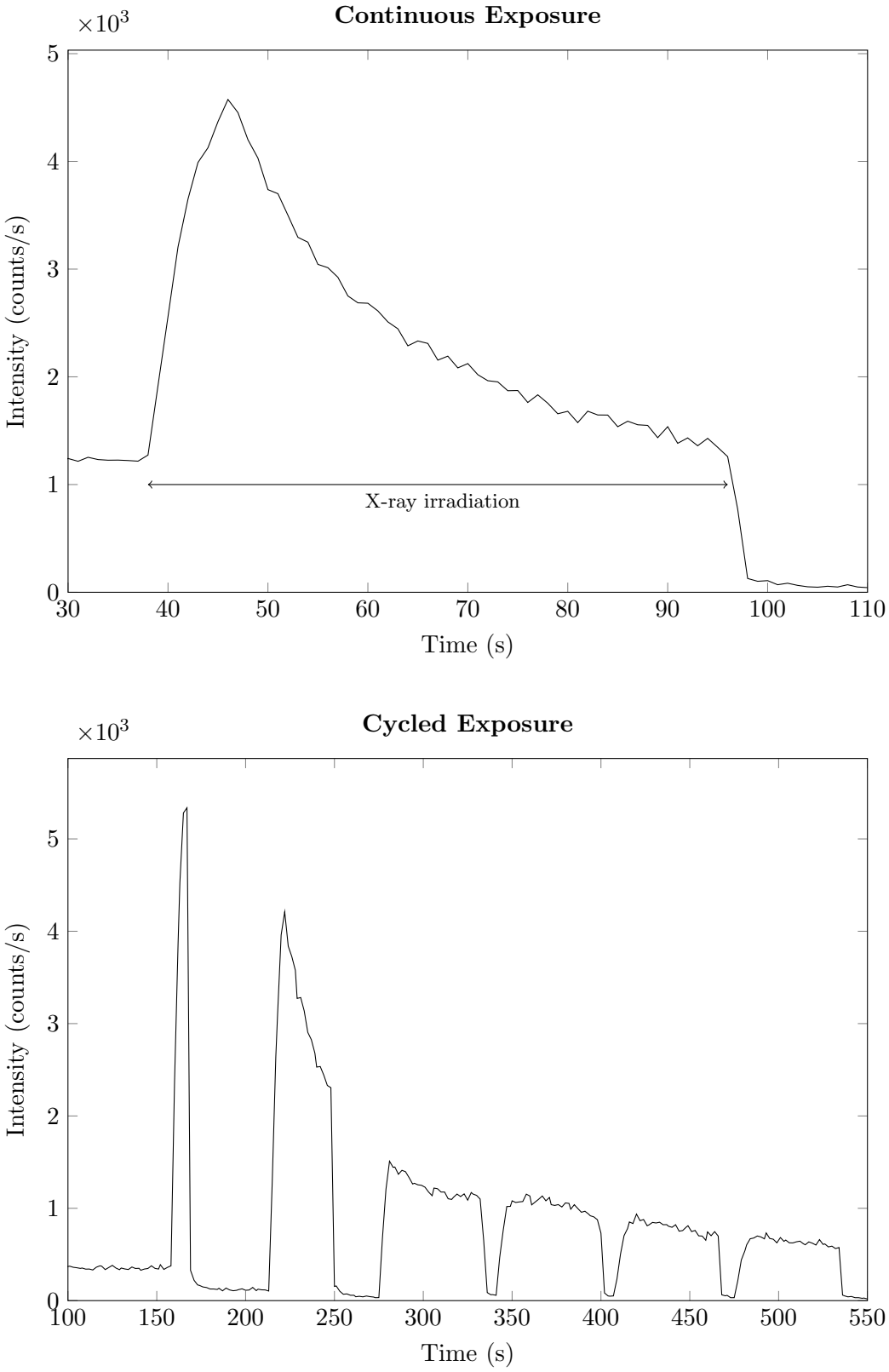

Figure 5.33: Photodarkening of FP fibres during X-ray exposure, shown by the diminishing transmission of 532 nm laser photons through the fibre under irradiation during the laser illumination. The plot showing cycled exposure clearly demonstrates the scintillation signal detected during irradiation cycles.

formed using $^{90}Sr/^{90}Y$ beta sources, shown in Figures 2.12, 5.19 and 5.20. For those measurements the OSL response is observed to approach a plateau, attributed in part to the short lifetime of the trapped population of electrons in FP glass. The result observed in Figure 5.34 is observed to reach a maximum after which it decreases; one possible cause could be the effect of photodarkening: after repeated measurements with an optical fibre, the OSL signal would be attenuated by the increasing transmission loss. This explains not only a maximum detected OSL intensity, but also the decreasing signal intensity in subsequent measurements.

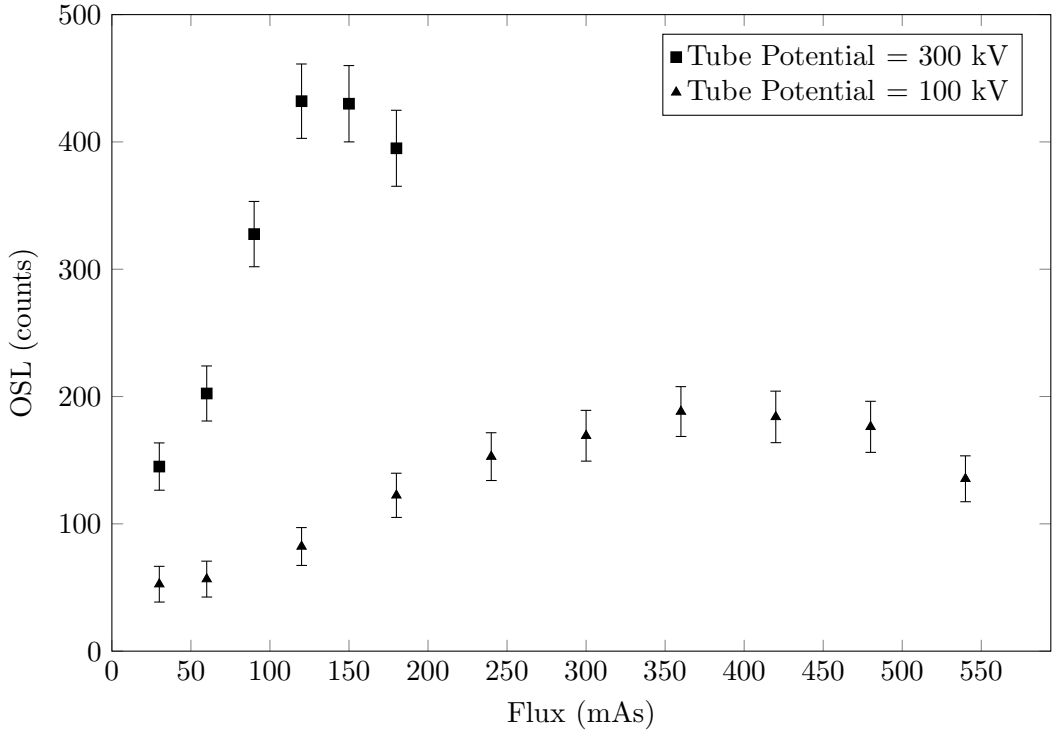

Figure 5.34: OSL from 200 µm fibre (F16) as a function of photon beam intensity at 100 and 300 kV tube potentials.

X-ray Tube Potential

Measuring the OSL response with respect to the X-ray tube potential is a key experiment: it is the first example of a measurement where the energy of the ionising radiation has been adjusted. Up to this point, experiments have been conducted using only constant particle energies: the 2.28 MeV beta particles produced by $^{90}Sr/^{90}Y$ beta sources, and X-rays at 100 or 300 keV. One might simplistically expect the OSL response to increase with respect to the X-ray energy, however as demonstrated in Figure 5.35, this is not the case. If we correlate the measured OSL intensity with the energy absorbed by the fibre, we see a greater absorption of energy when irradiating with lower photon energies. This was shown briefly in Chapter 2, Figure 2.19, where the depth-dose profile of photons at a range of energies in FP glass were simulated with PENELOPE. It was

seen that at depths on the same order as the optical fibre width (160 µm), more energy is deposited for photons in the 10 – 50 keV range than for photons in the 100 – 500 keV range. This can be explained simply by considering the linear energy transfer and dose build-up produced by photons of different energy. Low energy photons will be attenuated quickly and lose most of their energy without penetrating a long distance into the target material. Higher-energy photons, however, will penetrate further into a material without losing as much of their energy, and the majority of dose build-up will occur deeper into the material. In the context of optical fibre experiments, the aluminium plate on top of the fibre will affect the penetration of photons and the dose build-up. For photon energies too low, this 6 mm plate of aluminium may attenuate the majority of the energy. For slightly higher energies, photons may penetrate through the plate but also deposit some energy in the form of secondary electrons. This dose build-up occurring in the cover plate may then contribute to the dose absorbed by the fibre in the form of scattered photons and secondary electrons. For incident photons of higher energy, both the cover plate and the optical fibre will not be of sufficient thickness to absorb much energy, and the majority of the dose is deposited in the aluminium plate below the fibre, and the table on which the experiment sits.

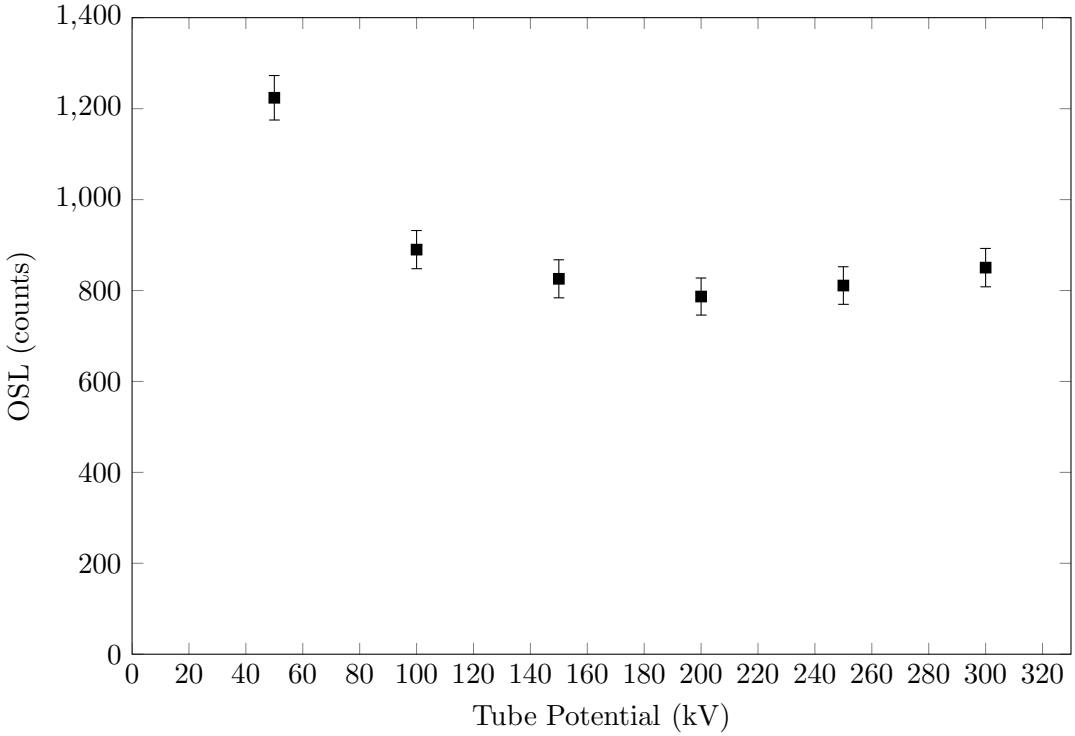

Figure 5.35: OSL response of 160 µm fibres (F16) with respect to X-ray tube potential at a constant beam intensity of 180 mAs.

Simulations were performed using PENELOPE whereby the approximate geometry of the optical fibre experiments were used. The simulated geometry consisted of an aluminium plate of 6 mm thickness on top of a 160 µm thick by 160 µm wide ring of

FP glass. The 5 mm aluminium side walls of the fibre holder were also included to each side of the fibre, as was the 20 mm aluminium plate of the fibre holder base. The photon source was positioned 295 mm away from the fibre, with a cone angle of 40°, as per the experimental setup. Simulations were performed at photon energies between 50 and 300 keV, each simulation was run for 10^8 primary particles and the energy absorbed in the glass element at the end of each simulation was then integrated. It should be noted that the output of the X-ray tube will follow a characteristic bremsstrahlung spectrum, however the X-ray photon energies used for simulations were monoenergetic. The result can be seen in Figure 5.36. The energy absorbed in the fibre volume with respect to photon energy followed a similar trend to that seen in Figure 5.35. Above approximately 70 keV, a beam of increasing photon energy will deposit a lower proportion of its energy in the fibre volume.

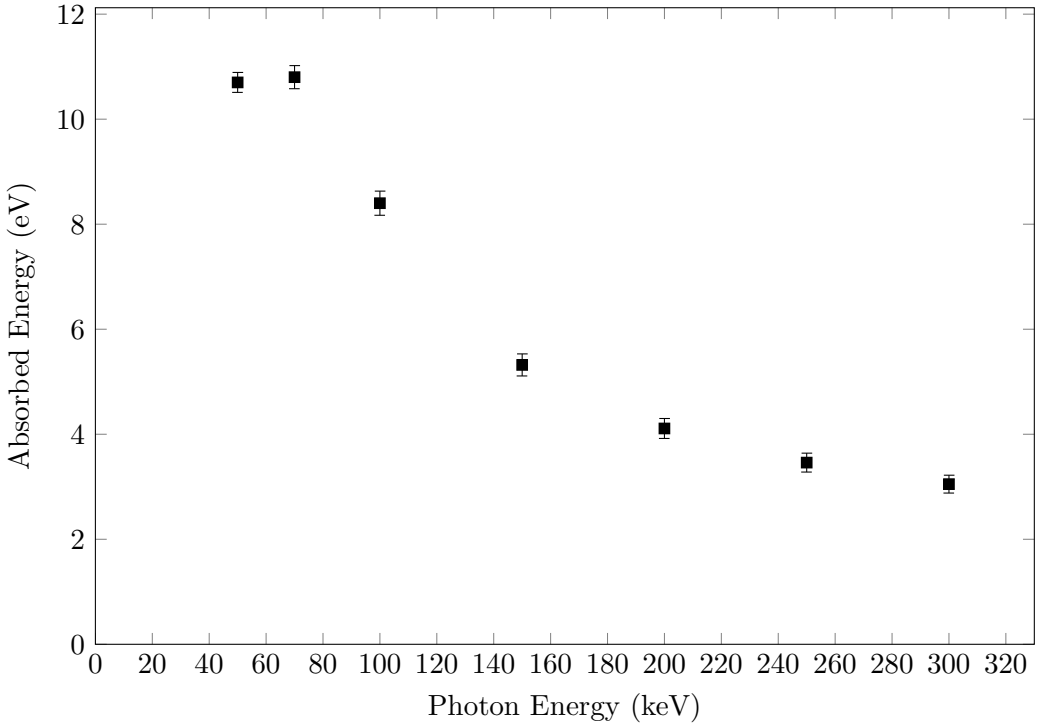

Figure 5.36: PENELOPE simulation of absorbed energy as a function of initial photon energy in FP glass.

Although simulations show a decreasing trend for absorbed energy with respect to the initial photon energy, experimental results indicate an OSL response which remains roughly consistent with tube potentials from 150 to 300 kV. A follow-up investigation using an X-ray source capable of tube potentials above 300 kV would reveal how this trend would continue.

Until this point, experiments were performed using the complete fibre holder, which includes a 6 mm aluminium cover plate. At lower X-ray tube potentials, and hence lower energy X-rays, this 6 mm of aluminium could have a significant effect on the energy

deposition in the optical fibre; this is due to the generation of secondary electrons and dose build-up in the aluminium layer, which in turn would deposit energy in the fibre. Measurements were therefore taken without this cover plate, fibres were instead held in place and optically isolated by carefully covering the fibre channel with black electrical tape, which has a negligible effect on X-ray transmission compared with the aluminium cover plate. Measurements were taken for tube potentials between 10 and 100 kV, results are shown in Figure 5.37: the OSL response with respect to tube potential is linear. In Figure 2.19 it is seen that photons with energies between 10 – 50 keV only penetrate approximately 400 – 4000 µm into FP glass. The emission spectrum of the X-ray tube would contain a large fraction of photons with lower energy than this, such that a large proportion of photons incident on the fibre would be absorbed within the fibre volume. In this regime, increasing the photon energy would therefore increase the amount of energy absorbed within the fibre, producing the linear response observed.

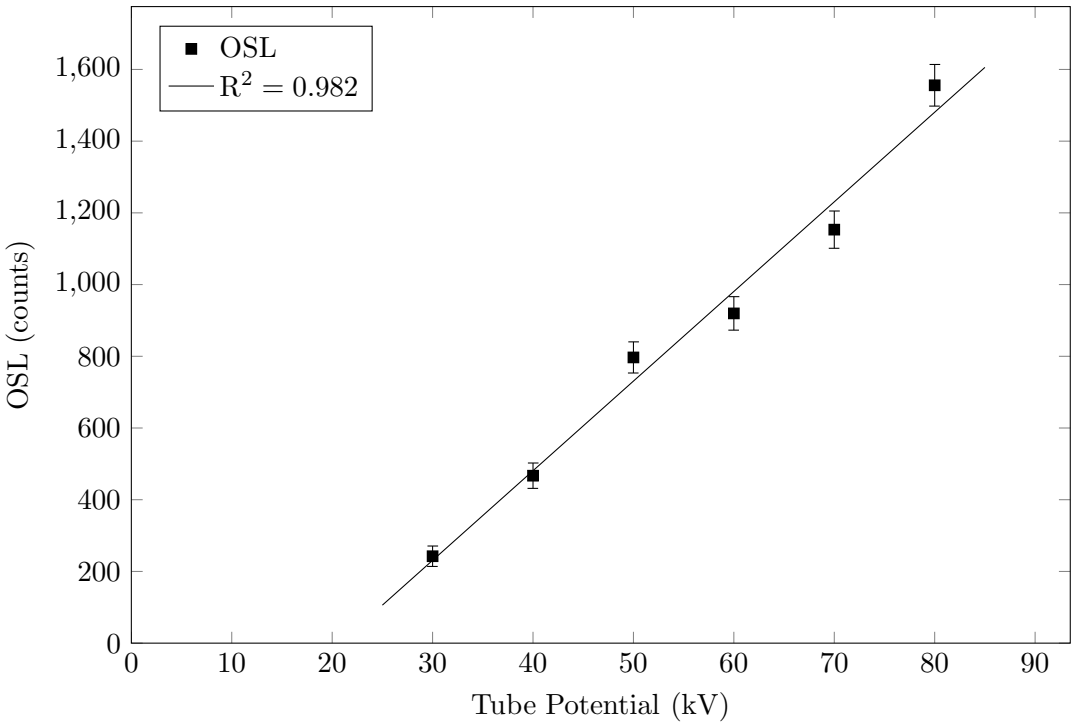

Figure 5.37: OSL from 160 µm fibre (F16) as a function of X-ray tube potential at a constant beam intensity of 60 mAs. Aluminium cover plate has been replaced with black tape.

5.7 Summary

This chapter has demonstrated the culmination of the work performed in previous chapters, and shown that the overall aim of the project is achievable. Previous chapters studied glass materials and optimised their behavior; they were then fabricated into optical fibres and again optimised. This chapter took these fibres and demonstrated their applicability as radiation detecting devices, using an intrinsic OSL response in

the fibre. OSL measurements were successfully demonstrated using single lengths of optical fibre, and at varying positions along the fibre. OSL was demonstrated using both 2.28 MeV beta particles and X-ray photons in the 20 – 300 keV energy range.

An experimental test-bed for measuring OSL signals from optical fibres was developed and optimised, enabling efficient testing of new optical fibres in an environment with low background noise. The test-bed is also suitable for RL and radiophotoluminescence detection in addition to OSL. The optimal material for OSL measurements was shown to be Tb^{3+}-doped FP glass melted under oxidising conditions, and OSL dosimetry has been shown to be feasible using both the 350 - 450 and 350 - 600 nm wavebands.

Experiments shown here offer an example of what is possible, but the parameter space in which future experiments may be performed is large. Experiments can be conducted testing the OSL response to radiation type, radiation energy, dose rate, optical stimulation wavelength and intensity, distributed sensing and point sensing.

Chapter 6

Investigation of the Radiation-Detecting properties of Silica Optical Fibres

In the previous chapters the radiation-detecting properties of fluoride phosphate glasses were explored. As was shown in chapter 2, it is not the only glass that produces an OSL response: silicate glasses were also demonstrated as being OSL-active materials. In this chapter, the luminescent properties of several silica glasses are compared with FP glass with respect to their effectiveness as a radiation-sensing material. Dosimetry measurements with silica optical fibres are also presented, followed by a comparison of silica with FP glass.

6.1 Introduction

As has been demonstrated in previous chapters, FP glass is a suitable material for optical fibre dosimetry, however the material does have a number of disadvantages, primarily related to its physical strength and transmission quality. Silica glass would potentially be an alternative to FP glass, as it is more mechanically robust, resistant to environmental effects and in general, due to the very low concentration of impurity ions, has better transmission quality in the relevant wavelength regions.

In the beginning of this project, the facilities available only allowed preform and fibre fabrication to be performed with soft glasses. Later in the project time-line, facilities capable of drawing silica optical fibres became available. This presented the opportunity to study silica as an alternative glass material to FP, and the work in this chapter reports the initial investigation into the potential of silica glasses for intrinsic OSL optical fibre dosimetry.

Silica glasses were therefore studied in much the same way as FP glasses were studied. An initial survey of a variety of glasses was performed, followed by luminescence characterisation of several samples which responded positively to OSL and TL tests. Optical fibres were then fabricated from this glass and radiation detection measurements performed with these fibres.

6.2 Silica Glass Samples

Previous work in Chapter 2 showed that silicate glasses, such as soda-lime-silicate and borosilicate glasses, gave an OSL response. This OSL response was seen to have slow decay rate, where readout of the sample required optical stimulation on the order of 10s of seconds in order to sufficiently deplete the trapped population of electrons. Although the integrated light-sum of the OSL response from these materials was found to be very intense compared to some other materials, the slow read-out rate is an impediment to many real-world applications. These silicate glasses were therefore ruled out as potential materials for study and silica glasses were considered instead.

Silica glass is a common material used for a multitude of applications; as such, there is wide variety of silica glasses available, each made with slightly different purity and fabrication conditions. A small selection of samples were chosen for initial analysis, and are summarised in Table 6.1. Samples of glass from optical-grade silica were sought based on their low loss, which is suitable for fabrication into optical fibres. Samples of both high purity silica (LWQ) and ultra-high purity silica (F300) were selected from Heraeus Quarzglas [128]. In addition, samples modified with boron, germanium and

phosphorus by the MCVD process [129, 130] were also sourced. These were obtained as off-cuts from preforms which were deposited on the inside of LWQ glass tubes; to isolate the MCVD-deposited glass the outer LWQ cladding layer was ground off.

Table 6.1: Silica glass samples analysed in this chapter.

Sample	Fabrication Method	Composition
LWQ	Flame Fusion	Silica
F300	Flame Hydrolysis	Silica
MCVD1	MCVD	Silica - P
MCVD2	MCVD	Silica - B, Ge, P

6.2.1 Fluorescence Emission

Experiments were attempted to obtain the emission spectra of several different silica glasses using the Princeton Instruments spectrofluorometer, but no emission signal was measured. This would be due to the low concentration of impurity ions present in these high-purity silica glasses; even for the 'lower-purity' glass, there are therefore very few defect centers which would provide radiative transitions in the material.

RL spectra were also attempted using the Princeton Instruments spectroflurometer, using the same method as is shown in Section 3.3.4, but again no signal was measured due to the low intensity of the RL signal.

6.3 Thermally and Optically Stimulated Luminescence Measurements

For initial analysis and sample screening, samples of silica glass were crushed and analysed in a Risø Reader as per the method described in Section 2.6.

6.3.1 Optically Stimulated Luminescence

Both of the wavelength regimes used for previous Risø Reader measurements were again used: 350 - 450 nm using 470 nm optical stimulation and a Hoya U340 filter, and 350 - 600 nm using 870 nm optical stimulation and a Schott BG39 filter. Irradiation times also remain consistent at 10 s, and OSL results are taken over 5 s. Before each measurement, samples are bleached out using a 300 s irradiation at 300 ℃ to remove any residual population of trapped electrons.

Certain silica samples have an intense OSL response, an example is the LWQ glass made by Heraeus Quarzglas, fabricated using the flame fusion method. Table 6.2 compares

the OSL response of two silica glasses: one glass produced by flame fusion (LWQ) shows an intense OSL response; the other sample is a silica produced by flame hydrolysis (F300), and shows a significantly lower OSL response. The OSL 'shine-down' curves are also shown in Figure 6.1. The high intensity of the LWQ glass OSL is attributed to impurities in the raw material used in the flame fusion method. In contrast glass produced by flame hydrolysis, being a vapour deposition method of fabrication, contains fewer impurities in the raw materials. A short description of the various methods used to produce high quality silica glasses for optical applications is provided in Appendix A.4. Trace impurities in the glass may act as recombination centres, fortuitously giving the glass the luminescent properties required for dosimetry. As was explained in Chapter 2, the production of OSL in a material can occur with only trace concentrations of dopant ions, and hence the impurities fortuitously present in the fused quartz would be enough to produce detectable OSL. The concentration of impurities is substantially lower in glasses produced by flame hydrolysis (vapour deposition), and hence they have a low OSL intensity in comparison with other silica glasses. Due to this, further investigation of silica used several samples of fused quartz manufactured using flame fusion (LWQ glass).

In Table 6.2 the OSL intensity is shown for measurements taken using a 7 mm thick HOYA U340 filter (stimulation at 470 nm) and a 3 mm thick Schott BG39 filter (stimulation at 870 nm). Results indicate OSL emission is primarily occurring in the transmission window of the BG39 filter, demonstrating that LWQ silica glass is suitable for use with a SPAD, as was shown in Chapter 5 for FP fibres.

Table 6.2: OSL response of LWQ and F300 silica glasses, taken for both wavelength regions using either a HOYA U340 filter or a Schott BG39. Beta irradiation applied for 10 s, and OSL intensities are normalised for mass.

Glass	**OSL (counts/g/Gy)**	
	275 - 400 nm	350 - 600 nm
LWQ	1.52E+06	0.96E+07
F300	3.21E+05	5.45E+05

Reproducibility Silica samples were also tested for their OSL response after several repeated measurements, as was previously done with both undoped and doped FP glasses in Sections 2.6.2 and 3.4.3. Again, this is performed to evaluate the ability of the material to be used for repeated measurements without accruing a population of residual trapped electrons.

Using the Risø Reader, samples were irradiated for 10 s, then the OSL response measured, followed by a specific bleaching time: 5 s or 30 s. This process was then repeated ten times in order to evaluate the ability of the material to be reset to its pre-irradiated

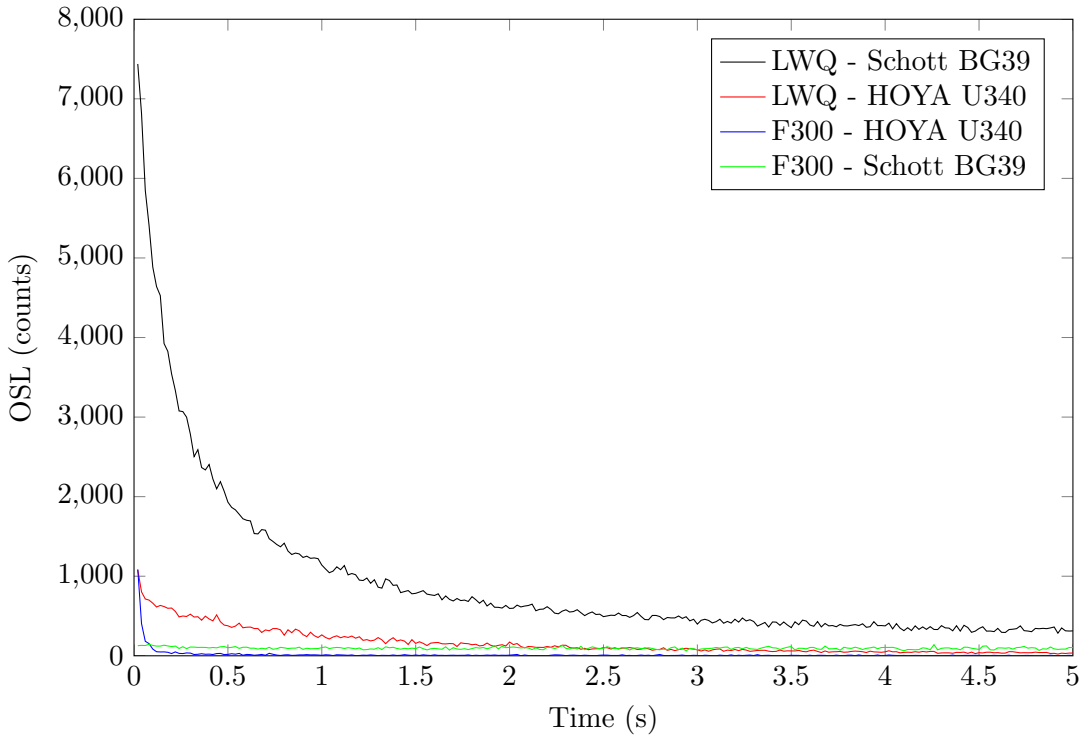

Figure 6.1: Comparison of OSL from high purity (LWQ) and ultra-high purity (F300) silica glasses. Results are taken using two stimulation wavelength and filter combinations: 870 nm stimulation with a Schott BG39 filter, and 470 nm stimulation with a HOYA U340 filter.

state. OSL measurements were taken using the Schott BG39 filter and 870 nm optical stimulation, results are shown in Figure 6.2.

From the increasing OSL response with measurement number observed, it is evident a fraction of the trapped population of electrons remains following OSL readout and bleaching. Following measurements where a greater amount of optical stimulation is applied to the samples, 976 mJ as opposed to 167 mJ, this same trend is still observed. The increase in intensity of the signal is, however, smaller when more optical stimulation is applied between measurements, as is expected. This residual trapped charge is attributed to deeper traps present in silica glass than were observed in FP glasses; these traps are analysed further in the next Section.

6.3.2 Thermoluminescence

Thermoluminescence was measured from several silica samples: beta irradiation was applied for 10 s, and TL heating to 300 ℃ was at 1 K/s. No filters were used for TL measurements, in order to reveal the total light sum. Results are shown in Figure 6.3, and the TL of undoped FP glass is also shown for comparison.

The silica glasses tested appear to have deeper TL traps than does FP1 glass: TL peaks appear at 140 ℃ in LWQ glass, silica glasses doped with phosphorous (MCVD1), and boron, germanium and phosphorous (MCVD2) exhibit peaks at slightly higher

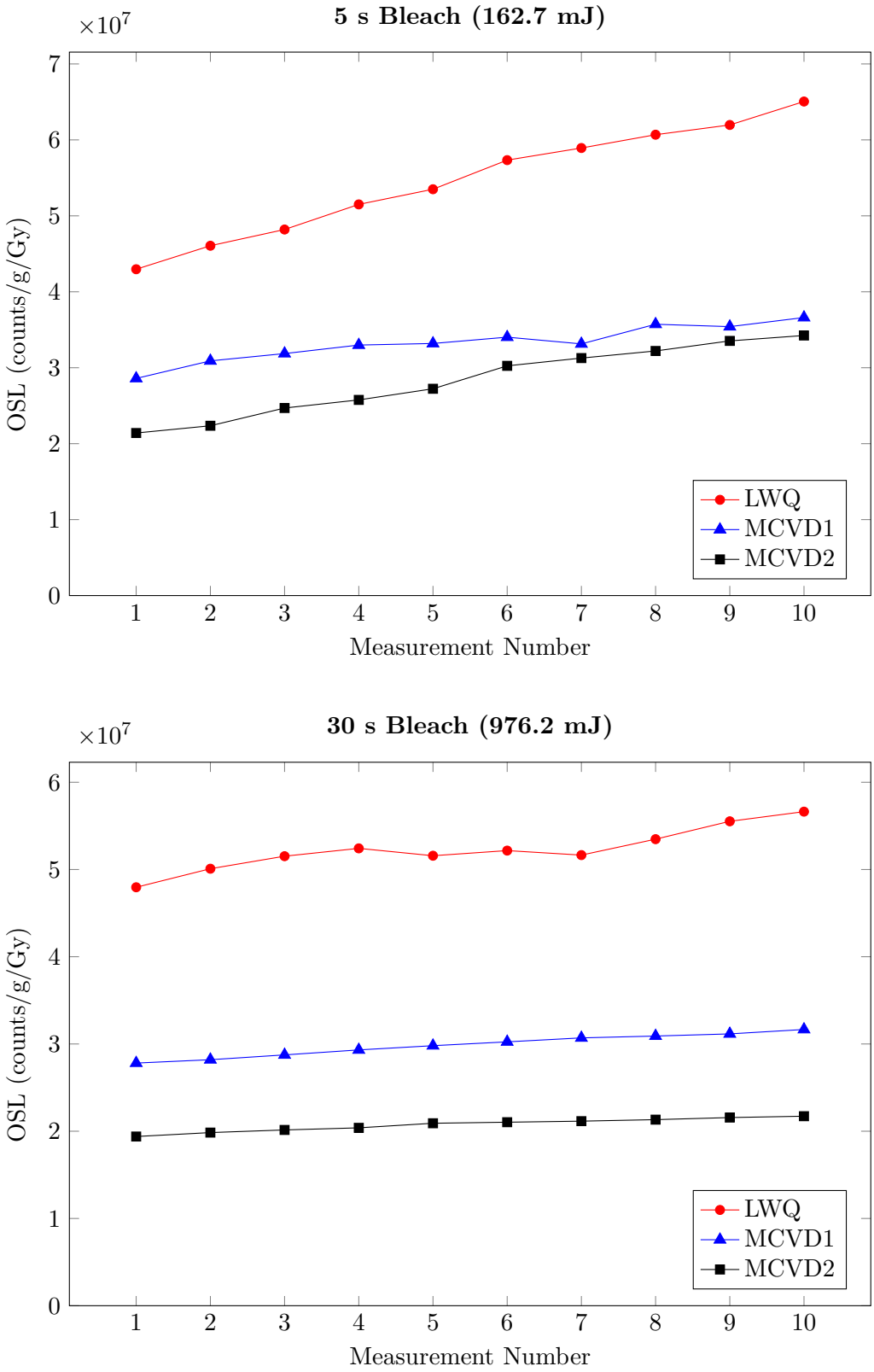

Figure 6.2: Reproducibility of silica samples LWQ, MCVD1 and MCVD2 glass in the 350 - 600 nm waveband, a Schott BG39 filter and 870 nm optical stimulation. Results are given for different bleaching times between measurements, 5 s and 30 s, the optical power incident on each sample is shown by the graph titles. Lines are provided only as a guide for the eye.

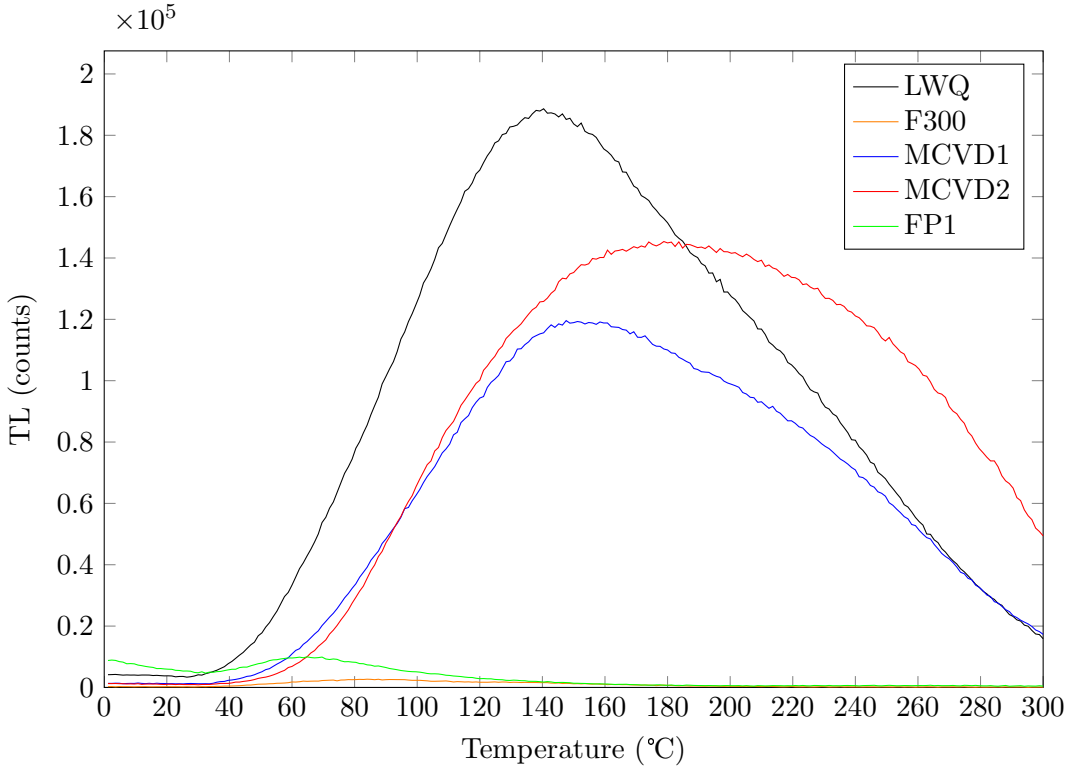

Figure 6.3: Thermoluminescence of silica glass samples. TL from undoped FP glass is also provided for comparison. No filters were used for TL here, in order to reveal total light sums.

temperatures. A significant finding is that the intensity of the TL response from silica glasses is also higher than that of FP glasses.

6.3.3 Thermoluminescence Emission Spectrometry

The TL of silica glasses was further studied using thermoluminescence emission spectrometry, as was described in Section 2.6.1. Samples were irradiated for 300 s under a $^{90}Sr/^{90}Y$ beta source followed by TL measurement, heating to 400 ℃ at 5 K/s with reheat subtracted. Due to the higher heating rate required, slight variation in the peak temperatures is seen between conventional TL and TL emission spectroscopy results. TL spectra are shown in Figure 6.4 for LWQ, MCVD1 and MCVD2. Results show the emission peak is centred at 400 nm, and does not vary with boron, phosphorous and germanium doping. The trap depths are affected, with samples MCVD1 and MCVD2 showing increased intensity and traps at higher temperatures. High intensity features at 400 ℃ are due to incandescence from the heating plate.

6.3.4 Initial Rise Thermoluminescence

Initial rise thermoluminescence was performed as per the method described in Section 2.6.1. Initial rise data is shown for LWQ in Figure 6.5. The initial rise results for LWQ, MCVD1 and MCVD2 glasses are shown in Tables 6.3, 6.4 and 6.5. Comparing to the

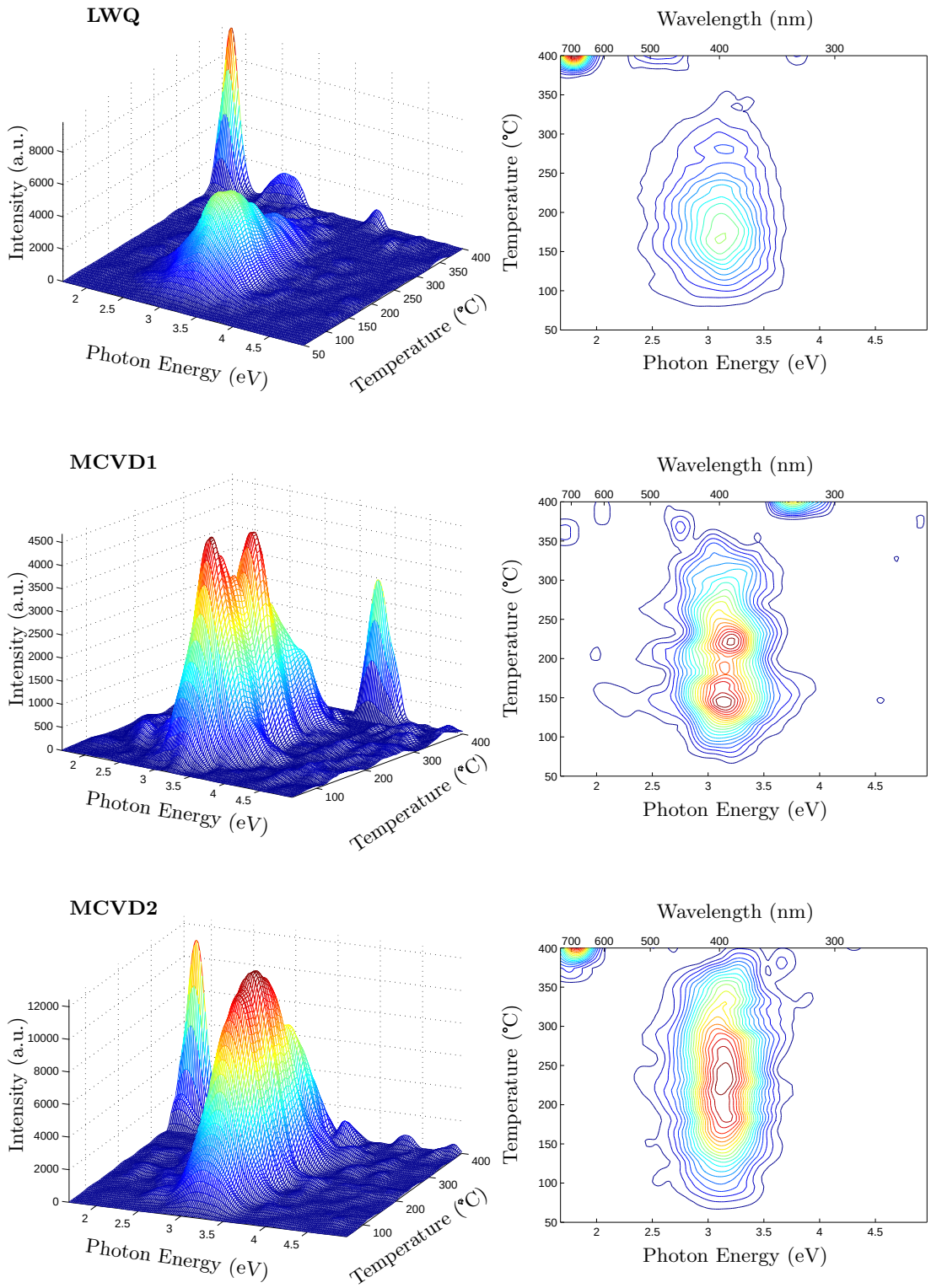

Figure 6.4: Thermoluminescence emission spectra of samples LWQ, MCVD1 and MCVD2, 3D and intensity contour plots. $^{90}Sr/^{90}Y$ irradiation time is 300 s, and the heating rate was 5 K/s.

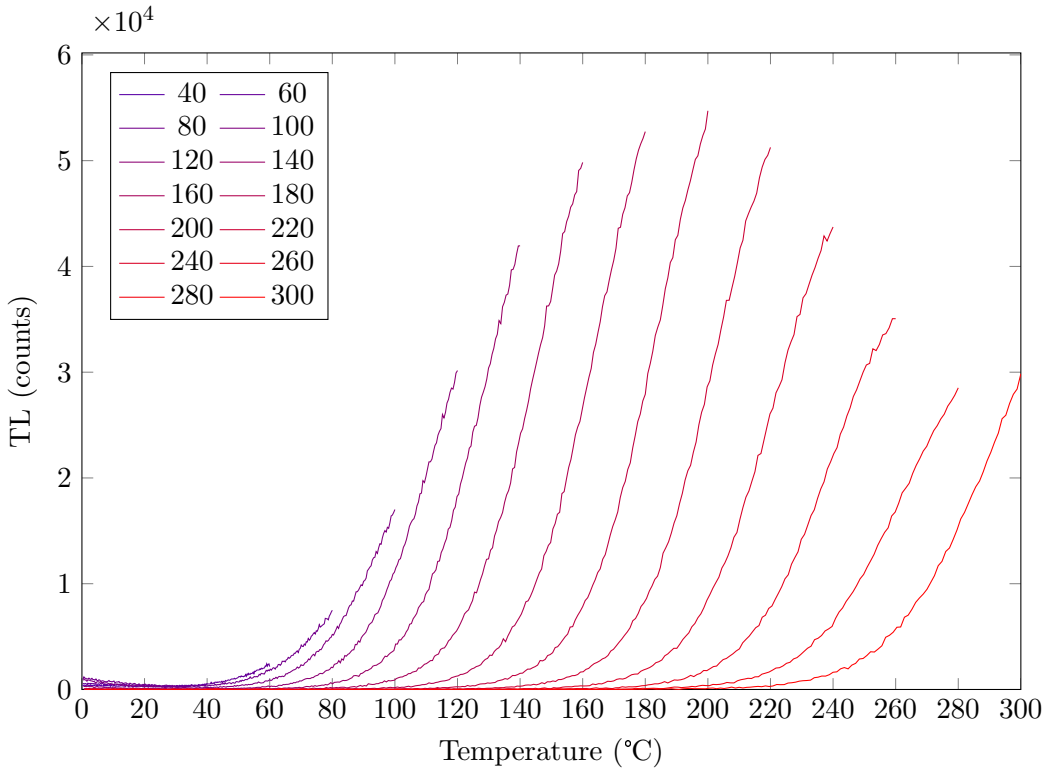

Figure 6.5: Initial rise thermoluminescence for LWQ silica. Measurements followed the procedure described previously in Section 2.6.1. Values of T_m given in the legend are in °C.

results found for FP glass in Chapter 2, the trap depths for LWQ silica are deeper and have longer lifetimes, with trap energies in the 0.65 - 0.85 eV range for LWQ, 1 - 1.3 eV for MCVD1 and 1.2 - 1.3 eV for MCVD2, indicating the glass will keep a greater fraction of its trapped population available for interrogation during an OSL measurement.

6.4 OSL in Silica Fibres and Canes

Experiments to detect the OSL response from silica optical fibres largely followed experiments performed for FP optical fibres, as reported in Chapter 5. All the experimental equipment, settings and procedures are similar to that described previously, experiments shown in this Section might therefore refer back to methods described in Chapter 5. Where necessary, extra information will be provided.

6.4.1 Fabrication of Silica Fibres and Canes

Silica fibres were fabricated out of Heraeus Quarzglas LWQ silica, chosen as a suitable candidate for producing silica fibres and canes due to the OSL and TL results shown in the previous Section, and also due to the commercial availability of the material. Like the FP fibres discussed in previous chapters, silica fibres were fabricated with a bare

Table 6.3: Activation Energy (E), Frequency Factor (s) and Lifetimes at T = 293 K (τ) for LWQ silica using initial rise data.

T_m (℃)	E (eV)	s (s^{-1})	τ (s)
60	0.41 ± 1.8E-02	7.8E+06	1.7E+02
80	0.54 ± 6.2E-01	2.3E+06	7.5E+02
100	0.44 ± 4.0E-02	3.1E+04	1.1E+03
120	0.56 ± 1.1E-02	7.4E+05	7.1E+03
140	0.68 ± 1.4E-02	8.4E+06	5.3E+04
160	0.82 ± 4.6E-02	1.7E+08	7.1E+05
180	0.97 ± 6.8E-02	3.0E+09	1.4E+07
200	0.95 ± 6.0E-02	6.9E+08	3.5E+07
220	1.01 ± 1.3E-01	1.1E+09	2.5E+08
240	1.07 ± 1.4E-01	1.4E+09	1.6E+09
260	1.16 ± 8.4E-02	4.4E+09	2.1E+10
280	1.18 ± 1.0E-01	2.7E+09	8.5E+10
300	1.13 ± 8.2E-02	3.4E+08	7.9E+10

Table 6.4: Activation Energy (E), Frequency Factor (s) and Lifetimes at T = 293 K (τ) for MCVD1 silica using initial rise data.

T_m (℃)	E (eV)	s (s^{-1})	τ (s)
40	0.57 ± 0.06	1.2E+08	64.1
60	0.77 ± 0.06	3.7E+10	495.8
80	0.84 ± 0.05	7.1E+10	3689
100	0.97 ± 0.04	1.0E+12	4.8E+04
120	1.03 ± 0.04	1.1E+12	4.1E+05
140	1.07 ± 0.04	9.4E+11	3.3E+06
160	1.14 ± 0.02	1.4E+12	3.2E+07
180	1.19 ± 0.02	1.2E+12	2.6E+08
200	1.28 ± 0.07	3.1E+12	3.9E+09
220	1.33 ± 0.13	2.6E+12	3.2E+10
240	1.38 ± 0.10	2.2E+12	2.6E+11
260	1.40 ± 0.14	1.0E+12	1.3E+12
280	1.44 ± 0.36	6.6E+11	7.6E+12
300	1.56 ± 0.70	3.1E+12	2.6E+14

Table 6.5: Activation Energy (E), Frequency Factor (s) and Lifetimes at T = 293 K (τ) for MCVD2 silica using initial rise data.

T_m (°C)	E (eV)	s (s^{-1})	τ (s)
40	0.49 ± 0.07	4.6E+06	60.5
60	0.71 ± 0.03	4.8E+09	409.0
80	0.78 ± 0.04	9.5E+09	2668
100	0.85 ± 0.09	2.5E+10	2.0E+04
120	0.93 ± 0.10	5.4E+10	1.7E+05
140	1.02 ± 0.07	1.7E+11	1.7E+06
160	1.08 ± 0.06	2.3E+11	1.5E+07
180	1.14 ± 0.07	3.4E+11	1.4E+08
200	1.23 ± 0.07	7.3E+11	1.7E+09
220	1.29 ± 0.13	1.0E+12	1.8E+10
240	1.39 ± 0.07	2.4E+12	2.7E+11
260	1.41 ± 0.10	1.2E+12	1.4E+12
280	1.43 ± 0.08	6.0E+11	7.1E+12
300	1.48 ± 0.08	5.7E+11	5.6E+13

unstructured geometry. Fibres were drawn with diameters of 160, 200, 250 and 300 µm. LWQ silica canes of 1000 µm were also drawn in order to compare with FP canes of similar diameter. Loss measurements were performed on the silica fibres, using the cutback method described in Section 4.4.1. Figure 6.6 shows the loss of silica fibres, the loss of FP fibres is also shown for comparison with the results shown in Chapter 4.

The loss of the silica optical fibre is higher than expected, with an average loss of 0.5 dB/m, the peak at approximately 1400 nm is expected due to water in the glass. For this material, a loss in the order of 0.1 dB/m is expected and has been obtained for LWQ fibres drawn with a wagon wheel microstructure using the same facilities [131], this is also shown in Figure 6.6. Loss measurements are also provided in Appendix A.4, Figure A.1 for comparison.

This high loss could again be attributed to the contamination of carbon onto the surface or into the glass, which was previously shown to produce high loss in Tb^{3+}-doped FP optical fibres. This loss could be caused by scattering from carbon impurities, or possibly crystallisation induced from contamination. Where previously carbon impurities were introduced from the crucible in which the glass was melted, in the silica glass impurities are likely to have come from the liner of the heating element used in the fibre drawing tower. Prior to the drawing of these fibres, a new liner was installed which required a certain 'burning in' period of at least 10 hours, during which loose material is burnt off from the surface. It is possible this element did not receive a sufficient 'burning-in' before the fabrication of these silica fibres, in which case impurities could have contaminated the silica glass, causing high losses due to scattering.

It is important to mention the LWQ silica canes were fabricated at a different time,

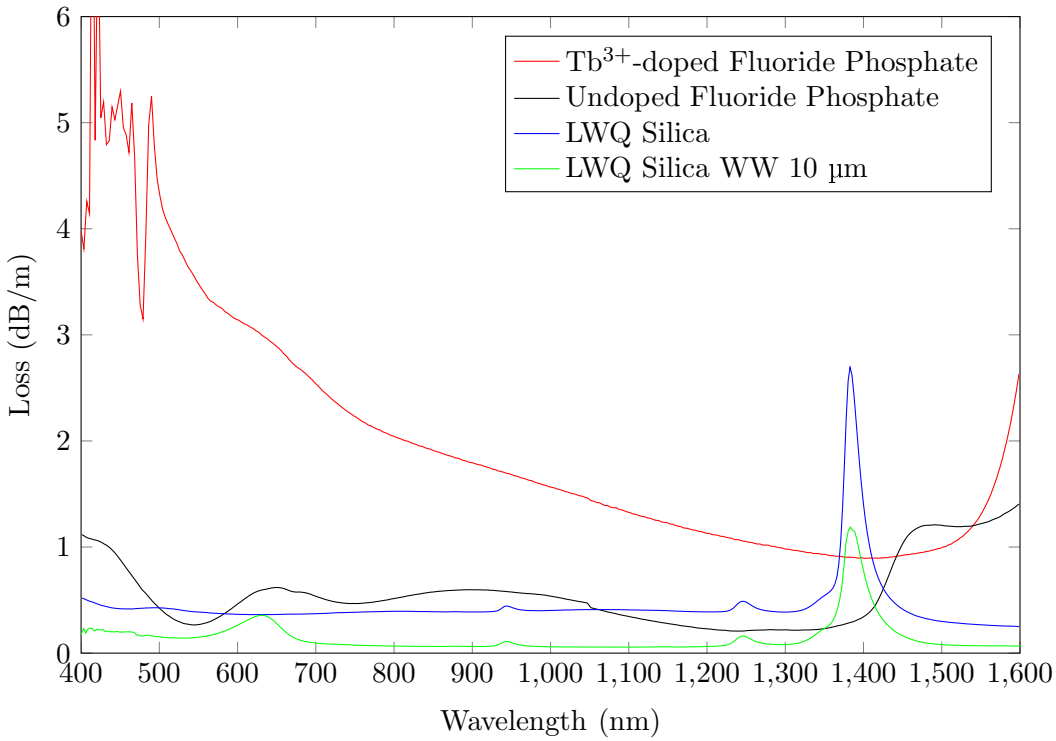

Figure 6.6: Comparison of LWQ and FP glass optical fibres. Both undoped (F15) and Tb^{3+}-doped (F19) FP fibres are provided. The bare silica fibre fabricated for this project (LWQ Silica) is compared with the loss of another fibre fabricated from the same glass for a different project (LWQ Silica WW 10 µm). This demonstrates the high loss measured for LWQ Silica, at 0.4 - 0.5 dB/m, higher than the expected 0.1 dB/m observed in the fibre LWQ Silica WW 10 µm. The expected H_2O peak at approximately 1400 nm is observed for both silica fibres.

prior to the furnace liner change. They therefore would not have been effected by the contamination likely experienced by the fibres. As a result of this, silica canes are expected to have lower loss than the fibres, with loss values closer to that reported in Appendix A.4. Due to the shorter length of canes, it is not possible to perform loss measurements to confirm this.

6.4.2 OSL in Optical Fibres

Optical fibres were tested for their OSL response using the same method described in Section 5.5, using silica fibres with 160 and 200 µm diameters and a 1 mm diameter cane. Irradiation of fibres with the $^{90}Sr/^{90}Y$ beta source was applied for 120 s, for optical fibres the dosage is approximately 15.5 ± 0.5 Gy. Results for the cane and for fibres are shown in Figure 6.7.

Over the measured length of 800 mm, little attenuation of the OSL signal is observed as is expected from the lower loss of silica fibres compared with FP. Longer lengths of silica glass were measured in both the 350 - 650 nm and 350 - 450 nm wavebands, and an example of the results can be seen in Table 6.6. Results show OSL detection is possible using longer lengths of fibre: intense OSL signals were measured in fibres with

lengths of 8-9 meters. Considering the loss of these silica fibres is higher than expected, as was discussed in Section 6.4.1, if new silica fibres are produced OSL results could feasibly be taken using even longer lengths.

These results reinforce the findings reported in Chapter 5, where radiation detection is performed using an OSL response within an optical fibre, and again demonstrate proof-of-concept of intrinsic OSL fibre dosimetry, now with an alternative material.

Table 6.6: Length of silica fibre at which an OSL signal is measurable using an absorbed dose of 15.5±0.5 Gy from a ^{90}Sr/^{90}Y beta source. Measurements were performed using both wavelength regimes: stimulation at 532 nm using a Schott BG3-BG39 filter stack, and stimulation at 852 nm using a Schott BG39 filter.

Fibre	Length (m)	RL (counts/s)	OSL (counts)
532 nm stimulation - BG3/BG39 filter stack			
160 µm	4.6	31 ± 5.5	933.5 ± 105.7
250µm	2.4	14 ± 3.7	254.9 ± 31.3
852 nm stimulation - BG39 filter			
160 µm	7.5	80 ± 8.9	447.3 ± 44.9
250µm	8.6	79 ± 8.9	385.7 ± 43.4

6.4.3 Dose Dependence

The OSL response to applied dose from a ^{90}Sr/^{90}Y beta source was measured using the same method described in Section 5.4.2. OSL measurements were performed on samples of 1 mm silica cane drawn from Heraeus LWQ silica, and the OSL response was measured with respect to the applied dose, as in Section 5.4.2, where both exposure time and source activity were used to adjust the applied dosage. For exposure time, this experiment was performed separately using both a PMT and a SPAD. For the experiment with the PMT, the experimental setup is the same as shown in Figure 5.15, using a 532 nm laser for stimulation and a Schott BG3 filter. For experiments using the SPAD, the setup is as shown in Figure 5.23, with the 852 nm laser for optical stimulation and a Schott BG39 filter.

Results can be seen in Figures 6.8, 6.9 and 6.10. An immediate observation is the linear trend observed in Figure 6.8 when using the PMT, this result is consistent with what is shown in the literature for Cu^{+}-doped silica [69, 71, 72]. In these studies PMTs were also used for luminescence detection, however exposure was performed with ^{60}Co gamma ray sources, and the optical stimulation in each case was at 790 nm at a power of approximately 200–250 mW. In contrast to this result, the trends observed in Figures 6.9 and 6.10 are polynomial. This could possibly be due to the different stimulation and detection regimes, where 852 nm stimulation and a Schott BG39 filter are used with the SPAD instead of the 532 nm stimulation and Schott BG3 filter used with the

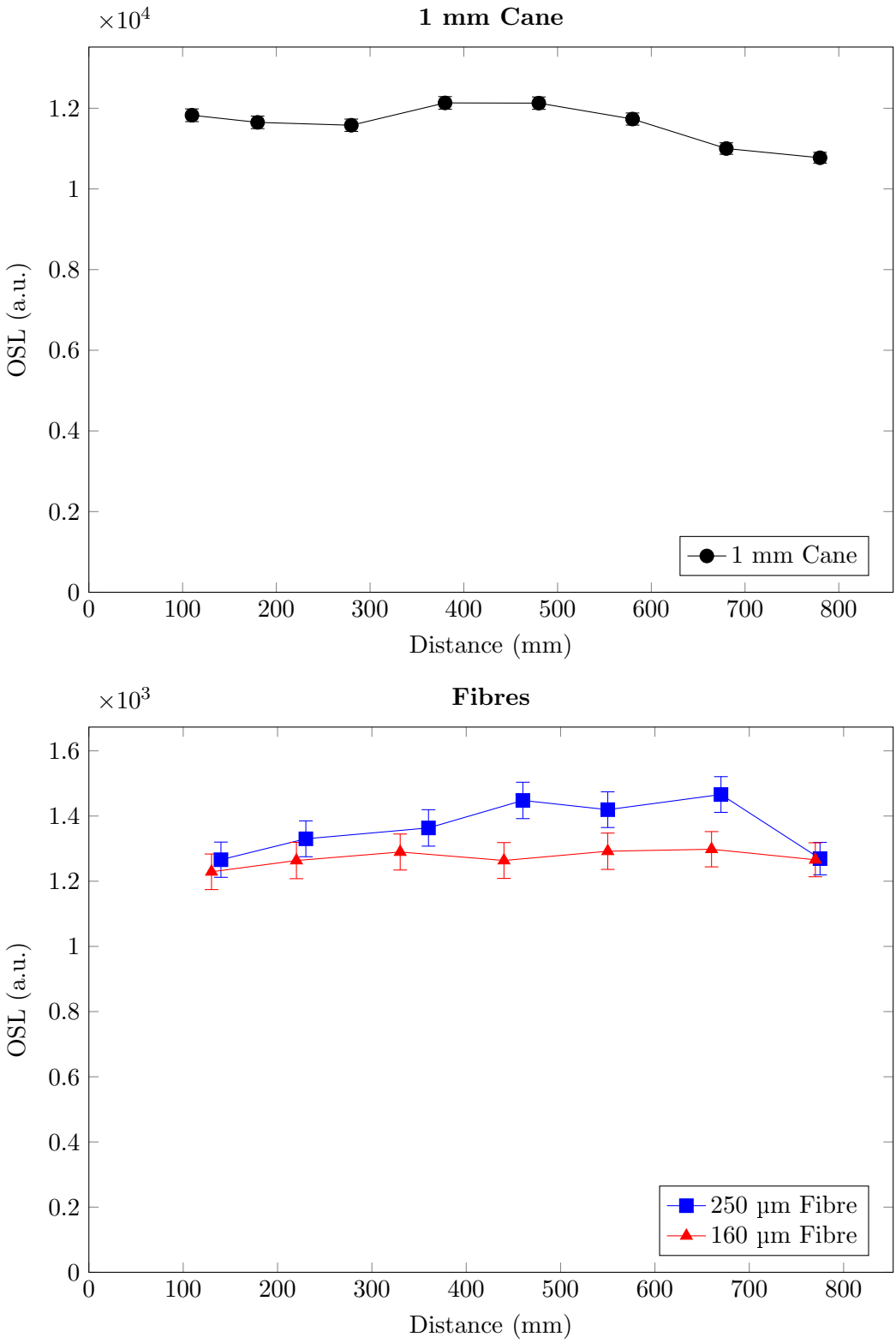

Figure 6.7: OSL intensity with respect to the position of the $^{90}Sr/^{90}Y$ beta radiation source along LWQ silica cane (top) and fibres (bottom). Lines are included only as a guide for the eye.

PMT. The possible explanation could be incomplete bleaching of the material during optical stimulation with 852 nm, leaving a small residual population of charge accruing after each measurement. As the dose for each measurement is increasing, the size of this residual excited population would also increase with each measurement, but this would be expected to produce a linear trend, not the polynomial trend observed in Figures 6.9 and 6.10.

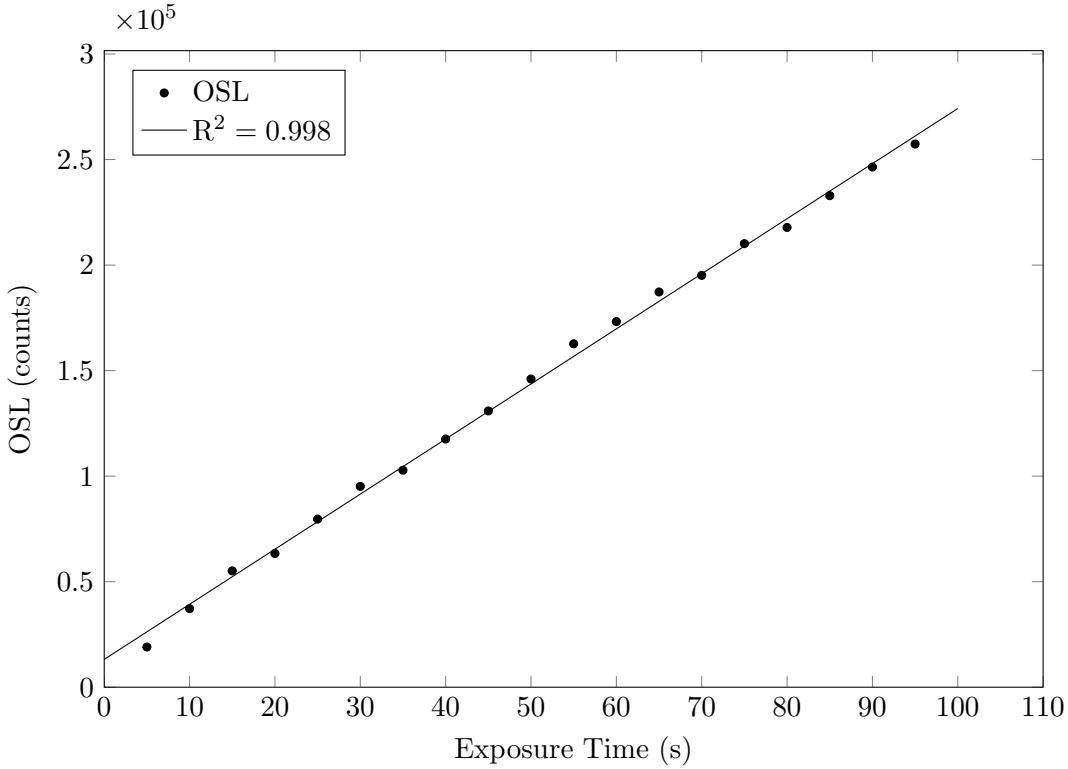

Figure 6.8: Dose dependence of OSL from 1 mm diameter LWQ silica cane. Detection using a PMT, optical stimulation at 532 nm and filtration with a Schott BG3.

6.4.4 X-ray Irradiation

Investigations of the effects of X-ray irradiation were conducted in parallel with experiments performed on FP glass, using the DSTO X-ray facility. The experimental methods used for measurements testing the response with respect to beam intensity and X-ray tube potential are almost identical to those shown in Section 5.6, with the exception of the length of silica fibre used. Due to the high loss[1] of the Tb^{3+}-doped FP glass (F17) only short lengths of 870 nm were used, the LWQ silica fibre had lower loss and therefore longer lengths were used, most experiments used lengths of approximately 1800 mm.

For all experiments using the X-ray facility optical stimulation was at 852 nm using the 100 mW laser source, a Schott BG39 filter was used for isolation of the OSL signal

[1]Both intrinsic fibre loss, and loss induced by photodarkening.

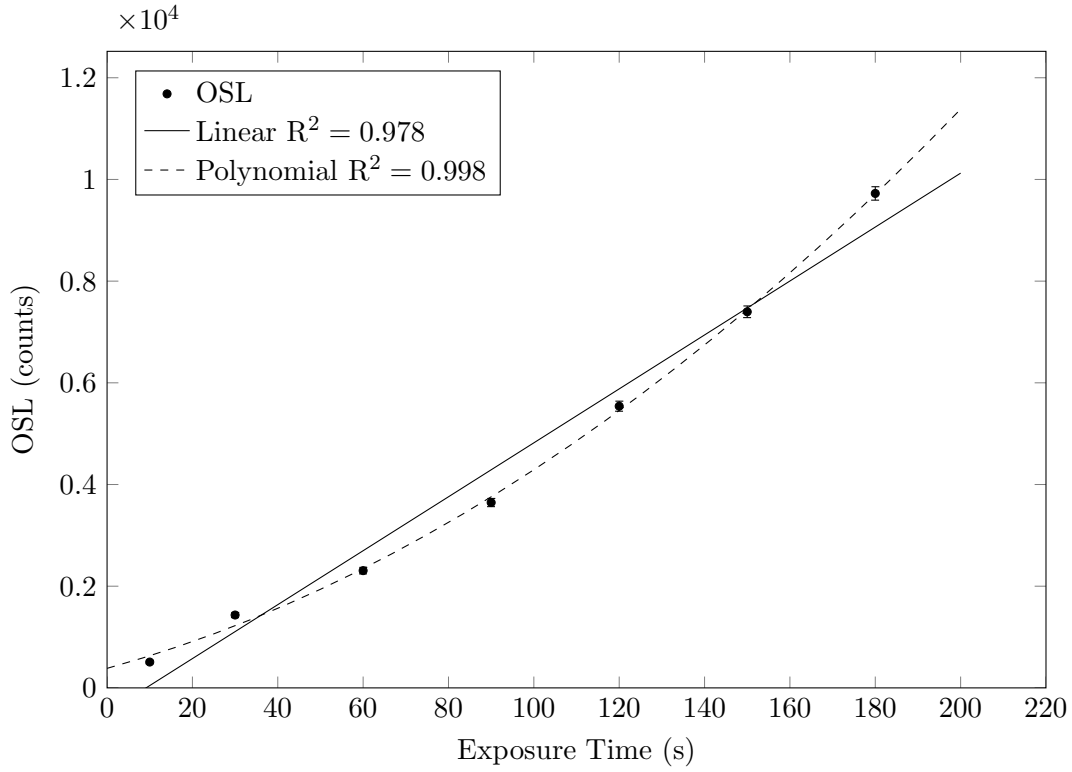

Figure 6.9: Dose dependence of OSL from 1 mm diameter LWQ silica cane. Detection using a SPAD, optical stimulation at 852 nm and filtration with a Schott BG39.

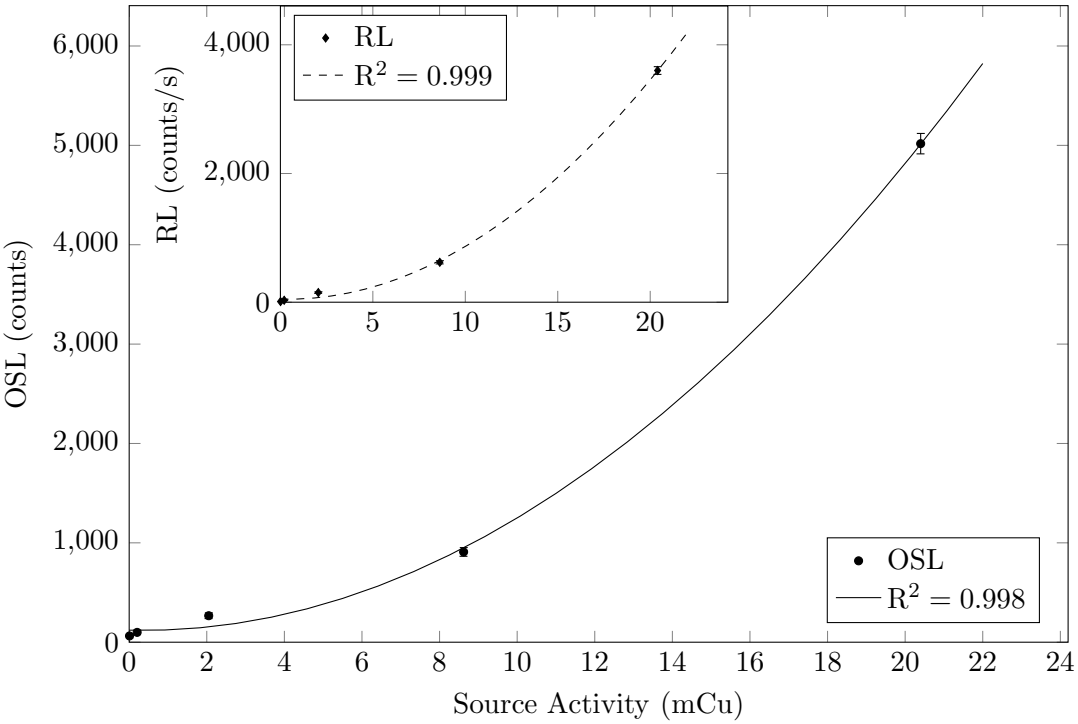

Figure 6.10: Dose dependence of OSL from 1 mm diameter LWQ silica cane. Detection using a SPAD, optical stimulation at 852 nm and filtration with a Schott BG39. Variation in dose is due to the activity of the $^{90}Sr/^{90}Y$ beta source. Inset: results were also recorded for the RL with respect to activity of the $^{90}Sr/^{90}Y$ beta source.

in the 350–600 nm region, and detection was performed using the Lasercomponents SPAD. A 532 nm laser was used in conjunction with neutral density filters to aid in alignment and optimisation of the optics.

Due to the higher OSL signal intensities measured compared with FP fibres, further tests were performed on silica which were not performed on FP glass, such as the OSL response as a function of fibre diameter and the OSL response with respect to the aluminium shielding thickness.

X-ray Beam Intensity

OSL as a function of beam intensity gives a linear response for tube potentials of both 100 and 300 kV, shown in Figure 6.11. The polynomial increase in OSL observed in Section 6.4.3 when using the $^{90}Sr/^{90}Y$ beta source is not observed here. There might therefore be some difference in dose deposition effect on the OSL between beta and X-ray irradiation.

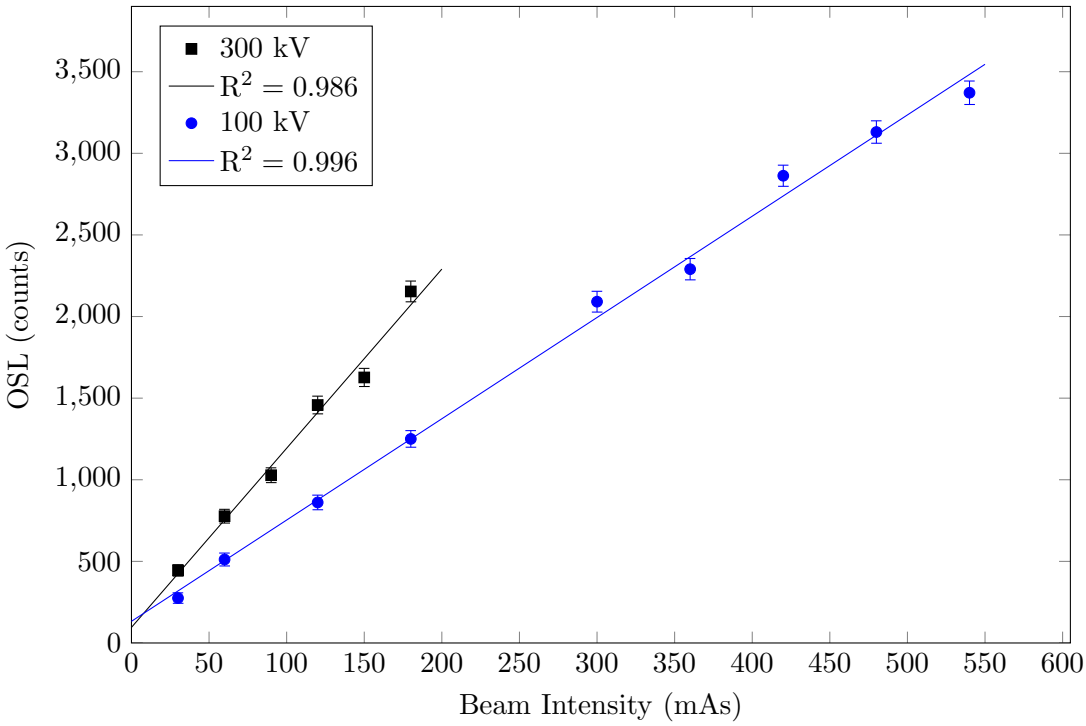

Figure 6.11: OSL response of LWQ silica fibre with respect to beam intensity at tube potentials of 100 and 300 kV.

X-ray Tube Potential

OSL as a function of the X-ray tube potential is shown in Figure 6.12 for fibres of several different diameters. Previously in Section 5.6.2 the OSL response for FP fibres was seen to decrease as a function of tube potential. Here, results for silica glass show

the opposite trend, where increasing the tube potential increases the OSL response. As was done previously for FP glass, simulations were performed in PENELOPE using the same parameters described in Section 5.6.2, where the FP glass material was changed to silica (SiO_2). The results of this simulation are shown in Figure 6.13, where the energy absorbed by the glass volume increases with respect to photon energies in the 70 – 300 keV range.

Measurements were also taken for silica fibres without the aluminium cover-plate of the fibre holder, as per the method described in Section 5.6.2, results are shown in Figure 6.14. Again, a linear trend is observed for the OSL with respect to the X-ray tube potential over a photon energy range of 30 - 80 keV.

Silica and FP glass appear to have a similar response to X-ray photon energies in the 30 - 100 keV range, when no aluminium cover-plate is between the X-ray head and the fibres. However at energies up to 300 keV, with the aluminium cover-plate in place, the response of FP glass and silica differ: the OSL of FP is seen to decrease with respect to energy, and the OSL from silica is observed to increase. This could be a result of the difference in composition and density between the two glasses, which affects the mass stopping power of the material. This could also be a measurement artifact due to the photodarkening observed in FP glasses when using photon energies between 100 - 300 keV: it could be the OSL response is following an increasing trend with respect to photon energy, but the increasing fibre loss results in a lower detected OSL signal at the fibre output.

Optical Fibre Diameter

The increase in OSL intensity with respect to the diameter of silica fibres can be seen in Figure 6.12. Due to the inflexibility of 300 µm fibres, lengths of 630 mm were used. This result agrees with every past experiment performed, where the OSL increases with respect to the mass or volume of irradiated glass.

Aluminium Shielding

Measurements were performed whereby the thickness of an aluminium absorber between the X-ray source and the optical fibre was changed. Thin sheets of aluminium were stacked on top of the fibre holder, then for each measurement a sheet was removed, decreasing the total shielding thickness. A beam intensity of 180 mAs and an X-ray tube potential of 100 kV were used for each measurement.

Results are shown in Figure 6.15(a), and show a significant drop in measured OSL intensity with respect to aluminium thickness. Between 0 and 12 mm the drop in

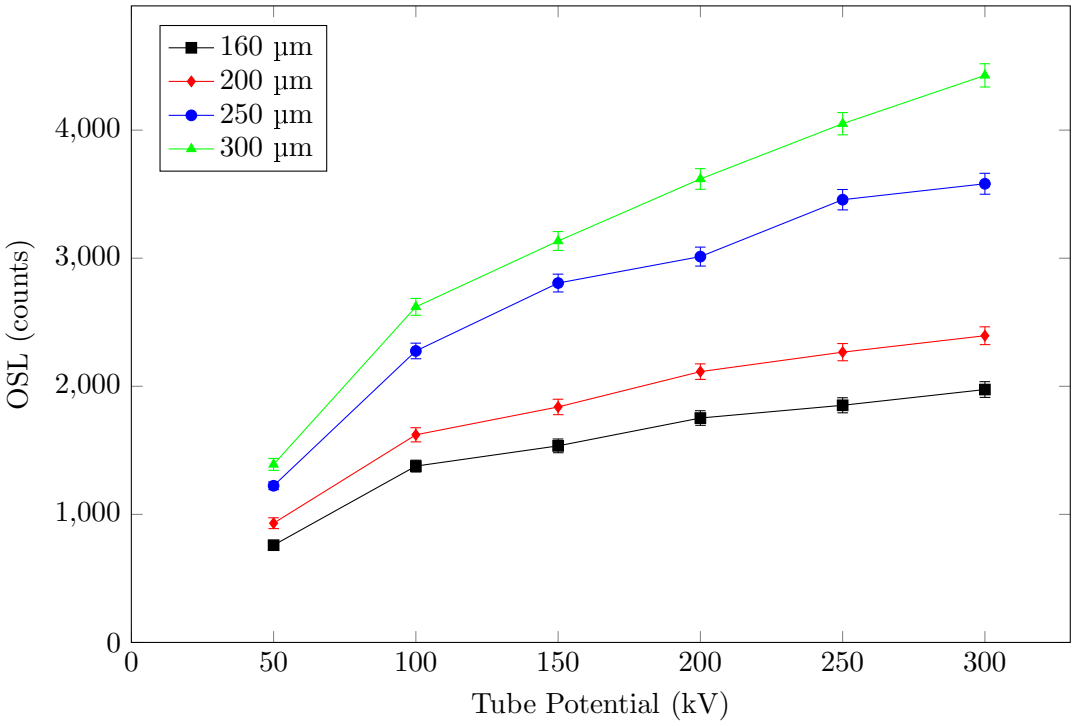

Figure 6.12: OSL response with respect to X-ray tube potential using LWQ silica optical fibres of varying diameter. Optical stimulation at 852 nm, using a Schott BG39 filter. Lines are included only as a guide for the eye.

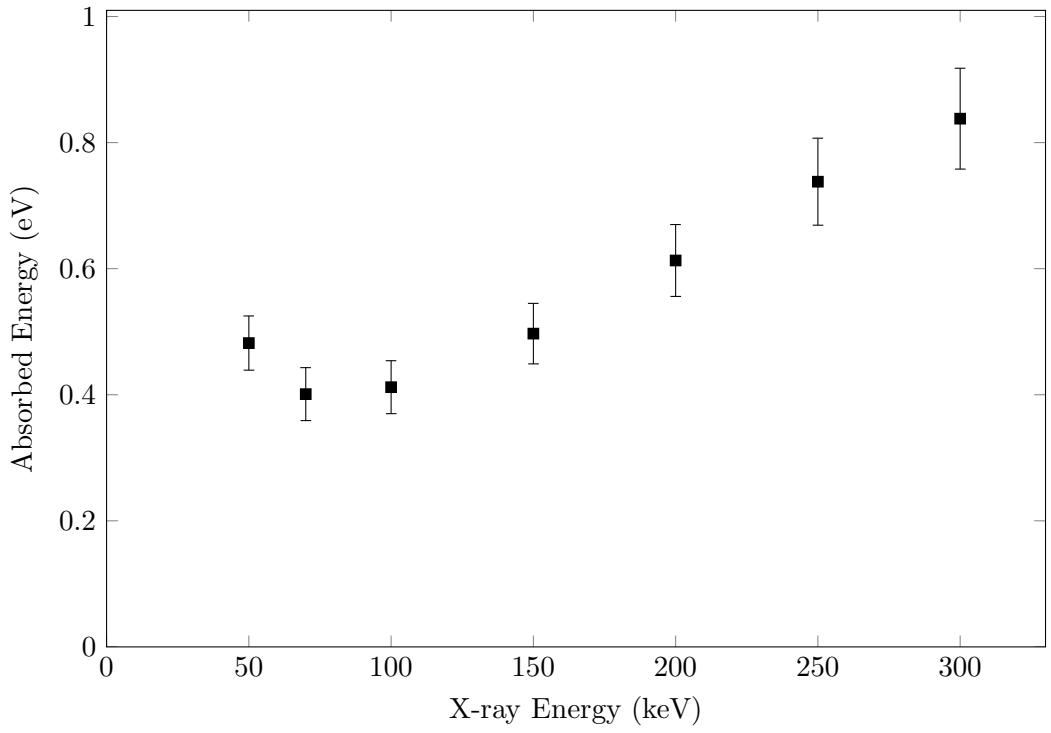

Figure 6.13: Simulation showing energy absorbed (dose) by silica fibre with respect to X-ray photon energy.

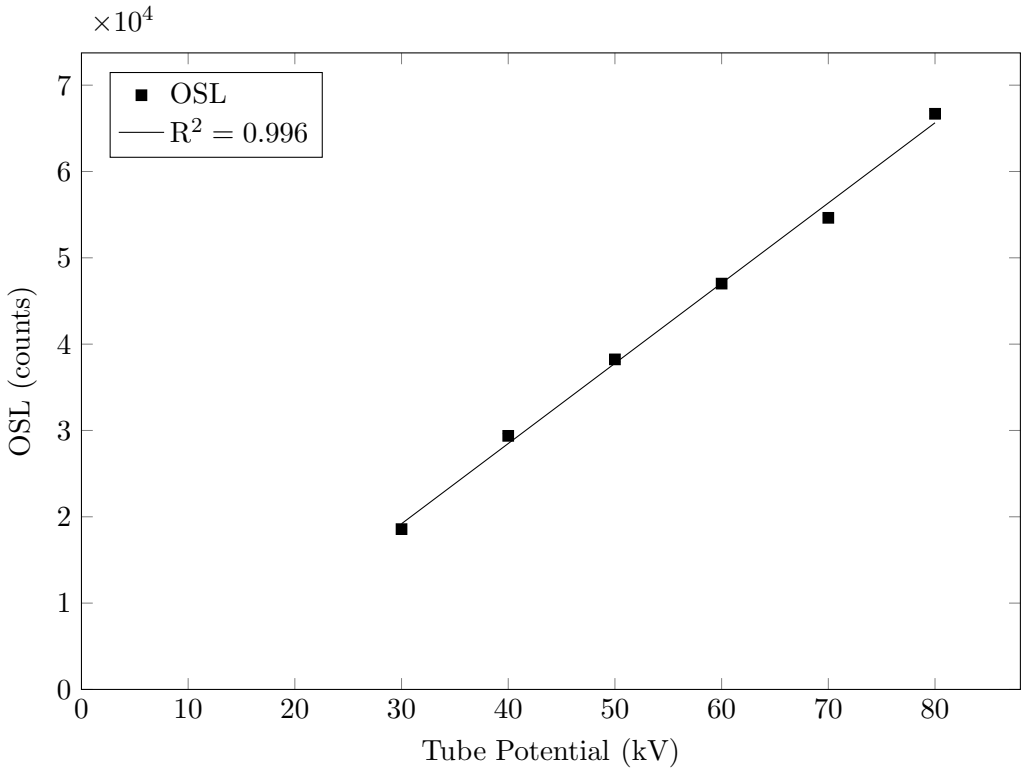

Figure 6.14: OSL response with respect to X-ray tube potential at a beam intensity of 600 mAs. Measurements taken without the aluminium lid of the fibre holder.

response is arguably linear, if the datum at a thickness of 4 mm is assumed to be an outlier. Following this, the OSL response remains consistent around 500 counts and does not decrease appreciably with the increase in aluminium thickness. Given the bremsstrahlung spectrum for a 100 kV tube potential, there will be a large proportion of photons in the 20 to 40 keV range, and a smaller proportion of photons in the wide 40 to 100 keV range. This spectrum may help to explain the results seen in Figure 6.15. The low energy photons will contribute a large fraction of the energy absorbed in the glass, however photons in this energy range will be quickly attenuated by layers of aluminium up to approximately 12 – 15 mm. The small proportion of higher energy photons will still be able to penetrate a significant distance through the aluminium layer and can deposit energy into the glass. This mixture of photon energies apparently explains why there is an initially rapid decrease in OSL intensity as the lower energy portion of the beam is absorbed, followed by a more gradual drop in intensity for thicker aluminium layers.

This scenario was simulated using PENELOPE, for 10, 40 and 100 keV photons. The absorbed energy with respect to aluminium thickness is shown in Figure 6.15(b). 20 keV photons are observed to deposit the highest amount of energy into the glass volume, however they are attenuated quickly. 100 keV photons do not deposit a large amount of energy in the glass volume, however they penetrate through a thick layer of aluminium and are still able to deposit a small amount of energy. Compiling the

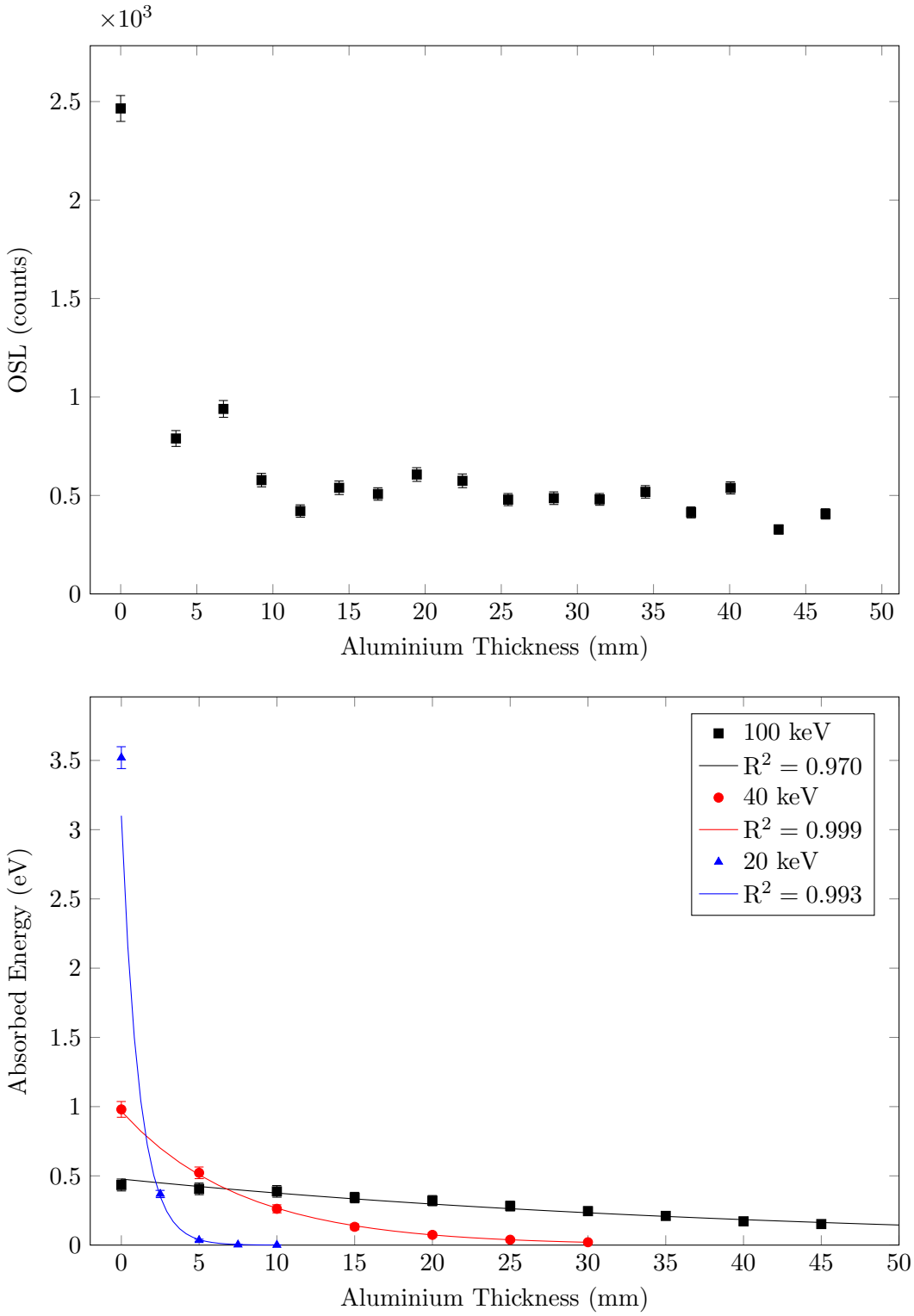

Figure 6.15: (a) OSL response with respect to thickness of aluminium shielding between the X-ray source and the fibre. (b) Simulation of absorbed energy in an FP glass volume behind aluminium layers of varying thickness using PENELOPE. Several different initial photon energies were simulated.

absorbed energy for these different photon energies, a trend similar to that shown in Figure 6.15 is observed. Although this is just one demonstration of the behavior of the fibre detector behind layers of shielding, it highlights the importance of considering the energy and type of the radiation being detected, and the environment in which the detector is placed. Depending on these parameters, further experiments would need to be performed with specific radiation types, energies and shielding materials relevant to the application for which the dosimeter would be used.

6.5 Comparison of Silica and Fluoride Phosphate Glasses

6.5.1 Transmission Loss

The loss of the silica glasses studied here (0.5 dB/m) are comparable to that of the best quality fluoride phosphate fibres fabricated for this project (0.5 dB/m), as was shown in Figure 6.6, the loss of fibres made from both of these materials could also potentially be improved. Based on results taken for other LWQ silica fibres, it is evident that this is achievable for the LWQ glass, whereas improvements in the loss of Tb^{3+}-doped FP fibres might require further research and optimisation.

This lower loss is an advantage when considering applications requiring long lengths of fibre, or faint optical signals. In each case, the transmission quality of the silica glass will make it more capable of transmitting a signal to the detector. LWQ silica fibres also appear to be less susceptible to photodarkening than FP fibre, which could be useful if they are required to remain in a radiation field for long periods of time.

6.5.2 Mechanical Strength and Jacketing

Optical fibres made of silica glasses have greater tensile and flexural strength than those made from fluoride phosphate glasses. For practical applications of optical fibres in various environmental conditions, this alone is a major advantage in favour of using silica fibres.

Jacketing of delicate optical fibres offers protection from deformation and stretching, the weakness of fluoride phosphate fibres may therefore be overcome. Jacketing of OSL-sensitive fibres is already a necessary step for practical applications, due to the light-tight environment required for storage of the dose information.

6.5.3 Thermal Properties

Silica glass requires higher temperatures for softening or melting than fluoride phosphate glass. FP glass is therefore more suitable for lab-based experimentation, due to the lower temperatures and less specialised equipment required. As was demonstrated in Section 3, FP glass can be melted in the laboratory and dopants introduced directly into the melt. This process is not possible for silica glass without furnaces and equipment capable of working at temperatures of up to 2000 °C.

6.5.4 Trap Lifetime

As seen from reproducibility measurements on both FP and silica glasses, FP has the ability whereby the population of trapped electrons is quickly removed and the material is 'reset' to its pre-irradiated state by a short period of optical stimulation. This was attributed to the shallow traps present in the material, and although doping with rare earth ions was found to create deeper traps, bleaching out the material was still found to be efficient. Silica, in contrast, contains deeper traps and removing the population of trapped electrons entirely was found to require more optical stimulation. If making a device using silica glass, intense optical stimulation will be required if repeated measurements need to be made to avoid buld-up of residual dose.

6.5.5 Doping of Glasses

The low solubility of rare earth and transition metal ions in silica makes doping of silica glass a non-trivial exercise. FP glass can be homogeneously doped using a melt-quench method, where the dopant compound is simply introduced into a melted glass. This is possible in FP glass due to its low melting point and also the high solubility of rare earth ions in this glass. In comparison, rare earth ions have a low solubility in silica glass and doping at high concentrations is difficult due to clustering. The facilities available to this project also do not include suitable equipment for the doping of silica glasses in molten form.

Doping with Cu^{+}-ions has been achieved previously by impregnating a porous glass with a solution containing copper ions, followed by sintering at 1000–1200 °C [132–134]. The sol-gel technique has also been used to produce doped silica glasses [26,70,135]. In each case, a porous silica is required for introduction of the dopant ion into the material.

Modified chemical vapour deposition (MCVD) is also a commonly used method for fabricating doped optical fibres [129, 130]. Boron, phosphorus and germanium can be introduced as a gas and deposited along with the silica formed from silica tetrachloride,

followed by consolidation into fused silica, which results in a preform of very pure silica containing layers of dopant ions in the core region. Alternatively, solution doping is used for rare earth and transition metal ions, whereby ions in a solution are diffused into the porous silica layer prior to consolidation into fused silica. This method of doping can achieve precise doping in layers in the core region of a preform. This method, however, is not capable of producing a preform homogeneously doped with the desired ion. For high dose rate applications, it is possible doping only in the core region would be adequate to produce sufficient volume of radiation-sensitive material for an effective OSL-active optical fibre, in which case the MCVD process would be potentially suitable. However, in situations where the whole fibre needs to be doped, this approach would be inappropriate.

An alternative to the MCVD process is the sintering of doped silica powders, a method which produces large, homogeneously doped fibre cores [136]. Unlike the MCVD process, SiO_2 is not deposited within a tube but rather particles of SiO_2 are suspended in an aqueous solution doped with the desired ions. Doped granulates are then sintered into homogeneous and bubble free silica rods; they can then be over-clad with other silica materials prior to fibre production. The performance of fibres fabricated from this method are comparable to those made by MCVD methods.

The fabrication of doped silica is therefore a process requiring specialised equipment and access to high-temperature furnaces. In the current context, soft FP glasses are a more appropriate material with which to explore the behavior of various dopant ions in glass, as they can be processed at much lower temperatures.

6.5.6 Luminescence

The OSL intensities for bulk FP and silica glasses, measured in the Risø Reader, are summarised in Table 6.7 and Figure 6.16. The oxidised Tb^{3+}-doped FP glass has the highest OSL response, in both the 275 – 400 nm and 350 – 600 nm wavebands, LWQ glass by comparison has a modest OSL intensity. This should imply that higher OSL intensities should be measured from Tb^{3+}-doped FP glass optical fibres than from silica fibres, however if the OSL results found in Chapters 5 and 6 are compared, this is not the case, measurements on silica consistently have higher OSL intensities compared to FP glasses. From this we can conclude that transmission loss has a significant impact on the effectiveness of the FP fibres, and even if the OSL signal is more intense in Tb^{3+}-doped FP glass, the low loss of silica glass when compared with Tb^{3+}-doped FP makes it more effective when in an optical fibre form.

Table 6.7: OSL response of silica glasses compared with doped and undoped FP1 glass, fabricated under both oxidising and reducing conditions, integrated from 0 - 0.2 s. '275 – 400 nm' indicates OSL in this wavelength region, achieved using a HOYA U340 filter and 470 nm stimulation. '350 – 600 nm' indicates emission in this wavelength region achieved with a Schott BG39 filter and 870 nm stimulation.

Sample	**OSL (counts/g/Gy)** $\times 10^5$	
	275 – 400 nm	**350 – 600 nm**
FP1 - Ox	75.6	8.8
FP1 - Red	107.3	12.3
Cu - Ox	268.8	30.1
Cu - Red	548.2	40.7
Mn - Ox	69.1	13.2
Mn - Red	38.7	10.1
Tb - Ox	1007	812.3
Tb - Red	77.4	60.3
LWQ	29.8	99.3
F300	2.8	5.6
MCVD1	17.7	36.1
MCVD2	11.3	33.7

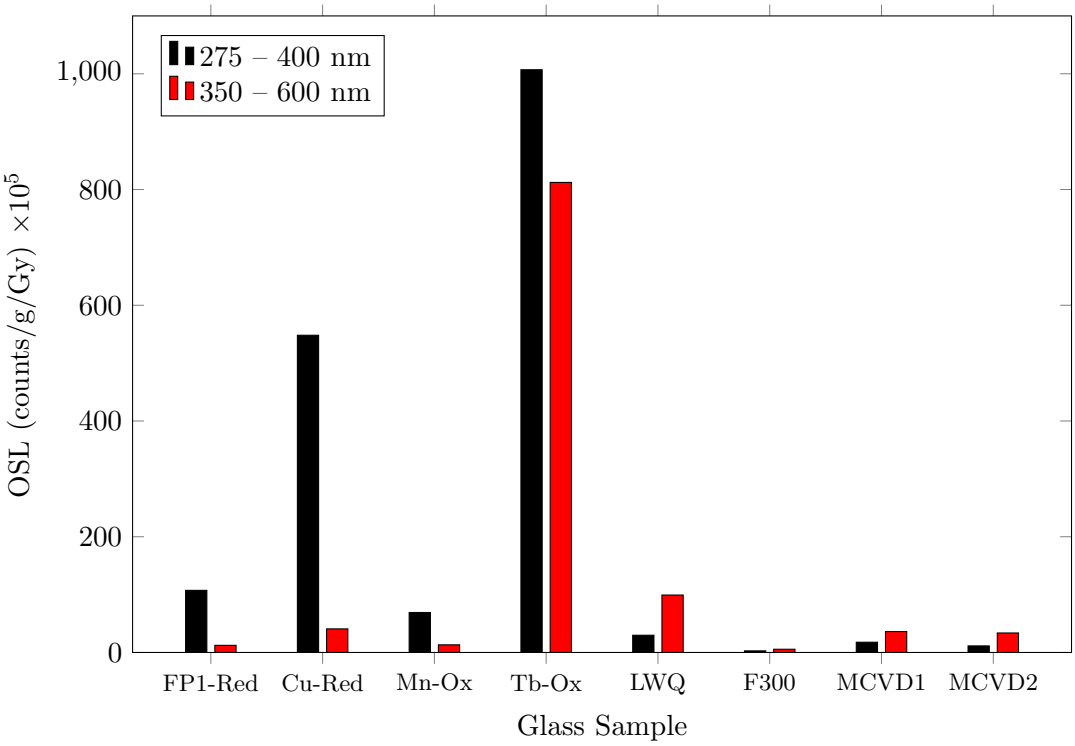

Figure 6.16: Plot of the OSL data provided in Table 6.7, shown for both 275 – 400 and 350 – 600 nm wavelength regions. OSL results for silica glasses are compared with selected FP samples, both doped and undoped.

6.5.7 Bleaching and Re-usability

While both silica glass and FP glass have reasonably rapid read-out times using the experimental methods here, undoped FP glass has the shallow trap structure which ensures a negligible amount of trapped charge remains after a short period of time. The 60 ℃ peak has a short lifetime, and any trapped charge remaining after stimulation soon becomes untrapped thermally, which is critically valuable for applications requiring quick and efficient bleaching of the fibre between measurements. On the other hand silica glass has a broad TL peak centered at 140 ℃; and due to the longer trapping lifetimes of these deeper traps, electrons will not be rapidly untrapped thermally at ambient temperature. It is slightly harder to ensure complete re-setting of the material between measurements without first heating the material to at least 300 ℃. The usefulness of FP glass in this area is identified mainly in undoped glasses, and due to the formation of deeper traps, samples doped with Cu^{+}, Mn^{2+} and Tb^{3+} can require more bleaching. As was shown previously, however, increasing the optical stimulation power and time can still efficiently optically bleach these glasses.

6.6 Conclusions

Silica glass is a very good candidate for many optical fibre dosimetry applications: it is shown to have intense OSL and TL signals if sufficient impurity ions are present in the glass to act as pseudo-dopants. LWQ silica glass was fabricated into optical fibres, and radiation-sensing measurements performed. OSL was successfully detected using lengths of 8 - 9 meters of fibre, demonstrating their potential as intrinsic OSL fibre dosimeters for distributed radiation sensing.

Compared to terbium doped FP glass, which has an OSL intensity at 1007×10^5 counts/g/Gy in the 275 - 400 nm waveband and 812.3×10^5 counts/g/Gy in the 350 - 600 nm waveband, silica glass has a lower OSL intensity at 29.8×10^5 counts/g/Gy in the 275 - 400 nm waveband and 99.3×10^5 counts/g/Gy in the 350 - 600 nm waveband. However, the good optical and mechanical properties inherent to silica glass set it above FP glass as an optical fibre material, particularly when considering transmission loss and the ability to transmit the OSL signal to the detector.

Chapter 7

Discussion, Conclusions and Future Work

A wide range of experimental work has been presented in previous chapters, covering materials characterisation, doping of glasses, optical fibre fabrication and dosimetry measurements using these fibres. This work will be summarised and put into the broader context of the state of the art of radiation dosimetry. Conclusions drawn from the experimental results will be discussed and compared, and an appraisal of the feasibility of the optical fibre dosimeter system for real-world applications will be presented. Following this, possible future directions for further research in the field of distributed optical fibre dosimetry will be discussed.

7.1 Summary of Experimental Work and Key Results

The material properties of fluoride phosphate glass, a soft glass identified as a suitable glass OSL phosphor, were studied. This involved characterisation of its composition, spectral, optical and luminescent properties. FP glass was identified as one of the few materials capable of acting both as an OSL phosphor and as a glass suitable for optical fibre fabrication. Furthermore it is a soft glass, enabling glass processing and optical fibre fabrication at relatively low temperatures.

Trace impurities in the glass were found to be suitable as electron and hole traps, to enable radiative transitions and so produce luminescence. TL and OSL measurements showed the glass contains many shallow traps with short-lifetimes, making it an easy material to optically bleach and one that would not retain dose information between successive measurements, and hence would not be subject to changing sensitivity. The intensity of the OSL response was found to be proportional to the applied dose, meaning the glass is suitable for quantitative dosimetry measurements.

The luminescence response of FP glass was found to be adjustable with the addition of various transition metal and rare earth elements. The spectroscopic properties of various doped FP glasses were studied and the most suitable dopant elements identified. The luminescence properties of these doped glasses were also measured and compared with both undoped glass and other doped glasses. Of the elements trialed, the addition of Tb^{3+} to the FP glass was found to be the most suitable for the aims of this project, as it was found to substantially increase the detectable OSL signal in the relevant wavelength region.

The parameters used for successful fabrication of optical fibres were established: extrusion of polished FP billets through a stainless steel die at 525 ℃ at a rate of 0.05 mm/min in a nitrogen atmosphere, followed by polishing of the preform using a diamond paste and 40 nm colloidal silica. The identification of crystal formation during the fibre drawing stage was identified as the major source of scattering loss in the resulting fibre, and careful polishing to remove the surface layer of preforms was identified as an efficient way to remove the effects of this crystal growth. Optical fibres with diameters between 160 – 300 µm were reproducibly fabricated from these preforms at a temperature of 755 ℃ and a feed rate of 2.5 – 3 mm/min under a nitrogen atmosphere, the loss of these fibres was in the 0.5 – 1 dB/m range in the absence of dopant ions. Fibre yield was dependant on the length of the preform fabricated, however lengths of between 50 – 100 m were consistently achieved.

Fabrication of optical fibres from Tb^{3+}-doped FP glass was also achieved, although the loss was increased due to the remelting process and/or the addition of Tb_4O_7

to the glass: loss values of 2 - 4 dB/m were measured. It was found that melting in a vitreous carbon crucible in a reducing environment produced high loss due to the introduction of carbon impurities into the glass. Melting in a platinum crucible in an open-air environment was subsequently found to produce fibres of significantly improved quality.

To demonstrate the feasibility of achieving the project aims: intrinsic OSL radiation sensing in optical fibres, dosimetry experiments were conducted using these fibres fabricated from FP glass. Due to the geometry of optical fibres, and the ephemeral nature of OSL signals, several experimental difficulties such as poor signal-to-noise, inefficient optical signal capturing, and prevalence of scattered stimulation photons were overcome in order to successfully detect an OSL response from FP glass optical fibres. The suitabilities of SPAD detectors for luminescence work was demonstrated, and they are confirmed as a smaller, more efficient alternative to PMT detectors.

Similar luminescence characteristics to those identified previously in the bulk glass material were again observed when the glass was drawn into optical fibre form. The response of Tb^{3+}-doped optical fibres was also investigated. The dosimetry capabilities of optical fibres were demonstrated for both β and X-ray radiation sources. Alternative radiation-induced phenomena, RL and photodarkening, were also identified in the optical fibres.

Following the demonstration of FP glass as a material capable of optical fibre dosimetry, silica glass was also tested as an alternative glass material. A certain type of silica glass, LWQ, was identified and characterised in a similar manner to the FP glass. This glass was then fabricated into optical fibres and tested under the same conditions as the FP glass with a resulting loss of 0.5 dB/m. The silica glass was found to produce an intense luminescence signal, but not higher than Tb^{3+}-doped FP glass. In optical fibre form, however, the lower loss of the silica fibres when compared to the Tb^{3+}-doped FP fibres was found to be a major advantage, and more intense signals were measured using longer lengths of optical fibre for both beta and X-ray irradiation.

7.2 Trap Lifetime of Fluoride Phosphate Glass

A useful property of undoped fluoride phosphate glass discovered in this work was its shallow distribution of electron traps, leading to a short lifetime at ambient temperature of the trapped electron population. This is an extremely useful property of the material, as it lends itself to complete re-setting of the material during each optical interrogation. All the electrons are readily removed from their traps and no deep traps exist in which electrons can accrue and remain for long lifetimes, removing the potential

consequence of a slowly changing dose response. This is especially useful when using longer stimulation wavelengths, which might not have the required photon energy to excite electrons from deeper traps, and when annealing the device is impractical.

The complete re-setting of a material during its duty cycle is important for applications requiring a series of repeated measurements, with minimal variation in the OSL and RL sensitivity, such as during radiotherapy treatments [137]. Many materials used for OSL and RL measurements have a tendency to preserve a fraction of the population in their traps, producing an accumulating background between each measurement cycle; this was observed in particular for Al_2O_3:C [34, 60, 61, 63]. To correct for this, calibrations have to be made in order to subtract the background from the true dose measurement [34]. Alternatively, materials are 'pre-dosed' until the background signal is at a consistent, unchanging level [61, 63].

Using a material which provides a consistent response between measurement cycles removes the need for any background calibrations to characterise the performance of the chip after repeated usage, or to 'pre-dose' it before measurements begin.

7.3 Feasibility of the Optical Fibre Sensor

The aim of this work was to explore the feasibility of optical fibre dosimeters which utilise an optically stimulated luminescence response within the optical fibre material. From the work presented in this thesis, it is evident this fibre sensor concept *is* feasible.

There are a number of advantages and disadvantages that may affect the practical use of the proposed fibre dosimeter. What may be a disadvantage in one environment, however, may be considered an advantage in another; it essentially comes down to the desired function of the fibre sensing device in its intended application. Some of these advantages and disadvantages will now be discussed, along with an evaluation of how this might effect practical usage of the optical fibre sensor.

Jacketing Fluoride phosphate optical fibres are fragile. Jacketing of optical fibres would be a necessity in almost all conceivable applications, not just for the mechanical protection they offer, but also for optical isolation. Due to the nature of the OSL mechanism, stray light incident on the fibre is going to prematurely stimulate an optical signal, ruining the function of the sensor, and excessive stray light could potentially destroy the SPAD or PMT detector in any environment that is not light-tight. Optically opaque jacketing will therefore be required, as well as an extra glass cladding layer to provide the refractive index contrast for confinement of the beam. The thickness and composition of the jacket material would need to be considered carefully, due to

interaction of ionising radiation with the jacket before reaching the optical fibre. Depending on the type and energy of the radiation being monitored, this jacket material may have a substantial impact on the function of the device. High energy photons would not be significantly affected by a jacket, whereas beta particles might be significantly attenuated depending on the jacket thickness, composition and beta particle energies. In some cases, interaction of the ionising radiation with the jacket might be advantageous, such as where dose build-up is achieved in the jacket layer, allowing an increased proportion of energy to be deposited in the underlying optical fibre.

Fibre Transmission Loss The transmission loss of the glass can be affected by glass fabrication, doping and photodarkening, but the importance of this loss will depend on the application. In some cases a long fibre will be desired, in which case the glass would need to be designed to produce a low-loss fibre, with other parameters such as sensitivity given secondary importance. In this case, a small signal propagated a long distance might be more useful than an intense signal which can only propagate along a short length of fibre. Other applications might require only a short length of sensitive fibre, in which case transmission quality can be sacrificed in order to produce an intense OSL signal. Photodarkening can also affect the loss, so in applications where the fibre will receive a high dose, a material less prone to photodarkening might be preferred.

Sensitivity Sensitivity of a dosimeter is fundamentally a measure of the number of photons produced by a unit volume of material when exposed to a unit dose. Hence a sensor can be made more effective either by increasing the sensitivity of the dosimeter material, or increasing the amount of material. As was discussed in the previous paragraph, increasing the sensitivity of the material may affect other parameters such as optical transmission quality. However, increasing the mass or volume of the active material may be impractical for a given application, either due to geometry constraints or due to the decreased flexibility of optical fibres with larger diameters. Consequently, the means of increasing the sensitivity of the device would be chosen depending on the application for which the device is to be used.

Trap Lifetime Fluoride phosphate was shown to be a material with shallow traps in which trapped electrons may be expected to have a trapping lifetime of only several tens of seconds to several minutes. For applications requiring a long integration time, five minutes for example, this glass would be an unsuitable choice as much of the trapped charge will decay before a measurement is performed. In contrast, for applications requiring a complete re-setting of the device between successive measurements, fluoride phosphate glass would be an excellent candidate: shallow traps would be efficiently

bleached by a short pulse of light and there are no deep traps to retain electrons, hence no residual dose accrues over successive measurement cycles. This accrual of residual dose has been shown to be a problem in other dosimeter materials, materials with this characteristic, such as FP glass, might be usefully employed in these areas.

Glass Materials The use of glass often comes at the price of material sensitivity. Many dosimeter crystals have been developed over the years [79], some of which are extremely sensitive. The use of glass as a dosimeter material can offer an interesting range of geometries not possible using dosimeter crystals. Optical fibres are the prime example, but other geometries may have useful applications, such as imaging plates, spheres or other 3D objects. As demonstrated in this thesis, different types of glass can potentially be used depending on the requirements of the application, and furthermore, these glasses can be tailored to the specific needs of an application. As was described in Section 6.5, where fluoride phosphate and silica glasses were compared, materials like fluoride phosphate are useful for experimentation due to the ability to easily alter the composition and doping of the glass.

Alternative Phenomena In the glasses tested, OSL was not the only radiation-sensing technique possible: RL and photodarkening were also observed. For some applications, these phenomena might be considered undesirable: photodarkening decreases the optical quality of a glass, and may be a problem for fibres with sensitivity limitations, or systems using long fibre lengths; RL may be considered noise, a large background signal over which the OSL signal would need to be detected. These properties of the glass must be considered when designing a dosimetry system and in some cases have the potential to make the whole system infeasible.

On the other hand, both RL and photodarkening could be used in conjunction with an OSL signal to make a multi-functional detector. For example, RL may be used to indicate the presence of a radiation event; performing an OSL measurement on the fibre would then indicate if the RL response was truly revealing the occurrence of a radiation exposure, or if the system has given a false positive for unrelated reasons. Photodarkening may be used to monitor a high dose rate radiation field over a long period of time by periodically testing the change in optical transmission (loss), while OSL could be used in the same fibre for one-off measurements.

This section has presented a variety of advantages and disadvantages of using glass optical fibre dosimeters and it is evident the feasibility of both FP and silica glass fibre dosimeters depend directly on the application for which they will be used.

7.4 With Respect to the State of the Art

The introduction to this work in Chapter 1 gave an overview of already existing fibre dosimeters and the mechanisms by which they operate. The use of OSL produced within the optical fibre element of a detector was identified as a niche that had not yet been explored, hence the overarching aim of this thesis was to fill this technological gap. This is the first example of an OSL material being developed specifically for use as an optical fibre material. This has been achieved, with the successful demonstration of dose-dependent OSL responses from optical fibres in a variety of environments.

The basic concept demonstration of the optical fibre radiation-sensing system is only the beginning: presented here is the potential of such materials to be configurable based on the specific aims of each application. The soft FP glass can be readily manipulated both compositionally and physically to optimise its luminescence behaviour, and the work shown here is but a small introduction for what could potentially be tested in the future.

Furthermore, considering application to dosimetry, OSL is not the only radiation-detecting mechanism available: for dosimeter crystals, one can find examples in the literature of both RL and OSL being utilised within the same device [60, 63]. In addition, we can see examples of both photodarkening [43–47, 65] and RL [26–29, 138] in optical fibres, however an optical fibre utilising both phenomena simultaneously is not common. What has been shown here is a fibre system capable of not just OSL, which in itself is unique, but a system capable of also utilising RL and photodarkening for radiation exposure detection and potentially for quantitative dosimetry measurements.

In addition to the overarching goal of exploring intrinsic OSL optical fibre dosimeters, several other interesting ideas have been explored which might gain a unique place in the established literature. For example, the means for fabrication of fluoride phosphate glasses into optical fibres has not been explored extensively. Existing work shows the use of the rotational casting method to fabricate the optical fibres [89, 109, 110], but also shown in this thesis is the fabrication of FP optical fibres using the extrusion technique, and in addition, an exploration of what could be done to optimise this technique. Outside of the field of dosimetry, FP glasses are useful as high refractive index, low dispersion, UV transmitting soft glasses [87–91, 105, 109, 139] and they have been explored as potential materials for producing lasers [101, 107, 140, 141]. Fluoride phosphate glasses are therefore useful in other fields, to which the work presented in this thesis might contribute.

Another innovation in this thesis is the use of a single photon avalanche diode as the detector integrated to a fibre. The majority of past and current experimental work in

the field of dosimetry utilises photomultiplier tubes and other such photon detecting devices, but not the recently introduced SPADs. SPAD devices are shown to be capable of higher quantum efficiency with a lower dark current, and are sensitivity over a wider range of wavelengths. A key advantage of SPADs is that their pixellated structure, in principle, allows size customisation to match single fibres. A large proportion of the experimental work performed for this project was accomplished with the use of a SPAD for detection of luminescence, and showed that these detectors are viable as an alternative detection system for low intensity signals, a critical advantage in applications which might require a smaller, more flexible device.

In summary, the work presented in this thesis fills a gap in the established technologies studied in the field of optical fibre dosimetry. Certain limitations and problems with the sensor design have been identified or confirmed, and in many cases use of already existing techniques would be preferable. The fact remains, however, that intrinsic optical fibre sensors could be used for certain applications and in certain environments where current dosimeter devices are incapable or inefficient. One such example is the monitoring of the radiation field across a wide area, a single optical fibre device is more efficient than a number of individual point sensors distributed across the environment. Optical fibres also make ideal probes due to their long and thin geometry, they are capable of insertion into tight or remote environments.

7.5 Alternative Ideas for Optical Fibre Dosimetry

Over the course of a project, it is natural to think about related possibilities outside the main sphere of the project goals. Several ideas for alternative methods in which optical fibres may be used to detect ionising radiation have been considered. While not directly relevant to the stated aim of this thesis, these alternative methods might potentially be useful in other dosimetry applications and are worth summarising here.

Combination Sensors Briefly discussed in previous sections, these optical fibres would use the multiple radiation-sensing phenomena available to optical fibres. As an example, there are four potential combinations possible using FP glass: OSL with RL, OSL with photodarkening and RL with photodarkening, and all three. Depending on the application, these combinations could be used to enrich the information extracted from the dosimeter. For example, two different sensing techniques could be used to double-check a detection event, to ensure the signal is not a false-positive. Another example is to use the RL component as a real-time sensor, with a cumulative dose

measurement provided by an OSL reading [1].

Radio-photoluminescence Radio-photoluminescence (RPL) dosimetry in glass materials has been demonstrated as a viable dosimetry method [142–145]. When ionising radiation interacts with the material it causes a change in the emission spectrum, due to ionisation of dopants or the formation of colour centres. The magnitude of change in the intensity of emission peaks in the material can therefore be used as a dosimetry method.

The literature suggests these glasses have only been used in their bulk form: no work suggests these glasses have been fabricated into optical fibres. The optical properties of such glasses would need to be studied as an initial part of such a venture, as the dopants and activator ions used to produce the RPL might affect the transmission quality. Such a fibre could potentially be a very useful device, solving the problem encountered when using OSL and RL: where luminescent photons produced are a direct result of the interaction of ionising radiation with the glass, and are thus low in intensity.

The signal produced by an RPL, being essentially a fluorescence signal, can be integrated for as long as is required to achieve suitable statistics, a method which is not possible when using OSL and RL. Furthermore, RPL could still be used for real-time monitoring, as the change in band-gap produced by any ionising radiation will simply create a fluorescence signal at a certain wavelength which can immediately be detected. Due to the change in the bandgap structure of the glass during irradiation, RPL glasses can be kept as a permanent record of the irradiation event. Otherwise, they can be reset using a thermal annealing cycle. This last point, however, is a severe drawback which prevents this method from being used in many applications where the device needs to be 're-set' between measurement cycles.

Spatial Resolution Achieving spatial resolution in a dosimetry fibre might be possible when using OSL, RPL or RL. Time-correlated measurements could be performed over long lengths of fibre, but would depend strongly on the decay time of luminescence following optical stimulation, high spatial resolution is achieved when this decay is on the order of nanoseconds.

Techniques also exist to probe an optical fibre at discreet spatial positions using counter propagating waves in the optical fibre, in which the frequency of each causes a beat pattern in intensity [146]. This could potentially be used in conjunction with OSL, where the intensity region creates the optical stimulation necessary for the OSL response to

[1] One could argue that integrating the RL signal will give a cumulative dose, but there are problems encountered using RL, such as the stem-effect, which might be solved by utilising an OSL component.

occur. It has been shown in Section 2.6.2 that the OSL response is intensity dependant up to a certain value, therefore this suggests the trapped population of electrons would not significantly be depleted by a low intensity signal in the fibre, and would only be efficiently untrapped by a higher intensity optical stimulation. This technique could also be tested in conjunction with a RPL fibre, where an intense signal will only be created when the high-intensity region reaches the irradiated region of the optical fibre, creating the fluorescence response.

Exposed Core and Microstructured Optical Fibres Alpha particles, due to the short distance over which they lose their energy, have not been considered within the scope of the work presented in this thesis. Even if an alpha particle were created directly adjacent to an optical fibre, its energy would be absorbed by the fibre jacket, and would not penetrate into the fibre core. To enable this interaction of alpha particles with a fibre core, exposed core optical fibres could potentially be used. The energy from the alpha particle could be deposited straight into the core of the fibre, creating a RL or OSL response. Various designs exist for exposed core optical fibres [147, 148], and would depend on the environment and application. One problem with this technique is the lack of optical isolation from the environment.

An alternative method might be to use a microstructured optical fibre using a wagon wheel geometry, where a small volume of liquid or gas can be loaded into a wagon wheel fibre, allowing direct interaction with the fibre core. This might be a potential method to use with liquids or gases containing alpha-emitting particles.

7.6 Future Directions

As is usually the case with research, more questions emerge than are ever adequately answered over the course of an investigation. Answering one question will usually create a handful more, opening up many avenues of potential further research. This project was no exception, and many unanswered questions and untrod paths still remain, waiting for the curious researcher. This section will discuss some of the potential future work most relevant to the stated aims of the project, that being the production of an OSL-based intrinsic optical fibre dosimeter.

Dopants in Fluoride Phosphate Glass An accessible avenue of further research is to further explore the effect of dopants on the OSL response of FP glass. Several transition metal and rare earth dopants were already studied, but further analysis of their effect on the luminescence and optical properties of the glass is needed. A wider

variety of other rare earth and transition metal dopants and co-dopants in FP glass could also be tested, potentially producing a material better optimised for dosimetry purposes. Work in this area can readily be continued using the methods for remelting, doping, characterising and fabricating FP fibres already demonstrated in this thesis: all that is required is the acquisition of additional FP bulk glass, and alternative dopant compounds where necessary.

Silica Glass An important area requiring further research is the use of silica glass. They were demonstrated as a robust and sensitive alternative to FP glass, however the work presented here only briefly touches on the diverse possibilities available with silica glasses. To begin, only a small range of silica glasses were studied here: there are many other varieties of silica glass available commercially which could be analysed, as silica glasses are available with a diverse range of composition and fabrication techniques.

Following a comprehensive study of silica glasses, further work would be needed on the doping of these silica glasses. Similar to FP glasses, doping of silica glass could potentially increase the optical and luminescent properties of a dosimeter fibre, but due to the high temperatures involved when processing silica glasses, suitable doping methods would need to be identified, followed by the fabrication of doped samples to analyse for their optical and dosimetry properties. Methods may include the MCVD technique, diffusion of ions into porous glass or the REPUSIL[2] method [136].

Design of a Field-Portable Device The experiments presented in this thesis were performed on a lab bench, using mostly free-space optics to allow maximum experimental flexibility. While somewhat portable, the experimental setup is unsuitable for immediate real-world application and remains as a proof-of-concept test-bed. Further work in this area could be enhanced by the simplification of the bench apparatus into a more compact, field-portable configuration. A system whereby various different optical fibres could be plugged into the compact device would allow efficient testing of new materials and fibres in a range of environments. A schematic of a potential system is shown in Figure 7.1(a), where all the elements used in the test-bed could be reduced in size and positioned inside a small, light-tight box connected directly to the SPAD. Further iterations of such a design could reduce the number of optics by making the lens out of the filter glass as is shown in Figure 7.1(b). In addition, a large laser could potentially be replaced with a smaller light source inside the box. Ideally, a field-portable device would be constructed without the use of free-space optics. If a suitable method of filtering out the stimulation laser in a fibre-couple system is developed, the entire system could potentially work using simple commercial fibre-connector compo-

[2]Reactive powder sintering of pure silica

nents. This is depicted in Figure 7.1(c). Due to the losses involved when using fibre connectors, however, the luminescence signal would need to be sufficiently intense so as to be detectable.

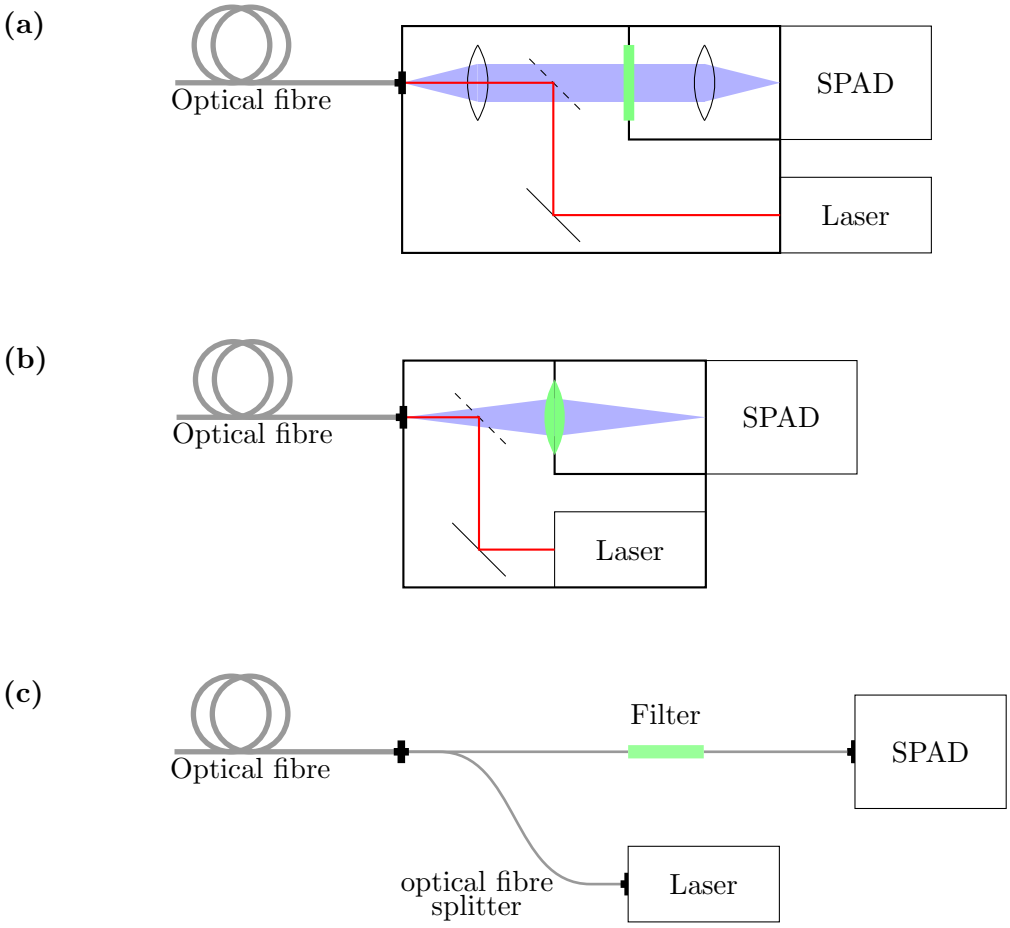

Figure 7.1: (a) Potential design of a field-portable fibre dosimetry test kit. (b) Potential design of a field-portable fibre dosimetry test kit with integrated stimulation laser and 'lens-filter'. (c) Field-portable OSL test rig without free-space optics, where all elements are fibre-coupled.

Simulations Many further simulations could be performed to explore the optical fibre sensors and their response to:

- different glass compositions
- different radiation types: alpha particles, beta particles, neutrons, photons
- the spectrum of energies of these radiation types
- various experimental environments and applications, such as dose rates
- different shielding materials around the fibre sensor
- distributed or point sensing, and spatial-resolution
- optimising applicability for OSL, RL or photodarkening

For example, simulations have been performed using the compositional data for FP1 glass, but there are several other FP glasses with varying composition which could also be used in simulations. With a couple of exceptions, the particle energies simulated here have generally been at 2.28 MeV, the energy at which the ^{90}Yr decay occurs, or in the 20 – 300 keV range output by the X-ray source used for experimental measurements. Further simulations could examine the behavior of these glasses using a wider range of particle energies.

In this thesis, simulations frequently used geometrical approximations to emulate the experimental conditions. These geometries could be refined in order to produce more detailed simulations, for instance microstructured fibres could be modelled, or varying layers of plastic cladding surrounding a glass fibre within an aluminium environment, or for high or low dose-rate environments. Simulations of this type will become more relevant when specific applications are identified and the real-world environment surrounding the optical fibre is known.

The use of other simulation software, such as GEANT4, could also be explored. While PENELOPE is suitable for simulating the energy transport of electrons, positrons and photons it cannot be used for particles such as neutrons or alpha particles.

Multifunctional Detectors Further research could study situations in which a combination of dosimetry phenomena could be used. For example, situations where RL or photodarkening could be used in conjunction with the OSL response. This was briefly explored in this thesis, where RL was measured before the OSL, but much more detailed work could develop this concept into a potentially powerful technique.

Alpha Particle Sensing Alpha particles have not been considered within the scope of this project, due to their short interaction length. Using the exposed core or microstructured optical fibre techniques discussed in the previous section, optical fibre based alpha dosimetry systems could be explored. A possible method of achieving this is to fabricate optical fibres from RL plastics, which would give an intense signal upon interaction with an alpha particle.

7.7 Conclusions

This thesis has demonstrated the development of an optical fibre dosimeter for distributed sensing of ionising radiation using an intrinsic optically stimulated luminescence response, results show this method is indeed possible.

There is ample scope for further development in this area. Although the goal was to achieve a relatively simple aim, this has proved deceptively simple and instead a rich suite of complex luminescence characteristics have been unveiled, leading to substantial investigation in this area. Further work could yield glasses of even greater sensitivity, or with improved optical properties. Improvements in optical fibre quality will also have a significant affect on the quality of the system, with even greater signal intensities available in longer lengths of fibre.

There is potential here for development of a device which can perform distributed dosimetry measurements, with a device that can be interrogated at will and which has the ability to be re-set and re-used for a long series of measurements. Such a device could be small and unobtrusive, and require very little power for operation. It offers an efficient and versatile alternative to current dosimetry techniques, and can perform measurements in a way not currently possible with any other dosimetry device.

Bibliography

[1] F. H. Attix and W. C. Roesch (Editors), *Radiation Dosimetry - Second Edition* (Academic Press, New York, USA, 1968).

[2] J. R. Greening, *Fundamentals of Radiation Dosimetry* (Adam Hilger Ltd, Bristol, United Kingdom, 1981).

[3] W. H. Hallenbeck, *Radiation Protection* (Lewis Publishers, Boca Raton, USA, 1994).

[4] S. N. Ahmed, *Physics and Engineering of Radiation Detection* (Elsevier - Academic Press, Amsterdam, 2007).

[5] H. Geiger and W. Müller, *Elektronenzählrohr zur Messung schwächster Aktivitäten*, Die Naturwissenschaften, 16 (1928) 617–618.

[6] H. Geiger and W. Müller, *Das Elektronenzählrohr*, Physikalische Zeitschrift, 29 (1928) 839–841.

[7] F. M. Khan, *The Physics of Radiation Therapy* (Williams & Wilkins, Baltimore, USA, 1994).

[8] R. Chen and S. W. S. McKeever, *Theory of Thermoluminescence and Related Phenomena* (World Scientific, Singapore, 1997).

[9] J. C. Allemand, L. R. Calvet, J. Cavan and J. C. Thevenin, *Optical scintillating fibres for particle detectors*, Nuclear Instruments and Methods in Physics Research, 225 (1984) 522–524.

[10] A. Acosta, M. Caria, S. Eraditato, L. Caloba and R. DeSalco, *Electron-pion discrimination with a scintillating fibre calorimeter*, Nuclear Instruments and Methods in Physics Research, A302 (1991) 36–46.

[11] L. Dusseau, D. Plattard, J. R. Vaillé, G. Polge, G. Ranchoux, F. Saigné, J. Fesquet, R. Ecoffet and J. Gasiot, *An integrated sensor using optically stimulated luminescence for in-flight dosimetry*, IEEE Transactions on Nuclear Science, 47 (2000) 2412–2416.

[12] C. Granja and S. Pospisil, *Quantum dosimetry and online visualization of X-ray and charged particle radiation in commercial aircraft at operational flight altitudes with the pixel detector Timepix*, Advances in Space Research, 54 (2014) 241–251.

[13] B. Ritter, K. Maršálek, S. Burmeister, G. Reitz and B. Heber, *A small active dosimeter for applications in space*, Nuclear Instruments and Methods in Physics Research A, 748 (2014) 61–69.

[14] D. J. Huntley, D. I. Godfrey-Smith and M. L. W. Thewalt, *Optical dating of sediments*, Nature, 313 (1985) 105–107.

[15] M. J. Aitken, *An Introduction to Optical Dating* (Oxford Science Publications, Oxford, United Kingdom, 1998).

[16] D. Greene and P. C. Williams, *Linear Accelerators for Radiation Therapy - Second Edition* (IoP Publishing Ltd, Bristol, United Kingdom, 1997).

[17] R. Dale and B. Jones (Editors), *Radiobiological Modelling in Radiation Oncology* (British Institute of Radiology, London, United Kingdom, 2007).

[18] K. Jordan, *Gel Dosimeters*, in *Proceedings of the 5th International School on Solid State Dosimetry, Recife, Brazil* (2013) 71–81.

[19] J. Byfield, P. Chan and J. E. Morgan, *A flexible fiber optics scintillation probe for intracavitary dosimetry*, Radiology, 92 (1969) 1120–1123.

[20] J. B. Birks, *The Theory and Practice of Scintillation Counting* (Pergamon Press, Oxford, United Kingdom, 1964).

[21] G. G. Knoll, *Radiation Detection and Measurement* (John Wiley & Sons, 2010).

[22] C. W. R., *Scintillations produced by the electronic "β-Rays" emitted by radium*, Nature, 73 (1906) 341.

[23] W. R. Leo, *Techniques for Nuclear and Particle Physics Experimen* (Springer-Verlag, Berlin, Germany, 1994).

[24] G. T. Reynolds and P. E. Condon, *Filament scintillation counter*, The Review of Scientific Instruments, 28 (1957) 1098–1099.

[25] L. Reiffel and N. S. Kapany, *Some considerations on luminescent fiber chambers and intensifier screens*, The Review of Scientific Instruments, 31 (1960) 1136–1142.

[26] G. Vedda, A. Chiodini, N. D. Martino, D. Fasoli, M. Keffer, S. L. A. Martnini, M. Moretti, F. Spinolo, G. Nikl, M. Solovieva and N. Brambilla, *Ce^{3+}-doped fibers for remote radiation dosimetry*, Applied Physics Letters, 85 (2004) 6356–6358.

[27] D. Wisniewski, L. A. Boatner, J. O. Ramey, M. Wisniewska, J. S. Neal and G. E. Jellison, *Exploratory research on the development of novel Ce^{3+}-activated phosphate glass scintillators*, IEEE Transaction on Nuclear Science, 55 (2008) 3692–3702.

[28] D. McCarthy, S. O'Keeffe, G. Leen and E. Lewis, *Optical fibre radiation dosimetry for low dose applications*, in *IEEE Sensors Conference* (2010) 1663 – 1666.

[29] D. He, C. Yu, S. Li and L. Hu, *Effect of Tb^{3+} concentration and sensitization of Ce^{3+} on luminescence properties of terbium doped phosphate scintillating glass*, Journal of Alloys and Compounds, 509 (2011) 1906–1909.

[30] A. Pappalardo, C. Calì, l. Cosentino, M. Barbagallo, G. Guardo, P. Litrico, S. Scirè and P. Finocchiaro, *Performance evaluation of SiPM's for low threshold gamma detection*, Nuclear Physics B, 215 (2011) 41–13.

[31] A. L. Huston, B. L. Justus, P. L. Falkenstein, R. W. Miller, H. Ning and R. Altemus, *Remote optical fiber dosimetry*, Nuclear Instruments and Methods in Physics Research B, 184 (2001) 55–67.

[32] A. Sliski, C. Soares and M. G. Mitch, *A fibre optic scintillator dosemeter for absorbed dose measurements of low-energy X-ray-emitting brachytherapy sources*, Radiation Protection Dosimetry, 120 (2006) 24–27.

[33] S. O'Keeffe, C. Fitzpatrick, E. Lewis and A. I. Al-Shamma'a, *A review of optical fibre radiation dosimeters*, Sensor Review, 28 (2008) 136–142.

[34] A. R. Beierholm, C. E. Andersen, L. R. Lindvold, F. Kjær-Kristoffersen and J. Medin, *A comparison of BCF-12 organic scintillators and Al_2O_3:C crystals for real-time medical dosimetry*, Radiation Measurements, 43 (2008) 898–903.

[35] A. M. C. Santos, M. Mohammadi, J. Asp, T. M. Monro and S. V. Afshar, *Characterisation of a real-time fibre-coupled beryllium oxide (BeO) luminescence dosimeter in X-ray beams*, Radiation Measurements, 53-54 (2013) 1–7.

[36] L. Archambault, J. Arsenault, L. Fingras, A. S. Beddar, R. Roy and L. Beaulieu, *Plastic scintillation dosimetry: Optimal selection of scintillating fibers and scintillators*, Medical Physics, 32 (2005) 2271–2278.

[37] C. H. Park, J. H. Moon and B. K. Seo, *Development of a scintillating fiber-optic sensor for the radioactive contamination measurement in a narrow area*, Radiation Measurements, 46 (2011) 687–693.

[38] S. Stefanowicz, H. Latzel, L. R. Lindvold, C. E. Andersen, O. Jäkel and S. Greilich, *Dosimetry in clincal static magnetic fields using plastic scintillation detectors*, Radiation Measurements, 56 (2013) 357–360.

[39] P. Pittet, A. Ismail, J. Ribouton, R. Wang, J. M. Galvan, A. Chaikh, G. N. Lu, P. Jalade, J. Y. Giraud and J. Balosso, *Fiber background rejection and crystal over-response compensation for GaN based in vivo dosimetry*, Physica Medica, 29 (2013) 487–492.

[40] L. Archambault, A. S. Beddar, L. Gingras, R. Roy and L. Beaulieu, *Measurement accuracy and Čerenkov removal for high performance, high spatial resolution scintillation dosimetry*, Medical Physics, 33 (2006) 128–136.

[41] S. Magne, S. Deloule, A. Ostrowsky and P. Ferdinand, *Fiber-coupled, time gated Al_2O_3:C radioluminescence dosimetry technique and algorithm for radiation therapy with LINACs*, IEEE Transactions on Nuclear Science, 60 (2013) 2998–3007.

[42] G. H. Sigel and B. D. Evans, *Effects of ionizing radiation on transmission of optical fibers*, Applied Physics Letters, 24 (1974) 410–412.

[43] B. D. Evans, G. H. S. Jr., J. B. Langworthy and B. J. Faraday, *The fiber optic dosimeter on the navigational technology satellite 2*, IEEE Transaction on Nuclear Science, 25 (1978) 1619–1624.

[44] A. F. Fernandez, S. O'Keeffe, C. Fitzpatrick, B. Brichard, F. Berghmans and E. Lewis, *Gamma dosimetry using commercial PMMA optical fibres for nuclear environments*, in *Proceeedings of SPIE*, volume 5855 (2005) 499–502.

[45] S. O'Keeffe and E. Lewis, *Polymer optical fibre for in situ monitoring of gamma radiation processes*, International Journal on Smart Sensing and INtelligent Systems, 2 (2009) 490–502.

[46] S. Ghosh, S. Das, M. C. Paul, K. Dasgupta, D. Bohra, H. S. Chaudhary, L. Panwar, P. K. Bhatnagar and S. G. Vaijapurkar, *Evaluation of the performance of high phosphorous with germanium codoped multimode optical fiber for use as a radiation sensor at low dose rates*, Applied Optics, 50 (2011) 80–85.

[47] A. V. Kir'yanov, S. Ghosh, M. C. Paul, Y. O. Barmenkov, V. Aboites and N. S. Kozlova, *Ce-doped and Ce/Au-codoped alumino-phospho-silicate fibers: Spectral attenuation trends at high-energy electron irradiation and posterior low-power optical bleaching*, Optical Materials Express, 4 (2014) 434–448.

[48] A. V. Faustov, A. Gusarov, M. Wuilpart, A. A. Fotiadi, L. B. Liokumovich, I. O. Zolotovskiy, A. L. Tomaschuk, T. de Schoutheete and P. Mégret, *Comparison of*

gamma-radiation induced attenuation in Al-doped, P-doped and Ge-doped fibres for dosimetry, IEEE Transaction on Nuclear Science, 60 (2013) 2511–2517.

[49] A. L. Huston, B. L. Justus and T. L. Johnson, *Fiber optic coupled, laser heated thermoluminescence dosimeter for remote radiaion sensing*, Applied Physics Letters, 68 (1996) 3377–3379.

[50] B. E. A. Saleh and M. C. Teich, *Fundamentals of Photonics* (John Wiley & Sons, Hoboken, USA, 2007).

[51] A. D. Kersey, M. A. Davis, H. J. Patrick, M. LeBlanc, K. P. Koo, C. G. Askins, M. A. Putnam and E. J. Friebele, *Fiber grating sensors*, Journal of Lightwave Technology, 15 (1997) 1442 – 1463.

[52] A. F. Fernandez, B. Brichard, F. Berghmans and M. Decreton, *Dose-rate dependencies in gamma-irradiated fiber Bragg grating filters*, IEEE Transaction on Nuclear Science, 49 (2002) 2874–2878.

[53] K. Krebber, H. Henschel and U. Weinand, *Fibre Bragg gratings as high dose radiation sensors*, Measurement Science and Technology, 17 (2006) 1095–1102.

[54] A. Gusarov and S. K. Hoeffgen, *Radiation effects on fiber gratings*, IEEE Transaction on Nuclear Science, 60 (2013) 2037 – 2053.

[55] M. S. Akselrod, A. C. Lucas, J. C. Polf and S. W. S. McKeever, *Optically stimulated luminescence of Al_2O_3:C*, Radiation Measurements, 29 (1998) 391–399.

[56] J. C. Polf, S. W. S. McKeever, M. S. Akselrod and S. Holmstrom, *A real-time, fibre optic dosimetry system using Al_2O_3:O fibres*, Radiation Protection Dosimetry, 100 (2002) 301–304.

[57] C. E. Andersen, M. C. Aznar, L. Bøtter-Jensen, S. A. J. Back, S. Mattsson and J. Medin, *Development of optical fibre luminescence techniques for real time in vivo dosimetry in radiotherapy*, in *Standards and Codes of Practice in Medical Radiation Dosimetry* (2002) 353–360.

[58] G. Ranchoux, S. Magne, J. P. Bouvet and P. Ferdinand, *Fibre remote optoelectronic gamma dosimetry based on optically stimulated luminescence of $Al_2O_3 : C$*, Radiation Protection Dosimetry, 100 (2002) 255–260.

[59] J. C. Polf, E. G. Yukihara, M. S. Akselrod and S. W. S. McKeever, *Real-time luminescence from Al_2O_3:C fiber dosimeters*, Radiation Measurements, 38 (2004) 277–240.

[60] M. C. Aznar, C. E. Andersen, L. Bøtter-Jensen, S. A. J. Back, S. Mattsson, F. Kjær-Kristoffersen and J. Medin, *Real-time optical-fibre luminescence dosime-*

try for radiotherapy: physical characteristics and applications in photon beams, Physics in Medicine and Biology, 49 (2004) 1655–1669.

[61] J. M. Edmund, C. E. Andersen, C. J. Marckmann, M. C. Aznar, M. S. Akselrod and L. Bøtter-Jensen, *CW-OSL measurement protocols using optical fibre Al_2O_3:C*, Radiation Protection Dosimetry, 119 (2006) 368.

[62] C. E. Andersen, J. M. Edmund and S. M. S. Damkjær, *Precision of RL/OSL medical dosimetry with fiber-coupled $Al_2O_3 : C$: Influence of readout delay and temperature variations*, Radiation Measurements, 45 (2010) 653–657.

[63] C. E. Andersen, S. M. S. Damkjær, G. Kertzscher, S. Greilich and M. C. Aznar, *Fiber-coupled radioluminescence dosimetry with saturated Al_2O_3:C crystals: Characterization in 6 and 18 MV photon beams*, Radiation Measurements, 46 (2011) 1090–1098.

[64] R. Gaza and S. W. S. McKeever, *A real-time, high-resolution optical fibre dosemeter based on optically stimulated luminescence (OSL) of KBr:Eu, for potential use during the radiotherapy of cancer*, Radiation Protection Dosimetry, 120 (2006) 14–19.

[65] A. F. Fernandez, B. Brichard, S. O'Keeffe, C. Fitzpatrick, E. Lewis, J. R. Vaille, L. Dusseau, D. A. Jackson, F. Ravotti, M. Glaser and H. El-Rabii, *Real-time fibre optic radiation dosimeters for nuclear environment monitoring around thermonuclear reactors*, Fusion Engineering and Design, 83 (2008) 50–59.

[66] A. M. C. Santos, M. Mohammadi and S. Afshar, *Investigation of a fibre-coupled beryllium oxide (BeO) ceramic luminescence dosimetry system*, Radiation Measurements, 70 (2014) 52–58.

[67] B. L. Justus and A. L. Huston, *Ultraviolet dosimetry using thermoluminescence of semiconductor-doped Vycor glass*, Applied Physics Letters, 67 (1995) 1179–1181.

[68] B. L. Justus, T. L. Johnson and A. L. Huston, *Radiation dosimetry using thermoluminescence of semiconductor-doped Vycor glass*, Nuclear Instruments and Methods in Physics Research, 95 (1995) 533–536.

[69] B. L. Justus, S. Rychnovsky, M. A. Miller, K. J. Pawlovich and A. L. Huston, *Optically stimulated luminescence radiation dosimetry using doped silica glass*, Radiation Protection Dosimetry, 74 (1997) 151–154.

[70] A. L. Huston, *Optically transparent, optically stimulable glass composites for radiation dosimetry*, United States of America, Patent No 5811822.

[71] B. L. Justus, K. J. Pawlovich, C. D. Merritt and A. L. Huston, *Optically and thermally stimulated luminescence characteristics of Cu^{+}-doped fuzed quartz*, Radiation Protection Dosimetry, 81 (1999) 5–10.

[72] B. L. Justus, C. D. Merritt, K. J. Pawlovich, A. L. Huston and S. Rychnovsky, *Optically stimulated luminescence dosimetry using doped fused quartz*, Radiation Protection Dosimetry, 84 (1999) 189–192.

[73] A. L. Huston, B. L. Justus, P. L. Falkenstein, R. W. Miller, H. Ning and R. Altemus, *Optically stimulated luminescent glass optical fibre dosemeter*, Radiation Protection Dosimetry, 101.

[74] A. L. Huston, P. L. Falkenstein, B. L. Justus, H. Ning, R. W. Miller and R. Altemus, *Multiple channel optical fiber radiation dosimeter for radiotherapy applications*, in *IEEE Sensors* (2002) 560.

[75] A. K. Jones and D. Hintenlang, *Potential clinical utility of a fibre optic-coupled dosemeter for dose measurements in diagnostic radiology*, Radiation Protection Dosimetry, 132 (2008) 80–87.

[76] J. A. Tanyi, S. P. Krafft, T. Ushino, A. L. Huston and B. L. Justus, *Performance characteristics of a gated fiber-optic-coupled dosimeter in high-energy pulsed photon radiation dosimetry*, Applied Radiation and Isotopes, 68 (2010) 364–369.

[77] J. Hecht, *Understanding Fiber Optics* (Pearson Prentice Hall, New Jersey, USA, 2006).

[78] S. C. Warren-Smith, E. Sinchenko, P. R. Stoddart and T. M. Monro, *Distributed fluorescence sensing using exposed core microstructured optical fiber*, IEEE Photonics Technology Letters, 22 (2010) 1385–1387.

[79] L. Bøtter-Jensen, S. W. S. McKeever and A. G. Wintle, *Optically Stimulated Luminescence Dosimetry* (Elsiver Science B. V., Oxford, United Kindom, 2003).

[80] C. Furetta and P. Weng, *Operational Thermoluminescence Dosimetry* (World Scientific, Singapore, 1998).

[81] M. J. Aitken, *Thermoluminescence Dating* (Academic Press, London, United Kingdom, 1985).

[82] R. D. Deslattes, E. G. Kessler, P. Indelicato, L. de Billy, E. Lindroth and J. Anton, *X-ray transition energies: new approach to a comprehensive evaluation*, Reviews of Modern Physics, 75 (2003) 35–99.

[83] J. Baró, J. Sempau, J. M. Fernández-Varea and F. Salvat, *PENELOPE: An algorithm for Monte Carlo simulation of the penetration and energy loss of electrons*

and positrons in matter, Nuclear Instruments and Methods in Physics Research B, 100 (1995) 31–46.

[84] F. Salvat, J. M. Fernández-Varea and J. Sempau, *PENELOPE-2008: A code system for Monte Carl simulation of electron and photon transport*, in *Nuclear Energy Agency Workshop Proceedings* (2008) .

[85] H. Liu and F. Gan, *Time-resolved fluorescence and energy transfer of Cu^{+}-doped fluorophosphate glass*, Journal of Luminscence, 40&41 (1988) 129–130.

[86] D. Ehrt and A. Brettschneider, *Redox behavior of copper ions in FP and P glass melts*, in *Proceedings of International Congress on Glass*, volume 3 (1995) 157–162.

[87] D. Ehrt, *Redox behavior of polyvalent ions in the ppm range*, Journal of Non-Crystalline Solids, 196 (1996) 304–308.

[88] H. Ebendorff-Heidepriem and D. Ehrt, *UV radiation effects in fluoride phosphate glasses*, Journal of Non-Crystalline Solids, 196 (1996) 113–117.

[89] X. Zou and H. Toratani, *Radiation resistance of fluorophosphate glasses for high performance optical fiber in the ultraviolet region*, Journal of Applied Physics, 81 (1997) 3354–3362.

[90] D. Ehrt, P. Ebeling and U. Natura, *UV transmission and radiation-induced defects in phosphate and fluoride-phosphate glasses*, Journal of Non-Crystalline Solids, 263&264 (2000) 240–250.

[91] U. Natura, T. Feurer and D. Ehrt, *Kinetics of UV laser radiation defects in high performance glasses*, Nuclear Instruments and Methods in Physics Research B, 166-167 (2000) 470–475.

[92] S. W. S. McKeever, *Thermoluminescence of Solids* (Cambridge University Press, Cambridge, United Kingdom, 1985).

[93] V. S. Kortov, I. I. Milman, V. I. Kirpa and J. Lesz, *Some features of α-Al_2O_3 dosimetric thermoluminescent crystals*, Radiation Protection Dosimetry, 55 (1994) 279–283.

[94] M. Zahedifar, L. Eshraghi and E. Sadeghi, *Thermoluminescence kinetics analysis of α-Al_2O_3:C at different dose levels and populations of trapping states and a model for its dose response*, Radiation Measurements, 47 (2012) 957–964.

[95] F. Ortega, J. Marcazzó, P. Molina, M. Santiago, M. Lester, J. Henniger and E. Caselli, *Analysis of the main dosimetric peak of Al_2O_3:C compounds with a model of interacting traps*, Applied Radiation and Isotopes, 78 (2013) 33–37.

[96] M. L. Chithambo, C. Seneza and F. O. Ogundare, *Kenetic analysis of high temperature secondary thermoluminescence glow peaks in a-Al_2O_3:C*, Radiation Measurements, 66 (2014) 21–30.

[97] J. R. Prescott, P. J. Fox, R. A. Akber and H. E. Jensen, *Thermoluminescence emission spectrometer*, Applied Optics, 27 (1988) 3496–3502.

[98] P. J. Fox, R. A. Akber and J. R. Prescott, *Spectral characteristics of six phosphors used in thermoluminescence dosimetry*, Journal of Physics D: Applied Physics, 21 (1988) 189–193.

[99] Y. Horowitz (Editor), *Microdosimetric Response of Physical and Biological Systems to Low- and High-LET Radiations* (Elsevier, 2006).

[100] L. Katz and A. S. Penfold, *Range-energy relations for electrons and the determination of beta-ray end-point energies by absorption*, Reviews of Modern Physics, 24 (1952) 28–44.

[101] A. Margaryan, A. Margaryan, J. H. Choi and F. G. Shi, *Spectroscopic properties of Mn^{2+} in new bismuth and lead contained fluorophosphate glasses*, Applied Physics B, 78 (2004) 409–413.

[102] H. Ebendorff-Heidepriem and D. Ehrt, *Relationships between glass structure and spectroscopic properties of Eu^{3+} and Tb^{3+} doped glasses*, Ber. Bunsenges. Phys. Chem., 100 (1996) 1621–1624.

[103] N. Duhamel-Henry, J. L. Adam, B. Jacquier and C. Linarès, *Photoluminescence of new fluorophosphate glasses containing a high concentration of terbium (III) ions*, Optical Materials, 5 (1996) 197–207.

[104] D. Ehrt, *Redox behaviour of polyvalent ions in the ppm range*, Journal of Non-Crystalline Solids, 196 (1996) 304–308.

[105] T. Djouama, A. Boutarfaia and M. Poulain, *Fluorophosphate glasses containing manganese*, Journal of Physics and Chemistry of Solids, 69 (2008) 2756–2763.

[106] H. Ebendorff-Heidepriem and D. Ehrt, *Formation and UV absorption of cerium, europium and terbium ions in different valencies in glasses*, Optical Materials, 15 (2000) 7–25.

[107] H. Ebendorff-Heidepriem and D. Ehrt, *Spectroscopic properties of Eu^{3+} and Tb^{3+} ions for local structure investigations of fluoride phosphate and phosphate glasses*, Journal of Non-Crystalline Solids, 208 (1996) 205–216.

[108] M. R. Baril, *Optical Dating of Tsunami Deposits*, Ph.D. thesis, Simon Fraser University (1997).

[109] X. Zou, K. Itoh and H. Toratani, *Transmission loss characteristics of fluorophosphate optical fibers in the ultraviolet to visible wavelength region*, Journal of Non-Crystalline Solids, 215 (1997) 11–20.

[110] M. Kochanowicz, J. Zmojda and D. Dorosz, *Fluorosilicate and fluorophosphate superfluorescent multicore optical fibers co-doped with Nd^{3+}/Yb^{3+}*, Optical Fiber Technology, 20 (2014) 245–249.

[111] J. Bei, T. M. Monro, A. Hemming and H. Ebendorff-Heidepriem, *Fabrication of extruded fluoroindate optical fibers*, Optical Materials Express, 3 (2013) 318–328.

[112] H. Ebendorff-Heidepriem and T. M. Monro, *Extrusion of complex preforms for microstructured optical fibers*, Optics Express, 15 (2007) 15086–15092.

[113] H. Ebendorff-Heidepriem, Y. Li and T. M. Monro, *Reduced loss in extruded soft glass microstructured fibre*, Electronics Letters, 43 (2007) 1343–1345.

[114] H. Ebendorff-Heidepriem, K. Kuan, M. R. Oermann, K. Knight and T. M. Monro, *Extruded tellurite glass and fibers with low OH content for mid-infrared applications*, Optical Materials Express, 2 (2012) 432–442.

[115] H. Ebendorff-Heidepriem and T. M. Monro, *Analysis of glass flow during extrusion of optical fiber preforms*, Optical Materials Express, 2 (2012) 304–320.

[116] *Optical Glass Data Sheets*, Schott Glass Company, www.schott.com.

[117] P. C. Pureza, P. H. Klein, W. I. Roberts and I. D. Aggarwal, *Influence of preform surface treatments on the strength of fluorozirconate fibres*, Journal of Materials Science, 26 (1991) 5149–5154.

[118] Y. D. West, E. R. Taylor, R. C. Moore and D. N. Payne, *Chemical Etching of AlF_3-based glasses*, Journal of Non-Crystalline Solids, 256 & 257 (1999) 200–206.

[119] H. W. Schneider, A. Schoberth, A. Staudt and C. Gerndt, *Fluoride glass etching method for preparation of infra-red fibres with improved tensile strength*, Electronics Letter, 22 (1986) 949–950.

[120] Y. Gao, O. Perrot, B. Boulard, J. E. Broquin, R. Rimet and C. Jacobini, *Preparation of PZG fluoride glass channel waveguides*, Journal of Non-Crystalline Solids, 213 & 214 (1997) 137–140.

[121] S. Schütz, M. Waldmann, R. Caspary and W. Kowalsky, *Erbium-doped fluoride glass waveguides for laser applications*, 12th International Conference on Transparent Optical Networks.

[122] Y. Ahn, J.-Y. Yoon, C.-W. Baek and Y.-K. Kim, *Chemical mechanical polishing by colloidal silica-based slurry for micro-scratch reduction*, Wear, 257 (2004) 785–589.

[123] J. Bei, T. M. Monro, A. Hemming and H. Ebendorff-Heidepriem, *Reduction of scattering loss in fluoroindate glass fibers*, Optical Materials Express, 3 (2013) 1285 – 1301.

[124] Y. M. Stokes, P. Buchak, D. G. Crowdy and H. Ebendorff-Heidepriem, *Drawing of micro-structured fibres: circular and non-circular tubes*, Journal of Fluid Mechanics, 755 (2014) 176–203.

[125] T. Iqbal, M. R. Shahriari, P. Foy and G. H. S. Jr, *Preliminary study of fiber drawing of ALF_3-based glasses*, Materials Science and Engineering, B12 (1992) 299–303.

[126] P. McNamara and D. R. MacFarlane, *Surface-defects on fluoride glasses induced during fiber drawing*, Materials Science Forum, 32 (1988) 219–224.

[127] G. A. Brinkman, *Doserates during isotope production*, International Journal of Applied Radiation and Isotopes, 33 (1982) 109–115.

[128] *Optical Glass Datasheets*, Heraeus Quarzglas, www.heraeus–quarzglas.com.

[129] J. B. MacChesney, *Materials and processes for preform fabrication - modified chemical vapor deposition and plasma chemical vapor deposition*, Proceedings of the IEEE, 68 (1980) 1181–1184.

[130] S. R. Nagel, J. B. MacChesney and K. L. Walker, *An overview of the modified chemical vapor deposition (MCVD) process and performance*, IEEE Journal of Quantum Electronics, QE-18 (1982) 459–476.

[131] E. Schartner, *Personal Communication*, (October, 2014).

[132] R. Debdnath and S. K. Das, *Site-dependent luminescence of Cu^+ ions in silica glass*, Chemical Physics Letters, 155 (1989) 52 – 58.

[133] R. Debnath and S. Kumar, *Dual luminescence of Cu^+ in glass*, Journal of Non-Crystalline Solids, 123 (1990) 271 – 274.

[134] R. Debnath, *Copper activated thermoluminescence dosimeter and method*, United States of America, Patent No 5651804.

[135] A. L. Yusoff, R. P. Hugtenburg and D. A. Bradley, *Review of development of silica-based thermoluminescence dosimeter*, Radiation Physics and Chemistry, 74 (2005) 459 – 481.

[136] M. Leich, F. Just, A. Langner, M. Such, G. Schötz, T. Eschrich and S. Grimm, *Highly efficient Yb-doped silica fibers prepared by powder sinter technology*, Optics Letters, 36 (2011) 1557–1559.

[137] S. M. S. Damkjær and C. E. Andersen, *Memory effects and systematic errors in the RL signal from fiber coupled Al_2O_3:C for medical dosimetry*, Radiation Measurements, 45 (2010) 671–673.

[138] J. M. Fontbonne, G. Iltis, G. Ban, A. Battala, J. C. Vernhes, J. Tillier, N. Bellaize, C. L. Brun, B. Tamain, K. Mercier and J. C. Motin, *Scintillating fiber dosimeter for radiation therapy accelerator*, IEEE Transaction on Nuclear Science, 49 (2002) 2223–2227.

[139] D. Ehrt, M. Carl, T. Kittel, M. Müller and W. Seeber, *High-performance glass for the deep ultraviolet range*, Journal of Non-Crystalline Solids, 177 (1994) 405–419.

[140] J. H. Choi, F. G. Shi, A. Margaryan, A. Margaryan and W. van der Veer, *Novel alkaline-free Er^{3+}-doped fluorophosphate glasses for broadband optical fiber lasers and amplifiers*, Journal of Alloys and Compounds, 450 (2008) 540–545.

[141] M. A. M. Gámez, A. V. Kiryanov, J. L. Lucio, C. Wiechers and G. A. Kumar, *Near-IR emission from holmium-ytterbium co-doped alkali bismuth gallate and fluorophosphate fiber glass preforms*, Journal of Alloys and Compounds, 473 (2009) 500–504.

[142] S.-M. Hsu, H.-W. Yang, D. Y. C. Huang, W.-L. Hsu, C.-C. Lu and W.-L. Chen, *Development and physical characteristics of a novel compound radiophotoluminescent glass dosimeter*, Radiation Measurements, 43 (2008) 538–541.

[143] Y. Miyamoto, T. Yamamoto, K. Kinoshita, S. Koyama, Y. Takei, H. Nanto, Y. Shimotsuma, M. Sakukura, K. Miura and K. Hirao, *Emission mechanism of radiophotoluminescence in Ag-doped phosphate glass*, Radiation Measurements, 45 (2010) 546–549.

[144] S. Fan, C. Yu, D. He, K. Li and L. Hu, *Gamma rays induced defect centers in phosphate glass for radio-photoluminescence dosimeter*, Radiation Measurements, 46 (2011) 46–50.

[145] W. K. Chung and D. W. Kim, *Characteristic study of a radio-photoluminescence glass rod detector for clinical usages: skin and inner body in-vivo verification*, Journal of the Korean Physical Society, 62 (2013) 670–676.

[146] A. Zadok, Y. Antman, N. Primerov, A. Denisov, J. Sancho and L. Thévenaz, *Random-access distributed fiber sensing*, Laser Photonics Review, 6 (2012) L1 – L5.

[147] S. C. Warren-Smith, H. Ebendorff-Heidepriem, T. C. Foo, R. Moore, C. Davis and T. M. Monro, *Exposed-core microstructured optical fibers for real-time fluorescence sensing*, Optics Express, 17 (2009) 18533–18542.

[148] R. Kostecki, H. Ebendorff-Heidepriem, C. Davis, G. McAdam, S. C. Warren-Smith and T. M. Monro, *Silica exposed-core microstructured optical fibers*, Optical Materials Express, 11 (2012) 1583–1547.

Appendices

Appendix A

Materials and Materials Properties

A.1 Initial Glass Screening

A wide cross-section of different glasses were tested for an OSL response, shown in the following table. The study was performed on several soft glasses, due to their availability, and the capabilities of the laboratory for manufacturing and fabricating soft glasses into optical fibres. Study was also performed on several different types of silica and silicate glasses, due to their availability both commercially and from recycled materials. Crucibles: C = vitreous carbon, Si = silica, Pt = platinum and Au = gold.

Glass Type	**Glass Number**	**Glass Name**	**Melting Conditions**	**Dopant**	**Conc. ions/cm^3 ($\times 10^{19}$)**
FP10	386	S10/4	Pt, air	–	
Fluoride	387b	S10/3/C	C, argon	–	
phosphate	406	S10/4/Tb 1	Pt, air	Tb	1
	406b	S10/4/Tb1/C	C, argon	Tb	1
	407	S10/4/Tb2.5	Pt, air	Tb	2.5
	408	S10/4/Tb5	Pt, air	Tb	5
	409	S10/4/Tb10	Pt, air	Tb	10
	419	S10/4/Eu1	Pt, air	Eu	1
	419b	S10/4/Eu1/C1	C, argon	Eu	1
	419c	S10/4/Eu1/C2	C, argon	Eu	1
	420	S10/4/Eu10	Pt, air	Eu	10
	421	S10/4/Eu100	Pt, air	Eu	100
	450	S10/4/Tb1, Eu 1	Pt, air	Tb–Eu	1–1
	502b	S10/11/Ce1/C	C, argon	Ce	1
	502c	S10/11/Ce1/C2	C, argon	Ce	1
	505b	S10/11/Ce0.5/C	C, argon	Ce	0.5
	514c	S10/11b/C	C, argon	–	
P100	466a	S100/3/V	Si, air	–	
Phosphate	466b	S100/3/R, L	Pt, air	–	
	466c	S100/3/R,O2	Pt, oxygen	–	
	467a	S100/3/Eu1/V	Si, air	Eu	1
	467b	S100/3/Eu1/R,L	Pt, air	Eu	1
	467c	S100/3/Eu1/R,O2	Pt, oxygen	Eu	1
	469a	S100/3/Tb1/V	Si, air	Tb	1
	469b	S100/3/Tb1/R,L	Pt, air	Tb	1
	469c	S100/3/Tb1/R,O2	Pt, oxygen	Tb	1
	471 = 477	S100/2/Eu1/Z	Si, air, sugar	Eu	1
	472	S100/2/Z	Si, air, sugar	–	
La10	No.16	La10	Au, air	–	
Tellurite	KK1134	La10/Ce1/Ce(IV)	Au, air	Ce	1
	KK1166	La10/Ce1/Ce(III)	Au, air	Ce	1
	KK1168	La10/Tb1	Au, air	Tb	1
	KK1170	La10/Eu1	Au, air	Eu	1
F2	F2	F2	–	–	
lead-silicate	F2G12	F2/Ce	–	Ce	–
SF6	SF6G03	SF6/Ce	–	Ce	–

A.2 Fluoride Phosphate Glasses

A.2.1 Summary of FP Glass Samples

A variety of FP glass samples were used for measurements, and representative samples were chosen to demonstrate the results shown in this Thesis. A complete summary of FP glass samples is provided here in the following table. The FP glasses listed are those used in analysis after the initial glass screening shown in the previous section, there is a small amount of overlap between the two tables. Abbreviations: comp. = composition, fab. atm. = fabrication atmosphere, red = reducing atmosphere, ox = oxidising atmosphere, conc. = concentration, rem. = remelted.

Sample Name	**Sample Code**	**Comp. Code**	**Fab. Atm.**	**Dopant**	**Conc.** (ppm)	**Source**
FP1	N-FK51A		ox			Commercial
FP1red			red			rem. N-FK51A
FP2	PK52A		NA			Commercial
FP3	386	FP10	ox			In-house
FP4	387b	FP20	red			In-house
FP5	406	FP10	ox			In-house
FP6	514c	FP10	red			In-house
FP7	339b	FP20	red			In-house
Cu-ox-10	CuM2		ox	Copper	10	rem. N-FK51A
Cu-ox-20	CuM3		ox	Copper	20	rem. N-FK51A
Cu-ox-30	CuM4		ox	Copper	30	rem. N-FK51A
Cu-ox-40	CuM5		ox	Copper	40	rem. N-FK51A
Cu-ox-50	CuM6		ox	Copper	50	rem. N-FK51A
Cu-ox-60	CuM7		ox	Copper	60	rem. N-FK51A
Cu-red-60	CuM7b		red	Copper	60	rem. N-FK51A
Cu-red-100	CuM8a		red	Copper	100	rem. N-FK51A
Cu-red-500	CuM9a		red	Copper	500	rem. N-FK51A
Cu-red-1000	CuM10a		red	Copper	1000	rem. N-FK51A
	MnRM1		ox	Manganese	274.9	rem. N-FK51A
Nb-ox	MnRM2		ox	Manganese	2749	rem. N-FK51A
Mn-red	MnRM2b		red	Manganese	2749	rem. N-FK51A
Tb-red	TbRM1a		red	Terbium	720	rem. N-FK51A
	TbRM2a		red	Terbium	7200	rem. N-FK51A
	TbRM3a		red	Terbium	7200	rem. N-FK51A
Tb-ox	TbRM4		ox	Terbium	7200	rem. N-FK51A
	TbRM5a		red	Terbium	720	rem. N-FK51A
	TbRM6a		red	Terbium	7200	rem. N-FK51A
	TbRM7		ox	Terbium	7200	rem. N-FK51A

A.2.2 Schott N-FK51A Fluoride Phosphate Glass

The glass used for the majority of experiments, and all doping and fibre fabrication work, was the commercially-acquired Schott N-FK51A glass. A summary of the glass properties is provided here, all data is taken from the Schott Optical Glass Datasheet (2013) [116].

General Properties	
$\alpha_{-30/=70^oC}$ [10^{-6}/K]	12.7
$\alpha_{+20/=+300^oC}$ [10^{-6}/K]	14.8
T_g [°C]	464
$T_{10}^{13.0}$ [°C]	463
$T_{10}^{7.6}$ [°C]	527
c_p [J/(g.K)]	0.690
λ [W/(m.K)]	0.760
AT [°C]	503
ρ [g/cm^3]	3.68
E [10^3N/mm^2]	73
μ	0.302
K [10^{-6}mm^2/N]	0.70
$HK_{0.1/20}$	345
HG	6
Abrasion Aa	528
B	1
CR	1
FR	0
SR	52.3
AR	2.2
PR	4.3
SR-J	3
WR-J	1

Constants of Dispersion Formula	
B_1	0.971 247 817
B_2	0.216 901 417
B_3	0.904 651 666
C_1	0.004 723 019 95
C_2	0.015 357 561 2
C_3	168.681 33

Relative Partial Dispersion	
$P_{s,t}$	0.2879
$P_{C,s}$	0.5465
$P_{d,C}$	0.3062
$P_{e,D}$	0.2388
$P_{g,F}$	0.5359
$P_{i,h}$	0.7429
$P'_{s,t}$	0.2858
$P'_{C',s}$	0.5909
$P'_{d,C'}$	0.2554
$P'_{e,D}$	0.2370
$P'_{g,F'}$	0.4759
$P'_{i,h}$	0.7373

Refractive Indicies			Internal Transmittance (τ_i)		
	λ (nm)	RI	λ (nm)	τ_i (10 mm)	τ_i (25 mm)
$n_{2325.4}$	2325.4	1.469 58	2500	0.891	0.75
$n_{1970.1}$	1970.1	1.472 71	2325	0.933	0.84
$n_{1529.6}$	1529.6	1.476 08	1970	0.976	0.94
$n_{1060.0}$	1060.0	1.479 59	1530	0.992	0.98
n_t	1014.0	1.479 99	1060	0.998	0.994
n_S	852.1	1.481 65	700	0.998	0.995
n_r	706.5	1.483 79	660	0.998	0.995
n_C	656.3	1.4848	620	0.998	0.996
$n_{C'}$	643.8	1.485 08	580	0.999	0.997
$n_{632.8}$	632.8	1.485 34	546	0.999	0.997
n_D	589.3	1.486 51	500	0.998	0.996
n_d	587.6	1.486 56	460	0.997	0.993
n_e	546.1	1.487 94	436	0.997	0.992
n_F	486.1	1.490 56	420	0.997	0.992
$n_{F'}$	480.0	1.490 88	405	0.997	0.993
n_g	435.8	1.493 64	400	0.997	0.993
n_h	404.7	1.496 18	390	0.997	0.992
n_i	365.0	1.500 46	380	0.995	0.988
$n_{334.1}$	334.1	1.505 01	370	0.99	0.976
$n_{312.6}$	312.6	1.509 11	365	0.985	0.963
$n_{296.7}$	296.7		350	0.948	0.875
$n_{280.4}$	280.4		334	0.831	0.63
$n_{248.3}$	248.3		320	0.618	0.3
			310	0.428	0.12
			300	0.262	0.035
			290	0.137	0.01
			280	0.058	

Constants of Dispersion dn/dT	
D_0	$-1.8310 \times^{-} 5$
D_1	$-7.8910 \times^{-} 9$
D_2	$-1.6310 \times^{-} 12$
E_0	$3.7410 \times^{-} 7$
E_1	$3.4610 \times^{-} 10$
$lambda_{TK}$[µm]	0.15

A.3 ICPMS/OES Detection Limits

Detection limits for each element in ICP-MS/OES analysis

Element	**Detection Limit (ppm)**
Ti	5
Cr	5
Co	0.1
Ni	1
Cu	1
Zn	1
Ga	0.1
Ge	0.1
As	1
Se	2
Rb	0.05
Y	0.05
Zr	0.1
Mo	0.1
Ag	0.1
Cd	0.1
In	0.01
Sn	0.1
Sb	0.05
Te	0.1
La	0.01
Ce	0.01
Pr	0.005
Sm	0.01
Eu	0.01
Yb	0.01
Hf	0.01
Ta	0.01
W	0.1

A.4 Silica Glass

Silica glass is fabricated by different methods, primarily (1) electrical or flame fusion and (2) flame hydrolysis.

1. In electrical or flame fusion, high-purity quartz is melted in a furnace and fused quartz is produced. The purity is limited by the purity of the raw material, which is subjected to extensive purification steps before fabrication of the glass.

2. In flame hydrolysis, silicon is deposited on a surface by hydrolysis of silicon tetrachloride, creating a nanoporous silica body, which is then dehydrated and sintered to produce fused silica. As the process occurs chemically, the resulting glass is very pure.

Both methods produce very pure glasses suitable for optical applications. The purity produced by flame hydrolysis is superior, however the process is more involved and expensive. The purity of fused quartz and fused silica are shown in Table A.1.

Table A.1: Example of purity of commercial silica glasses. Data taken from Heraeus Quarzglass.

Elements (ppm)	Fusion	Hydrolysis
Al	15	<0.04
Ca	0.5	<0.02
Cl	-	1500
Cr	<0.05	<0.001
Cu	<0.05	<0.001
Fe	0.1	<0.03
K	0.4	<0.01
Li	0.6	<0.002
Mg	0.05	<0.01
Mn	<0.05	<0.0005
Na	0.3	<0.01
Ti	1.1	<0.03
Zr	0.7	0.8

The loss of optical fibres fabricated from a flame fusion silica glass, Heraeus Quarzglass LWQ, is shown in Figure A.1. These measurements are used for comparison with LWQ silica fibres fabricated as part of this project.

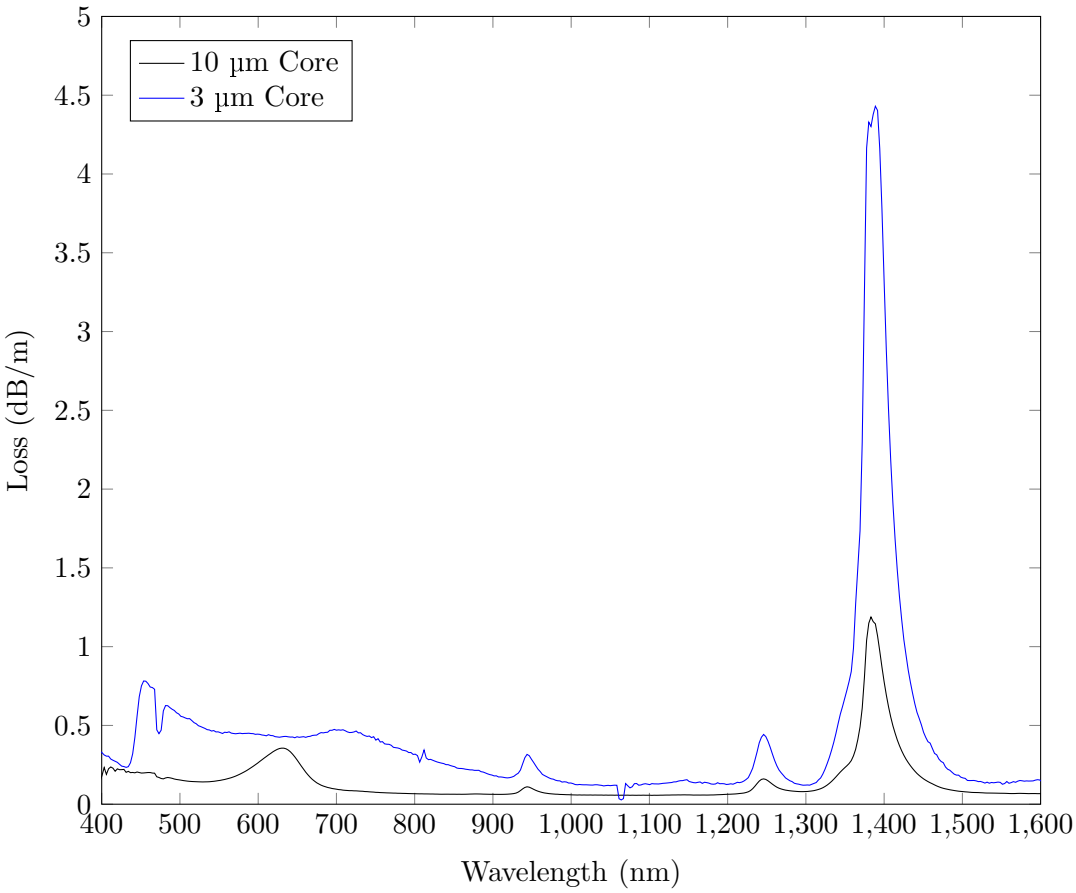

Figure A.1: Loss of LWQ silica optical fibres with wagon wheel microstructured geometry.

A.5 Fluoride Phosphate Glass Radiation Interaction Values

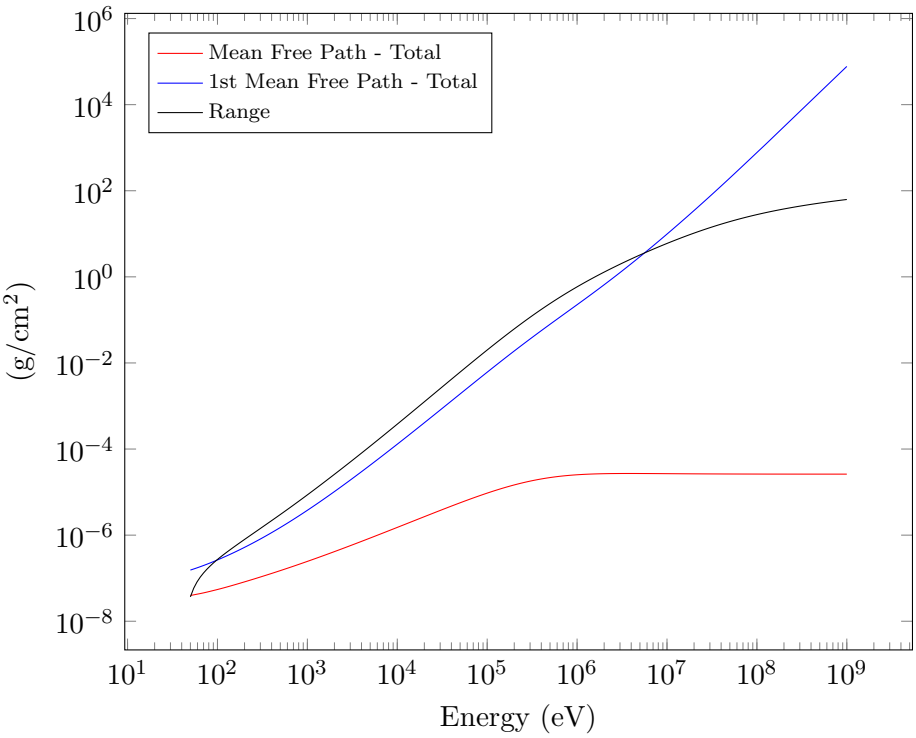

Figure A.2: Electron mean free path and range in fluoride phosphate glass.

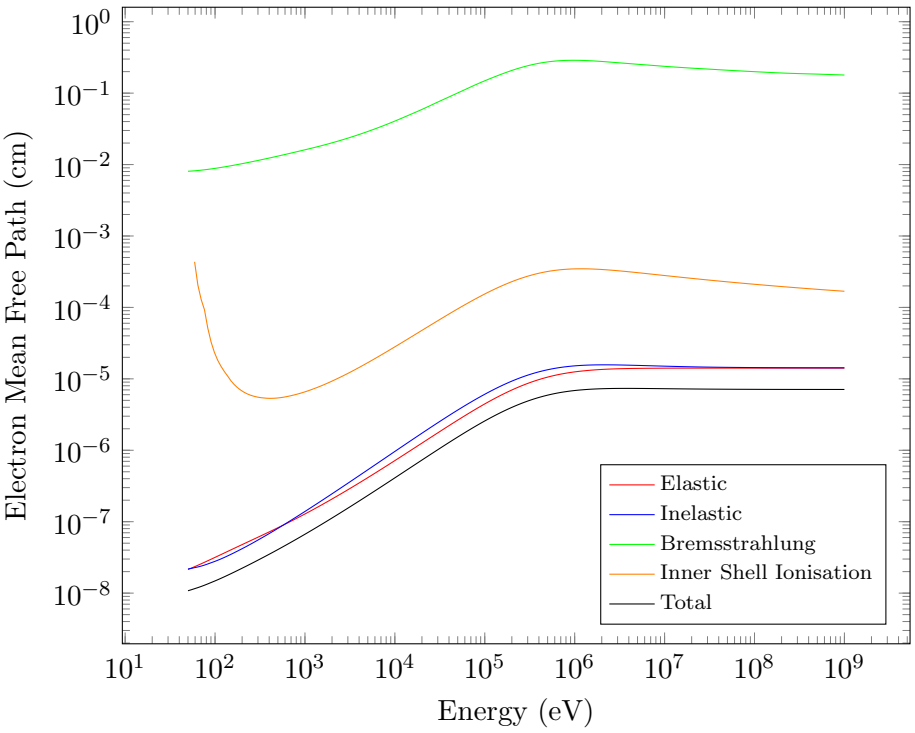

Figure A.3: Electron mean free paths in fluoride phosphate glass.

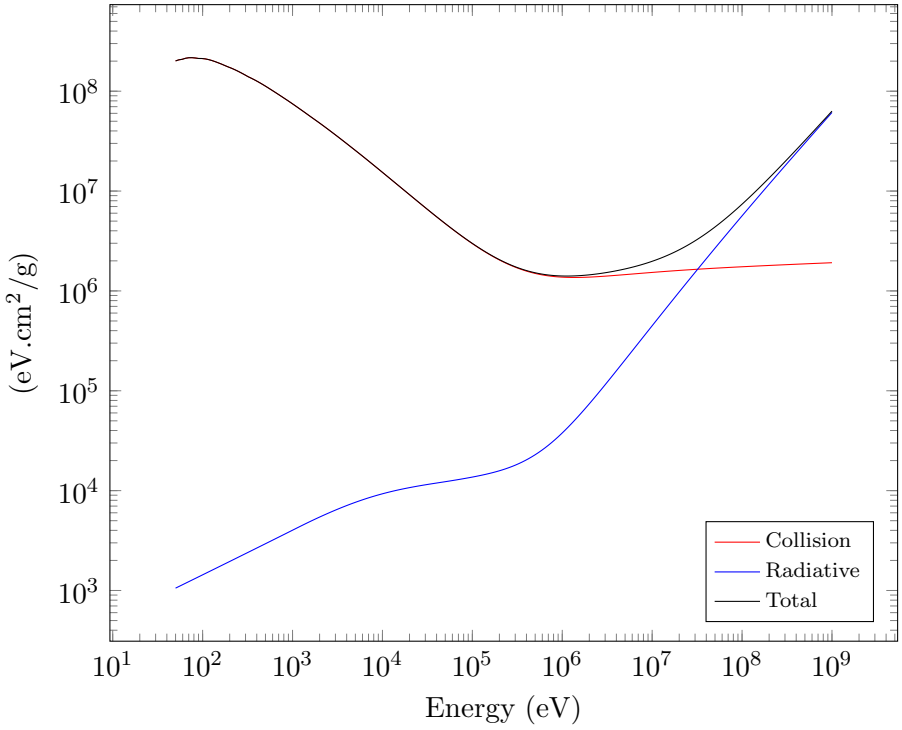

Figure A.4: Electron Stopping Powers in fluoride phosphate glass.

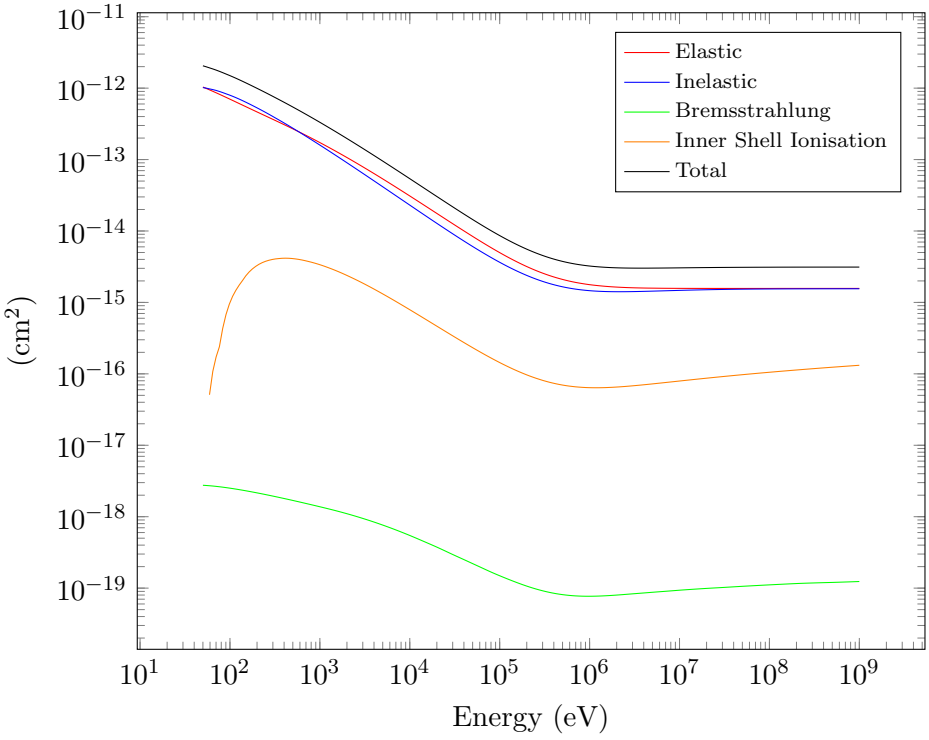

Figure A.5: Electron Cross Sections in fluoride phosphate glass.

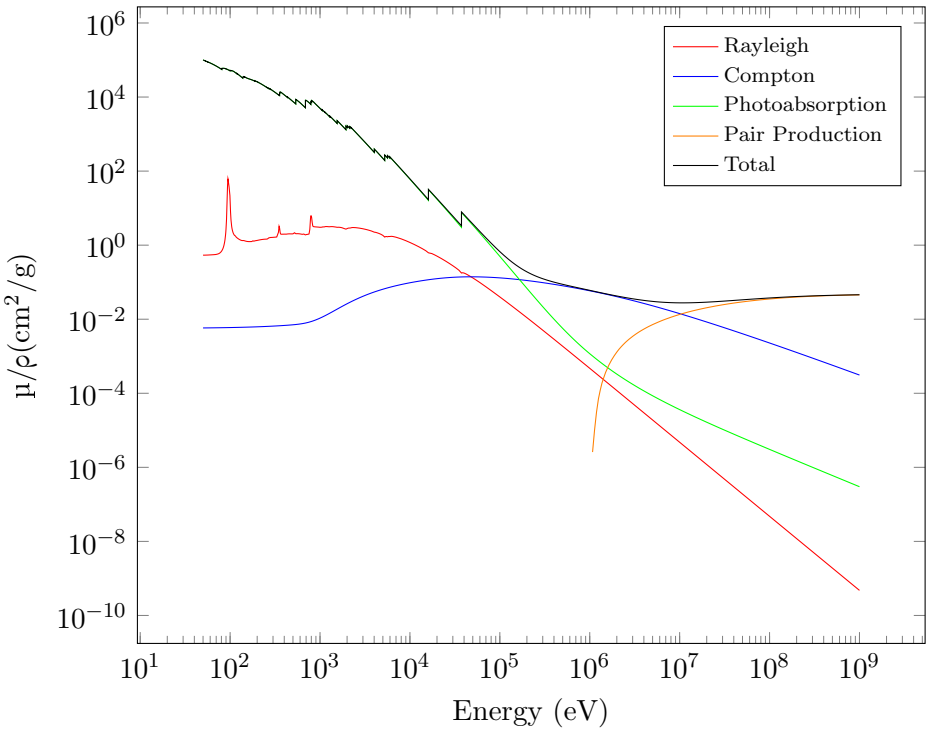

Figure A.6: Photon mass attenuation coefficients in fluoride phosphate glass.

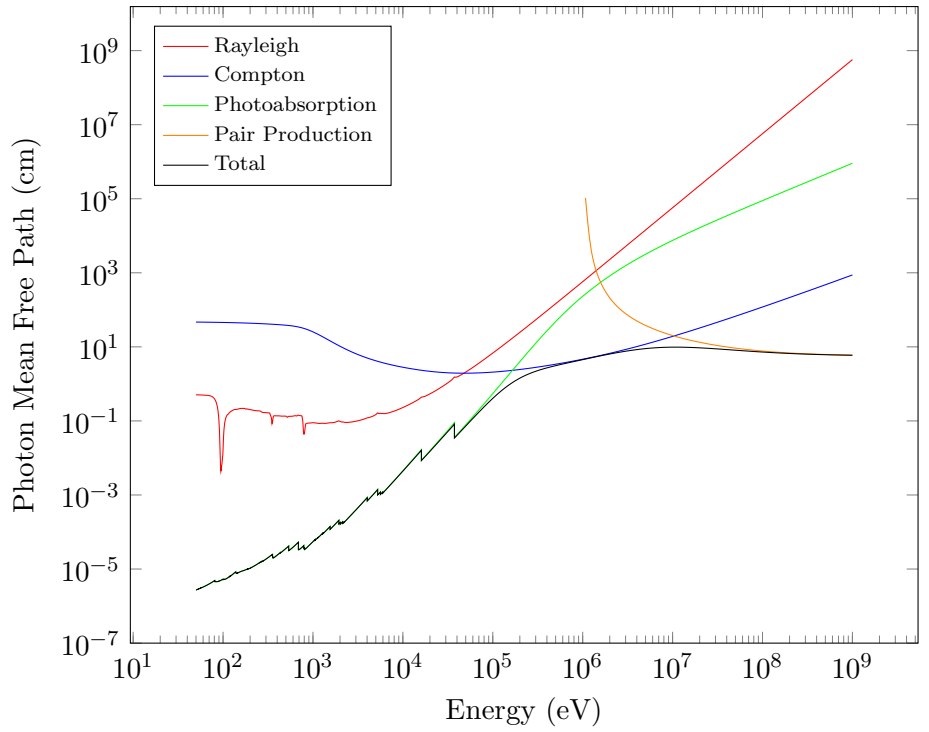

Figure A.7: Photon Mean Free Paths in fluoride phosphate glass.

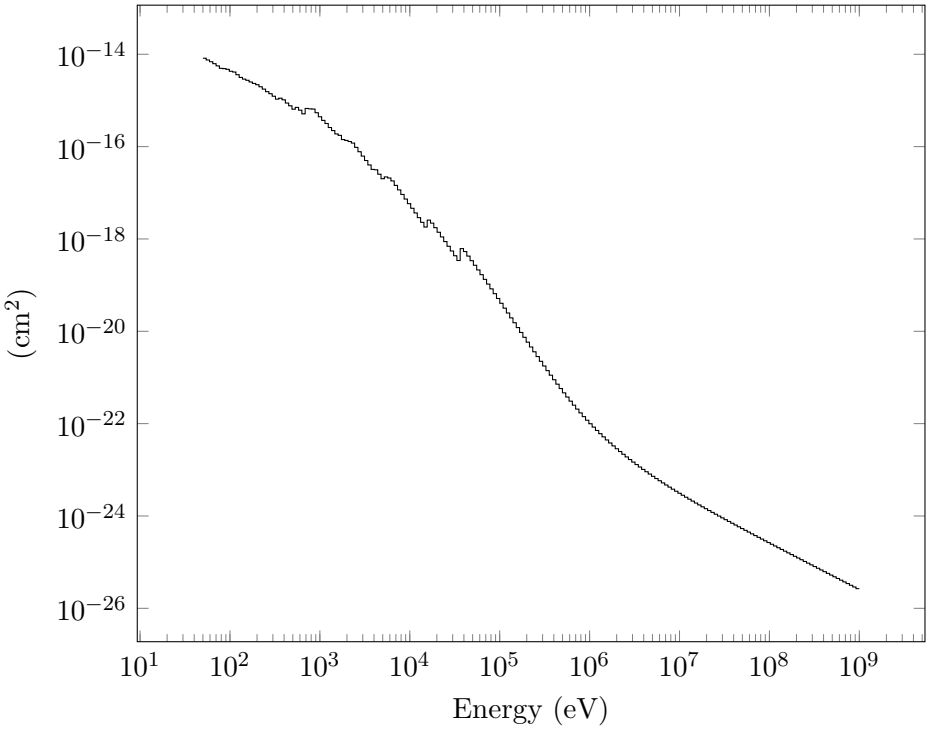

Figure A.8: Photoelectric cross-section ceiling in fluoride phosphate glass.

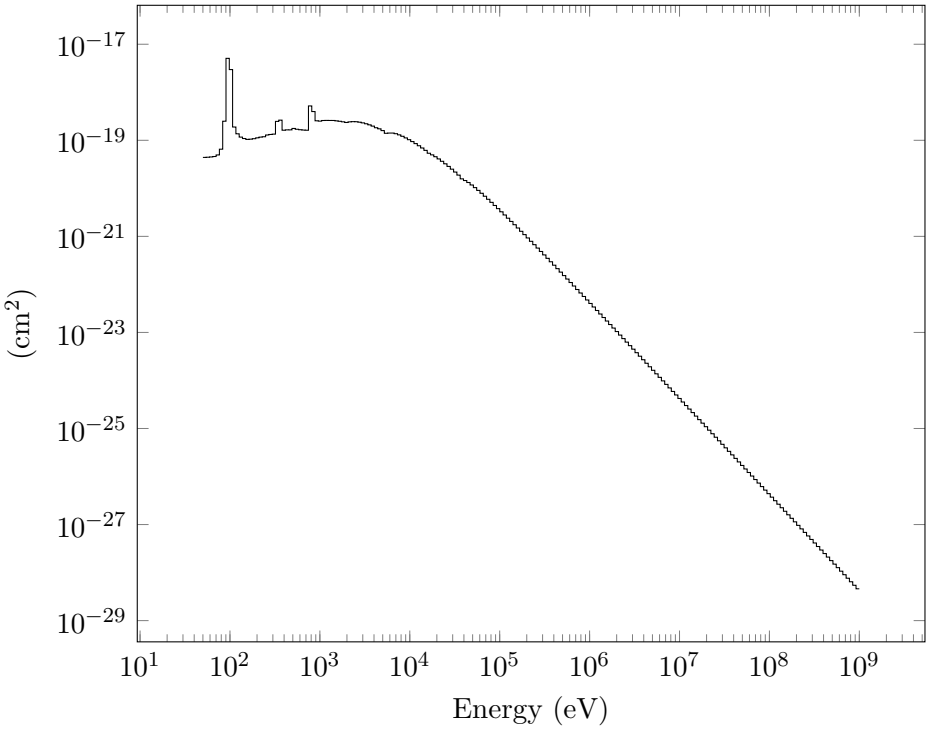

Figure A.9: Rayleigh cross-section ceiling in fluoride phosphate glass.

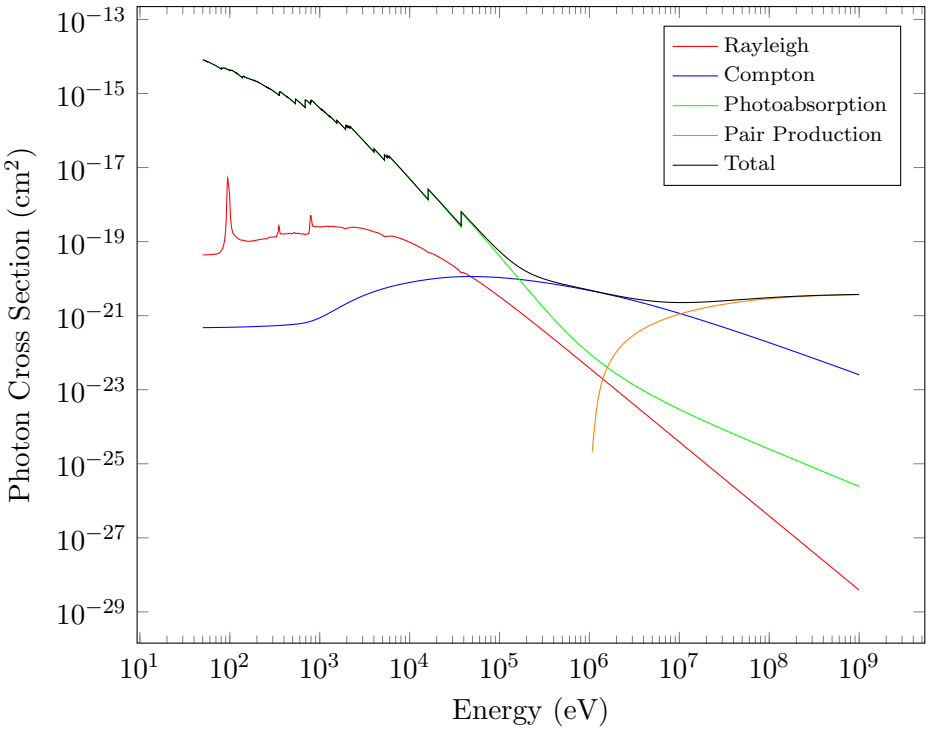

Figure A.10: Photon Cross Sections in fluoride phosphate glass.

Appendix B

Instrumentation and Fabrication Facilities

B.1 Risø TL/OSL DA-20 Reader

Usage of the Risø DA-20 TL/OSL Reader is described in this Section, a schematic diagram of the main functions of the instrument is provided in Figure B.1.

B.1.1 Sample Preparation

Glass samples are first crushed using a polished agate mortar and pestle. Polished agate is used so as not to contaminate samples with mineral ground off the surface of a stone mortar and pestle, which might contribute to the OSL and TL signal. Throughout the grinding stage, the glass is put through a seive to collect grains of between 250 - 350 µm, which are retained, and the remainder discarded. Next, the glass grains are mounted onto the 10 mm stainless steel sample discs used by the Risø Reader. discs are first weighed and then placed beneath a mask which leaves a 5 mm diameter circle exposed in the middle, after which they are sprayed with silicon oil. Glass grains are then placed on the disc in this 5 mm exposed face, after which the mask is removed, leaving a 5 mm diameter circle of glass grains stuck to the disc. Discs are weighed again to determine the mass of glass which has been mounted, they are then ready for analysis in the Risø Reader, the TL emission spectrometer and the single aliquot reader.

B.1.2 Sample Irradiation

In the Risø Reader, sample discs are loaded onto the sample carousel, which contains 48 places. Where possible, samples are only placed in every second sample position, to avoid cross-irradiation of samples during the irradiation stage.

The unit contains a 1.48 Bq $^{90}Sr/^{90}Y$ beta source, mounted 7 mm above the sample disc in a lead housing and operated pneumatically using pressurised nitrogen. Between the beta source and the sample is a 0.125 mm beryllium window which acts as a window to the measurement chamber in order to enable a vacuum.

Operation of the beta source is under computer control, and the software enables irradiation times as short as one second.

B.1.3 Luminescence Detection

Following irradiation, both TL and OSL measurements can be performed on the samples. The sample carousel moves the sample from the irradiation position to the luminescence detection position. A lift, which also acts as the TL heater plate, then lifts the sample into position for optical or thermal stimulation and luminescence detection. The distance between the sample and the PMT detector face is 55 mm, and the collection solid angle is 0.4 steradians.

Optically Stimulated Luminescece (OSL) Once the sample is in position, optical stimulation is applied to the sample using either 470 nm or 870 nm. 470 nm (with a FWHM of 20 nm) is produced by 4 clusters of LEDs, each containing 7 individual LEDs, the total power from the 28 LEDs is 80 mW/cm^2 at the sample position. When using 470 nm stimulation, a Hoya U340 filter is used in front of the PMT to absorb the scattered stimulation light but pass the luminescence produced in the sample. A Schott GG-420 long-pass filter is used to attenuate the short wavelength wing of the LED spectrum which overlaps slightly with the detection window of the Hoya U340 filter.

The 870 nm optical stimulation (with a FWHM of 40 nm) is provided by 3 LED clusters, each containing 7 individual LEDs, the total power from the 21 LEDs is 145 mW/cm^2 at the sample position. A Schott BG39 filter is used in front of the PMT to absorb scattered stimulation light.

Thermoluminescence (TL) When performing TL measurements, the sample is heated using the combined lift/heater-plate on which the sample is held in position be-

neath the PMT. Heating is applied at a constant rate, set by the user, and in this Thesis most measurements were performed at 1 K/s. During TL measurements, nitrogen is used to purge the sample chamber to avoid oxidation at the elevated temperatures, this nitrogen flow also assists in cooling the heater plate and sample following a measurement.

Although it is not necessary to use an optical filter in front of the PMT during TL measurements, because there is no optical stimulation applied, filters may still be used to analyse TL from certain wavebands of the TL emission.

A quartz window is positioned permanently between the sample and the PMT to avoid contamination of the PMT detector face with silicon oil, which can be evaporated from the sample disc due to the elevated temperatures used during TL analysis.

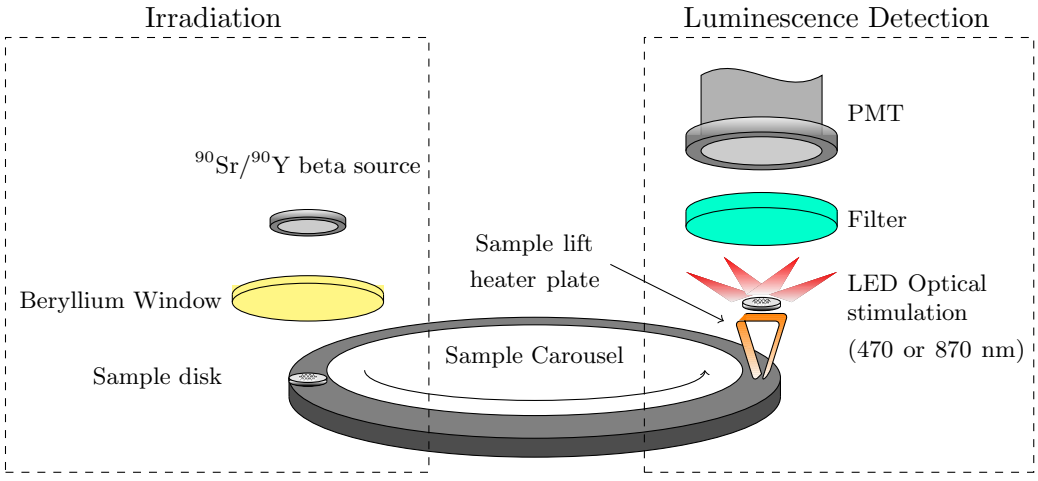

Figure B.1: Schematic diagram of a Risø DA-20 TL/OSL Reader, showing both the irradiation and luminescence detection functions.

B.2 Glass Fabrication

Facilities used for remelting and doping of FP glasses are shown in Figure B.2, the crucibles and moulds used for both reducing and oxidising melts are also shown in Figure B.3.

B.3 Extrusion Machine

The extrusion machine used for all extrusions of FP glass into fibre preforms is shown in Figure B.4. Extrusion of preforms contains the following procedure:

- A 30 mm diameter billet of FP glass is cleaned in isopropyl alcohol in an ultrasonic bath.

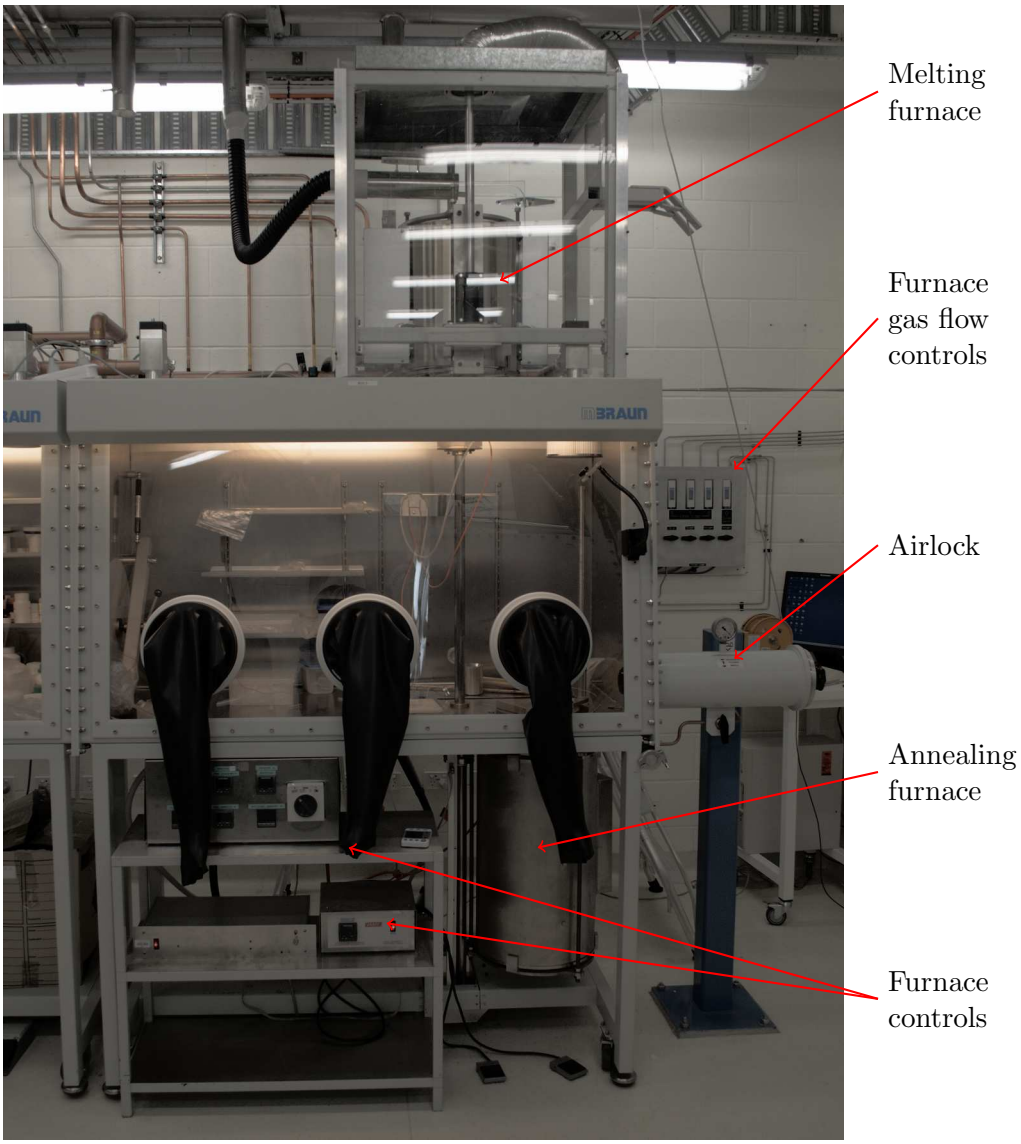

Figure B.2: Glass melting facilities. Top: nitrogen atmosphere glovebox for batching and melting of fluoride glasses. Bottom: open air melting and annealing furnaces.

Figure B.3: Crucibles and glass moulds used for remelting and doping of FP glasses. Vitreous carbon crucibles are used for reducing environment melts; the platinum crucible is used for open air, oxidising environment melts. Brass moulds are polished before use.

- Extrusion die pieces are washed. Stainless steel: ultrasonic bath once in detergent, once in distilled water. Macor: ultrasonic bath in isoproyl alcohol.
- The glass billet and die are assembled inside the body, and the body placed in the extrusion machine, after which all thermocouples are attached. The furnace is closed and positioned carefully to ensure a uniform temperature across the body.
- The heating profile for FP glass is programed into the heater.
- Heating is begun, and the extrusion machine is used to monitor the thermal expansion and slumping of the glass during the heating stage.
- Once the glass is at the extrusion temperature and has dwelled at this temperature for 40 minutes, extrusion is begun.
- Following extrusion, furnaces are cooled quickly. This is to ensure the preform is not left hanging under its own weight at an elevated temperature, which can result in a taper along the preform length.
- Once cool the preform is removed, then inspected, measured and finally annealed to remove any residual stresses in the glass. Following this, it is ready for any further treatment before fibre drawing.

B.4 Fibre Draw Tower

The optical fibre drawing tower used for all optical fibre and cane fabrication of FP fibre trials is shown in Figure B.5. The fibre drawing process is a straightforward procedure involving several steps:

- Following preform processing, it is cleaned by immersing in isopropyl alcohol in an

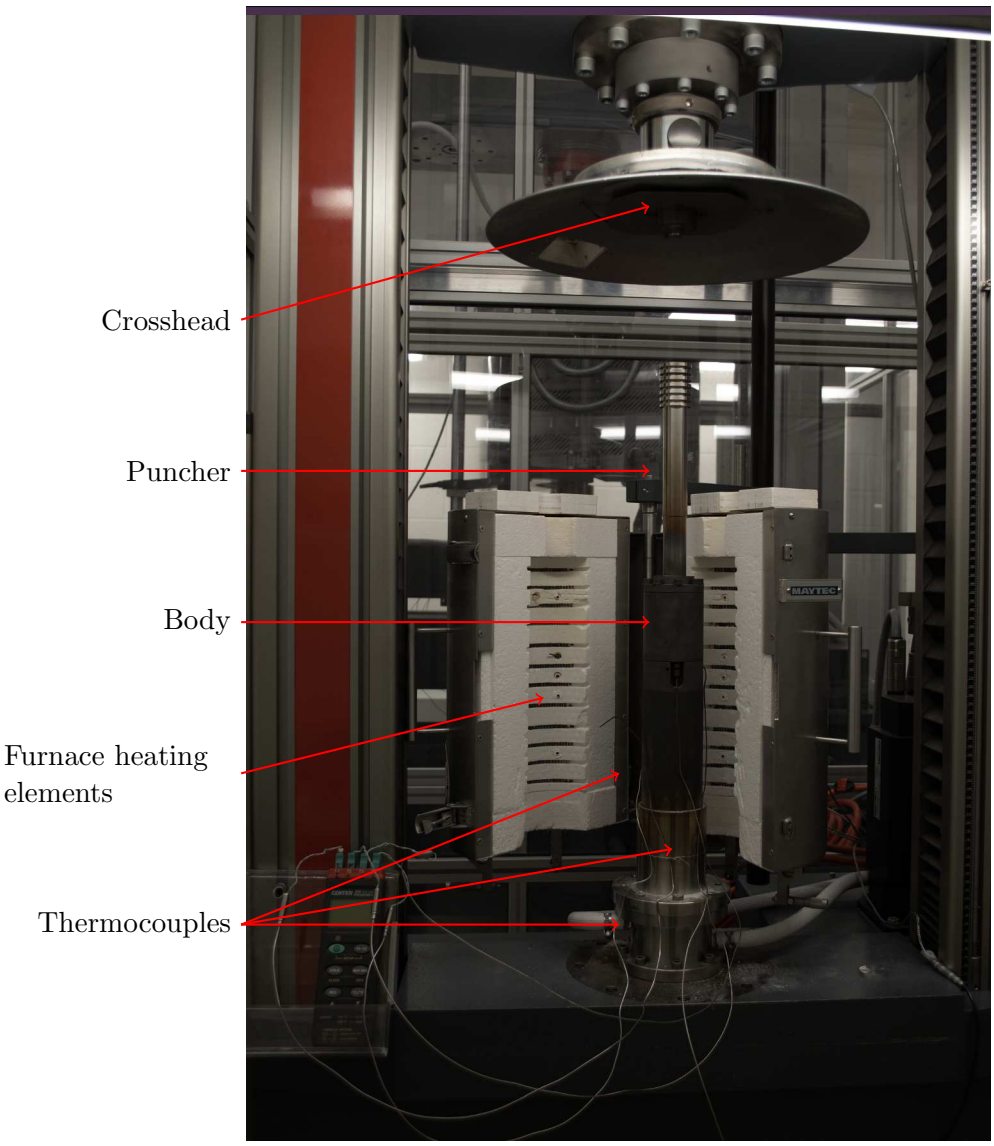

Figure B.4: Soft glass extrusion machine, used for all extrusions of fluoride phosphate preforms. The inside of the body is shown by a cross section diagram in Section 4.2, Figure 4.1.

ultrasonic bath for 15 minutes. This process is then repeated with fresh isopropyl alcohol.

- Preform is placed in the holder suspending it inside the radio frequency furnace at the top of the draw tower. For FP glass, a graphite suseptor is used in the furnace due to the presence of fluorine, which might react with a stainless steel susceptor.
- The furnace is purged with N_2 to remove oxygen and provide stable atmospheric conditions for the duration of the fibre draw.
- The furnace is ramped up first to 500 ℃, and then to the desired drawing temperature (i.e. 755 or 800 ℃).
- The temperature is then held at this value as the preform heats up enough to cause a 'drop'. This is where the glass softens to the point where it will drop under its own weight.
- Once the drop has fallen a sufficient distance it is cut off from the fibre, and the fibre then pulled onto the drum, routing it first through the tension measurement wheel.
- The preform feed is then started, which slowly feeds the preform into the hot zone of the furnace. Simultaneously, the drum is started and the speed of rotation is adjusted to achieve the desired fibre diameter. The fibre diameter is measured near the top of the fibre draw.
- Fibre is then drawn until the necessary yield is obtained. After this point, the feed rate and drum speed can be adjusted to obtain fibre of a different diameter. For FP fibres, this was done several times to achieve fibre bands of varying diameter.
- As the end of the preform nears the hot zone in the furnace, fibre drawing is halted. The fibre yield is then re-spooled onto a portable fibre drum, separating the different bands.
- Optical fibres are then characterised with loss measurements soon after they are drawn, to avoid loss due to degradation of the fibre from the ambient environment.

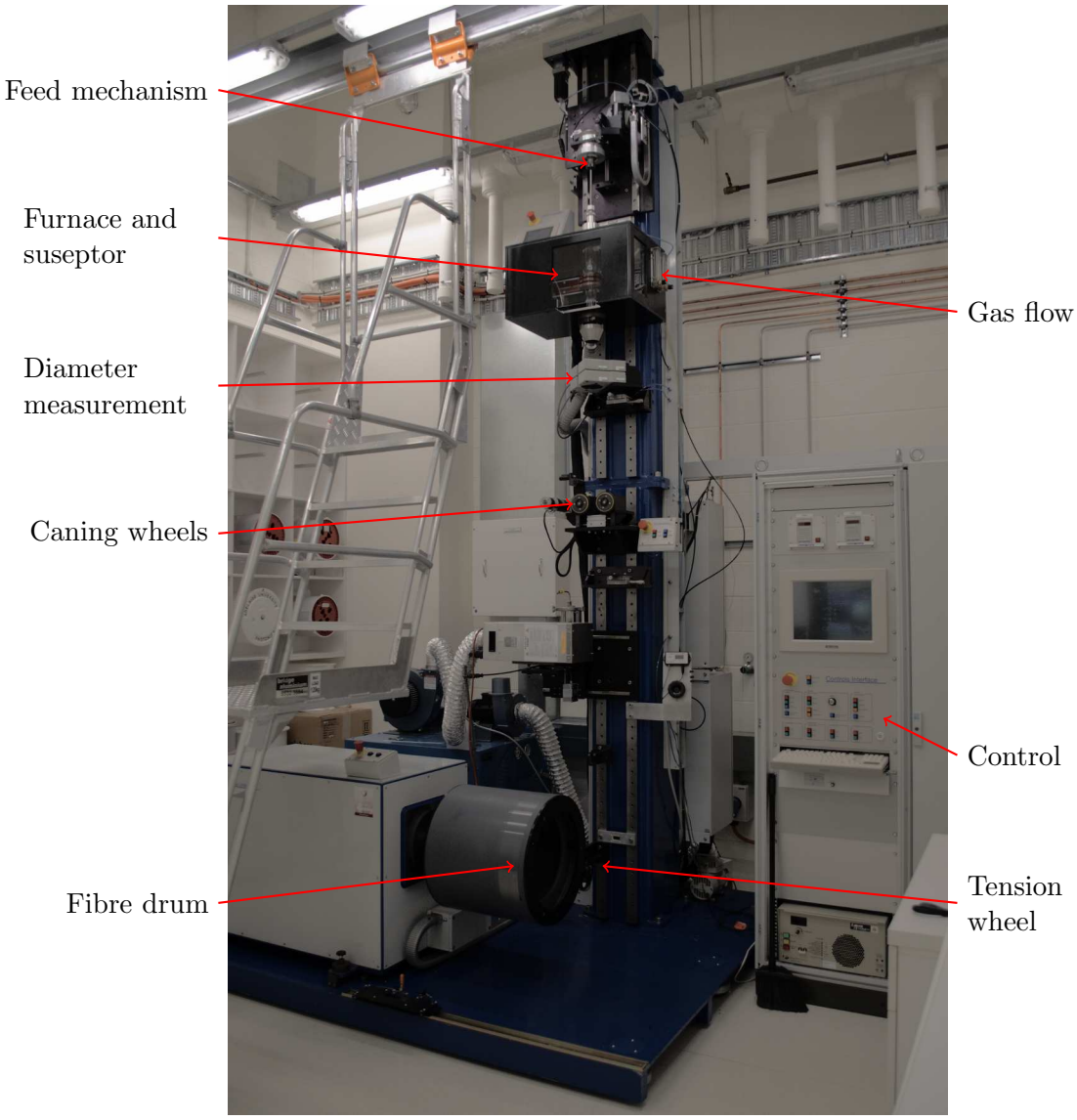

Figure B.5: Soft glass optical fibre draw tower.

Appendix C

Fabrication Data

C.1 Extrusion Data

Summary of the parameters used for each extrusion trial.

Trial	Material	Dimensions (mm)	T (℃)	Speed (mm/min)	N_2 (L/min)	Force (kN)	Dopant Conc. (ppm wt)
E1	SS	30x35	515	0.2			
E2	SS	30x35	525	0.2		7.5	
E3	graphite	30x35	506	0.1	0		
E4	macor	30x35	525	0.1	1		
E5	graphite	30x35	515	0.1	1		
E6	graphite	30x35	515	0.1	1	5.8	
E7	macor	30x33	515	0.037	1	6.5	
E8	macor	30x70	525	0.05	1	1.65	
E9	macor	30x35	525	0.05	1	2.8	
E10	macor	30x70	525	0.05	1	2.6	
E11	macor	30x70	525	0.05	1	3	
E12	macor	30x70	525	0.05	1	2.5	
E13	macor	30x70	525	0.05	1	1.7	
E14	SS	30x35	525	0.05	1	1.7	
E15	SS	30x35	528	0.05	1	5	7200
E16	SS	30x35	528	0.05	1	5.5	7200
E17	SS	30x38	525	0.05	1	4	720
E18	SS	30x38	531	0.05	1	4.5	7200

C.2 Fibre Drawing Data

Summary of parameters used for each fluoride phosphate fibre drawing trial. All draws used a gas flow rate of 7 (top) and 2 (bottom) l/min. F = pull failure.

Trial	Preform	Gas	Band	Diameter (µm)	Temp. (°C)	Feed Rate (mm/min)	Speed (m/min)
F1	E1	$N_2 + O_2$	1	160	747	1.4	5.2
			2	160	740	1.2	5.4
			3	160	737	1.2	5.1
F2	E2	$N_2 + O_2$	1	160	742	1.2	5.4
			2	160	748	1.4	6.4
			3	160	740	1.5	6.4
F3	E3	N2	1	160	745	1.3	5.6
			2	160	745	1.4	6.3
F4	E4	N2	1	160	745	1.6	7.4
			2	160	745	2	9
			3	160	745	2.5	10.1
F5	E5	N2	F				
F6	E6	N2	1	160	755	3	6
			2	160	755	1.5	6
F7	E7	N2	F				
F8	E8	N2	F				
F9	E9	N2	1	160	755	2.5	9
			2	160	755	3	8.6
			3	160	755	3.5	16
			4	160	754	3.8	17
			5	160	754	3.8	17.7
F10	E10a	N2	1	160	755	2.5	6.6
			2	160	755	3.5	16.8
			3	160	758	3	16.8
			4	160	758	3	16
			5	160	758	4.5	16
			6	160	758	4.5	13
F11	E10b	N2	1	160	755	2.4	10.2
			2	160	755	3	12.2
F12 (cane)	E12	N2	1	1300	745	3	
			2	1100	743	4	
F13 (cane)	E13a	N2	1	1000	745	4	
			2	800	745	1.5	
			3	600	745	2	
F14	E13b	N2	1	500	740	2.5	
			2	450	740	2.5	
			3	400	740	2.5	
			4	350	748	2.5	
			5	300	748	2.5	
			6	250	748	2.5	
			7	200	748	2.5	
			8	160	748	2.5	
F15	E14	N2	1	200	765	2.3	5.7
			2	160	765	2.3	9.7
F16 (cane)	E15	N2	1	1000	765	3.5	
			2	800	770	3.5	
			3	600	770	3.5	
			4	400	770	3.5	
F17	E16	N2	1	160	788	1.8	7.6
			2	200	788	1.8	5
			3	250	788	2.5	4.3
F18	E17	N2	1	160	800	2	8.6
F19	E18	N2	1	160	800	2.5	4.5
			2	200	800	2.5	9.1

Appendix D

PENELOPE Simulations

D.1 Stopping Power Calculations

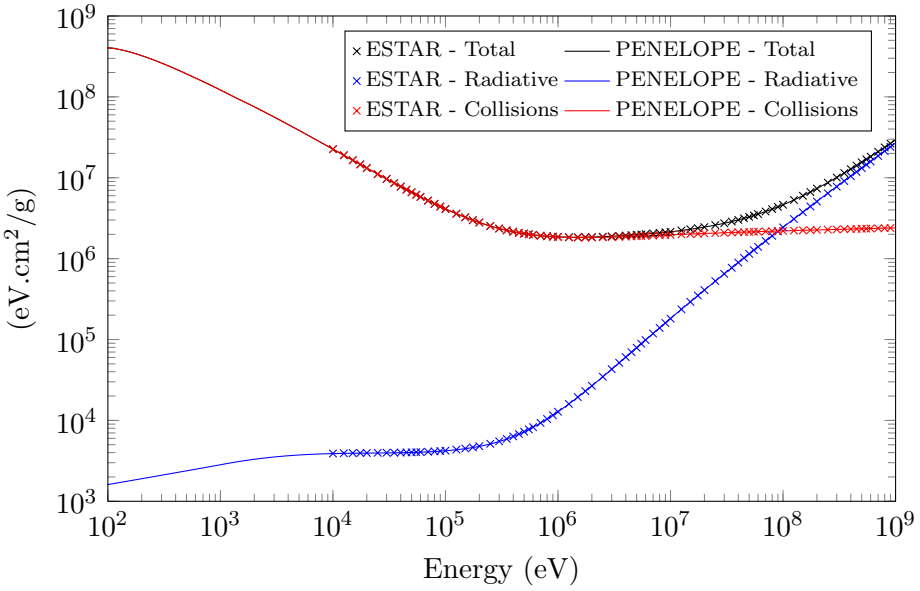

Figure D.1: Comparison of stopping power values for electrons in water, calculated using PENELOPE and ESTAR.

D.2 Electron and Photon Absorption in FP Glass

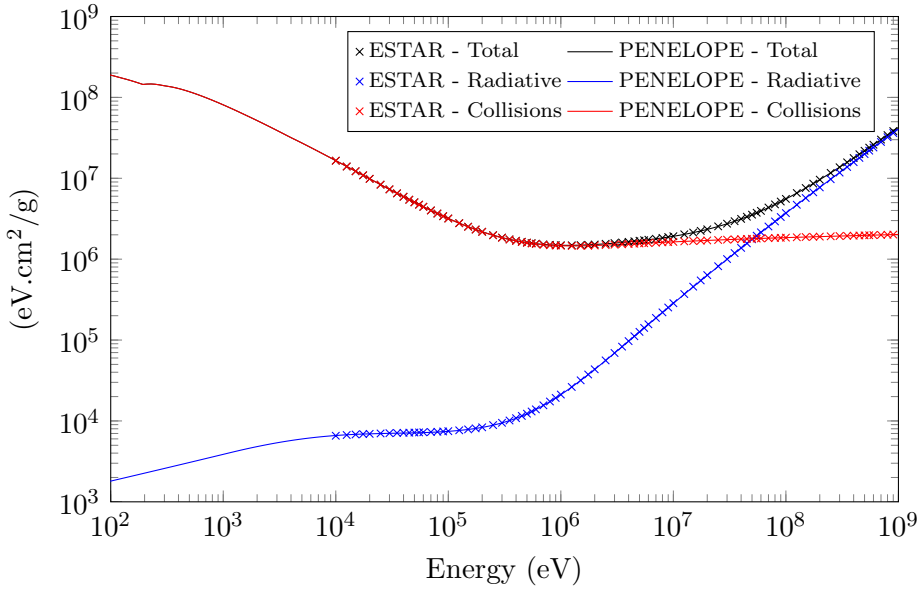

Figure D.2: Comparison of stopping power values for electrons in aluminium, calculated using PENELOPE and ESTAR.

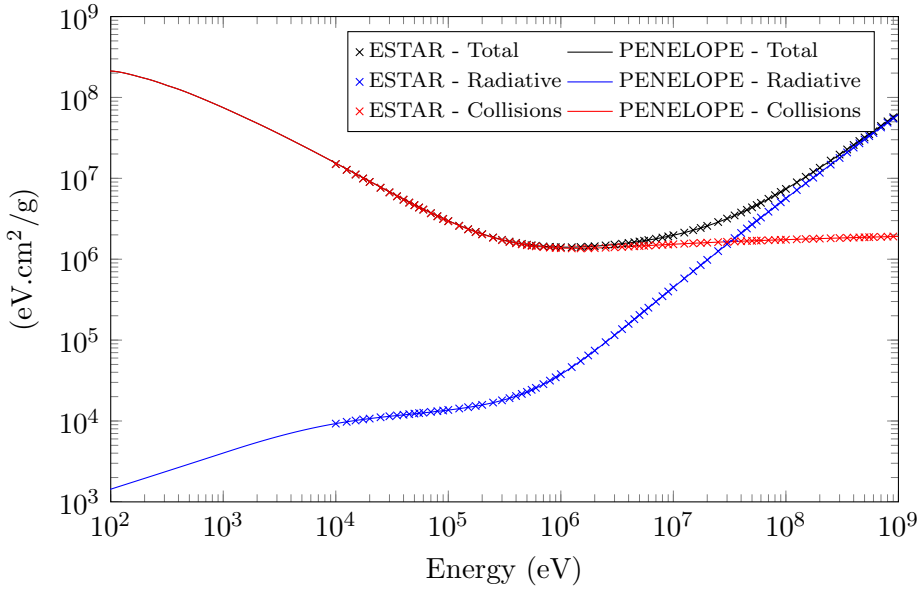

Figure D.3: Comparison of stopping power values for electrons in fluoride phosphate glass, calculated using PENELOPE and ESTAR.

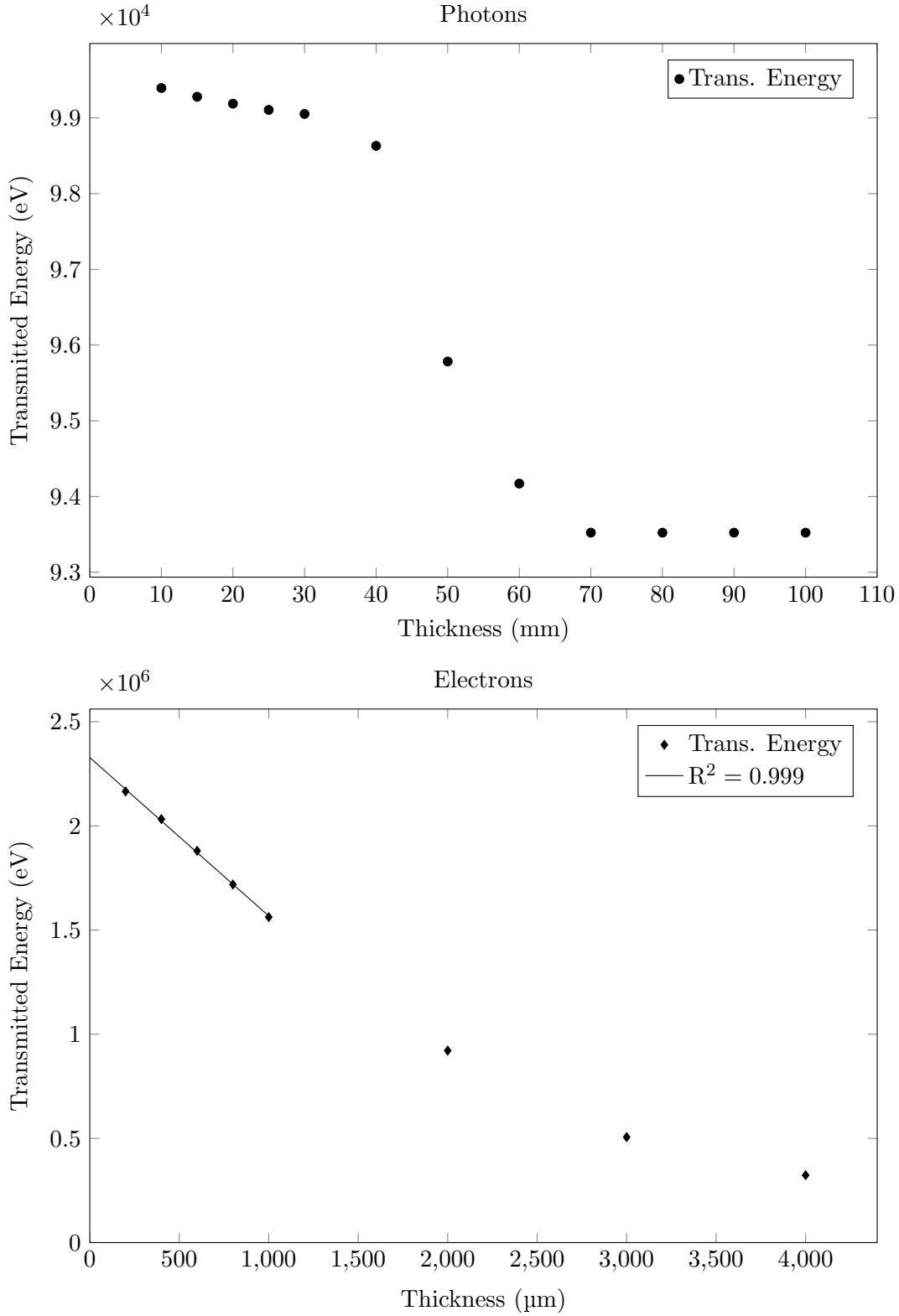

Figure D.4: Simulated energy of transmitted primary particles from a 2.28 MeV electron beam (left) and a 100 keV photon beam (right) by layers of FP glass with varying thickness. Simulation was performed using PENELOPE.

D.3 Examples of Simulation Input Files

Simulation of Depth dose with a 2.28 MeV electron beam.

```
TITLE  Parallel electron beam on an FP slab
       .
GSTART >>>>>>>> Beginning of the geometry definition list.
LAYER        0.00 +0.80  1
CENTRE       0.00  0.00
CYLIND   1   0.00  3.00
GEND   <<<<<<<< End of the geometry definition list.
       .
       >>>>>>>> Source definition.
SKPAR  1        [Primary particles: 1=electron, 2=photon, 3=positron]
SENERG 2.28e6           [Initial energy (monoenergetic sources only)]
SPOSIT 0 0 -1.0                    [Coordinates of the source centre]
SCONE  0 0 0                            [Conical beam; angles in deg]
       .
       >>>>>>>> Material data and simulation parameters.
MFNAME FPglass.mat                          [Material file, up to 20 chars]
MSIMPA 1.0e3 1.0e3 1.0e3 0.05 0.05 1e3 1e3    [EABS(1:3),C1,C2,WCC,WCR]
       .
       >>>>>>>> Counter array dimensions and pdf ranges.
NBTL   0 0.15 150          [Track-length interval and no. of TL-bins]
       .
       >>>>>>>> Energy-deposition detectors (up to 25).
ENDETC 0.0 1.0e7 180              [Energy window and number of bins]
EDSPC  spc-enddet-01.dat        [Output spectrum file name, 20 chars]
EDBODY 1 1                      [Active body; one line for each body]
       .
       >>>>>>>> Dose and charge distributions.
DOSE2D 1 1 100 100    [Tally 2D dose and charge dists. in body KL,KC]
       .
       >>>>>>>> Job properties
RESUME dump.dmp                [Resume from this dump file, 20 chars]
DUMPTO dump.dmp                   [Generate this dump file, 20 chars]
DUMPP  60                                    [Dumping period, in sec]
       .
NSIMSH 1e6                      [Desired number of simulated showers]
TIME   1e6                         [Allotted simulation time, in sec]
       .
END                                  [Ends the reading of input data]
```

Simulation of Depth dose with a 2.28 MeV photon beam.

```
TITLE  Parallel electron beam on a water slab
       .
GSTART >>>>>>>> Beginning of the geometry definition list.
LAYER        0.00 +60.0  1
CENTRE       0.00  0.00
CYLIND   1   0.00  3.00
GEND   <<<<<<<< End of the geometry definition list.
       .
```

```
       >>>>>>>> Source definition.
SKPAR  2        [Primary particles: 1=electron, 2=photon, 3=positron]
SENERG 2.28e6           [Initial energy (monoenergetic sources only)]
SPOSIT 0 0 -1.0                    [Coordinates of the source centre]
SCONE  0 0 0                            [Conical beam; angles in deg]
       .
       >>>>>>>> Material data and simulation parameters.
MFNAME FPglass.mat                          [Material file, up to 20 chars]
MSIMPA 1.0e3 1.0e3 1.0e3 0.05 0.05 1e3 1e3    [EABS(1:3),C1,C2,WCC,WCR]
       .
       >>>>>>>> Counter array dimensions and pdf ranges.
NBTL   0 0.15 150          [Track-length interval and no. of TL-bins]
       .
       >>>>>>>> Energy-deposition detectors (up to 25).
ENDETC 0.0 1.0e7 180              [Energy window and number of bins]
EDSPC  spc-enddet-01.dat        [Output spectrum file name, 20 chars]
EDBODY 1 1                      [Active body; one line for each body]
       .
       >>>>>>>> Dose and charge distributions.
DOSE2D 1 1 100 100    [Tally 2D dose and charge dists. in body KL,KC]
       .
       >>>>>>>> Job properties
RESUME dump.dmp                [Resume from this dump file, 20 chars]
DUMPTO dump.dmp                   [Generate this dump file, 20 chars]
DUMPP  60                                    [Dumping period, in sec]
       .
NSIMSH 1e6                      [Desired number of simulated showers]
TIME   1e6                         [Allotted simulation time, in sec]
       .
END                                  [Ends the reading of input data]
```

Simulation of X-rays onto FP glass volume within a volume approximating the aluminium fibre holder.

```
TITLE  20 deg photon cone on FP on Al fibre holder w.r.t. photon energy
       .
GSTART >>>>>>>> Beginning of the geometry definition list.
LAYER        -1.1 -0.5  1
CENTRE       0.00  0.00
CYLIND   1   0.00  10.0
LAYER        -0.5 -0.016  2
CENTRE       0.00  0.00
CYLIND   1   0.00  7.0
CYLIND   1   7.5  10.0
LAYER        -0.016 0.00 0.0  3
CENTRE       0.00  0.00
CYLIND   2   7.484  7.5
LAYER        0.00 +2.00  4
CENTRE       0.00  0.00
CYLIND   1   0.00  10.00
GEND   <<<<<<<< End of the geometry definition list.
       .
       >>>>>>>> Source definition.
```

```
SKPAR  2        [Primary particles: 1=electron, 2=photon, 3=positron]
SENERG 50e3           [Initial energy (monoenergetic sources only)]
SPOSIT 0 0 -29.5                    [Coordinates of the source centre]
SCONE  0 0 20                            [Conical beam; angles in deg]
       .
       >>>>>>>> Material data and simulation parameters.
MFNAME Al.mat                          [Material file, up to 20 chars]
MSIMPA 1.0e3 1.0e3 1.0e3 0.05 0.05 1e3 1e3    [EABS(1:3),C1,C2,WCC,WCR]
MFNAME FP_glass.mat                         [Material file, up to 20 chars]
MSIMPA 1.0e3 1.0e3 1.0e3 0.05 0.05 1e3 1e3    [EABS(1:3),C1,C2,WCC,WCR]
       .
       >>>>>>>> Counter array dimensions and pdf ranges.
NBTL   0 0.15 150          [Track-length interval and no. of TL-bins]
       .
       >>>>>>>> Energy-deposition detectors (up to 25).
ENDETC 0.0 300e3 180              [Energy window and number of bins]
EDSPC  spc-enddet-01.dat        [Output spectrum file name, 20 chars]
EDBODY 3 2                      [Active body; one line for each body]
       .
       >>>>>>>> Dose and charge distributions.
DOSE2D 3 2 100 100    [Tally 2D dose and charge dists. in body KL,KC]
       .
       >>>>>>>> Job properties
RESUME dump.dmp                [Resume from this dump file, 20 chars]
DUMPTO dump.dmp                   [Generate this dump file, 20 chars]
DUMPP  60                                    [Dumping period, in sec]
       .
NSIMSH 1e8                       [Desired number of simulated showers]
TIME   1e8                         [Allotted simulation time, in sec]
       .
END                                   [Ends the reading of input data]
```

Simulation of X-rays onto FP glass volume within a volume approximating the aluminium fibre holder without its lid, being replaced instead by an 0.1 mm layer of PVC.

```
TITLE  20 deg photon cone on FP on Al fibre holder w.r.t. photon energy
       .
GSTART >>>>>>>> Beginning of the geometry definition list.
LAYER        -0.55 -0.5  1
CENTRE       0.00  0.00
CYLIND   1   7.00  8.0
LAYER        -0.5 -0.016  2
CENTRE       0.00  0.00
CYLIND   2   0.00  7.0
CYLIND   2   7.5  10.0
LAYER        -0.016 0.00 0.0  3
CENTRE       0.00  0.00
CYLIND   3   7.484  7.5
LAYER        0.00 +2.00  4
CENTRE       0.00  0.00
CYLIND   2   0.00  10.00
GEND   <<<<<<<< End of the geometry definition list.
```

```
      .
      >>>>>>>> Source definition.
SKPAR  2        [Primary particles: 1=electron, 2=photon, 3=positron]
SENERG 50e3           [Initial energy (monoenergetic sources only)]
SPOSIT 0 0 -29.5                    [Coordinates of the source centre]
SCONE  0 0 20                            [Conical beam; angles in deg]
      .
      >>>>>>>> Material data and simulation parameters.
MFNAME PVC.mat                          [Material file, up to 20 chars]
MSIMPA 1.0e3 1.0e3 1.0e3 0.05 0.05 1e3 1e3    [EABS(1:3),C1,C2,WCC,WCR]
MFNAME Al.mat                         [Material file, up to 20 chars]
MSIMPA 1.0e3 1.0e3 1.0e3 0.05 0.05 1e3 1e3    [EABS(1:3),C1,C2,WCC,WCR]
MFNAME FP_glass.mat                          [Material file, up to 20 chars]
MSIMPA 1.0e3 1.0e3 1.0e3 0.05 0.05 1e3 1e3    [EABS(1:3),C1,C2,WCC,WCR]
      .
      >>>>>>>> Counter array dimensions and pdf ranges.
NBTL   0 0.15 150          [Track-length interval and no. of TL-bins]
      .
      >>>>>>>> Energy-deposition detectors (up to 25).
ENDETC 0.0 300e3 180              [Energy window and number of bins]
EDSPC  spc-enddet-01.dat        [Output spectrum file name, 20 chars]
EDBODY 3 2                      [Active body; one line for each body]
      .
      >>>>>>>> Dose and charge distributions.
DOSE2D 3 2 100 100    [Tally 2D dose and charge dists. in body KL,KC]
      .
      >>>>>>>> Job properties
RESUME dump.dmp                [Resume from this dump file, 20 chars]
DUMPTO dump.dmp                   [Generate this dump file, 20 chars]
DUMPP  60                                    [Dumping period, in sec]
      .
NSIMSH 1e8                       [Desired number of simulated showers]
TIME   1e8                         [Allotted simulation time, in sec]
      .
END                                   [Ends the reading of input data]
```

Simulation of X-rays onto silica glass volume within a volume approximating the aluminium fibre holder.

```
TITLE  20 deg photon cone on FP on Al fibre holder w.r.t. photon energy
      .
GSTART >>>>>>>> Beginning of the geometry definition list.
LAYER        -1.1 -0.5  1
CENTRE       0.00  0.00
CYLIND   1   0.00  10.0
LAYER        -0.5 -0.016  2
CENTRE       0.00  0.00
CYLIND   1   0.00  7.0
CYLIND   1   7.5  10.0
LAYER        -0.016 0.00 0.0  3
CENTRE       0.00  0.00
CYLIND   2   7.484  7.5
LAYER        0.00 +2.00  4
```

```
CENTRE       0.00  0.00
CYLIND   1   0.00  10.00
GEND   <<<<<<<< End of the geometry definition list.
       .
       >>>>>>>> Source definition.
SKPAR  2        [Primary particles: 1=electron, 2=photon, 3=positron]
SENERG 50e3           [Initial energy (monoenergetic sources only)]
SPOSIT 0 0 -29.5                    [Coordinates of the source centre]
SCONE  0 0 20                            [Conical beam; angles in deg]
       .
       >>>>>>>> Material data and simulation parameters.
MFNAME Al.mat                          [Material file, up to 20 chars]
MSIMPA 1.0e3 1.0e3 1.0e3 0.05 0.05 1e3 1e3    [EABS(1:3),C1,C2,WCC,WCR]
MFNAME SiO.mat                          [Material file, up to 20 chars]
MSIMPA 1.0e3 1.0e3 1.0e3 0.05 0.05 1e3 1e3    [EABS(1:3),C1,C2,WCC,WCR]
       .
       >>>>>>>> Counter array dimensions and pdf ranges.
NBTL   0 0.15 150          [Track-length interval and no. of TL-bins]
       .
       >>>>>>>> Energy-deposition detectors (up to 25).
ENDETC 0.0 300e3 180              [Energy window and number of bins]
EDSPC  spc-enddet-01.dat        [Output spectrum file name, 20 chars]
EDBODY 3 2                      [Active body; one line for each body]
       .
       >>>>>>>> Dose and charge distributions.
DOSE2D 3 2 100 100    [Tally 2D dose and charge dists. in body KL,KC]
       .
       >>>>>>>> Job properties
RESUME dump.dmp                [Resume from this dump file, 20 chars]
DUMPTO dump.dmp                   [Generate this dump file, 20 chars]
DUMPP  60                                    [Dumping period, in sec]
       .
NSIMSH 1e8                       [Desired number of simulated showers]
TIME   1e8                         [Allotted simulation time, in sec]
       .
END                                   [Ends the reading of input data]
```

Simulation of X-rays onto silica glass volume within a volume approximating the aluminium fibre holder without its lid, being replaced instead by an 0.1 mm layer of PVC.

```
TITLE  20 deg photon cone on FP on Al fibre holder w.r.t. photon energy
       .
GSTART >>>>>>>> Beginning of the geometry definition list.
LAYER        -0.55 -0.5  1
CENTRE       0.00  0.00
CYLIND   1   7.00  8.0
LAYER        -0.5 -0.016  2
CENTRE       0.00  0.00
CYLIND   2   0.00  7.0
CYLIND   2   7.5  10.0
LAYER        -0.016 0.00 0.0  3
CENTRE       0.00  0.00
```

```
CYLIND   3   7.484  7.5
LAYER        0.00 +2.00  4
CENTRE       0.00  0.00
CYLIND   2   0.00  10.00
GEND   <<<<<<<< End of the geometry definition list.
       .
       >>>>>>>> Source definition.
SKPAR  2        [Primary particles: 1=electron, 2=photon, 3=positron]
SENERG 50e3           [Initial energy (monoenergetic sources only)]
SPOSIT 0 0 -29.5                    [Coordinates of the source centre]
SCONE  0 0 20                            [Conical beam; angles in deg]
       .
       >>>>>>>> Material data and simulation parameters.
MFNAME PVC.mat                          [Material file, up to 20 chars]
MSIMPA 1.0e3 1.0e3 1.0e3 0.05 0.05 1e3 1e3    [EABS(1:3),C1,C2,WCC,WCR]
MFNAME Al.mat                         [Material file, up to 20 chars]
MSIMPA 1.0e3 1.0e3 1.0e3 0.05 0.05 1e3 1e3    [EABS(1:3),C1,C2,WCC,WCR]
MFNAME SiO.mat                          [Material file, up to 20 chars]
MSIMPA 1.0e3 1.0e3 1.0e3 0.05 0.05 1e3 1e3    [EABS(1:3),C1,C2,WCC,WCR]
       .
       >>>>>>>> Counter array dimensions and pdf ranges.
NBTL   0 0.15 150          [Track-length interval and no. of TL-bins]
       .
       >>>>>>>> Energy-deposition detectors (up to 25).
ENDETC 0.0 300e3 180              [Energy window and number of bins]
EDSPC  spc-enddet-01.dat        [Output spectrum file name, 20 chars]
EDBODY 3 2                      [Active body; one line for each body]
       .
       >>>>>>>> Dose and charge distributions.
DOSE2D 3 2 100 100    [Tally 2D dose and charge dists. in body KL,KC]
       .
       >>>>>>>> Job properties
RESUME dump.dmp                [Resume from this dump file, 20 chars]
DUMPTO dump.dmp                   [Generate this dump file, 20 chars]
DUMPP  60                                    [Dumping period, in sec]
       .
NSIMSH 1e8                      [Desired number of simulated showers]
TIME   1e8                        [Allotted simulation time, in sec]
       .
END                                  [Ends the reading of input data]
```